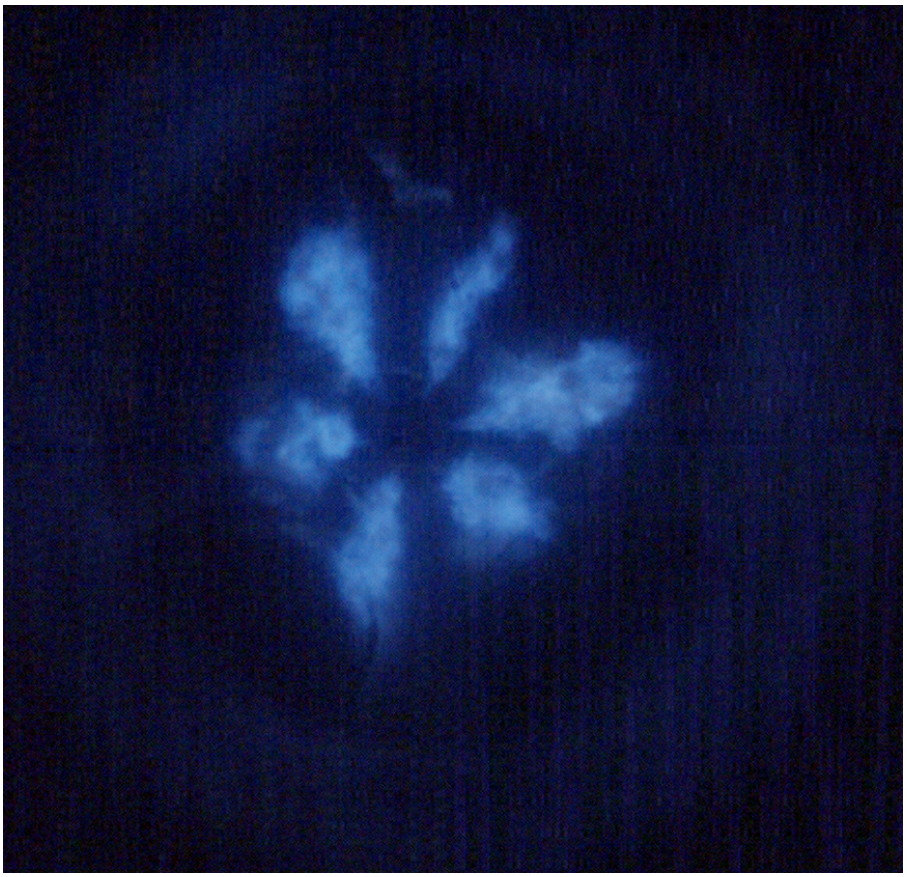

Passive Pre-Chamber Ignition Combustion and Performance Analysis

Master's thesis in Automotive Engineering

Elvin Zanjani 19960702

DEPARTMENT OF MECHANICS AND MARITIME SCIENCES

CHALMERS UNIVERSITY OF TECHNOLOGY
Gothenburg, Sweden 2023
www.chalmers.se

Master's thesis 2023

Passive Pre-Chamber Ignition Combustion and Performance Analysis

Elvin Zanjani

CHALMERS
UNIVERSITY OF TECHNOLOGY

Department of Mechanics and Maritime Sciences
Division of Combustion and Propulsion Systems
Department of Combustion and Fuel, Aurobay
Chalmers University of Technology
Gothenburg, Sweden 2023

Passive Pre-Chamber Ignition Combustion and Performance Analysis
Elvin Zanjani

Supervisor: Ayolt Helmantel, Aurobay, Combustion and Fuel, Technical Expert.
Supervisor: Slavej Tanov, Aurobay, Combustion and Fuel, Senior Analysis Engineer.
Supervisor CFD: Jaasim Mubarak Ali, Aurobay, Senior Simulation Engineer.
Examiner: Lucien Koopmans, Combustion and Propulsion Systems, Head of Division.

Master's Thesis 2023
Department of Mechanics and Maritime Sciences
Combustion and Propulsion Systems
Department of Combustion and Fuel, Aurobay
Chalmers University of Technology
SE-412 96 Gothenburg
Telephone +46 31 772 1000

Cover: Optical Measurement of PC1 Jets, 6 bar IMEP @ 1500RPM.

Typeset in LaTeX
Printed by Chalmers Reproservice
Gothenburg, Sweden 2023

Passive Pre-Chamber Ignition Combustion and Performance Analysis
Elvin Zanjani
Department of Mechanics and Maritime Sciences
Department of Combustion and Fuel, Aurobay
Chalmers University of Technology

Abstract

This study investigates the possibility of using a passive pre-chamber as a primary ignition source in an experimental single-cylinder gasoline-powered engine under stoichiometric conditions. The engine utilizes the Miller cycle and has the same bore and stroke dimensions to the production engine Aurobay VEP Gen3 LP, with modified cylinder head and piston resulting in a compression ratio of 13.45:1. Three Tenneco passive pre-chambers with different jet orientations were tested and compared against each other and a baseline spark plug. To evaluate the setups fuel efficiency and emissions, a minimap consisting of 11 operating points was generated by power-weight averaging the WLTP cycle. A VVT sweep was conducted to find the optimal camshaft phasing for each setup and operation point except one. The minimap was repeated three times over three consecutive days to assess the setups repeatability and robustness, and performance comparisons were made. A WOT (Wide Open Throttle) test was conducted to compare the setups full-load performance. This was complemented with a heat loss test, were one minimap run was conducted with all the setups running with the same input settings, including combustion phasing, camshaft phasing and mass airflow. Additionally, a cooled-EGR test was conducted to investigate the potential of reducing in-cylinder heat transfer losses using external cooled-EGR.

The WOT test and minimap cycling revealed three regions for the pre-chamber setups. During high load operation, a region dubbed as the "High Load Gain" region was identified, where the ability to advance combustion phasing resulted in a reduction in fuel consumption. On the other hand, during part load operation, a region dubbed the "Excess Heat Loss" region was observed, where the short combustion duration and inability to advance combustion phasing resulted in excessive in-cylinder heat losses. However, with the aid of cooled-EGR, these heat losses could be effectively reduced, leading to an increase in fuel conversion efficiency. Finally, the "Low Load Balanced" region was identified, where the total heat losses between the setups became comparable. This was mainly due to the pre-chamber setups advanced VVT settings, which trapped internal-EGR and reduced the in-cylinder heat losses adequately enough to be offset by the exhaust heat losses, resulting in comparable heat losses between all of the setups.

The tests concluded that the performance differences between the pre-chambers were minimal, with the simplest pre-chamber performing equally well as the rest. However, the performance difference between the pre-chamber and the baseline spark plug was substantial, with the pre-chamber outperforming the spark plug in repeatability, robustness, and fuel consumption in almost every test conducted, with

the highest gain in fuel consumption observed at high load, with the reduction exceeding 6%. Therefore, the results of this thesis strongly suggest that pre-chamber technology has great potential for application in future Aurobay engines and is a promising avenue for future research and development.

Acknowledgements

It's has been a fun and exciting journey, during which I have had the privilege of meeting many incredible people. I feel fortunate to have had the opportunity to learn from these bright minds. Every day was filled with excitement and learning opportunities, and I enjoyed every second of my time here at Aurobay. However, like all good things, everything must come to an end. I dedicate this section to all the incredible people who helped me throughout my adventurous journey.

I would like to start by expressing my deepest gratitude and thanks to my main supervisors Ayolt Helmantel, Slavej Tanov and Jaasim Mubarak Ali for all of their incredible and exceptional supervision and guidance during my time with this thesis. Thank you all for the incredible help and support, and allocating time to answer questions whenever necessary. It was truly an honor and a privilege to work with and learn from such exceptional professionals. I was always curious of pre-chamber technology and I remember my first internship at the company, where I first met Ayolt and remember us discussing how exciting pre-chamber technology looks. To later be granted the opportunity to tests this incredible ignition source by Ayolt and his team was absolutely a dream come true. Thank you so very much! I will like to also extend my gratitude to the other members of the combustion team Mattias Berntsson and Martin Eriksson for the delightful company, help and for allocating time for all of the necessary support, especially with regards to optical measurements and resolving test bed related issues when the equipment decided to malfunctioned. *Tack så mycket till er båda!*

Furthermore, I express my gratitude to our group leader Camilla Odermalm for welcoming me into the group and providing all the necessary support and assistance. I would also like to thank our remaining group members Andreas Josefsson, Hans Linder, Iman Shahram, Jens Lundmark, Alexandre Marchet, Andreas Wikberg, Danilo Pires and Ebba Andrén for all the fun chitchat during fika and lunch. It was a pleasure working with you all. I would also like to express my thanking to Sajjad Radmehr and Daniel Constantin, who introduced me to the company and the world of combustion engine development. I cannot thank you enough for allowing me to pursue my passion for these incredible machines. This thesis would not have been possible without your initial trust and support.

Lastly, I would like to extend my sincere gratitude to my examinator Lucien Koopmans for his valuable feedback and guidance throughout this thesis. Your expertise and insights have been incredibly helpful in shaping my work, and I am grateful for your time and effort.

Elvin Zanjani, Gothenburg, March 2023

Bu magistr dissertasiyasını sevimli əmim Samir Maguerramova həsr edirəm. Ümid edirəm ki, yenidən görüşə bilərik.

List of Acronyms

Below is the list of acronyms that have been used throughout this thesis listed in alphabetical order:

ATDC	After Top Dead Center
AHR	Accomulated Heat Release
BMEP	Brake Mean Effective Pressure
BDC	Bottom Dead Center
BTDC	Before Top Dead Center
BTE	Brake Thermal Efficiency
CO	Carbon Monoxide
CO_2	Carbon Dioxide
CoV	Coefficient of Variance
CI	Compression ignition
CAD	Crank Angle Degree
CLMEP	Combustion Loss Mean Effective Pressure
CFD	Computational Fluid Dynamics
DOC	Diesel Oxidization Catalyst
DPF	Diesel Particulate Filter
DFI	Direct Fuel Injection
EIVC	Early Intake Valve Closing
EGR	Exhaust Gas Recalculation
EXMEP	Exhaust Mean Effective Pressure
eVVT	Exhaust Variable Valve Timing
FuelMEP	Fuel Mean Effective Pressure
FMEP	Friction Mean Effective Pressure
GHG	Green House Gases
H_2O	Water
HTIMEP	Heat Transfer Mean Effective Pressure
HC	Hydrocarbons
HRR	Heat Release Rate
IC	Internal Combustion
iVVT	Intake Variable Valve Timing
IMEP	Indicated Mean Effective Pressure
ISFC	Indicated Specific Fuel Consumption
$ISNO_x$	Indicated Specific NO_x
ISCO	Indicated Specific CO
ISTHC	Indicated Specific THC

LNT	Lean NO_x Trap
MBT	Maximum Brake Torque
MFB	Mass Fraction Burned
MEP	Mean Effective Pressure
NO_x	Nitrogen Oxides
NVH	Noise Vibration Harshness
OEM	Original Equipment Manufacturer
PMEP	Pump Mean Effective Pressure
PFI	Port Fuel Injection
PC	Pre-Chamber
PV	Pressure Volume
RoHR	Rate of Heat Release
RMF	Resdual Mass Fraction
RPM	Revolutions Per Minute
RMax	Pressure Rise Rate
SI	Spark Ignited
SP	Spark Plug
SCR	Selective Catalytic Reduction
S_L	Laminar Flame Speed
S_T	Turbulent Flame Speed
TJI	Turbulent Jet Ignition
THC	Total Hydrocarbons
TDC	Top Dead Center
TKE	Turbulent Kinetic Energy
UHC	Unburned Hydrocarbons
VVT	Variable Valve Timing
WOT	Wide-Open Throttle
WLTP	World-wide Harmonized Light-Duty Test Cycle

Nomenclature

Below is the nomenclature of indices, sets, parameters, and variables that have been used throughout this thesis.

Parameters & Variables

γ	Isentropic Coefficient
r_c	Compression Ratio
η	Efficiency
λ	Air–fuel Equivalence Ratio
θ_d	Flame-development Angle
θ_b	Rapid Burning Angle
θ_o	Overall Burning Angle
$\theta_{50\%}$, AI50	Combustion Phasing
$IMEP_g$	Indicated Mean Effective Pressure Gross
$IMEP_N$	Indicated Mean Effective Pressure Net
CoV_{IMEP_N}	Coefficient of Variance of $IMEP_N$
σ_{IMEP_N}	Standard Deviation of $IMEP_N$
ϕ	Equivalence Ratio
OH^*	Hydroxyl Radical
CH^*	Methylidyne Radical
η_f	Fuel Conversion Efficiency
$W_{indicated}$	Indicated Work
η_{th}	Thermal Efficiency
Q_n	Net Heat Released
Q_{LVH}	Lower Heating Value
m_f	Massflow Fuel
J	Joules

$P_{Indicated}$	Indicated Power Produced
P	Pressure
V	Volume
θ	Crank Angle
N	Engine Speed [RPM]
V_d	Piston Swept Volume
Q_{cr}	Crevice Heat Flow
Q_{ht}	Heat Transfer
Q_{ch}	Chemical Energy Released During Combustion, Gross Heat-Release
$Q_{ch_{net}}$	Net Heat-Release
η_{ComEff}	Combustion Efficiency
°C	Degree Celsius

Contents

List of Figures

List of Tables

1
Introduction

The automotive industry is on a constant path of improvement and the internal combustion engine is no exception. Though many established automobile companies aim to electrify their fleet, combustion and hybrid powered automotive vehicles still account for a considerable share of the global market [1]. This is therefore a solid indication that there is still a considerable demand for automobiles powered by the internal combustion engine and will be for some time in the future. It should therefore come as no surprise that the internal combustion engine continues and will continue to be developed for the considerable future and will come to play an important role in the life's of many people around the world for the foreseeable future.

1.1 Background

In the recent centuries the development of technology has enabled improvements in living standards across the planet. These advancements are not only driven by convenience but also with the urge to find improvements that would revolutionise the way ordinary citizens would normally conducted their way of life. The advent of the automobile in the latter part of the 19th century in one such item that revolutionised the way people commuted. As Henry Ford once famously quoted *"If I had asked my customers what they wanted they would have said a faster horse"* indicating that people of the times where themselves unaware of the revolution that technology would bring them. This revolution was enabled by the invention of two crucial thermodynamic cycles that to this day still dominate the transport sector. These two cycles are the Otto-cycle invented by Nikolas Otto in 1876 and the Diesel-cycle by Rudolf Diesel in 1892.

Automotive vehicles powered by the spark ignited (SI) internal combustion (IC) engine based on the Otto-cycle and the compression ignition (CI) IC engine based on the Diesel-cycle both utilise chemical combustion of liquid fuels to produce mechanical power. With this however a new form of challenge has emerged and its predominately associated with the emission of greenhouse gases formed in the combustion process of these fossil based liquid fuels in these two cycles. It is widely recognised today that emissions such as carbon dioxide (CO_2) and water vapor (H_2O) are among the main contributors to global warming and in a recent publication by the European Environment Agency[2], the transport sector accounts for 27% of the total greenhouse gas emissions in the European Union as illustrated in

Figure 1.1.

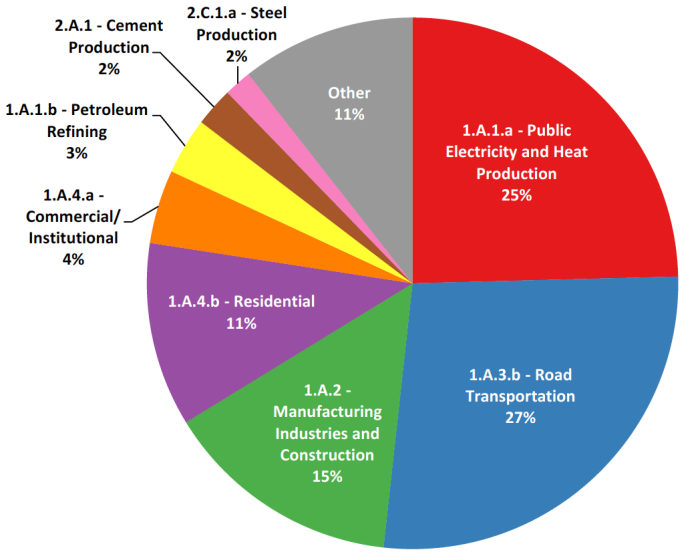

Figure 1.1: Carbon dioxide sector wise contribution to GHG in the European Union, image from [2].

The increased concentration of GHGs (Green House Gases) in the earths atmosphere has led to the elevation in the global average temperatures due to the gases effectively trapping heat energy inside the planet and not letting it dissipated back into the space. Metaphorically, its effects are like the one found in green houses in the agriculture industry, hence the name. The hypothesis regarding GHGs is supported by the records of data gathered throughout history regarding the global average temperature and this is illustrated in Figure 1.2. As seen, the annual mean has in the recent decades shown an increasing trend. The increased temperature has increased the melting of the ice covers near the poles, which in turn has resulted in an increase in sea levels. Other effects that are bounded by the increase in average global temperatures are the shifts in weather patterns causing the presence of warmer and prolonged seasons and the increase in droughts which subsequently lead to forest wild fires that savages many parts of the world.

Other emissions that are a bi-product of combustion such as nitrogen oxides (NOx), particle matter (PM), unburned hydrocarbons (UHC) and carbon monoxide (CO) all pose a threat to human health as they are extremely poisonous. The air quality in urban areas also suffers as a result of these emission and according to the European Implementation Assessment [4] poor air quality was responsible for 379000 premature deaths in 2018 alone. Both of these effects on human health and global warming has not gone unnoticed by the governing bodies around the world and their effective answer has been the introduction of legislation regarding emissions standards which dates back to the 1960s. The first emission standard was enacted during this time period in California as a means to combat the smog problem that was emerging in Los Angeles [5]. Europe, USA and Japan all followed suit and introduced emis-

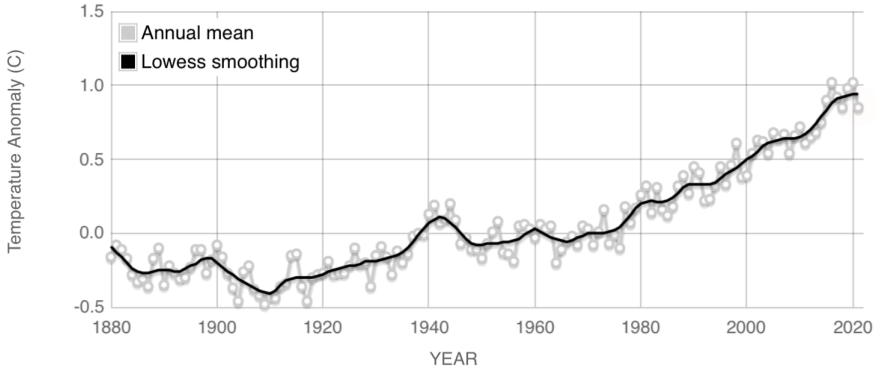

Figure 1.2: Global temperature annual mean, 1880 to 2020, image from [3].

sions standards into there respective jurisdiction as a means to control air pollution. Stricter legislation mandated car manufacturers to install after-treatment systems to be able to compile with these new standards. The 3-way catalytic converter became common for the SI IC engine after the introduction of electronic engine control, which had the ability to purposely fluctuate the combustion conditions withing a narrow band around stoichiometric ($\lambda = 1$), constantly alternating between slightly rich ($\lambda < 1$) and slightly lean ($\lambda > 1$). This allows for effective reduction or conversion of the harmful CO, HC and NOx to CO_2, H_2O and nitrogen (N_2). The after-treatment system for the diesel powered CI IC engine driven primarily at lean ($\lambda > 1$) conditions is unable to make use of the 3-way catalytic converter due to it being inoperative as conditions diverge from stoichiometric. This means that the conventional diesel powered CI IC engine after treatment system is composed of a diesel oxidization catalyst (DOC), selective catalytic reduction (SCR) or lean NOx traps (LNT) and the diesel particulate filter (DPF) which naturally implies that the entirety of the system is more complex and expensive. Although the introduction of these systems combined with advancements in engine technology has alleviated the emission dilemma, emission legislation continues however to grow stricter and stricter by the decade. Its therefore of great interest and urge to develop efficient engines to further reduce the impact these emissions to not only be able to meet these new requirements but also for the benefit of both the environment and air quality.

The focal point of development with regards to the gasoline powered SI IC engine has been the combustion process and thermal efficiency. These are two areas of of dedication which not only help with reducing the tailpipe emissions but also improves fuel economy. With regards to these points, the CI IC engine has some major advantages that triumph the SI engine. One of these major advantages is the lack of a throttle which, depending on load, accounts for up to 30% of the losses in a SI IC engine [6]. Technologies such as the early intake valve closing (EIVC) camshafts and cooled exhaust gas recirculating (EGR) do alleviate the issue of pumping losses for the SI IC engine but at the cost of reduced main charge turbulence and combustion stability since the EGR tolerance is effectively governed by the ignition process to reliably and reputably ignite the mixture. Another major advantage of the CI IC

engine is due to it obtaining a much higher compression ratio which in turn yields higher thermal efficiency. The compression ratio of SI IC is limited by the tendency of the end-gases to self-detonate leading to knocking combustion which when left unchecked can lead to catastrophic engine failure. One possible solution to tackle the above mentioned issues regarding knock, reduction in turbulence induced by using EIVC or the combustion stability degradation due to EGR is the use of a pre-chamber ignition system.

1.2 Motivation and Challenges

Pre-chamber combustion utilizes a separate volume located on the cylinder head separated via a set of orifices. During the compression stroke, air/fuel mixture is forced into this volume and when this mixture ignites, the pressure difference between the main chamber and the pre-chamber will drive the propagating flame front into the orifice, creating a hot and turbulent jet. Depending on the number of orifices the pre-chamber contains, the hot jets will be ejected into the main combustion chamber in several directions, creating several dispersed ignition sites. All of these hot jets will thus become a source of ignition for main bulk mixture in the main chamber to combust. Due to the rapidness of the main chamber combustion initiated by the pre-chamber, it is of high interested for the automotive industry. The multiple high energy ignition sites in combination with high turbulence introduced into main chamber lead to a fast burning combustion characteristic which is an attractive solution to mitigate the initiation of knock, reinstate losses burn-rate initiated by EIVC camshafts (Miller cycle) [7] and to increase the cooled exhaust gas recirculation (cooled-EGR) ignition limit.

Despite these potential benefits in combustion burn-rate, to the best of the author's knowledge, it has only been implemented in production for one light duty automobile vehicle, that being the sports car Maserati MC20 which also utilizes a spark plug inside the main chamber [8]. The reason for this lack of relevancy is believed to be, other than the increase in complexity imposed by such ignition source, is its inherent sensitivity to the control environment as was pointed out by Sir Harry Ricardo whom first proposed the pre-chamber engine back in 1918 [9]. This point is still valid today some 100 years later as demonstrated by D. E. Lee et al [10] as the cycle to cycle variation during low load operating resulted in inconsistent combustion and engine operation.

The potential enhancement in efficiency as a result of the pre-chamber is an attractive proposition and their inherent sensitivity can be prevailed as proven by the major OEMs like MAHLE Powertrains and Hitachi [11] [12] whose research indicate that stable and reputable combustion is achievable. As such, the motivation behind this research is thus to validate if stable engine operation is possible in combination with beneficial technologies that compile with the aim of better thermal efficiency such as the Miller cycle and higher compression ratio using a passive pre-chamber as the primary ignition source.

1.3 Research objective and Investigation Conduct

The research objective of this thesis is to validate the stability and performance of the main chamber combustion initiated by the passive pre-chamber in a test environment. The test rig is equipped with a single cylinder engine closely resembling the geometry of the production engine VEP Gen3 LP bore and stroke. To aid with the research objectives and the validation process, research questions where generated and this thesis will thereby look to answer the following questions:

- Is the passive pre-chamber generating consistent and repeatable results?
- How does the orientation of the pre-chamber effect the combustion characteristics and performance?
- What are the efficiency improvements (if any) in comparison to a conventional spark plug setup?

The first question will focus on robustness of the combustion cycle and the generated results. This will be conducted by repeated mini-map cycling. It is of importance that the test results generated can be repeated and that the system as a whole is robust. The second question looks to address the combustion characteristics as a function of pre-chamber orientation. The three passive pre-chambers variants are supplied by Tenneco and are configured to have different jet penetration orientation. As such, the investigation will include the effects of the different turbulence wake induced by the different orientations on the main chamber burn-rate. The third question looks to address the performance of the pre-chamber compared to a conventional spark plug with the help of theoretical analysis.

The research questions can be summarised as criterias that the pre-chamber has to fulfil, with particular heavy emphasis being placed on the first and second question. Stable running in all loads and speeds operations is paramount for this system to be deemed a success and if any point was to fail, it is important to understand why it failed and what can be done to mitigate this. The investigation is aimed to be conducted in as realistic manner therefore conventional gasoline 95E10 at stoichiometric conditions is to be used throughout testing (with the only exception being during the WOT test, where 98 octane fuel was instead used) to enable the option to run 3-way catalytic converter effectively.

2

The Spark Ignited Internal Combustion Engine

The spark ignited internal combustion engine is highly complex with multiple moving parts that all accumulate to convert of liquid or gaseous fuels into mechanical power. As such, it is important to study the relevant background information to understand the working principles of this engine. In this chapter, the working principles of the spark ignited internal combustion engine and the associated challenges will be explored.

2.1 Spark Ignited Internal Combustion Engine Fundamentals

2.1.1 The Otto-Cycle

The working principle of the spark ignition (SI) internal combustion engine (sometimes referred to the Otto engine, gasoline or petrol engine) is based on the Otto-cycle proposed by Nikolaus Otto in 1876. This cycle is based on four strokes: intake stroke, compression stroke, expansion stroke and exhaust stroke [6] [13].

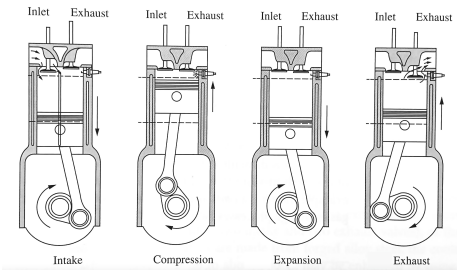

(a) Four strokes of the Otto cycle, reproduced from [6].

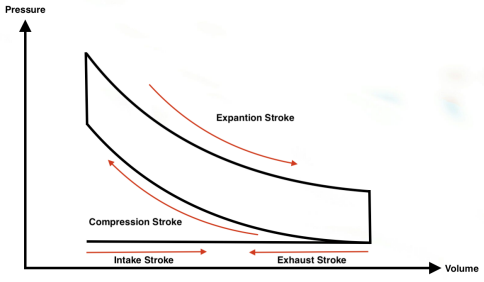

(b) PV diagram, Otto Cycle.

Figure 2.1: Otto Cycle

The following section, and this thesis in fact, will primarily focus on the compression and expansion stroke where chemical combustion commences leading to subsequent heat release which causes the piston to move and produce mechanical power. The

other strokes will be explored but only in the sense that they may benefit from the different combustion process initiated by the pre-chamber.

2.1.2 Combustion Process of the Conventional Direct Injection SI Engine

The combustion process of the conventional SI IC engine is highly complex and is characterised by a self-sustaining thin reaction sheet (or a pre-mixed flame) where exothermic reactions occur. The liquid fuel is injected with high pressure during the intake stroke to yield atomisation and to maximise homogeneous mixing with the incoming air. The airflow inside the cylinder during the intake stroke can be characterised as a tumble motion and motion aids in the mixture preparation and the burn-rate which will be discussed later in this section. The homogeneous mixture is then compressed during the compression stroke and ignition commences as the piston reaches top dead center (TDC). Ignition is initiated by discharging a high voltage between the electrode gap in the spark plug which in-turn leads to a spark that ignites the compressed mixture. The ignition of this mixture gives rise to a flame kernel and a reaction sheet which in its earliest instance of appearance is approximately spherical in shape, propagating and consuming the unburned mixture at a slow flame speed in all direction. This flame speed is termed the laminar flame speed to emphasize the speed of consumption of the unburned mixture normal to the flame front. The temperature profile of the reaction sheet as it consumes the unburned homogeneous mixture is depicted in Figure 2.2 with its division into the typical zones that yields it distinct characterises. Consumption starts in the preheat zone whereby the unburned mixture is heated by conduction by the consumed mixture ahead of it in the conduction zone. The mixture then gets consumed into the conduction zone where mass diffusion of species and conduction from the mixture in the preceding zone further raises its temperature. When the temperature of the mixture is high enough, a fuel oxidation chemical reactions will occur. The reaction zone is the predominant area whereby the main bulk of the chemical energy of the fuel is released.

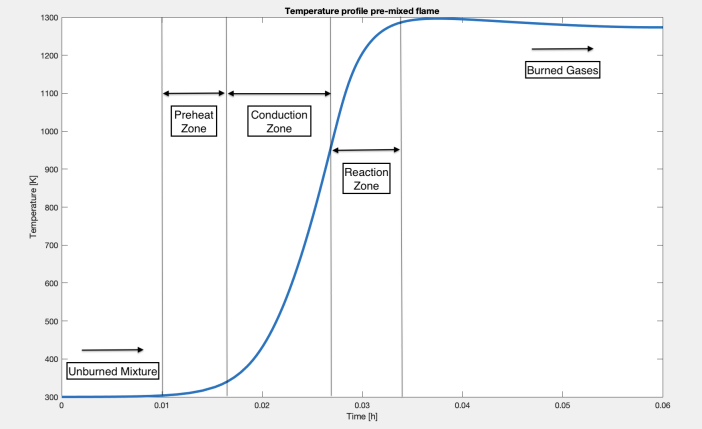

Figure 2.2: Temperature profile of a pre-mixed flame at 1 Bar and 300K isooctane. Derived from Cantera.

The self-sustaining nature of the reaction sheet as depicted in Figure 2.2 is what whats commonly dubbed as propagation. The rate of consumption of the unburned mixture is determined by mixture content and the diffusion and reaction rate of the fuel. Any change in these parameters will effect the slope of the temperature profile and thereby the thickness of the flame as it is defined by the addition of the pre-heat, conduction and reaction zone. A thicker flame yield a slower burn due to the increase in time required for the mixture to reach the temperature whereby fuel oxidation can occur. The burn rate is however most effected by the turbulence present in the combustion chamber during combustion phase. Turbulence wrinkles and distort the reaction sheet, substantially increasing its area and thereby the rate of which unburned mixture can be consumed.

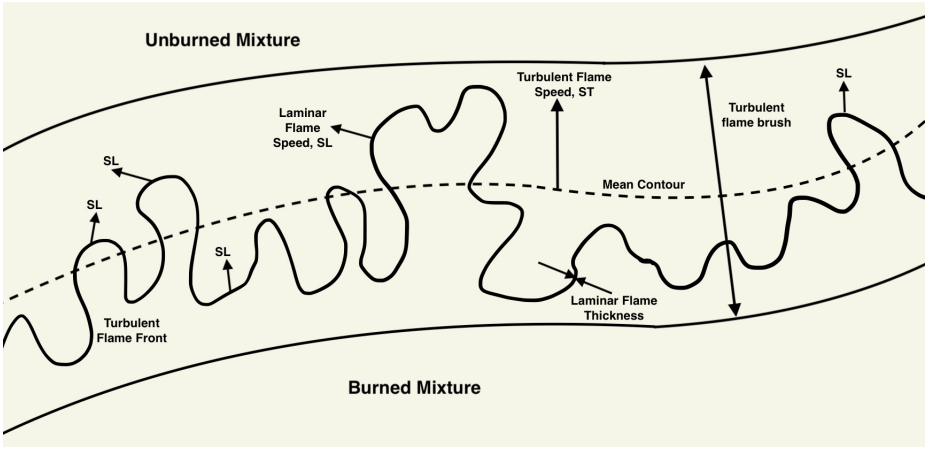

Figure 2.3: Turbulent Flame Brush.

The speed of which the distorted and wrinkled reaction sheet consumes the unburned mixture ahead of it is known as the turbulent flame speed (S_T). The flame will propagate locally at the laminar flame speed (S_L) but the mean contour of the flame brush will move and consume the unburned mixture at the turbulent flame speed.

As the rate of combustion changes due distortion of the flame front, the accumulated heat release rate will change as a function of crank angle. The accumulated heat release curve (or the mass fraction burned curve) showcases the burning angles as the main bulk combustion commences and three phases exists, flame-development angle, rapid-burning angle and overall burning angle as illustrated in Figure 2.4. Flame-development angle, θ_d, is the crank angle interval in which spark is discharges (θ_S) and 10% of the charge burned ($MFB_{0-10\%}$). This angle is used to determine delay between the spark, which gives rise a spherically shaped kernel with a mean flame contour speed of laminar flame speed, and a rapidly evolving flame front whereby the consumption of the bulk unburned mixture commences. This is primarily influenced by the flow field and mixture composition in the vicinity of the spark plug. The rapid burning angle, θ_b, is measured from 10% to 90% of charge consumption ($MFB_{10-90\%}$) and is the interval whereby the bulk of the mixture is consumed. The turbulent flame brush is fully evolved, consuming the bulk mixture at a turbulent flame speed and extinguishing as it hits the cylinder walls. The overall burning

angle (θ_o) is the combined angle of the flame development and the rapid burning angle which yields the duration of combustion. As soon as the flame extinguishes against the cylinder wall, heat from the combustion chamber will start conducting to the combustion chamber walls and this magnitude of heat transfer increases as the cycle is drawn out.

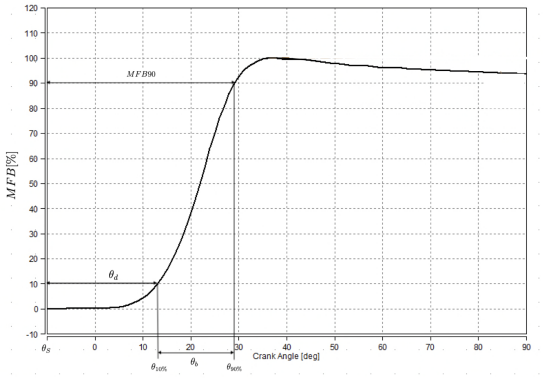

Figure 2.4: Mass fraction burned (MFB) as a function of crank angle, wide open throttle (WOT).

The heat transfer and crevice flow losses during combustion are depicted in Figure 2.5. The red line in the figure is the net heat released (Q_n) which indicate the net energy released during combustion. The blue line indicates the total available input energy (Total Input Energy, Fuel Energy, mfQ_{LHV}) before and after combustion. The combustion inefficiency's include crevice losses, losses due to unburned hydrocarbons (UHC) not participating in the combustion process and incomplete combustion that causes dissociation which result in carbon monoxide (CO) emissions. This loss is depicted as the jolt in the Total Input Energy curve which results in a reduction in the net available energy (Energy After Combustion). The difference between the accumulated heat release and the blue line (Energy After Combustion) is the loss due to heat transfer to the exposed surfaces in the combustion chamber.

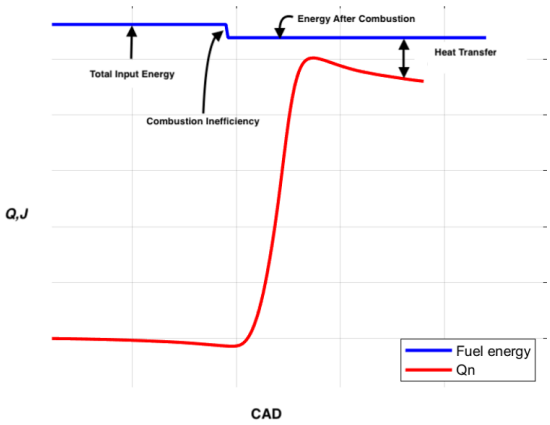

Figure 2.5: Accumulated heat release curve in Joules (J) as a function of crank angle (CAD).

The derivative of the accumulated heat release will yield the rate of heat release (RoHR) which is depicted as the blue line in Figure 2.6a. The maximum burn rate, or the maximum value of the RoHR, always occur around 50% MFB ($\theta_{50\%}$), as can be seen Figure 2.6a. This parameter,($\theta_{50\%}$), is used for the phasing of combustion and represents the extent of which the center of combustion and maximum heat release rate is shifted from the maximum brake torque (MBT). MBT should always be targeted to around 6-8 CA ATDC. The maximum in cylinder pressure, depicted in Figure 2.6b, is close to $\theta_{90\%}$ whereby the flame front is close to making contact with the chamber walls. As contact of the wall is established, the reaction sheet will quench, marking the end of combustion. The temperature in the combustion chamber is still high and heat will start conducting to all of the surfaces in the chamber and this can be seen in Figure 2.5 as *Heat Transfer*. The total losses accumulated during one full cycle will be explored in more detail later in this section. As the piston approaches BTC, the exhaust valve will open and the pressure difference between the combustion chamber and the atmosphere combined with the piston transversing up in the combustion chamber (commencing the exhaust stroke) will drive the exhaust gases out. As the piston approaches TDC, the intake valve will open and the cycle repeats.

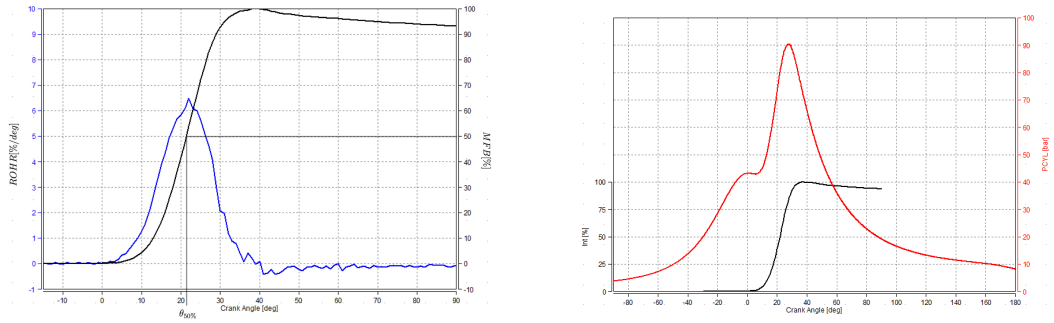

(a) Rate of heat release ($RoHR$) as a function of crank angle degree.

(b) Pressure curve as a function of crank angle degree.

Figure 2.6: MFB superimposed on Pressure and RoHR curve as a function crank angle degree, WOT.

2.1.3 Coefficient Of Variance CoV_{IMEP_N}

As one can imagine, not every cycle will exhibit the same behavior as variation in mixture content, air-fuel mixing and flow field within the cylinder and near the spark plug all generate differences in burn-rate cycle-to-cycle. The cycle-to-cycle variation thereby not only effects the torque output at any given instance due to fast or slow burning cycles, it also effects the driveability of the vehicle. A common example of cyclic variation is the pressure trace, see Figure 2.7, as the difference in mixture burn rate causes the in-cylinder pressure trace and heat-release rate to differ cycle-to-cycle. The strategy that is implemented to measure these cyclic variations, derived from the pressure trace, is the coefficient of variation in indicated mean effective pressure CoV_{IMEP_N}:

$$CoV_{IMEP_N}[\%] = \frac{\sigma_{IMEP_N}}{\overline{IMEP_N}} * 100 \tag{2.1}$$

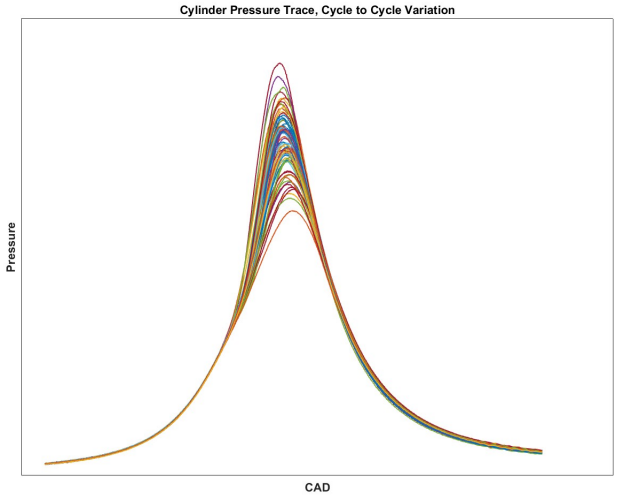

Figure 2.7: Cycle To Cycle Variation, 3 bar IMEP @ 1500RPM, $CoV_{IMEP_N} = 2.3$, Spark Plug.

Where σ_{IMEP_N} is the standard deviation of $IMEP_N$ over a predetermined set of cycles and $\overline{IMEP}$ is the mean $IMEP_N$ over this set of cycles. The rule of thumb is to achieve CoV_{IMEP_N} of below 3%.

2.1.4 Mean Effective Pressure and Losses

The common way of expressing the engine work output is in the relation to the swept volume V_d and this is termed mean effective pressure (MEP) [14]. The two commonly used terms in relation to the MEP is brake mean effective pressure (BMEP) and indicated mean effective pressure (IMEP) but there are more available terms and these terms can conveniently be used to express the losses endued in a IC engine. The sankeydiagram in Figure 2.8 illustrates the energy cascade from the energy content of the fuel to the brake output power from the engine.

The fuel energy content can be expressed as fuel mean effective pressure or FuelMEP. This is in basic terms the theoretical energy content of the fuel before the onset of air mixing and combustion. As combustion commences, there will be losses endured due to combustion inefficiency (CLMEP, see Figure 2.5 and the accompanying text) and the final heat generated by the combustion process is QMEP. Not all of the total heat generated will induce work on the piston and a sizable margin of the heat will be transferred to the exposed surfaces (HTMEP) and exhaust (EXHMEP). The remaining heat energy used for work extraction on the piston is expressed as indicated mean effective pressure gross or $IMEP_g$ (GMEP is also expressed terms). This can also be described as the total extraditable work over the compression and expansion stroke in the Otto-cycle. However during the entirety of the four stroke

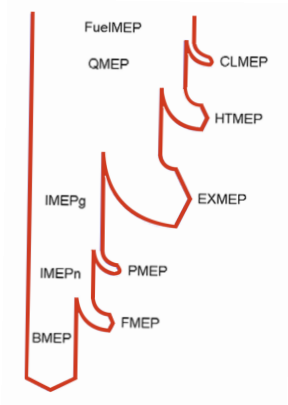

Figure 2.8: Sankeydiagram over energy flow from fuel to work expressed in mean work. Reproduced from [14].

cycle, the gas exchange process will induce losses due to the difference in pressure between the exhaust and intake manifold. The latter will, in most cases, be less meaning work is required to overcome the pressure depression and this dubbed pumping losses or with respect to the sankeydiagram, PMEP. Subtracting losses due to pumping with the total extraditable work generates indicated mean effective pressure net or $IMEP_N$. Work is however required to overcome the frictional force endorsed by all of the different internally moving engine parts and to drive the different auxiliaries attached to said engine. Subtracting all of the frictional forces from the net extractable work ($FMEP - IMEP_N$) yields the final harvested power is dubbed brake mean effective pressure or BMEP. Losses therefore represent a sizable majority of the input energy and in the following section will explore these losses in more detail.

2.2 Efficiency Challenges Associated with the SI Engine

The thermal efficiency of the first engines developed using the Otto-cycle was around 11% and since then, various technological improvements have been made to improve this poor performance. With respect to the combustion process and accordance with this thesis, some of the focal points of development regarding the Otto-cycle based IC engine can be summarised as follows:

- Compression ratio which limits the temperature ratio that the gas can expand upon. This in turn governs how much of the fuel can be converted into mechanical power.
- Excess heat losses to exhaust.
- Work relating to pumping, or pumping losses, due to excessive throttling of the induction air at part or low load operation.

2.2.1 Losses Related to Compression Ratio

The theoretical thermal efficiency of the Otto-cycle is explained by observing its governing equation:

$$\eta_{th} = 1 - \frac{1}{r_c^{\gamma-1}} \tag{2.2}$$

Whereby r_C is the compression ratio and γ is the isentropic coefficient of the in-cylinder charge. This equation, therefore, assumes that the swept volume of the compression stroke equals the swept volume of the expansion stroke. In the case of the Miller cycle, the effective compression ratio reduces meaning a reduction in the swept compression volume. However, the expansion ratio remains the same as the compression ratio, thus the equation still applies. As observed from the equation, as the compression ratio increases, so does the efficiency of the cycle. This is because the compression ratio is directly coupled to the temperature ratio in which the gas expands upon during the expansion stroke when the piston is traversing from top dead center (TDC) to bottom dead center (BTC). When the gas expands through a higher temperature ratio, more work is extracted per energy content of the fuel. The isentropic coefficient is determined by both the temperature and mixture content and this value is around 1.32 $\pm$0.015 depending on the cycle to cycle variation at stoichiometric conditions. As the mixture is made progressively more lean or diluted with EGR, this value increases which in turn also increases the thermal efficiency of the cycle.

Even though this relationship between compression ratio and efficiency was well known at the times of early development of the Otto-cycle IC engine, this ratio did not exceed 4. The reason for this limiting factor was the available fuels which lead to severe knock if this ratio was not respected. Ever since, improvement in the quality of the fuel and various other improvements has resulted in the raising this ratio and today this value, depending on the method of induction, is around 9-14.5. However, it could be argued that the same boundary conditions that limited early development of the SI IC engine still apply today as knock is one of the major limiting factors of why this ratio is not elevated to even greater values.

2.2.2 Part Load Operation Losses and the Miller Cycle

In part load operation of the SI IC engine, pumping losses are a prevalent phenomenon that works against the efficiency of the engine. Control over load, or airflow, is initiated by the use of a throttle. As such, when part load operation is required the air pressure in the intake manifold usually falls below atmospheric pressure. In order to draw air into the cylinder from the intake manifold, the piston is required to do work against the manifold depression and this is termed pumping work or loss. The losses generated here can be reduced with the help of various mechanisms and one such mechanism is the utilisation of the Miller cycle, or early intake valve closing (EIVC). The Miller cycle builds upon the Otto-cycle however with a slight modification and that being the closure of the intake valve commences

earlier then it otherwise would, effectively reducing the swept volume by the means of EIVC.
By closing the intake valve early, the manifold pressure has to increase to allow the compensation for the reduction in in-cylinder mass that this would otherwise give. The effective compression ratio is reduced as well, resulting in lower in-cylinder temperatures by the end of the compression stroke which subsequently results in the mitigation of knock buildup. The drawback is that the charge air motion, and subsequently the turbulence of the in-cylinder air is reduced, reducing the turbulent flame speed and thereby the burn rate.

2.2.3 Exhaust Losses and Knock

The excess heat loss to the exhaust is mainly controlled by the unburned mixture content and the combustion phasing, although it can also be influenced by other factor such as inlet temperatures and pressure. As mixtures diverge too lean or rich from stoichiometric, adiabatic flame temperature and laminar flame speed tend to drop due to less availability of either the reactant or the oxidiser, leading to an reduction in exhaust temperature and enthaply. For the rich case, the abundance of unburned hydrocarbons at the end of the expansion stoke also helps to cool the combustion bi-products, which also reduces the exhaust temperatures however negatively effects the fuel consumption. Combustion phasing is a parameter that not only governs the exhaust heat losses and temperature but also the performance of the engine. As combustion is phased from MBT, i.e retarded from MBT, a lesser fraction of the total enthalpy energy released during the exothermic combustion is now extracted as work on the piston, being instead mostly dispositioned to the exhaust. The rule of thumb is that the combustion timing should always be set so to achieve 50% mass fraction burned (MFB) at around 6-8° after TDC, however this is not always achieved for all loads and speeds due to the retardation of timing for knock suppression.

Knock in a SI engine is classified into 2 different categories, post-ignition knock which is when the unburned mixture in the end gases auto-ignites ahead of the advancing flame after spark onset and pre-ignition knock which is auto-ignition of the mixture before spark onset. Knock of both kinds have a higher probability of occurrence if the in-cylinder temperature and pressure are high. During post-ignition knock, the end gases have a higher probability to auto-ignite or detonate due to prolong heat exposure and compression against the cylinder wall by the propagating flame combined with heat conduction and radiation by said flame. These factors causes the end gases temperature, pressure and density to increase. As this happens, the unburned mixture in the end gases may undergo exothermic chemical reactions which can lead to there products auto-igniting. Overheating surfaces and/or deposits left by the previous combustion cycle which causes localized regions of exothermic centers known as hotspots are also known to cause the end gases to auto-ignite. If the end gases auto-ignition, a very rapid release of energy occurs. A pressure wave is frequently generated, which oscillates in the combustion chamber that produce an notorious sharp metallic ringing noise. Since these reactions and

subsequent exothermic products require time to produce, consumption of the end gases by the advancing flame front before these reaction occur is therefore vital. Pre-ignition knock is when the mixture detonates before the onset of spark due to excessive heat exposure and can be very destructive due to the high levels of heat and pressure released when the piston is still traversing up in the combustion camber. If both of these phenomenons where to be left unchecked, they could destroy the engine outright. The most common form of knock is post-ignition knock and this is managed by phasing the combustion timing and thereby reducing the peak in-cylinder pressure and temperature. This however reduces the combustion efficiency and the harvested power since optimal timing is now sacrificed for the well being of the engine.

2.3 Pre-chamber Ignition

Pre-chamber ignition thereby presents itself as an interesting solution to tackle the above mentioned issues regarding knock with respect to both higher compression ratio and timing retardation while also reinstating the loss in the charge air motion and thereby the turbulence induced by Miller valve timing.

2.3.1 Pre-chamber Configurations

Pre-chamber ignition, or sometimes referred to as turbulent jet ignition (TJI), utilises an auxiliary pre-chamber volume connected to the main chamber by a set of orifices. Two forms of the pre-chamber exists, passive and active, see Figure 2.9. Passive pre-chamber relies on the compression stroke to force air-fuel mixture through the orifices into the pre-chamber volume while active pre-chamber, working on the same principles as the passive, differentiates itself by allocating a separate injector for directly injecting fuel into the pre-chamber volume to ensure adequate fuel supply. The spark plug for both forms are situated within the pre-chamber

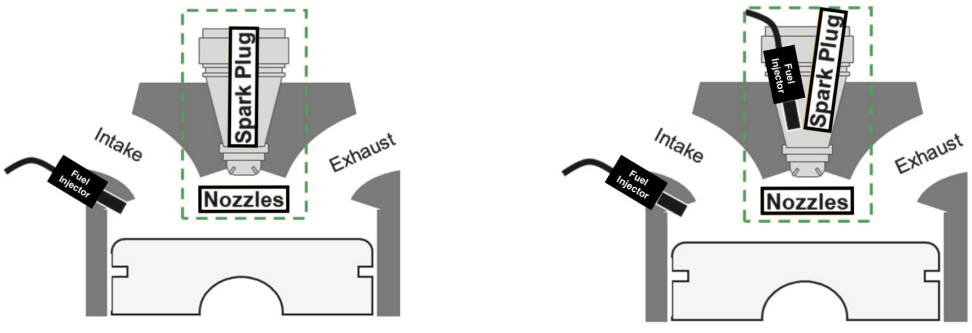

(a) Passive Pre-chamber Configuration.

(b) Active Pre-chamber Configuration.

Figure 2.9: Pre-chamber Configuration. Reproduced from [11].

volume and when the mixture ignites, the pressure difference between the main

chamber and the pre-chamber will drive the propagating flame front into the orifice, creating a hot jet. Depending on the number of orifices the pre-chamber contains, the hot jets will be ejected into the main combustion chamber in several directions, creating several dispersed ignition sites. All of these hot jets will thus become a source of ignition for main bulk mixture in the main chamber to combust. Because of the subsequent rapidness of the main bulk combustion, the risk of knock onset is greatly reduced, paving the way for higher compression ratios and efficiency gains. The difference between the two configurations are based on the inherent control over mixture inside the pre-chamber. The passive pre-chamber relies on the compression stroke for adequate air-fuel supply which subsequently causes difficulty in charge precision which can lead to main chamber ignition varying cycle to cycle. For the active pre-chamber, since a injector is allocated for its fuel supply, its charge mixture can more precisely be controlled meaning less variation in ignition. However, since this pre-chamber design requires an additional fuel system, it will naturally be more complex in terms of cost and packaging. Active pre-chamber technology can be seen today in natural gas power plants [15] whereby passive pre-chamber can be seen in Formula 1 [16], where its used to enhance the efficiency of internal combustion engine and in the newly developed Maserati Nettuno engine which utilizes both a passive pre-chamber and another spark plug situated inside the main chamber for there MC20 sports car [8].

3

Pre-chamber Combustion Fundamentals

The concept of pre-chamber ignition is not new and research surrounding it is extensive. This section will look to explore the fundamental mechanism behind pre-chamber ignition and its governing parameter by exploring the extensive research available and presenting the most relevant findings with respect to this thesis.

3.1 Origins of the Pre-chamber and Sir Harry Ricardo Concept

The first patent to be applied that bears the closest resemblance to the pre-chamber of today was submitted in 1918 by Sir Harry Ricardo [9]. The design was composed of an engine with 3 valves, where one intake valve was allocated for induction of air into the main combustion chamber, one valve for air-fuel mixture into the pre-chamber volume and the last valve being for exhaust. The idea of this concept, as with the stratified Otto engine [13], was to minimize the in-cylinder heat losses by keeping the temperature of the working fluid as low as possible. The theory behind this was that as the temperature of the working fluid increases, so does its specific heat (not be confused with specific heat ratio) which results in less heating of the working fluid by the fuel. After ignition of the mixture inside the pre-chamber, it should be *"simultaneously mixed with the air in the cylinder"* and obtaining a very low mean density which would yield a lower maximum temperature and thereby lower the heat losses. The focus thereby of this concept was not to achieve fast combustion but rather stratified combustion with minimal heat losses to cylinder walls. This concept also showcased the inherent sensitivity of the pre-chamber and to quote Ricardo himself *"...if not just right, it may be very wrong; a very small change in form or dimension may upset the whole system..."*.

3.2 Pre-chamber Ignition Jet Formation and Main Chamber ignition

Pre-chamber ignition and the subsequent jet formation process is highly complex and is a function of various geometric parameters that effect the thermodynamic and fluid dynamic properties of the working fluid which combine to form and sustain a jet. The aim of this section is thereby to create an understanding of the governing

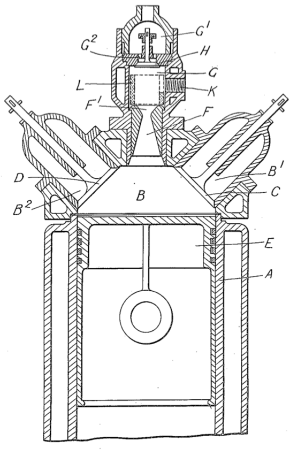

Figure 3.1: Ricardo's Pre-chamber Concept.

parameters that determines the formation of the jet and the main chamber ignition process.

As the mixture inside the pre-chamber volume ignites, a flame kernel will form in the same manner as explained in Section 2.1.2. The flame kernel will continue to grow, propagating towards the pre-chamber walls and the orifice [17] [18]. The flame front will push a very small portion of the reactants out of the pre-chamber volume via its orifice and as flame front reaches the orifice, a jet will appear. This is illustrated in Figure 3.2. The first observation is that as the jet appears and the flame front continues to grows inside the pre-chamber, the jet length will adjust according to the consumption rate (the rate at which the unburned mixture is consumed) inside the pre-chamber volume. While the figure confirms this assumption, the jet characteristics are also highly dependent on other parameters such as orifice diameter, number of orifice, pressure gradient near the orifice and the pre-chamber fuel-air ratio. These factors will be discussed in the coming sections.

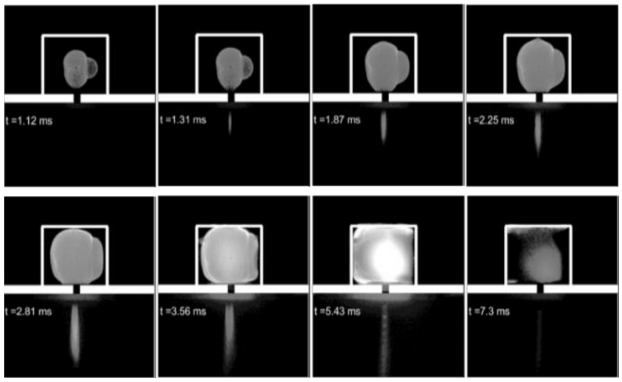

Figure 3.2: OH^* signals, pre-chamber ignition to jet formation. 3mm Orifice, ethylene, $\phi = 1$. [19].

The structure of the jet, as studied by Allison et al and Mastorakos et al [19], was cylindrical in shape consisting of both fresh reactants and combustion products with

the latter being located in the center of the core and the former adjacent the the orifice wall. The reaction zone area, thereby, is cylindrical in shape between the interface of these two layers. This is observed in the temperature profile of the flame kernel and jet in the LES studies depicted in Figure 3.3. It can clearly be seen that temperature at the center of the jet is higher, indicating the area containing combustion products.

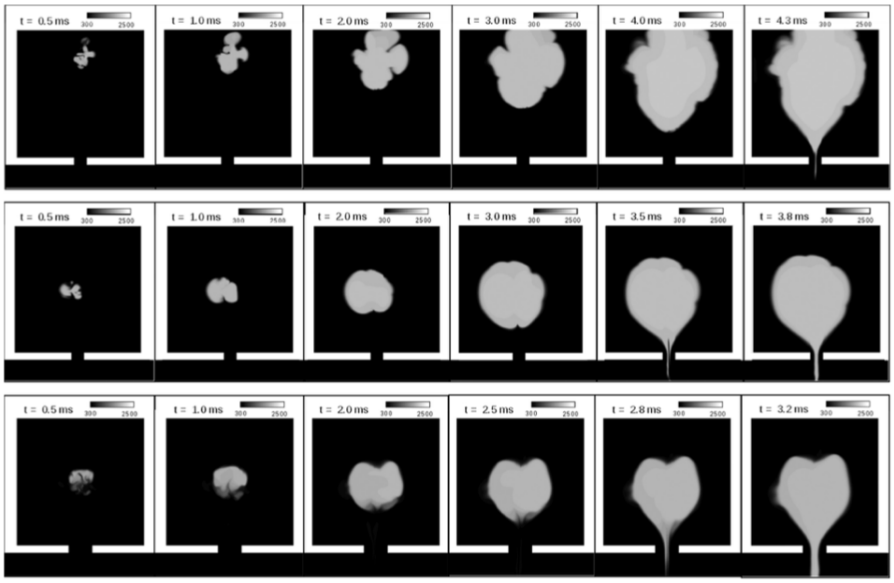

Figure 3.3: Temperature profiles of kernel formation from LES for top (top row) and center (center and bottom row) spark location. Orifice diameter = 3 mm (top and center row), Orifice diameter = 6 mm (bottom row), methane at $\phi = 1$. Image from [18].

As the jet enters the main-chamber, it will mix and react with its charge and combust. The ignition mechanism was studied by Biswal et al. [20] and their conclusion was that two ignition mechanism exist, jet ignition and flame ignition. Auto-ignition by hot jet, jet ignition, is when the jet is free from flame kernels with it only containing hot combustion products. The hot combustion products will mix and react with the mixture inside the main chamber which raises its temperature to auto-ignition temperate and main chamber combustion commences. This ignition mechanism is illustrated in Figure 3.4. As observed, very little to no OH^* radicals (radical used to track heat release) are present in the jet as it ejected from the pre-chamber, with OH^* radicals only appearing as the hot combustion products in the jet heat up the main chamber charge leading to heat release. This was also observed by Yamaguchi et al in "Pattern 1" as the orifice diameter was shrunk [21].

Ignition by flame kernel, or flame ignition as expressed by Biswas et al, is when the flame contained OH^* radicals, as seen in Figure 3.5 and thereby ignition of the main chamber was commenced by the aid of the heat released during the formation of these radicals. This was also observed by Yamaguchi et al [21] in "Pattern 2, 3, 4" as the orifice diameter was made progressively bigger.

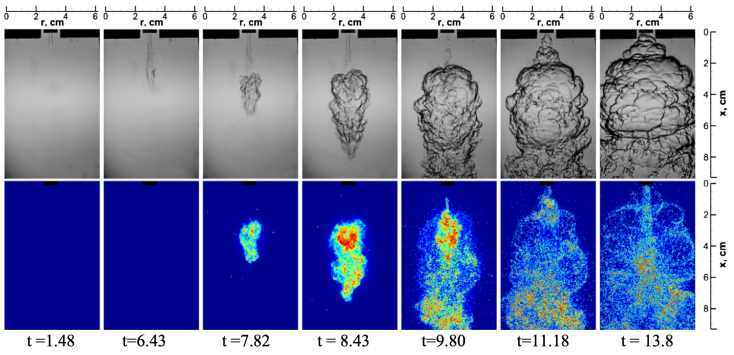

Figure 3.4: Schlieren (top) and OH^* chemiluminescence (bottom), Jet ignition. Orifice diameter = 4.5 mm, initial pressure = 0.1 MPa, initial temperature = 500K, methane at $\phi = 1$. Imagine from [20].

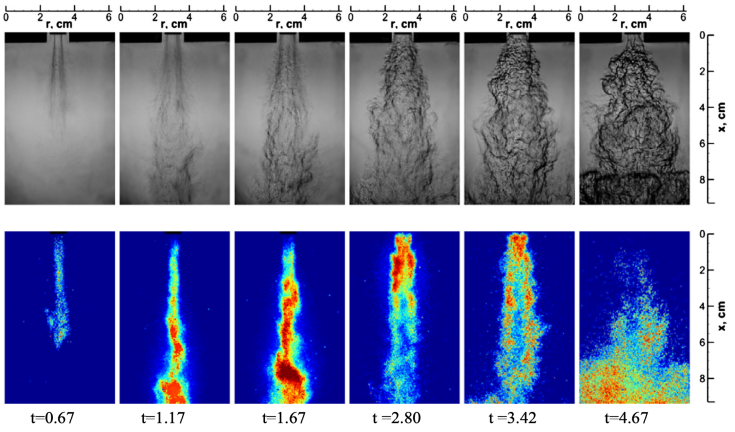

Figure 3.5: Schlieren (top) and OH^* chemiluminescence (bottom), Flame ignition. Orifice diameter = 4.5 mm, initial pressure = 0.4 MPa, initial temperature = 500K, methane at $\phi = 1$. Image from [20].

The delay between pre-chamber combustion and the main chamber ignition is termed "ignition delay". The study by Biswal et al. demonstrated that ignition can only take place as the jet is decelerating, due to the otherwise excess stretching of the flame and pre-heat zone. This is illustrated in Figure 3.6 and as seen, ignition for all cases only commenced as the jet slowed down to well below Mach 0.3.

The ignition process is however enhanced for the case when flame ignition is present due to the presence of higher quantity OH^* in the jet structure. The difference in ignition delay between these two jet formations are illustrated in Figure 3.7. This means that the ignition delay is not only affected by the jet velocity but also the jet formation and structure type. The jet structure is heavily dependent on geometries of the pre-chamber, equivalence ratio, fuel type, residual mass fraction (RMF) within the pre-chamber and flow fields around the spark location. These governing factors and more is to be explained in the section to come.

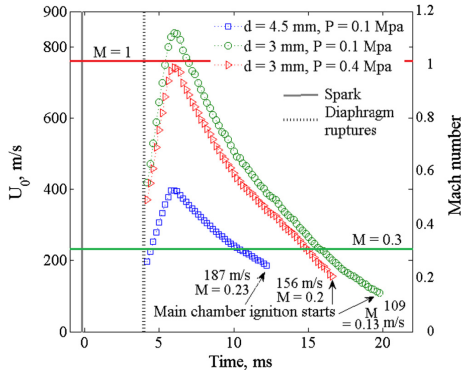

Figure 3.6: Ignition delay as a function of jet speed and time. Image From [20].

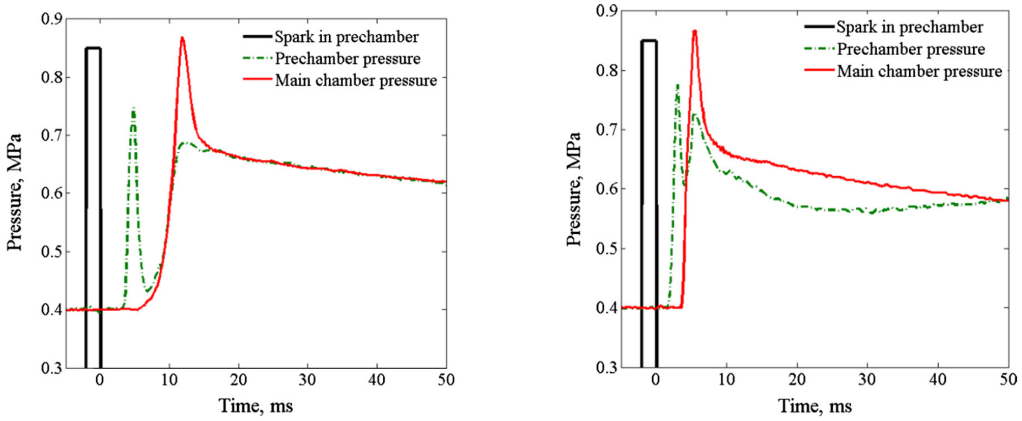

(a) Jet ignition, ignition delay.

(b) Flame ignition, ignition delay.

Figure 3.7: Ignition delay with respect to jet ignition mechanism. Figure from [20].

3.2.1 Geometry Effects

The geometric effects on the pre-chamber ignition mechanism is its most dominating factor. The parameters to consider are the orifice diameter, the number of orifice, pre-chamber volume and volume shape. These parameters will combine and yield different jet structures and this section aims to give an overview of the geometric effects on the jet formation and structure.

3.2.1.1 Orifice diameter effects

Pre-chamber orifice diameter has a dominating effect on the jet structure as its directly linked to the quenching of jet against orifice walls, pressure build up in the pre-chamber volume before jet emergence and the RMF scavenging attributes. The quenching of the jet towards the orifice walls effectively governs the jet mechanism that was observed by Biswal et al. This was also observed by Yamaguchi et al [21] in "Pattern 1" as the ante-cluster recording the ions in the jet drop to zero as the jet was passing through a narrow orifice, indicating the termination of the jet issuing

forward into the main chamber. Allison et al also observed jet quenching with the termination of CH^* radicals (radical used to mark flame reaction zone) in the jet as the quenching distance excised the diameter of the orifice and thereby quenched the reaction zone area. This effect is illustrated in Figure 3.8.

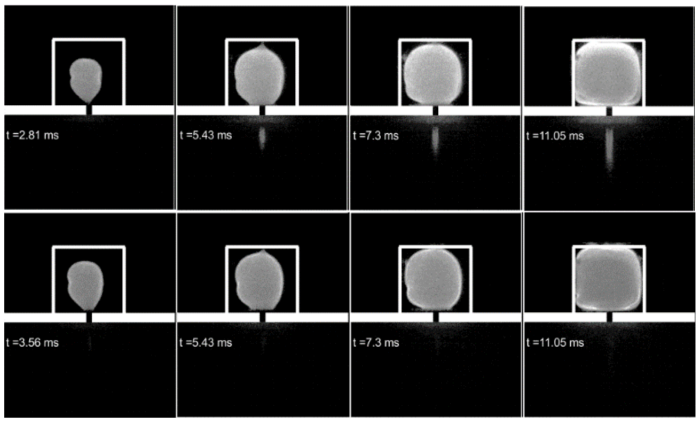

Figure 3.8: OH^* radicals (*Top Row*) and Quenching of CH^* radicals as the jet passes the orifice (*Bottom Row*). Orifice diameter of 3mm with methane at $\phi = 1$. Image from [19].

The quenching distance for low turbulent flow (a reasonable assumption for a small volume such as in the pre-chamber) is proportional to the temperature however inversely proportional to the pressure and laminar flame speed. Therefore, as pressure, and thereby the laminar flame speed, increases, the quenching distance reduces and this is what gave rise to flame ignition as claimed by Biswal et al. A direct result of either increasing the pressure or orifice diameter is that the OH^* radicals will appear much sooner in time and with higher intensity. These effects can be seen as pre-chamber pressure increases in Figure 3.5 compared to Figure 3.4 and as the diameter increases if comparing the OH^* chemiluminescence intensity in Figure 3.9.

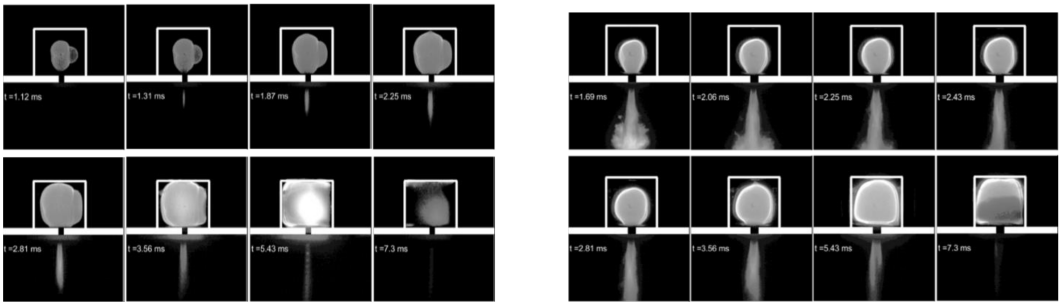

(a) Orifice diameter = 3 mm. **(b)** Orifice diameter = 6 mm.

Figure 3.9: OH^* chemiluminescence, ethylene $\phi = 1$. Figure from [19].

The orifice diameter effects on the pre-chamber pressure rise and the maximum pressure build up is paramount. As the orifice diameter reduced, the flame front will arrive later to the orifice, leading to more of the mixture being consumed which

results in a higher pressure rise [17]. The other reason is the resistance of orifice to the viscous gas inside the pre-chamber [22] [23] and less reactance being ejected due to this gas inertia. This inertia also allows more of the mixture to be consumed, thereby increasing the pre-chamber pressure and reducing the quenching distance to the pre-chamber walls which also yields more consumption. The result of higher pressure build up and pressure difference between the pre-chamber and main chamber leads to a steep pressure gradient during which the jet is ejected (see Figure 3.10b). This, thereby, results in an high jet speed, deeper main chamber jet penetration and higher turbulence inducement. The deeper the penetration of the jet, the more of the main chamber volume is being engulfed by the hot jets and the more directions the reaction zone area can spread before coalescence [24]. This also means that the ignition delay will be longer with higher jet speeds [21] [20] [25] however the overall burn rate $\theta_{90\%}$ can be faster. Smaller diameter orifice also increase the risk of choking which can result in excess heat loss in the pre-chamber. The effect of orifice diameter is illustrated in Figure 3.10a. As the diameter was made smaller, a higher pressure build up was measured in the pre-chamber and vise versa for the bigger diameter. Note that the ignition timing for these three pre-chambers are different which will also effect the pressure build up. Nevertheless the high pressure difference is an indication of higher jet velocity and of flow restriction.

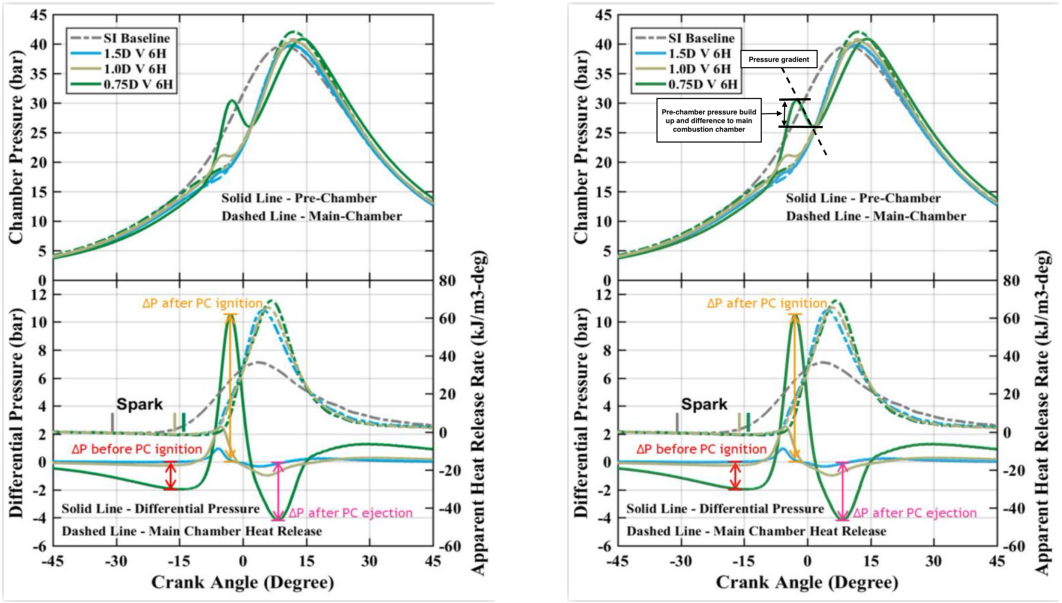

(a) Pre-Chamber Pre-chamber Orifice Diameter Effect.

(b) Pressure Difference and Gradient.

Figure 3.10: Difference in pressure build up with respect to different orifice diameter with constant volume. Figures from [25].

The orifice diameter also has an instrumental effect on the residuals fraction and the scavenging properties of the pre-chamber. Pre-chambers with smaller orifices are harder to scavenge due to the flow restriction and the viscous forces of the gas. This becomes especially important during part and low load operation due to degrading combustion stability as a direct result of the excessive RMF in the pre-chamber

volume [25] [7]. This, thereby, results in a weak jet incapable of igniting the bulk mixture in the main chamber. To summarise then, on the one hand smaller orifices induce higher jet velocities, deeper penetration and more turbulence inducement but on the other hand, the higher risk of quenching of the OH^* and CH^* against the orifice walls and compromised scavenging attributes.

3.2.1.2 Orifice count effects

The orifice count has its biggest effect on the pressure build up and relieving while also distributing of the ignition sites across the main combustion chamber [24] [25] [12]. The pressure build up and relieving can be seen in Figure 3.11. As the orifice count increases, the pressure difference between the main and pre-chamber reduces due to less overall flow restriction as a result of the increase in total orifice area. The HRR is the same for all cases and this is believed to be due to the increase in total orifice area aiding in the mass charging of the pre-chamber during the compression stroke prior the ignition. As the pressure build up for 10 orifices is lower than compared to 6 and 8 orifices, the jet speed and penetration length thereby also lower. The better distribution of the ignition sites (increased ignition volume) and earlier coalesce due to jets being closer together maybe a reason for the burn-rate not varying between the pre-chamber specifications for this test.

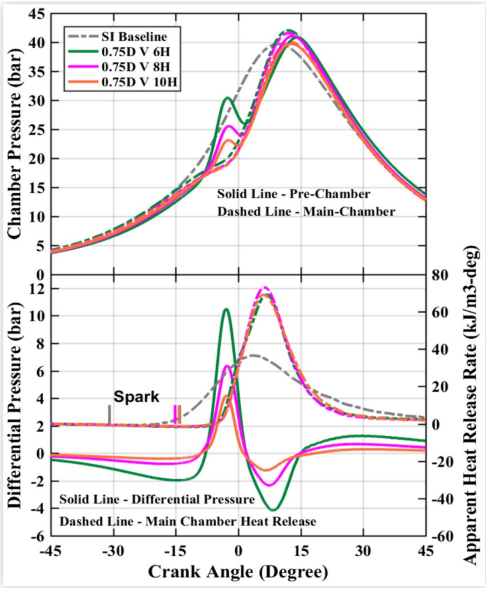

Figure 3.11: Orifice count effect. Constant pre-chamber volume and Orifice diameter. Figure from [25].

.

The difference between higher orifice count can more clearly be seen in Figure 3.12 by C. Redtenbacher. Four points of interaction are apparent and these where analysed with the following conclusions. As the orifice count increase, point 1 a minor difference in the penetration depth, which is to be expected due to the pressure gradients being almost comparable. Point 2, 3 and 4 are where the major differences are observed. As the jet speed, jet penetration and turbulence generated in

the variant with less orifice are slightly higher, its ignition properties are thereby compromised as observed in the HRR curve. The variant with more orifices will ignite the mixture faster due to it inheriting lower initial jet speed and the fact that ignition only takes place as the jet has decelerated. However, the higher turbulence and deeper jet penetration of the variant with fewer orifices (black line) is decisive as the HRR overtakes the HRR with more orifices at the later stages of combustion.

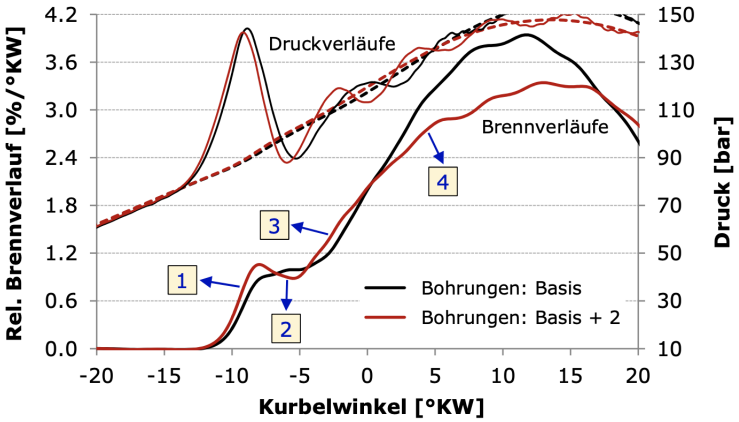

Figure 3.12: Orifice count effect. Back line: Base number of orifices, Red line: Base orifices + 2. X-axis: Crank angle degree, y-axis left: Relative combustion process [%/CAD], y-axis right: Pressure [Bar]. Top lines: Pressure gradient, Bottom lines: HRR. Constant pre-chamber volume and orifice diameter. Figure from [24].

.

The difference between a pre-chamber with bigger orifices and one with more orifices lies primarily in the distribution of the jets in the combustion chamber. While both configurations should in theory result in nearly identical pressure build-up and flow restriction (see Figures 3.15a, 3.15b, and 3.11), the size and number of orifices affect the degree to which the pre-chamber jets engulf and ignite the main chamber charge. More orifices will naturally results in more of the mixture being engulfed and ignited, which can in some cases be more beneficial due to the enhanced scavenging properties with minimal compromise to the in-cylinder apparent heat release rate (AHRR) curve. As seen in Figure 3.11, as the orifice count increases, the in-cylinder AHRR curve remains roughly consistent, even though the pressure difference and gradient are reduced. It is worth noting, however, that the quenching distance remains an important consideration in pre-chamber design. A pre-chamber with bigger orifices is less likely to quench as it traverses the channels which is desirable at some operation points. This is especially true during low load operation where low in-cylinder pressure attributes to higher quenching distances which effects the ignition properties of the jet. Thereby, if this attribute is tuned correctly, more orifices can help to distribute the ignition sites more readily around the main combustion chamber. However, this will result in less turbulence inducement which is beneficial for heat loss however not for combustion duration and knock mitigation. Nevertheless, the choice of configuration is strongly tied to its operating environment and should be tuned accordingly.

3.2.1.3 Volume and Volume Shape effects

The pre-chamber volume och its design is instrumental to both the burn rate and the turbulent flame speed inside the pre-chamber due to allowing the build up of turbulent kinetic energy (TKE) [26]. Its effect is the increase in distortion of the reaction sheet area which increases the burn rate and thereby the pressure rise before the flame front reaches the pre-chamber orifice. H. Ge et al research concluded that altering the height of the pre-chamber at point A and the throat diameter of point B in Figure 3.13 resulted in higher TKE and thereby higher burn-rate and pre-chamber combustion speed. The effect of higher TKE and burn-rate in the pre-chamber is visible if analysing the pressure trace and the HRR in the pre-chamber and main chamber as illustrated in Figure 3.14. As seen, the bigger volume with higher TKE generate an much higher burn-rate and maximum pressure which results in higher jet speeds, penetration depth and turbulence build up.

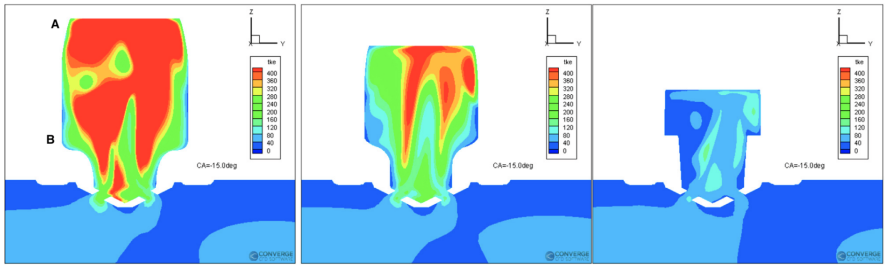

Figure 3.13: TKE build up for three different shapes of the pre-chamber volume (Large (SVM67), Medium (DOE56) and Small(RegTree64), Right to Left). Image from [26].

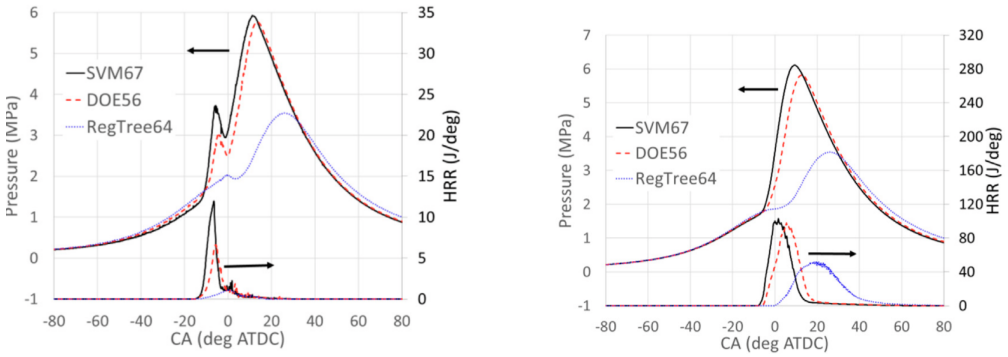

(a) Pre-Chamber Pressure Trace and HRR.

(b) Main Chamber Pressure Trace and HRR.

Figure 3.14: Pressure and HRR Trace of Main and Pre-Chamber. Pre-chamber Volume Large (SVM67), Medium (DOE56) and Small(RegTree64) Figure from [26].

Yu et al [25] conducted tests which included altering the pre-chamber volume while keeping the number of orifices fixed. The size of the orifices changed however, see Figure 3.15a and 3.15b. During the test with smaller orifices (0.75mm, Figure 3.15a), the differential pressure between the pre-chamber and main combustion chamber before ignition became greater as the pre-chamber volume increased. After the spark,

the maximum pressure rise just before jet formation and ejection for all volumes became almost identical. The most notable difference between these pre-chamber configurations is the gradient of the differential pressure curve after reaching its peak (bottom figure in Figure 3.15a, approximately -5 CA) and the gradient of the chamber pressure curve in the pre-chamber after reaching its first peak (top figure in Figure 3.15a, approximately -5 CA). The smaller pre-chamber volume exhibits marginally greater pressure gradient in both cases. As the jet is ejected close to the tip of both of these curves, the jet exit velocity, and thereby jet penetration depth and turbulence inducements, is determined by both of these gradients. The result of a steeper gradient can be seen in the AHRR, with the smaller volume exhibiting higher AHRR as the jet penetrates deeper into the main combustion chamber with higher turbulence. After ignition and jet ejection process, the differential pressure for the pre-chamber with the larger volume again became greater, which results in higher flow rate back into the pre-chamber. For bigger orifices, the orifice resistance to the viscous gas inside the pre-chamber is less, resulting in less flow restriction and more of the reactance being ejected during the pre-chamber combustion phase. Additionally, the flame front will reach the orifices earlier, as was explored in Section 3.2.1.1. As the flame front reaches the orifices earlier, combined with higher fresh mixture rejection, leads to less of the theoretical internal pre-chamber mass being burned, evident by the lower differential pressure rise and pressure difference between the two chambers. The resulting jet is thereby not as effective as with the resulting jets from the smaller orifice size. This thereby confirms that larger pre-chamber volumes does not always correlate with higher pre-chamber mass consumption leading to higher pressure difference, with the smaller pre-chamber volume performing equally well during this test.

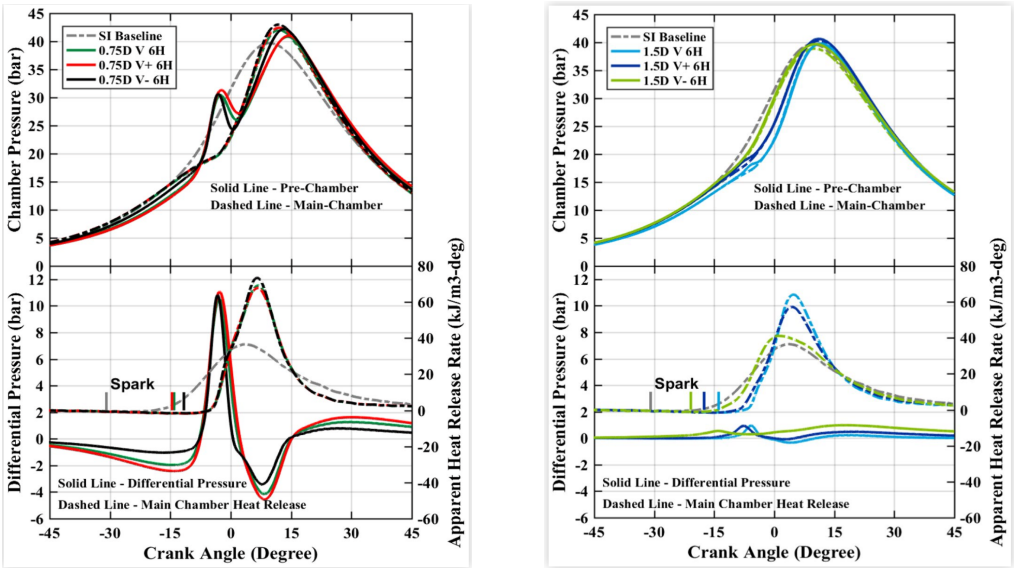

(a) Orifice Diameter of 0.75mm, Alternating Volume.

(b) Orifice Diameter of 1.5mm, Alternating Volume.

Figure 3.15: Volume Effects with Varying Orifice Size and Fixed Orifice Count. Figures from [25].

The effects of RMF, as explained in Section 3.2.1.1, has a large influence on combustion stability and repeatability of combustion. This is especially true for low load operation where high pre-chamber RMF can lead to main chamber misfire due to weak pre-chamber flame development as was observed by D. E. Lee et al [10]. According to their study, smaller volume ($629.3mm^3$) combined with bigger orifice diameter ($1.5mm$) yielded less misfire likelihood due to more uniformity of the air-fuel mixture in the pre-chamber and less localization of the RMF near the spark plug, see Figure 3.19b. However its important to note that all of there pre-chamber configurations yielded misfire. Nevertheless smaller volume and increase in-cylinder pressure reduced the effect of misfire but did not fully mitigate the issue, as seen in Figure 3.16. The effect of RMF on pre-chamber combustion will be explored in Section 3.2.3 including the tactics used to mitigate main chamber misfire.

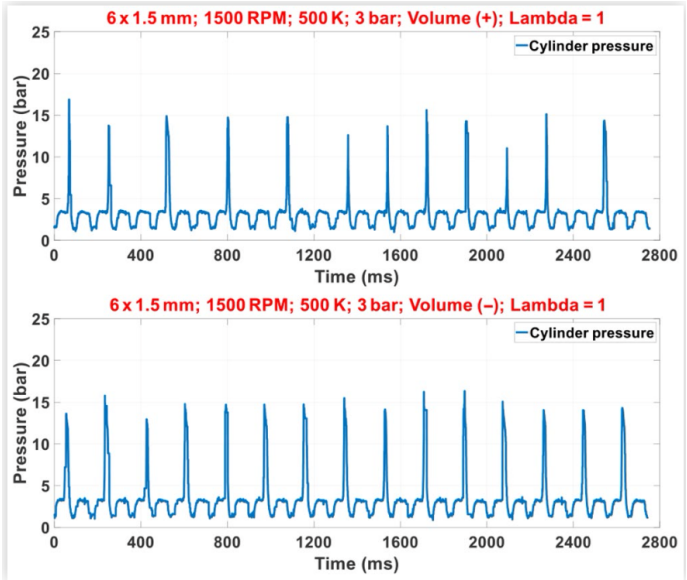

Figure 3.16: Volume effect on pressure trace. In cylinder pressure at start of ignition = 3 bar, Volume (-) = $629.3mm^3$ and Volume (+) = $809.4mm^3$. Image from [10].

The drawback of bigger volume is the heat losses due to the increase in pre-chamber wall surface area. The increased surface area of bigger pre-chamber volume increases the heat transfer rate and can lead to thermal efficiency loss. The heat losses are illustrated in Figure 3.17a and break thermal efficiency (BTE) Figure 3.17b from Yu et al. [25] running with Miller camshaft. An increase in pre-chamber volume leads to increased heat losses and the degradation in the BTE value. It can however be noted that bigger volumes in combination with smaller orifice area also increases the consumption rate, thereby effecting the jet penetration depth and the in-cylinder turbulence intensity, which can cause combustion to take place closer to main chamber walls and the burn duration to be shorter. Faster combustion in combination with a shorter proximity to the main chamber walls and higher turbulence inducement can also cause excess in-cylinder heat losses. Important to note is the baseline (conventional spark plug setup), labeled *SI baseline* for both figures and there performance when compared to the pre-chamber with bigger volume.

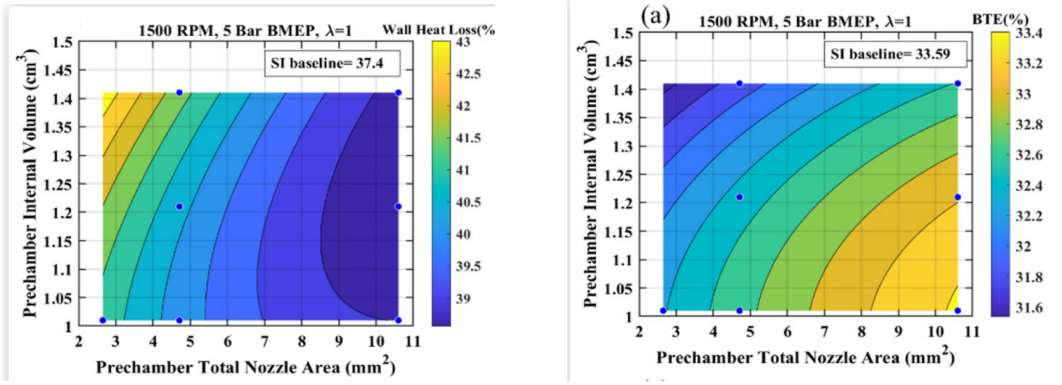

(a) Wall Heat Losses. **(b)** BTE.

Figure 3.17: Wall heat losses and BTE. Note Baseline values for both figures. Figure from [25].

The research by Hitachi [27] using volumes exceeding $2000mm^3$ also yielded poor efficiency at $\lambda = 1$ due to excess heat losses. This test was conducted with elevated compression ratios of approximately 14.

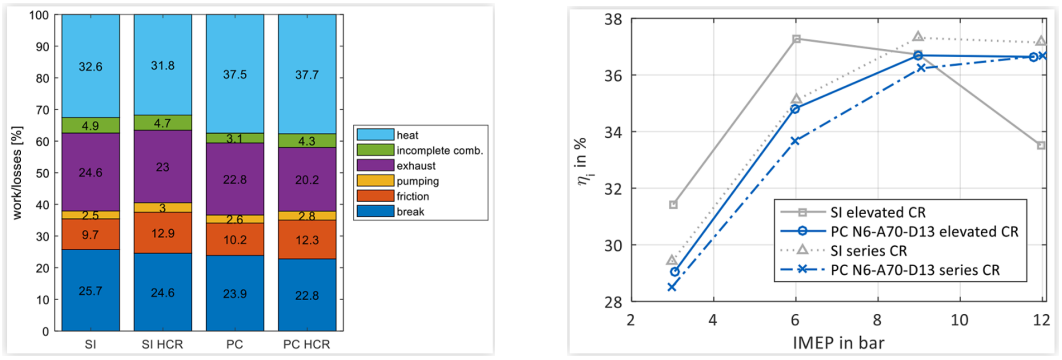

(a) Heat Losses, 6 Bar IMEP. **(b)** Indicated efficiency.

Figure 3.18: Heat losses and Indicated efficiency. Engine speed at 1500RPM. N6-A70D13: 6 Orifice pre-chamber with 1.3mm diameter. Figure from [27].

3.2.2 Pre-chamber Fuel Type

The induced turbulence by the pre-chamber and the subsequent rapid main chamber combustion is one of its major benefits. The pressure difference between the pre- and main chamber governs the jet exit velocity, the deepness of the jet penetration into the main combustion chamber and the turbulence build up inside the main chamber [24] [25] [28] [23]. The turbulence build up and deep in-cylinder penetration leads to a short rapid burning angle, despite the fact that that the high jet velocity induces a longer ignition delay as the jet has to decelerated before ignition can take place [20], see Figure 3.6. Apart from the already explained parameters effecting jet velocity, fuel type has a major effect on the pressure build up due to the inherent properties of

the fuel [17]. Fast burning fuels such as ethanol, ethylene and hydrogen will inherent higher laminar flame speed due to the higher reaction rate leading to higher pre-chamber pressure rise, pressure difference and gradient, also effecting the jets exit velocity.

3.2.3 Air-fuel Ratio, Residuals and Spark Location Effects

A low residuals concentration is instrumental for the pre-chamber pressure build up and the subsequent survivability of the jet. The effects of increasing RMF in the pre-chamber is a reduced of the reaction rate which thereby results in a reduction in the laminar flame speed in the pre-chamber. This in-turn enlarges the pre-heat and conduction zone (see Figure 2.2) which generate a thick reaction sheet. In accordance with Mastorakos [19] and P.M Allison [17], some of the reactants will be ejected and this will primarily be the mixture closest to the pre-chamber orifices. As the mixture closest to the pre-chamber orifices contains the least RMF, as shown in the CFD studies (see Figure 3.19 and 3.20), the relative amount of fresh mixture inside the pre-chamber reduces even further. The end result is a overall slow pre-chamber burn, thick flame, low pressure build up and high quenching distance. The slow flame propagating inside the pre-chamber will correspond to a jet that will be weak. The weakness is further exacerbated due it quenching against the pre-chamber orifices walls and thereby losing both heat and its reactive core. The jet will enter the main chamber and the turbulent eddies of the jet will start dissipating heat to the cooler main chamber charge. The temperature of the jet will drop rapidly leading to it being incapable of igniting the mixture in the main chamber [20] leading to full main chamber misfire.

The effect of RMF is most noticeable at low load [10] [7], where high in-cylinder cycle-to-cycle RMF variation caused misfire which lead to unstable running of the engine. Studies regarding CFD analysis of the RMF in the pre-chamber are presented in Figure 3.19 and 3.20 and its effect on the pressure trace in Figure 3.16. Figure 3.19a depicts the effect of both Miller camshafts and standard camshaft on the lambda and residuals distribution. According to M.Sens et al, the RMF increased by 4.5% while using the Miller camshafts. The result is a increased burn delay inside the pre-chamber which is further exacerbated by the poor lambda distribution which lead to their research switching to an active pre-chamber at low load operation.
Its is therefore of interest to examine the possible solutions to mitigate this inherent weakness of the pre-chamber. Its been proven that the positioning of the spark plug is an important factor in the flame development phase in relation to the RMF [26] [10]. Figure 3.20 illustrations the RMF distribution with the + denoting the spark plug location. The large (SVM67) and medium (DOE56) size volumes shows lower concentration of RMF near the spark plug, which is more beneficial for ignition and flame development while the smaller volume (RegTree64) show higher concentration of RMF near the spark plug. The end result can be seen in Figure 3.14, as the HRR and pressure rise is more rapid for the cases with less RMF fraction near spark plug. This finding was also argued by D.E.Lee as the non-uniformity of the air-fuel mixture combined with the high localisation of the RMF near the spark plug lead

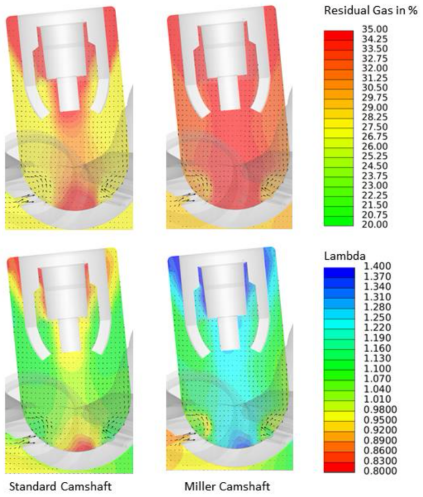

(a) RMF and λ distribution inside the pre-chamber for standard (left) and Miller (right) camshaft. Image from [7].

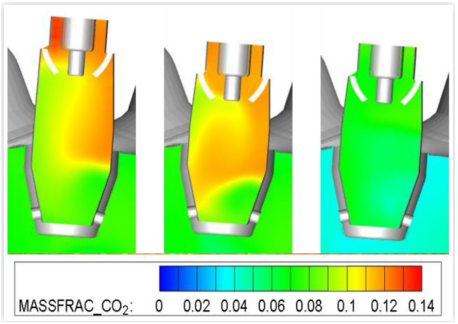

(b) Volume effect and Pressure effects on RMF. Left most figure: In cylinder pressure at start of ignition: 3 bar, Volume: 809.4mm^3. Middle figure: In cylinder pressure at start of ignition: 3 bar, Volume (-): 629.3mm^3. Right most figure: In cylinder pressure at start of ignition: 6 bar, Volume: 809.4mm^3. Image from [10].

Figure 3.19: CFD Analysis of RMF in the pre-chamber.

to unstable running of the engine.

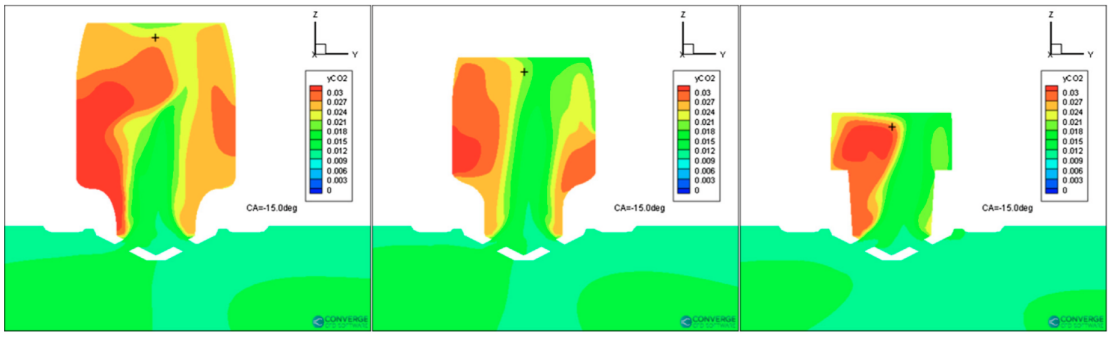

Figure 3.20: $CO2$ distribution for three different shapes of the pre-chamber volume (Large (SVM67), Medium (DOE56) and Small(RegTree64), Right to Left). + denoting spark plug location. Image from [26].

Increasing the intake and in-cylinder pressure or lambda (enleanment of the mixture) has both proven to be an solution for mitigating main-chamber misfire. Figure 3.21 from D.E Lee et al. [10] illustrates both the case of increased in-cylinder pressure

(right) and lambda (left).

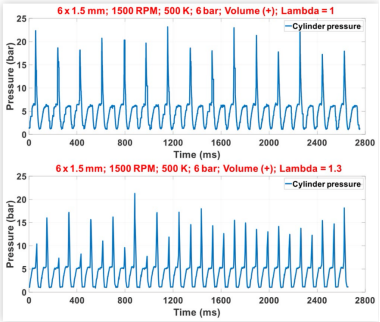

(a) λ effect on misfire, λ varied from 1 (Top) to 1.3 (Bottom).

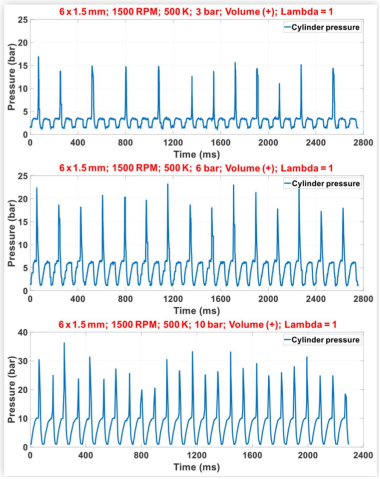

(b) Pressure effect on misfire, $\lambda = 1$, Pressure = 3(Top), 6 (Middle) and 10 (Bottom) Bar.

Figure 3.21: Low load misfire mitigation solutions. Volume(+) = $809.4mm^3$. Figure from [10].

As Figure 3.21b depicts, progressively increasing the intake and in-cylinder pressure mitigated misfire. The most likely reason for this is the higher intake pressure promoting beneficial gas exchange properties which results in less RMF being trapped in the combustion chamber. This, thereby, leads to an overall less residual being trapped in the pre-chamber leading to a more stable and repeatable combustion. The higher pressure also force more reactants into the pre-chamber as a result of the density increase of the in-cylinder gas. The higher value of lambda effect on misfire mitigation is likely due to the residuals containing more oxygen as opposed to if the conditions where stoichiometric which aids the combustion characteristics in the following cycle.

The effect of the spark location on the jet length was studying by P.M Allison et al [17] and according to their research, when the spark is created by electrodes located in the middle of the pre-chamber, the flame front reaches the orifice earlier then if the spark electrodes are located at the top of the pre-chamber. The result is thus that the jet appearance is earlier as-well as jet duration, with respect to the OH^* chemiluminescence, is longer with centrally mounted electrodes, see Figure 3.22. This may be due to the initial rejection of the reactance being less, leading to more mixture being consumed and a longer OH^* chemiluminescence duration.

The effects of varying the air-fuel ratio in the pre-chamber has its effect on both the jet mechanism and jet length. The jet mechanism, when operating the pre-chamber rich was studied by Gussak et al [29][30][31]. Upon ignition of a rich

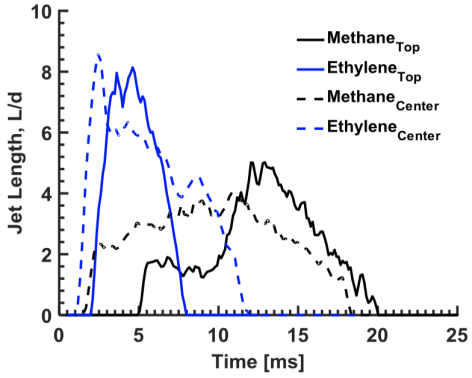

Figure 3.22: Jet length calculated from OH^* chemiluminescence with respect to spark location. Jet length normalized by orifice diameter of 3mm for methane and ethylene, $\lambda = 1$. Image from [18].

mixture, a low temperature torch jet containing combustion and chemically active products were ejected into the main chamber causing it to ignite. This system, the "avalanche activated combustion" or "Lavinia Aktyvasdia Gorenia" ("LAG"), set out to demonstrate the advantages of torch ignition by utilizing a auxiliary pre-chamber to ignite a mixture inside the main chamber. The studies also set out explore the different parameters that provided the best mixture of combustion stability and repeatability, ignition delay and combustion rate for their torch combustion system. To archive the shortest ignition delay, the highest combustion rate, the best stability and relatable combustion the following parameters were optimised: The pre-chamber volume was to be kept small, no larger then 2-3% of the combustion volume, the auxiliary mixture combustion (pre-chamber consumption) was is not to exceed 1-2% of the main mixture charge, orifice channels must be angularly positioned and have a cross-section area of 0.03-0.04 cm^2 per 1 cm^2 of pre-chamber volume and the length to diameter ratio should be 1:2 to ensure a small pressure gradient between the pre-chamber and the combustion chamber.

P.M Allison and K. Bureshaid et al [17] [28] studied the jet formation mechanism for both rich and lean cases. For lean cases, K. Bureshaid et al studied the effects of air-fuel ratio with ethanol(E85) and isooctane with an active pre-chamber in passive operation and concluded that the combustion was slower and jet penetration was lower for both cases when pre-chamber operated lean from stoichometric. This might be due to the laminar flame speed and peak pressure being lower which thereby delays the first appearance of the jet and the jet penetration length. P.M Allison studied the effects of the equivalence ($\phi(= 1/\lambda)$) on jet length with respect to the OH^* chemiluminescence and concluded that operating the pre-chamber rich yielded a longer jet, see Figure 3.23. This was also observed by K. Bureshaid et al in their experiments where the pre-chamber was progressively made rich. The possible explanation to the increase in jet length due to rich operation is the burning of the ejected reactance close to the pre-chamber. According to P.M Allison and Mastorakos, the pre-chamber flame front will push some of the reactance out of the pre-chamber through the orifices. The ejected reactance at time of spark is still in

the vicinity of the pre-chamber orifice and it is possible that the jet arrive and burns the ejected mixture as it transverses deeper into the main chamber, see Figure 3.24.

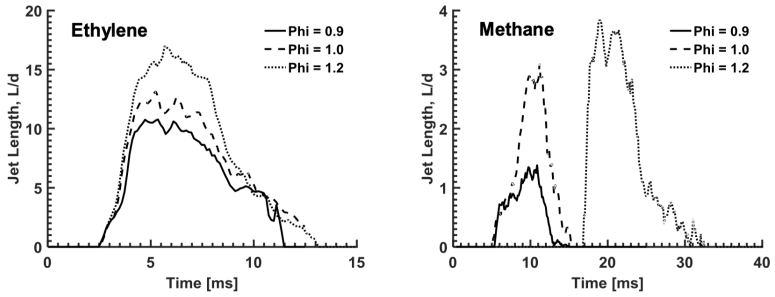

Figure 3.23: Jet length calculated from OH^* chemiluminescence, spark from top for both ethylene and methane case, length normalised by nozzle diameter of 3mm. Image from [18].

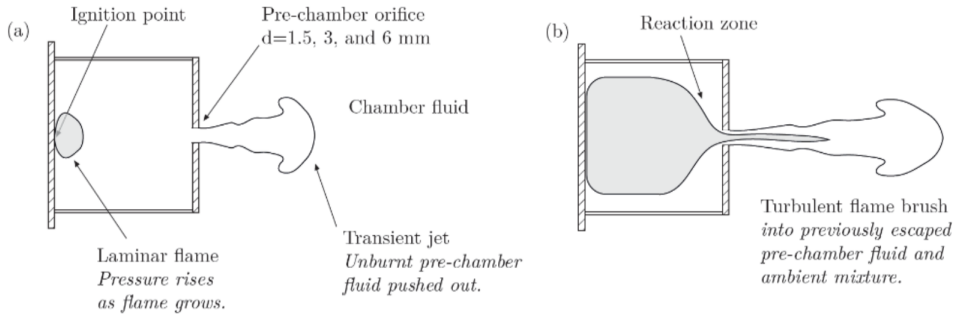

Figure 3.24: Kernel growth as the initial reactance is ejected. Image from [18].

3.2.4 Overview of Pre-Chamber Ignition System

As expressed in the introduction of the chapter, the pre-chamber ignition process and the subsequent jet formation are highly complex. Therefore, this section provides a simple overview of the different geometric and parametric effects on the pre-chamber attributes and combustion process, which subsequently affect the jet formation and ejection. Table 3.1 summarizes these affects from 0 to 3, with 3 indicating that the geometric and parametric effect results in a highly affects aforementioned characteristics and 0 indicating the its effect is minimal. This table should be viewed with the intention of adjusting one parameter or geometry while the rest remain constant.

It is however vital to note that, though this table is meant to summarize the different effects on the pre-chamber combustion, the pre-chamber pressure build up process and subsequent jet formation is highly complex. Therefore, caution is advised when viewing this table as its only intended yield a simple overview. It should also be noted that the different geometric and parametric effects tend to affect each other and can lead to multiple aforementioned characteristics being affected. For example,

changing the orifice size changes the scavenging attributes of the pre-chamber, which can also lead to the air-fuel ratio and RMF being positively effected, which lead to different ignition attributes of the formed jet, which means that the jet speed is affected ect. These impacts were not considered in the making of this table.

Pre-chamber Geometry and Parameter Effects	Reduced Quenching and Ignition Mechanism	Jet Speed, Penetration Depth, Turbulence Inducement and Ignition Delay	Flow Restriction, Scavenging	Pre-chamber Heat Loss
In-cylinder Pressure	3	3	3	1
Orifice Size	3	3	3	2
Orifice Count	1	3	3	2
Pre-chamber Volume Size	1	2	2	3
Pre-chamber Volume Shape (Pre-chamber TKE)	2	3	0	3
Pre-chamber Fuel Type	3	3	0	3
Air-Fuel Ratio	3	3	0	3
RMF, EGR	3	3	0	3
Spark Plug Location	1	2	0	1

Table 3.1: Pre-Chamber Geometric and Parametric Effect on the Pre-chamber Attribute and Combustion Processes. Table range, 3 = Highly Affected and 0 = Minimal Affect.

3.2.5 MAHLE Prototype Engine Results

This section examines prototype engines utilizing passive pre-chamber ignition as the main ignition source, with a specific example from MAHLE. The discussion will focus on results rather than jet formation and mechanisms, and the engines will be operated under stoichiometric conditions ($\lambda = 1$) in line with this thesis.

3.2.5.1 MAHLE Di3 Demonstrator Engine

The MAHLE Di3 engine is a demonstrator engine with intention of representing a 50% downsized engine displacing 2.4 liter [11]. The resulting engine was a 1.2 liter turbocharged, 3-cylinder inline, operating with conventional spark plug ignition and direct injection. The achieved performance of this engine a peak BMEP of 30 bar and a peak power output of 120 kW. This engine was later enlarged to 1.5L while still sharing maximum resemblance to the 1.2L version. The parameters of the 1.5L are presented in Table 3.2. The fuel used for this test was gasoline 95 RON

with 5% ethanol content. In its untouched form, using a conventional spark plug as its primary ignition source, the engine achieved a peak BTE of 36.7%. As the compression ratios increased to 12.8 and 14.7, low-pressure EGR and Miller cycle (EIVC) where added, the peak BTE increased to 40%.

Parameter	**Value**
Displaced volume	1.497 litres
Bore & stroke	83 mm & 92.2 mm
Base Compression ratio	9.25:1
Number of valves per cylinder	4
Power	141 kW @ 5000-5500 rev/min
Torque	334 Nm @1600-3500 rev/min
Fuel injection system	Direct injection (200 bar)
Variable valve timing	Inlet & Exhaust, both with 60°CA range

Table 3.2: MAHLE Di3 Demonstrator Engine Baseline. Values from [11].

To demonstrate the enhancements in combustion characteristics, the passive pre-chamber was initially installed into the 1.2L version of the engine. The results from this initial test are Figure 3.25.

The enhancement in rapid-burning angle (10-90% MFB, b), combustion phasing (a) and stability (CoV_{IMEP} or CoV_{NMEP}, c), maximum pressure (e) and rate of pressure rise (RMax, d) are clear. The jets produce hot distributed ignition sites which causes combustion to be rapid and this rapidness can be seen in RMax and 10-90% MFB. Phasing of combustion (50% MFB) showcases that the pre-chamber is still operating at MBT up until 16 bar BMEP while the conventional spark plug required timing adjustments from 14 bar BMEP. However the pre-chamber is actually yielding lower BTE values up until 16 bar BMEP when compared to the conventional spark plug and this is most likely associated with the thermal losses due to the induced turbulence and rapidness of the combustion.

The test was then commenced with the 1.5L version of the engine aided with beneficial technologies that look to take advantage of the enhanced burn-rate and targeted the enhancement of BTE. These beneficiary technologies where added in steps beginning with are higher compression ratios (+5.5) and spark plug, reverting to port fuel injection (PFI) and passive pre-chamber, the following step included the Miller cycle, followed by low pressure EGR and concluding by reverting back to direct injection. The results are presented in Figure 3.26.

As the figure shows, the first step of increasing the compression ratio and reverting to PFI in combination with the passive pre-chamber presents an increase in BTE up until 10 bar BMEP. The significant increase in knock at higher loads resulted from the increase in compression ratio and switching to PFI had a detrimental effect on engine BTE, which the phasing of MFB50 indicates. Adding the Miller cycle (EIVC) improved the BTE by across the whole load range, both due to combustion phasing being less retarded in comparison to the last step due to reduced mixture temper-

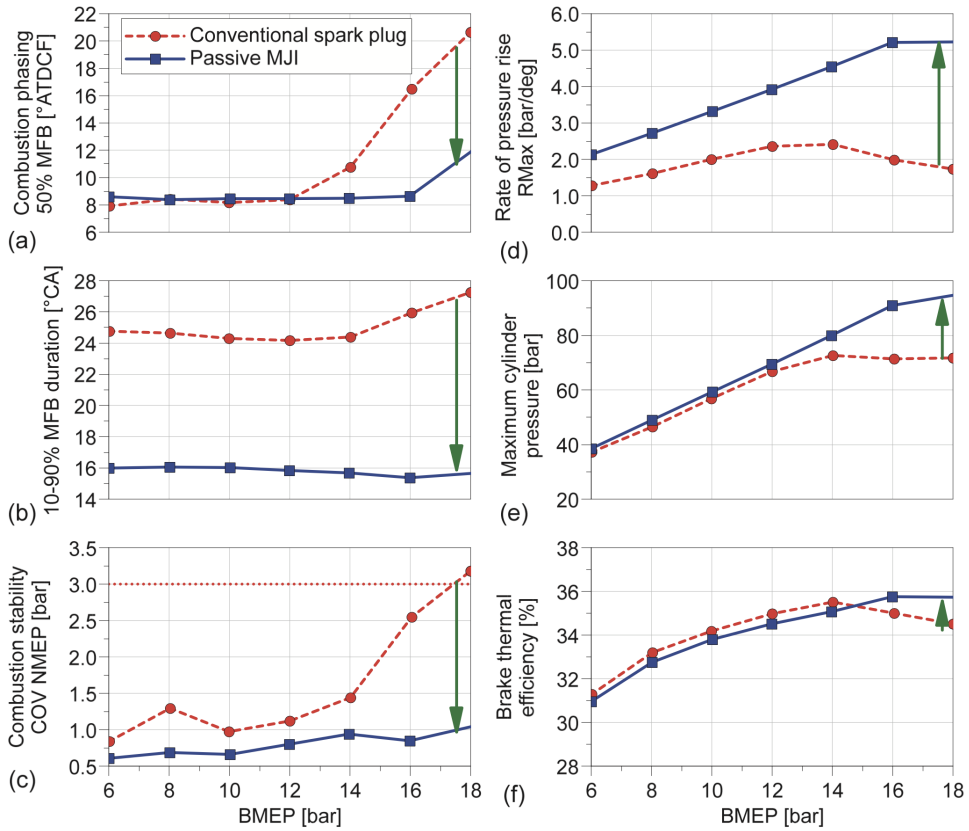

Figure 3.25: Initial passive pre-chamber testing on 1.2L Di3 engine 10.5:1 CR, 3000RPM load sweep from 6 to 18 bar BMEP. Figure from [11].

ature at the end of the compression stroke and reduced pumping losses. Adding cooled-EGR further improves the BTE and this is also due to combustion phasing and reduced pumping losses. EGR increases the specific heat capacity of the mixture which results in lower peak combustion peak temperatures and pressures. This thereby suppresses the build up of knock and phasing can be moved closer to MBT while also reducing the burn-rate which improve NVH (Noise Vibration and Harshness). The step in which DFI is reintroduced and PFI is omitted shows modest gains, if any, in efficiency, even with its the charge air cooling effect.

3.2.5.2 MAHLE Prime Mover Engine

The MAHLE prime mover engine is based on the MAHLE Di3 engine but developed to have a similar torque and power profile as the Volkswagen 1.5 litre TFSI EVO engine [11]. The specifications of the engine are similar to the parameters shown in Tabel 3.2, with the difference being the usage of PFI instead of DFI, an elevated compression ratio to 12.8:1, low-pressure EGR and Miller cycle. Figure 3.27 shows the results from a load sweep test from 4 to 18 bar BMEP at 3000RPM. The figure includes the baseline (black line) engine without any modification, operating with the same parameters as shown in Table 3.2. The compression ratio was then raised and a run with the conventional spark plug and Miller cycle was done (red line). The ignition source was then changed to the passive pre-chamber and the test was

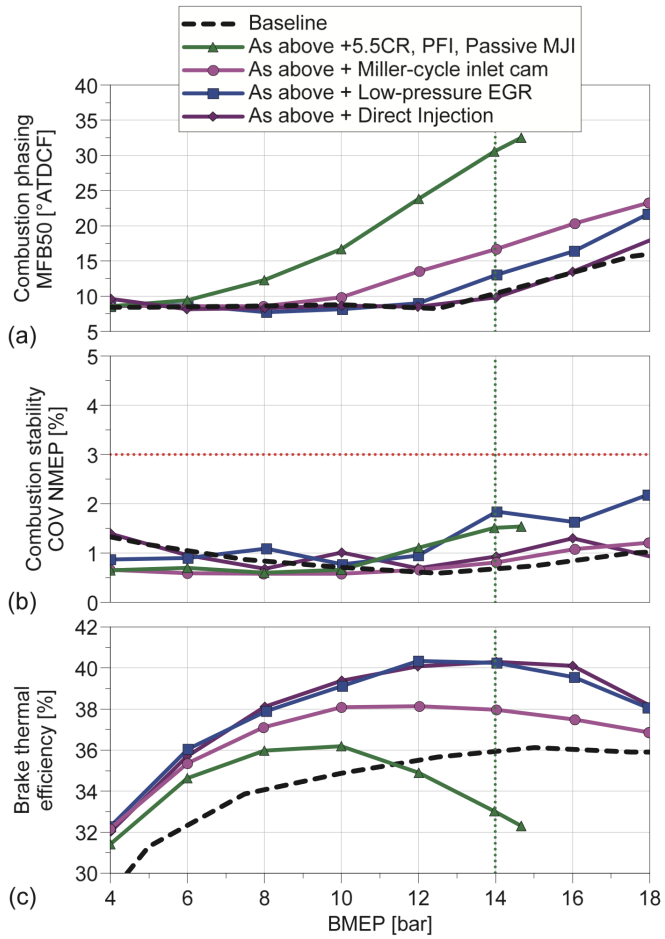

Figure 3.26: Baseline spark plug and passive pre-chamber testing in combination of beneficiary technologies on 1.5L Di3 engine, 14.7:1 CR, 3000RPM load sweep from 4 to 18 bar BMEP. Figure from [11].

done again (blue line). The test concluded with the introduction of a low pressure EGR (green line).

As illustrated in Figure 3.27a, the combustion phasing (MBF50) for the engine operating with an compression ratio and convectional spark plug becomes knock limited at 10 bar BMEP, requiring retarding of the timing. The introduction of the passive pre-chamber enables the combustion phasing to match the baseline run. The stability of the engine is also enhanced with the introduction of passive pre-chamber and the stability issues above 16 bar BMEP as observed with the conventional spark plug ignition did not occur when the pre-chamber was used. The BTE curve again showcases the efficiency gains when switching to the Miller cycle, raising the compression ratio and introducing the passive pre-chamber. The rapid combustion characteristic induced by the pre-chamber is able to consume the end gases before it reaches auto-ignition temperature leading to the combustion phasing being closer to MBT as opposed to the run with the conventional spark plug. The end result can be seen in the BTE curve as the conventional spark plug starts contracting at higher load while the pre-chamber improves higher efficiency across the entirety of the load

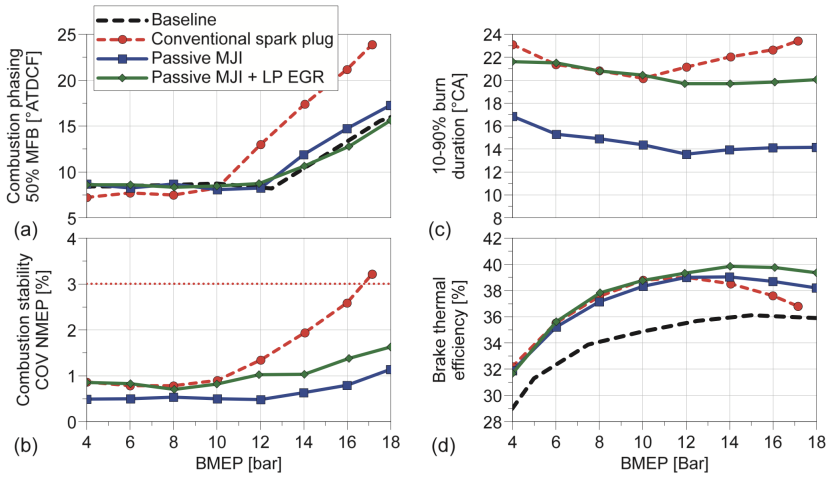

Figure 3.27: Passive pre-chamber testing in combination of beneficiary technologies on 1.5L Di3 engine, 12.8:1 CR, 3000RPM load sweep from 4 to 18 bar BMEP. Figure from [11].

range. Introducing EGR reduces pumping losses and suppresses the build up of knock which is witnessed in both the MBF50, rapid burning phase curve (Figure 3.27) as well as the BTE curve. Phasing is thereby advanced closer to MBT and the efficiency is further enhanced.

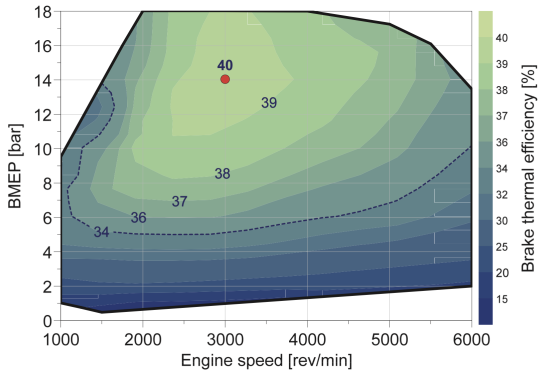

Figure 3.28: BTE plot, 12.8:1 CR. Figure from [11].

The full BTE map for *Passive MJI + LP EGR* is shown in Figure 3.28. The peak power harvested from the engine is 110kW at 5500RPM while delivering peak BMEP of 18 bar from 2000 to 4000RPM. The engine is capable of achieving BTE values exceeding 34% over a wide range of engine speeds and load with the maximum value being 40% extracted at 14 bar BMEP and 3000RPM.

4

Experimental Method

To adequately execute this research, a single cylinder test engine was dedicated for this purpose. The test engines stroke and bore geometry are based on the Aurobay Gen3 VEP LP with Miller camshafts, redesigned cylinder head with narrower valve angles and a modified piston that combined result in the elevated compression ratio of 13.45:1. The methods and equipment utilised for the execution of this thesis will be explored in finer detail in this chapter.

4.1 Test Engine

The engine used in this study is a single cylinder engine based on the Aurobay Gen3 VEP LP. As such, the engines bore and stoke is identical that of its origin. The full engine specifications are listed in Table 4.1.

No. of cylinders	1
Stroke	93.2 [mm]
Bore	82 [mm]
Compression ratio	13.45 w/o PC, 13.25 with PC
Fuel	Gasoline 95E10, 98E5
Number of Intake Valves	2
Number of Exhaust Valves	2
Fuel system	Direct injection
Ignition system	Conventional Spark or Passive Pre-chamber

Table 4.1: Engine Specification.

To accommodate a higher compression ratio, the cylinder head was redesigned with the valve angles with intake valve being altered from 16 to 14 degrees and exhaust valve from 23 to 18. A matching piston was designed to accommodate this narrow valve angles setup with a flatter bowl. The achieved compression ratio without the passive pre-chamber was thereby 13.45:1, and with the passive pre-chamber, 13.25:1. The test engine is equipped with variable camshaft phasing that will be used throughout testing to find the optimal settings for the best fuel consumption ($ISFC$) for the baseline and all pre-chamber specifications.

4.2 Baseline Spark Plug and Pre-Chamber Specification

The three pre-chambers with built-in spark plug were supplied by Tenneco and their specification can be seen in table 4.2. All of the pre-chamber have the same volume, orifice count and diameter however differing jet orientation.

Nozzle diameter	Number of nozzles	Total surface area	Pre-chamber Volume	V/A
1.2 mm	6	6.72 mm^2	630.5 mm^3	92.91

Table 4.2: Pre-chamber Configuration.

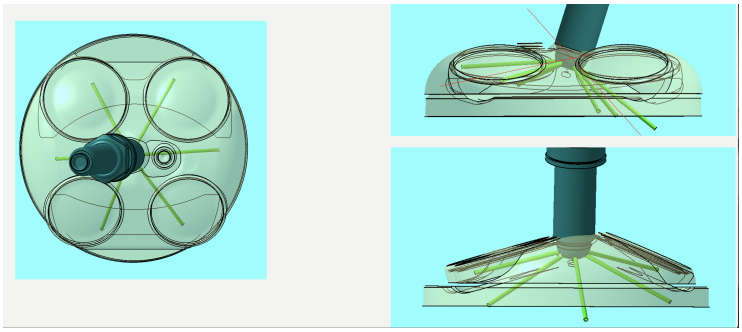

Figure 4.1: Pre-Chamber Jet Orientation 1, PC1.

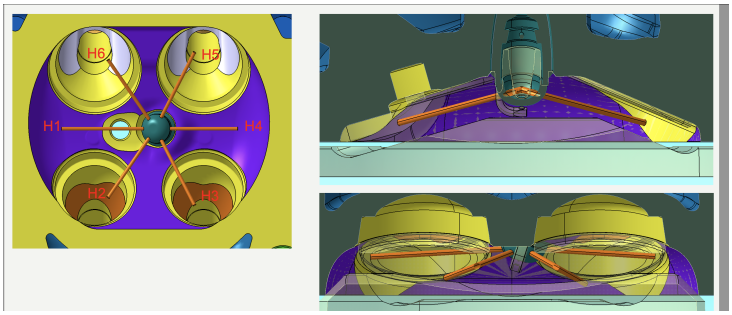

Figure 4.2: Pre-Chamber Jet Orientation 2, PC2.

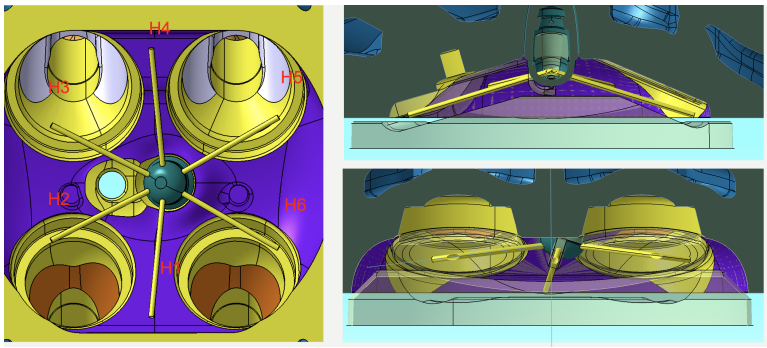

Figure 4.3: Pre-Chamber Jet Orientation 3, PC3.

The pre-chamber orientations selected for this thesis were specifically chosen to investigate its effect on the combustion process. The threads that hold the different

ignition sources on the cylinder head are angled, meaning that these threads, and thereby the ignition source, do not follow the vertical line relative the piston. This, therefore, implies that if the pre-chamber jets are to be symmetric relative to the combustion chamber, the orifices have to be placed in a specific way on the pre-chamber caps. To clearly verify what difference the orientation makes, one of the pre-chambers, pre-chamber 1, does not have orifices symmetrically placed relative the combustion chamber, with it only being symmetrical to its own axis (see Figure 4.1). This, thereby, means its easier install, essentially being the most "plug-and-play" of the three configurations. Pre-chamber 2 and 3, however, due have orifices that are symmetrical to the main combustion chamber. This naturally implies they have to be installed into the cylinder head a more specific manner to align the orifices correctly into the main combustion chamber. The difference between pre-chamber 2 and 3 are mainly difference in jet ejection pattern, as seen in Figure 4.2 and Figure 4.3 depicting the jet ejection pattern for pre-chamber 2 and 3 respectively. The naming nomenclature used in the remainder of the thesis to identify the pre-chamber will be pre-chamber 1 or PC1, referring to jet orientation of the top row of Figure 4.3, pre-chamber 2 or PC2, referring to the middle row, and pre-chamber 3 or PC3 referring to the bottom row.

4.3 Analysis

To effectively evaluate the differences in the setups, analysis will commence were relevant parameters are compared and assessed. The relative importance of each parameter will depend on the testing session, and this section will present an overview of the parameters used during each of these sessions.

4.3.1 Repeatability and Robustness Analysis

The definition of repeatability implies that the output can be reproduced with the same input parameters. For the sake of this test, the three runs on the three consecutive days is to confirm that the results gathered are trustworthy, repeatable and that the system as a whole is robust. The test procedure for all operating points is to achieve the adequate IMEP with the minimum required airflow and combustion phased to MBT or knock limit. All input parameters such as fuel pressure, oil temperature, iVVT, eVVT, coolant temperature and intake temperature and pressure are always set as target values and will not always be constant as these parameters continuously fluctuate around this target input value. Nevertheless as the test expands through days, some small variations in these input parameters are to be expected. Therefore it is of interest to analysis the effect of these small variations. Robustness in this instance is therefore not only defined as how well the setup reproduces the output value (ISFC) but also how sensitivity the setup is to very small changes of the input parameters. The operating point is deemed repeatable if the system manages to reproduce the result with respect to ISFC atleast once during the testing sessions. The setup is however only deemed robust if all produced values are within the set boundary condition. The boundary conditions for repeatability and robustness are summarised in the following statements:

For a specific operating point to be deemed repeatable, it must fulfil the following boundary condition:

- The operating point is deemed repeatable if its reproduced during the test session within the median ISFC $\pm$ 0.5 g/kWh at least once.

For the operating point to be deemed robust, it must fulfil the following boundary condition:

- The operating point for the specific system is deemed robust if each ISFC value in that specific operating point fall within the median ISFC $\pm$ 1 g/kWh.
- The operating point fulfils the boundary condition of repeatable.

For the setup as a whole to be deemed robust, it must fulfil the following boundary condition:

- Fulfil the boundary condition for robust atleast 7 times for 7 different operating points.

The parameter in the boundary conditions that defines if an operating point in the minimap is repeatable and the setup robust will be the spread of the ISFC values with respect to the median. The median was chosen as opposed to the mean because all operating points were repeated three times, which meant that if one of the results was an outlier, the mean could be affected significantly. The median result however, will always be close to another one of the results.

To streamline this thesis, the minimap run that contains the least variance from the median will be used as the representative run for the remainder of the analysis in the Results section. All plots will however be available in the appendix.

4.3.2 Performance Analysis

The parameters that will be used when comparing the performance of each ignition source will be the fuel conversion efficiency (η_f) and the indicated specific fuel consumption ($ISFC$). Both of these parameters determine the efficiency, performance, and the work produced by the engine with respect to the fuel consumption. The indicated fuel conversion efficiency is a measure of how effectively the fuel is converted into indicated work, and is typically measured as percentage. The indicated specific fuel consumption is a measure of how much fuel an engine consumes per unit of energy produced. It is commonly used in the automotive industry to evaluate engine efficiency. By comparing the fuel conversion efficiency and the indicated specific fuel consumption of the different ignition sources, it is possible to evaluate their performance and determine which one is the most efficient.

$$ISFC[g/kWh] = \frac{mf_{Fuel}}{P_{Indicated}} \tag{4.1}$$

$$P_{indicated} = IMEP_n * V_d * \frac{N}{2} \tag{4.2}$$

$$\eta_f = \frac{W_{indicated}}{mf_{Fuel} * Q_{LHV}} \tag{4.3}$$

Where mf_{Fuel} is the mass flow of fuel, $P_{Indicated}$ is the indicated power produced, V_d is the piston swept volume, N the engine RPM, $W_{indicated}$ is the indicated work and Q_{LHV} is the lower heating value of the fuel. These parameters will be utilised during the comparisons for the different setups during all of the testing sessions.

4.3.3 Emission Analysis

The emissions analysis will comprise of analyzing the nitrogen oxide NO_x, carbon monoxide CO, and unburned hydrocarbons THC. The parameters utilized for this analysis will be the indicated specific (IS) engine out emissions, such as $ISNO_x$, $ISCO$, and $ISTHC$. The indicated specific engine out emissions is a measure of the amount of pollutants emitted per unit of indicated energy produced. By analyzing the $ISNO_x$, $ISCO$, and $ISTHC$ of the different ignition types, it is possible to evaluate their emissions performance and determine which one produces the least emissions. It is important to note that NO_x, CO and THC are considered as harmful emissions and regulated by most of the countries, thus having low values these emissions would be desired for the engine to meet the regulations. THC and CO are also indicators of incomplete combustion and hence less efficient engine operation.

$$ISNO_x[g/kWh] = \frac{mf_{NO_x}}{P_{Indicated}} \tag{4.4}$$

$$ISCO[g/kWh] = \frac{mf_{CO}}{P_{Indicated}} \tag{4.5}$$

$$ISTHC[g/kWh] = \frac{mf_{THC}}{P_{Indicated}} \tag{4.6}$$

4.3.4 Accumulated Heat Release and Heat Transfer Analysis

Heat release analysis provides a fundamental insight into combustion process during the cycle. Since the pre-chamber combustion process differs from the conventional spark plug, it is of interest to analyse the heat release and the losses relative to the conventional spark plug. The test engine is equipped with a piezoelectric sensor to measure the in-cylinder pressure. The heat release theory, described by Heywood [6], is based on the first law of thermodynamics:

$$\frac{dQ_{ch}}{d\theta} = \frac{\gamma}{\gamma - 1} P \frac{dV}{d\theta} + \frac{1}{\gamma - 1} V \frac{dP}{d\theta} + \frac{dQ_{cr}}{d\theta} + \frac{dQ_{ht}}{d\theta} \tag{4.7}$$

Where P is the measured in-cylinder pressures, V is cylinder volume and γ the specific heat ratio. However for pre-chamber combustion, this heat release theory has to be complemented by the heat release inside the pre-chamber volume. Due to the lack of a piezoelectric sensor inside the pre-chamber, this pressure trace could not be generated and will thus be excluded. It is therefore important to note that calculations will not completely agree with reality and its estimated that this error

is around 2.5% [25]. Q_{ch} represent the chemical energy released during combustion, or the gross heat-release, and this term can therefore be expressed as:

$$\frac{dQ_{ch}}{d\theta} = \frac{1}{d\theta}(m_{fuel} * Q_{LHV} * \eta_{ComEff}) \tag{4.8}$$

Where m_{fuel} is the inputted fuel mass during the cycle, Q_{LHV} is the lower heating value of the fuel and η_{ComEff} is the combustion efficiency, which is determined by the exhaust gas compassion. With the aid of the piezoelectric sensor, the in-cylinder pressure is measured and thereby the net heat release can be determined:

$$\frac{dQ_{ch_{net}}}{d\theta} = \frac{\gamma}{\gamma - 1}P\frac{dV}{d\theta} + \frac{1}{\gamma - 1}V\frac{dP}{d\theta} \tag{4.9}$$

The derivation of the in-cylinder heat transfer can thereby be determined to:

$$\frac{dQ_{ch}}{d\theta} - \frac{dQ_{ch_{net}}}{d\theta} = \frac{dQ_{ht}}{d\theta} + \frac{dQ_{cr}}{d\theta} \tag{4.10}$$

Therefore, the losses due to heat transfer and crevice flow can be correctly estimated. The pre-chamber can be modeled as a crevice flow loss, due to the gas that flows into the pre-chamber during the compression stroke. However, as $\frac{dQ_{cr}}{d\theta}$ is function of the working fluid temperature, the temperature in the pre-chamber cannot accurately be determined due to the lack of a sensor to monitor its state. Nevertheless, as combustion in the pre-chamber will raise the working fluids temperature and thereby contribute to the heat transfer, this crevice flow loss will be combined into the heat transfer loss. The crevice flow loss that normally is contributed by the flow into different regions in the combustion chamber is assumed to flow back into the main combustion chamber which then either oxidises into incomplete combustion or flows into the exhaust as HC, and this will therefore be accounted for in the combustion efficiency term η_{ComEff} (see Equation 4.8). Therefore, the expression that will be utilised estimate the heat transfer losses will be:

$$\frac{dQ_{ch}}{d\theta} - \frac{dQ_{ch_{net}}}{d\theta} = \frac{dQ_{ht}}{d\theta} \tag{4.11}$$

Which after integration terms in Equation 4.11 will yield the accumulated heat release rate depicted in Figure 4.4.

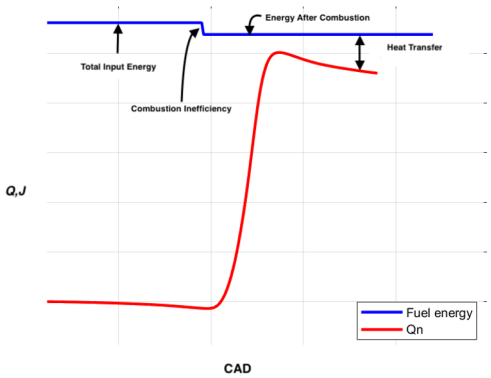

Figure 4.4: Accumulated Heat Release Rate and Heat Transfer Approximation.

4.3.5 Energy Balance

In order to understand the distribution of the energy losses, an energy balance calculation is to be performed. The calculations used in the energy balance follow the first law of thermodynamics and use the available measurable data in the test bed. Figure 4.8 illustrates the control volume around the engine with the various inputs and outputs. The first law of thermodynamics implies that energy cannot be created or destroyed, only be converted from one form to another. By performing an energy balance calculation, it is possible to determine the energy inputs and outputs for the engine and understand how the energy is being used and where it is being lost. The control volume around the engine in Figure 4.8 illustrates the various inputs and outputs such as the fuel energy, heat loss, mechanical energy, and exhaust energy which are used in the energy balance calculation.

With this control volume, the following equations can be utilised to calculate the various energy losses:

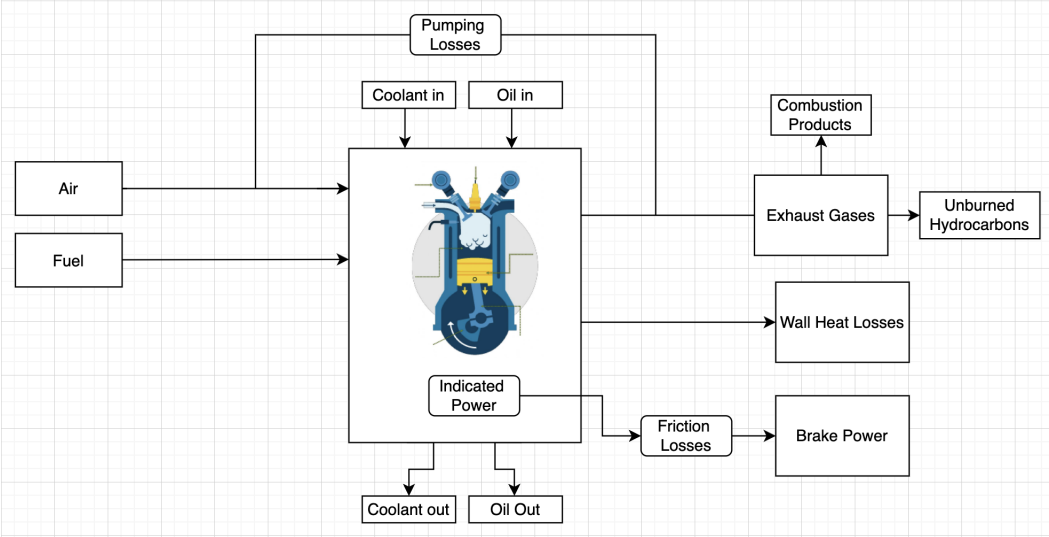

Figure 4.5: Control Volume around Engine.

$$InputEnergy_{Fuel} = m_{fuel} * Q_{LHV}, [\frac{J}{Cycle}] \tag{4.12}$$

$$Combustion\ Inefficiency = InputEnergy_{Fuel} - m_{fuel} * Q_{LHV} * \eta_{ComEff}, [\frac{J}{Cycle}] \tag{4.13}$$

The combustion efficiency (η_{ComEff}) is derived by the gas compassion and crevice losses. Therefore, this term will take into account the losses due to unburned hydrocarbons HC and the combustion products CO and H_2. Thus, these losses can be ignored for the rest of the calculations.

$$Indicated\ Work = IMEP_n * V_d, [\frac{J}{Cycle}] \tag{4.14}$$

$$Pumping\,Work = PMEP * V_d, [\frac{J}{Cycle}] \tag{4.15}$$

$$Exhaust\ Heat\ Losses\ =\ (m_{Exhaust} * Cp_{Exhaust}) * (T_{Exhaust} - T_{Intake})[\frac{J}{Cycle}]$$

For the exhaust heat loss evaluation, an internal equation derived for estimating $Cp_{Exhaust}$ will be utilized. For the most accurate estimation of the loss decomposition, losses to blow-by, coolant and oil should be taken into account in accordance with the control volume. However, reliable measurement of these parameters is not available and will thus not be included in the calculation. These losses are therefore accounted for in the in-cylinder losses. The in-cylinder losses can thereafter be calculated as:

$$InCylinderLosses = EnergyFuel - CombustionInefficiency - InidcatedWork - Pumping\,Work - Exhaust\ Heat\ Losses[\frac{J}{Cycle}]$$

The in-cylinder heat losses therefore includes the wall heat losses and does not solely represent it. Therefore, the energy balance calculation will be utilized during the disposition of the losses to obtain a comprehensive overview of the distribution of the input energy. The heat transfer calculation utilizing the accumulated heat release rate expressed in Section 4.3.4 will be employed for the elaborated in-cylinder heat transfer evaluation to better understand its effect as a result of the different ignition types.

4.4 Test Procedure

4.4.1 Daily Test

The test procedure for both the baseline spark plug and the pre-chambers should be done in a similar fashion to enable easy comparison of the data. However, this will only be true if the test bed is producing consistent and reliable results. Therefore, each day of testing will commence with a daily test consisting of 4 operating points, as depicted in Figure 4.3. This will help ensure that the results obtained from the test bed are trustworthy, and that any variations in the results are due to the ignition source and not due to variations in the test bed. The generated results from each day of daily test will be compared to the previous days to observe if the output parameters are consistent. Only if the results obtain consistency will testing presume as schedule.

4.4.2 Minimap and Robustness Test

The operating points that make up the minimap are based on the WLTC (Worldwide Harmonized Light-Duty Test Cycle) cycle and are determined by the power

Speed [RPM]	Load [IMEP]	Back Pressure [kPa]	SOI	Rail Pressure [MPa]
2000	17	130	300	20
2000	Fuel Cut	-	-	-
1750	9	105	280	20
1500	6	105	280	20

Table 4.3: 4-point daily test, $\lambda = 1$.

weighting functions for each operation point. The WLTC is a driving cycle that is used to test the emissions and fuel consumption of vehicles in a standardized way, and it is designed to simulate real-world driving conditions. The power weighting functions are used to assign different weights to different operating points, depending on the expected power demand during that point in the cycle. By using the WLTC cycle and power weighting functions, the minimap is able to accurately represent the operating points that are most relevant for the specific engine, and this allows for a more comprehensive and realistic assessment of the engines performance. These weights are demonstrated in Figure 4.6a with Figure 4.6b representing the chosen operating points. The engine and vehicle chosen for the generation of this minimap are specifically tailored for the engine used in the test bed. Thus, the vehicle used is the Volvo V60 equipped with the Gen3 VEP LP. One additional point was added to complete the load sweep at 2000RPM.

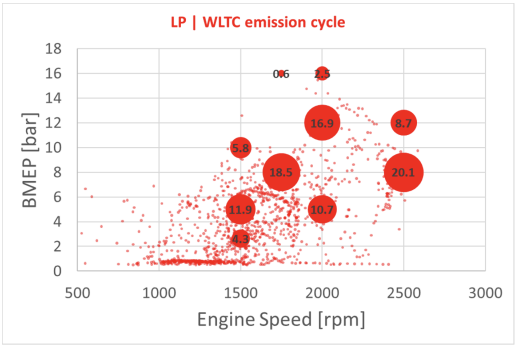

(a) WLTC Load-Speed Power Weighted Average Weigths.

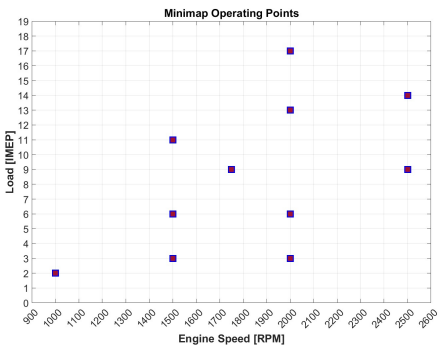

(b) Minimap Operation Points Plot.

Figure 4.6: WLTC Cycle and Minimap operation points.

The minimap was ran three times in three days in succession to validate the robustness and repeatability of the pre-chamber and spark plug.

4.4.3 Variable Valve Train Sweep and Boundary Conditions

The hardware modification made to the engine allocated for this thesis differs significantly from the standard Gen3 VEP LP that it is not immediately obvious what the optimal variable valve timing (VVT) settings would be for the minimap operation points. This is further complicated by the different ignition process taking place for the case with the pre-chamber. To find the optimal setting for the VVT,

Speed [RPM]	Load [IMEP]	Lambda [λ]	Power Weighted Average	Intake Temperature [°C]
1000	2	1	0.6	45
1500	3	1	4.3	45
1500	6	1	11.9	35
1500	11	1	5.8	30
1750	9	1	18.5	30
2000	3	1	ADDITIONAL	30
2000	6	1	10.7	30
2000	13	1	16.9	30
2000	17	1	2.5	30
2500	9	1	20.1	30
2500	14	1	8.7	30

Table 4.4: Engine Load-Speed Minimap Targets.

a VVT sweep is conducted of the possible settings for each operation point in the minimap for both the baseline spark plug and PC1. A smaller and more compact VVT sweep is also conducted for PC2 and PC3 (see section 4.4.3.1 for further details). These settings will then be used for the consecutive minimap runs for both the pre-chambers and the baseline spark plug. See Figure 4.7 and Table 4.5 for the VVT settings that will be tested during the VVT sweep. The choice of the optimal VVT settings will be determined by the fuel consumption, or more specifically, the indicated specific fuel consumption (ISFC [g/kWh]). However, the choice of the optimal point can only be made if the engine is operating within the specific boundary conditions set for driveability (CoV_{IMEP}), combustion phasing ($MFB50$ or $AI50$) and the percentage of engine out O_2 emissions for the effective operation of the 3-way catalytic converter. The only exception to these boundary conditions is the lowest operation point (2 bar IMEP @ 1000RPM) where engine out O_2 emissions will be excluded. These operating boundary conditions can be seen in Table 4.6.

To illustrate how the choosing procedure for the optimal VVT setting would look like, an example will now be presented. Figure 4.9a shows the results from VVT sweep for 11 bar IMEP at 1500RPM from the baseline spark plug and Figure 4.9b shows the chosen VVT settings. The figure 4.9a showcases O_2, $AI50$, CoV_{IMEP}, knock and ISFC. As already discussed, the target is minimum ISFC within the set boundary conditions. For this example, all conditions satisfy CoV_{IMEP} due to it being within the set boundary; however, all settings below 10 iVVT are not usable due to it exceeding the boundary of AI50. The area of maximum overlap is also made redundant due to the excess O_2 emissions. This only leaves the lower right corner of the map usable, which is also the area where the best ISFC is achieved. It's also worth noting that points in between the tested VVT sweep may yield an ISFC that is within the boundaries. For example, if the setting 40/10 iVVT/eVVT would have resulted in an ISFC of 220, however, an O_2 output of 1.17, then eVVT would be increased from 0 with steps of 2 until the limit of 0.7 O_2 emissions is reached. When the limit is reached, the result is recorded and the ISFC noted, if this in turn is better then the result generated at 42/0, then it would be used.

iVVT	eVVT
0	0
10	0
20	0
30	0
42	0
0	10
10	10
20	10
30	10
42	10
0	20
10	20
20	20
30	20
42	20
0	30
10	30
20	30
30	30
42	30

Table 4.5: VVT Settings.

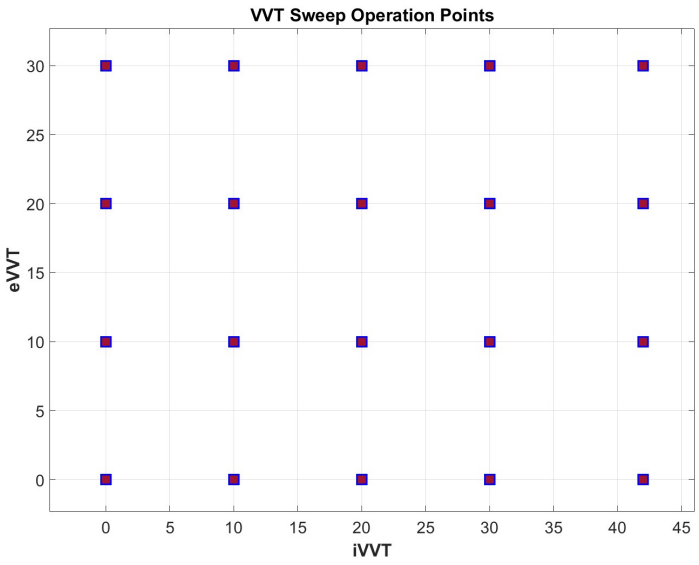

Figure 4.7: VVT Settings Plot.

Boundary Conditions	Value
CoV_{IMEP}	$< 3\%$
$AI50$	$< 30°$ ATDC
O_2	$< 0.7 \pm 0.1$ %
Knock	2 ± 0.3

Table 4.6: VVT Sweep Boundary Conditions.

4.4.3.1 VVT Sweep Strategy for Pre-Chamber 2 and 3

Due to all pre-chambers having similar geometric shapes, it is reasonable to assume that the jet formation and penetration characteristics will remain unchanged (ignoring the difference in gas exchange properties due to the orifices pointing in different directions). The first pre-chamber to be tested was PC1 and because of the completely different ignition mechanisms presented by the pre-chamber, it is reasonable to perform a full VVT sweep to analyze the combustion process as the VVTs are adjusted. Following the hypothesis that the jet formation and penetration characteristics remain unchanged, a smaller and more compact VVT sweep will be done for PC2, which will only test the adjacent VVT settings of the most optimal VVT setting obtained from the full PC1 VVT sweep. Figure 4.4.3.1 gives an illustration of the strategy implemented for this "compact and smaller" VVT sweep. If any of the adjacent point show better fuel consumption within the set boundary conditions,

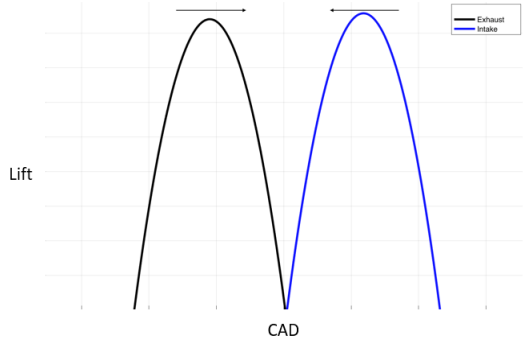

Figure 4.8: VVT Angles. Positive VVT setting for either iVVT or eVVT phases the duration in the arrows direction.

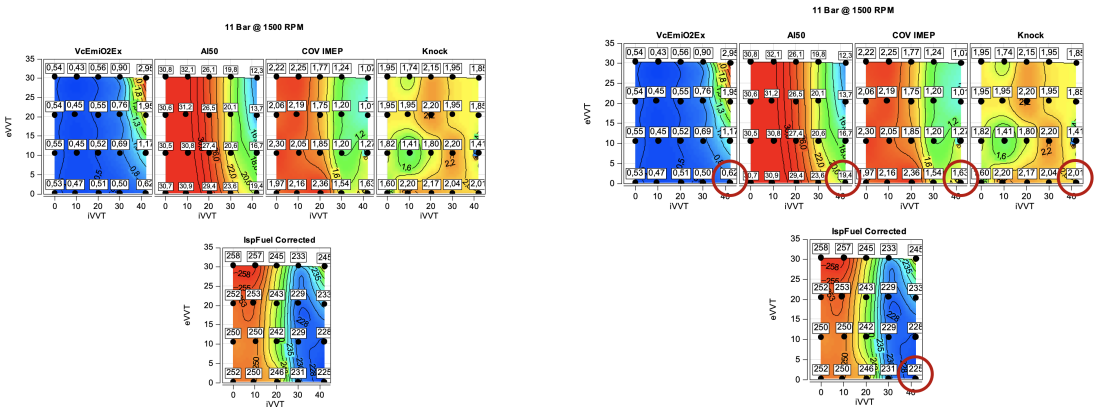

(a) VVT Sweep Results.

(b) Chosen VVT setting (Red Circles).

Figure 4.9: Baseline VVT sweep, 11 Bar IMEP at 1500RPM.

then that VVT setting will be used for that specific pre-chamber. This approach will help save time and resources while still providing valuable information about the performance of the different pre-chambers.

If the results observed from the PC1 and PC2 VVT sweeps show the same pattern of output results, that is, the best usable VVT settings are the same for both setups, then PC3 will not receive the full "smaller and compact" VVT sweep. This is because PC2 and PC3 are similar in orientation and, due to the time constraints presented in the project, it is thereby fully assumed that the optimal VVT settings for PC2 are the same as for PC3. However to ensure that there are no significant differences, a even smaller VVT sweep for will be conducted for PC3 only testing the adjacent VVT settings for the operation points that generate similar ISFC values. The settings for the VVT positions tested for PC3 are illustrated in Table 4.7. If the results from this even "smaller and compact" VVT sweep generate optimal VVT settings that are the same for PC2, then it would be reasonable to assume that the optimal VVT settings for PC2 are the same as for PC3.

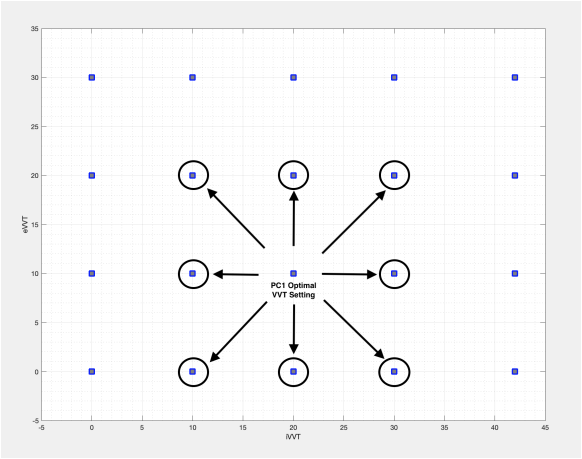

Figure 4.10: VVT Sweep Strategy for PC2 and PC3

Engine Speed [RPM]	Load [IMEP, Bar]	iVVT/eVVT
2500	9	42/0, 35/0, 35/10, 30/0
1750	9	42/0, 42/10
1500	6	42/20, 42/30
1500	3	20/10, 30/0

Table 4.7: VVT Sweep Testing Settings for PC3

4.4.4 Heat loss and Energy Balance Test Direct Comparison

In order to thoroughly understand the heat losses of the different ignition setups, it is important to conduct a test that compare them directly under similar conditions. Therefore, an additional minimap and wide-open throttle test (see section 4.4.5) will be conducted for the pre-chambers with the same VVT settings, mass flow of air and combustion phasing as the baseline spark plug when optimally operated. The data will then be used to generate the accumulated heat release (AHR) and energy balance bar plots for direct comparison between the ignition sources.

4.4.5 Wide open throttle and EGR test

To understand the performance of the different setups during full load operation, a wide-open throttle (WOT) test will be conducted. All pre-chambers and baseline spark plug will be subjected to the WOT test targeting the torque figure of the production version Gen3 VEP LP. However, if the baseline spark plug fails to reach the adequate load, then the pre-chamber WOT test will be conducted twice (not including the WOT test allocated for heat loss and energy balance calculation). Once to reach the same load (IMEP) as the baseline spark plug for direct performance comparison and once targeting the torque figure of the production engine. These operating points are shown in Table 4.8 using the same boundary conditions stated in section 4.4.3. The fuel utilised for this test will be 98 octane.

In addition to the WOT test, an high pressure cooled-EGR test will also be con-

ducted to understand its effect on pre-chamber performance. This test will be carried out on three operating points from the minimap, as outlined in Table 4.9. For each operating point, the EGR levels will be increased until combustion becomes unstable i.e $CoV_{IMEP} > 3$ or the EGR valve is fully open. The fuel consumption, heat loss, and energy balance will then be calculated and compared with the test without EGR input.

Speed [RPM]	Torque [Nm]	Intake Temperature [°C]
1500	75.05	30
2100	69.25	30
4800	74.9	30

Table 4.8: WOT Test Target Values

Speed [RPM]	Load [IMEP, Bar]	Intake Temperature [°C]
2500	14	30
2500	9	30
1750	9	30

Table 4.9: EGR Test Operating Points

5
Results

This thesis aims to compare the performance and viability of pre-chamber ignition systems to that those of the baseline spark plug. To do this, the optimal settings for variable valve timing must first be determined. A VVT sweep was conducted for the baseline spark plug and PC1, while a smaller, more compact sweep was conducted for PC2 and PC3 (as described in 4.4.3.1). Following the successful completion of this sweep, three minimap runs were conducted on consecutive days, during which various parameters such as ISFC, combustion duration, thermodynamic heat losses, efficiency, and emissions were compared. Additionally, one more minimap run was conducted for the pre-chambers using the same input settings as the baseline spark plug, during which the energy balance, in-cylinder and exhaust heat losses were calculated and compared. To investigate whether the fuel conversion efficiency and combustion heat losses could be further improved, an EGR test was also conducted for PC3. Testing was concluded with a WOT test for all pre-chambers and the baseline spark plug, to evaluate the ignition sources behavior under high engine load and speed. All test results were analyzed using AVL Concerto, Microsoft Excel, Matlab, and Python while the engine was controlled with AVL Puma and ETAS INCA.

Please take note that the ISFC values obtained from the VVT sweeps for the Baseline and PC1 may not align perfectly with those obtained from the minimap runs. This is because a recalibration session for the test facility was scheduled during the testing phase, which resulted in a slight adjustment in the TDC position in AVL Indicom. This may cause slight differences in the ISFC results, however, it does not affect validity of the chosen VVT settings and minimap runs since the minimap runs took place after this recalibration session.

5.1 VVT Sweep

The main objective of the VVT sweep is to identify the optimal camshaft phasing for the best fuel consumption each ignition source. The camshaft phasing plays a crucial role in the gas exchange process, helping to maintain optimal volumetric efficiency throughout the engine's operating range. This engine also utilizes the Miller cycle or EIVC, which means that the swept volume and the effective compression ratio are controlled by the means of the IVC. Advancing the IVC (increasing iVVT) reduces the effective compression ratio, effecting the compression temperatures, which helps to prevent knock buildup while also reducing pumping losses. However, excessive

advancement of the iVVT will negatively effects on the volumetric efficiency while also leading to excessive overlap between the intake and exhaust valves. This can subsequently result in either fresh air escaping into the exhaust manifold, causing an increase in O_2 concentration (affecting the conversion efficiency of the three way catalyst) or trapping too much hot RMF (internal-EGR) in the combustion chamber. Excessive overlap leading to high internal-EGR promotes an extension of the pre-heat and conduction zone (see Figure 2.2), which subsequently leads to longer combustion duration. As more RMF is trapped, combustion will continue to deteriorate, eventually leading to misfire, causing THC and O_2 concentration in the exhaust to spike. In some cases, combustion can start knocking due to the hot gases prompting an increase in temperature of the end-gases. It is thereby important to find the optimal setting for the VVT for the most efficient operation of the engine to gain the best balance between the benefits of the Miller cycle while keeping both the mass flow needs to meet the power output and limiting the in-cylinder RMF.

The first VVT sweep was performed with the baseline spark plug, and the results are presented in Figure 5.1 with respect to $ISFC$ (g/kWh).

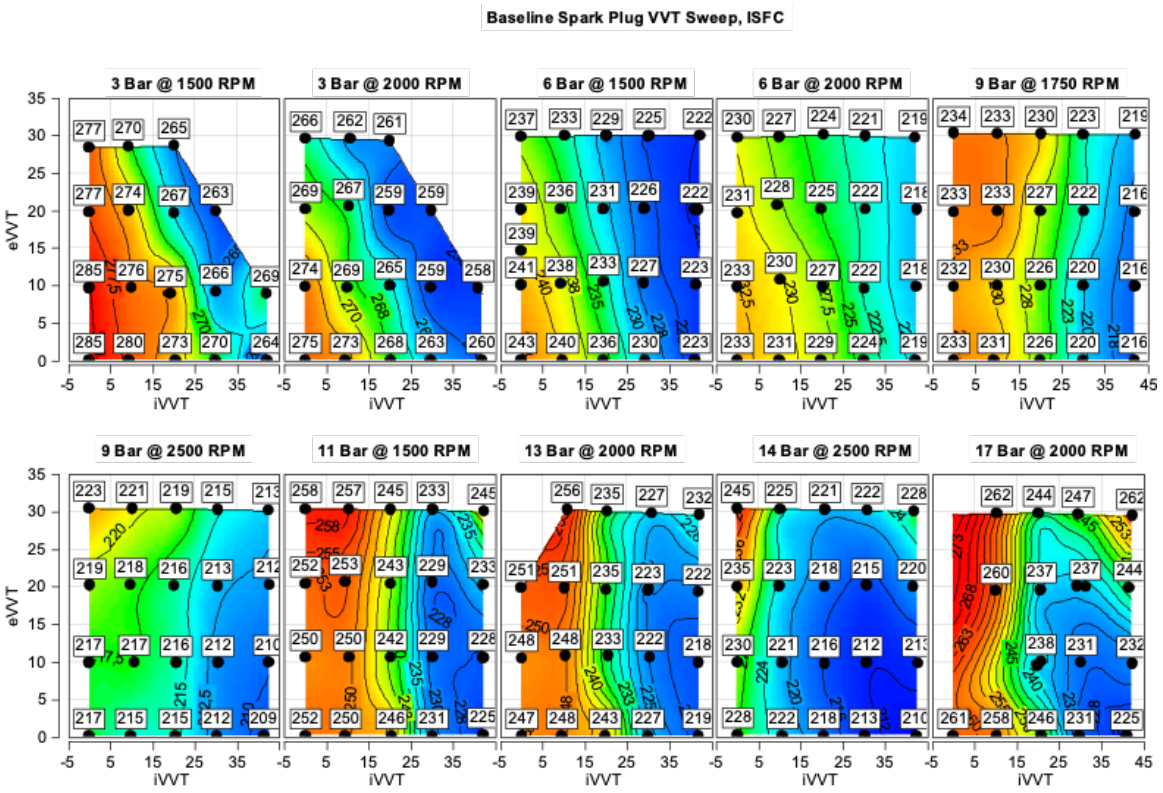

Figure 5.1: VVT Sweep for Baseline Spark Plug, ISFC $[g/kWh]$.

The figures showing the VVT sweeps with respect to AI50, O_2 emissions and the CoV_{IMEP} for the baseline spark plug are presented in the Appendix as Figures A.1, A.2 and A.3, respectively. With respect to the boundary conditions, the optimal VVT settings for the baseline spark plug are presented in Table 5.1.

Engine Speed [RPM]	Load [IMEP, Bar]	iVVT	eVVT
2500	14	42	0
2500	9	42	0
2000	17	35	0
2000	13	42	5
2000	6	42	10
2000	3	15	15
1750	9	42	0
1500	11	42	0
1500	6	42	20
1500	3	20	15
1000	2	0	0

Table 5.1: Optimal VVT settings for Baseline Spark Plug.

The results of the VVT sweep for PC1 is shown in Figure 5.2 with respect to ISFC. The figures showing the VVT sweeps with respect to AI50, O_2 emissions and the CoV_{IMEP} for PC1 are presented in the Appendix as Figures A.4, A.5 and A.6 respectively. The chosen VVT settings for with respect to the boundary conditions is presented in Table 5.2.

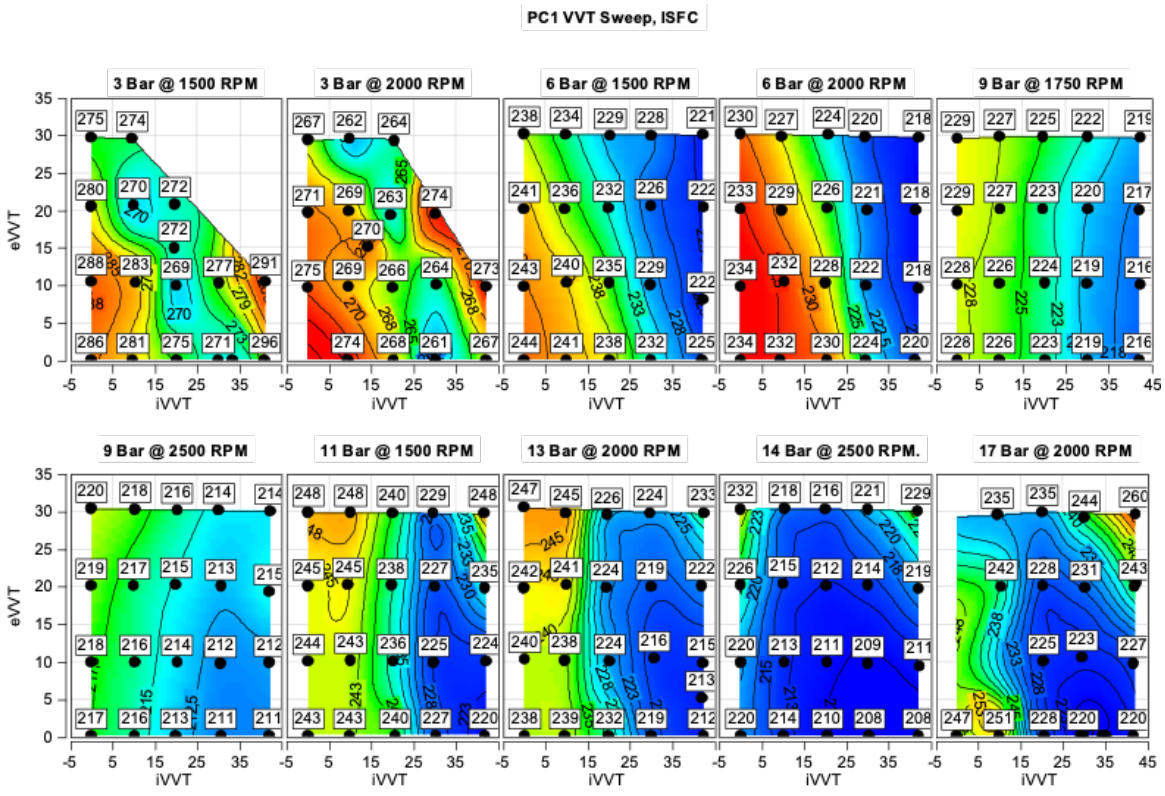

Figure 5.2: VVT Sweep for PC1, ISFC $[g/kWh]$.

Engine Speed [RPM]	Load [IMEP, Bar]	iVVT	eVVT
2500	14	42	0
2500	9	35	0
2000	17	35	0
2000	13	42	0
2000	6	42	20
2000	3	30	0
1750	9	42	0
1500	11	42	0
1500	6	42	20
1500	3	30	0
1000	2	0	0

Table 5.2: Optimal VVT settings for PC1.

The results of the VVT sweep for PC2 are shown in Figure 5.3 with respect to ISFC. The figures showing the VVT sweeps with respect to AI50, O_2 emissions and the CoV_{IMEP} for PC2 are presented in the Appendix as Figures A.7, A.8 and A.9 respectively. The optimal VVT settings for PC2 was shown to be identical to PC1.

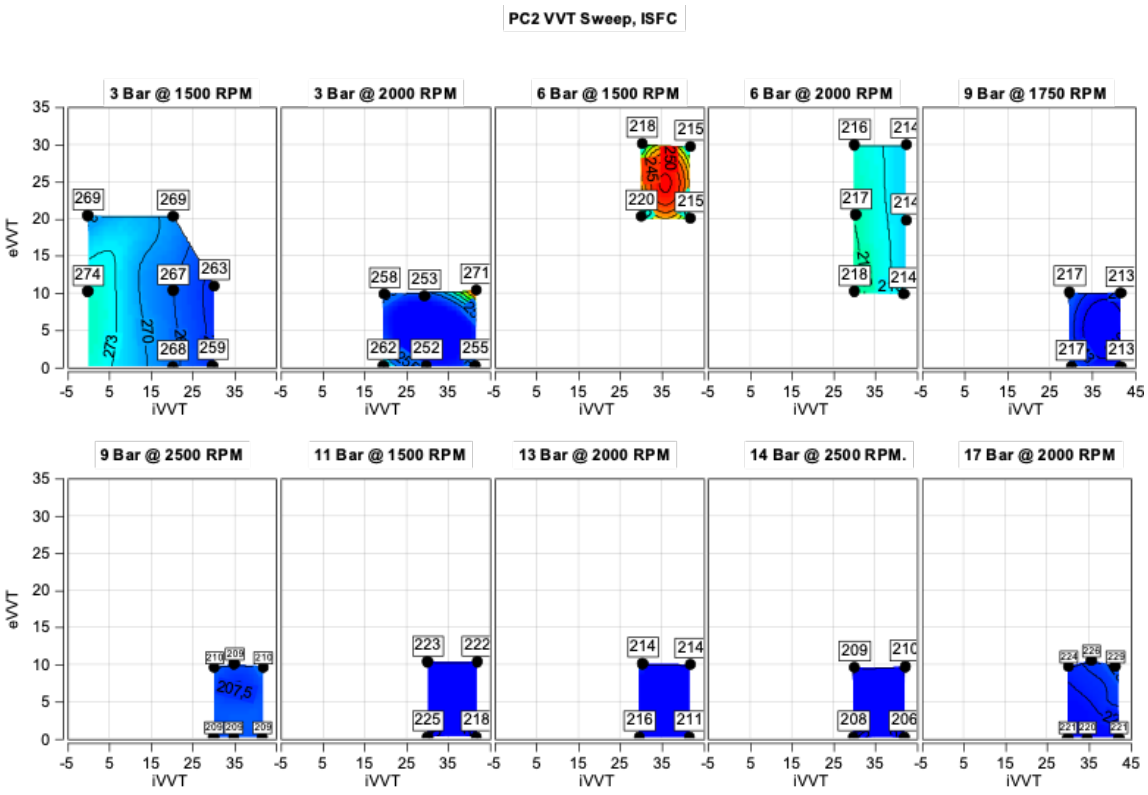

Figure 5.3: VVT Sweep for PC2, ISFC $[g/kWh]$.

As outlined in Section 4.4.3.1, PC3 was only subjected to a smaller and more compact VVT sweep. The results of this VVT sweep revealed no significant differences in

comparison to PC2. Therefore, the optimal VVT settings for PC3 were determined to be the same as those for PC2.

The key observation that can be acquired from these results when comparing the ignition sources is the difference in cycle-to-cycle variation (CoV_{IMEP}) and the combustion phasing (AI50). The improvements in cycle-to-cycle variation becomes apparent as loads exceed 3 bar IMEP, across all VVT settings, with the cyclic variations becoming less pronounced as the load increases.

During high load operation, the jets exhibit stable behavior, with low quenching distance due to high in-cylinder pressure, thereby reducing the risk of jet quenching and extinguishing against the orifice walls. However, there is a higher likelihood of jet choking at these high loads, as evidenced by the pressure trace oscillations. As the jets travel at supersonic speeds, a pressure pulse is generated, which is visible in the in-cylinder pressure trace, see Figure 5.4. When this is the case, the jet penetration depth is likely high due to the jet velocity being high. This, thereby, causes high in-cylinder turbulence production and later coalescence of propagating flames, translating to a short combustion duration. In addition, therefore, the VVT sweep also demonstrates the knock mitigation properties of the pre-chamber. When comparing the AI50 graphs (see figures A.4, A.7 and A.1 for PC1, PC2 and baseline spark plug respectively), combustion phasing is advanced for all VVT settings across all operating points in the map. This can be both a benefit and a drawback, as will be explored in Section 5.2. Nevertheless, the knock mitigation benefits of the pre-chamber are most clear at loads above 10 bar IMEP, as demonstrated by the improvements in ISFC.

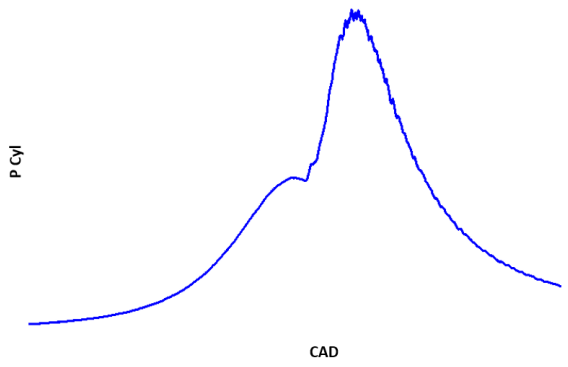

Figure 5.4: Pressure Trace Oscillations.

However, as engine loads decrease below 4 bar IMEP, the acceptable operating VVT window with respect to CoV_{IMEP} for the pre-chamber becomes smaller in comparison to the baseline spark plug, as can be seen when comparing CoV_{IMEP} in Figures A.3 and A.6. It's especially interesting to note the rapid decline in combustion stability for the pre-chambers with advanced VVT setting, especially at 3 bar @ 1500RPM, whereas the spark plug's decline is more gradual. The O_2 concentration were, in some operating points, slightly higher for the pre-chamber,

but this factor played no major role in the choice of the optimal VVT setting, as it was always within the boundary condition for the VVT setting that was preferred for optimal ISFC.

The VVT sweep thereby demonstrates the strengths and weakness of the pre-chamber. At loads above 5 bar IMEP, the pre-chamber is proven to be very capable in increasing the combustion stability and reducing the fuel consumption. However, at low loads, the pre-chamber is proven to be sensitive to highly advanced VVT settings. This is due to its contribution to excessive trapping of internal-EGR leading to a rapid degradation of the mixture quality inside the pre-chamber, which compromises the jet formation quality and thereby its ignition attribute. This consequently lead to degrading main chamber combustion stability as the jets are too weak to ignite the main chamber charge. As a result, the VVT window of acceptable CoV_{IMEP} is much narrower for the pre-chamber, and the combustion stability degrades rapidly if this window is exceeded.

5.2 Heat Transfer Losses and Energy Balance

The fundamental difference between the ignition sources discussed in this thesis lies in the ignition process, which results in variations in the combustion duration and turbulence inducement. The utilization of highly turbulent, high-energy, and dispersed jets is the reason for this difference, which subsequently impacts the intensity of heat released and the heat lost. In order to thoroughly analyze these differences, it is crucial to minimize the effect of external factors on the final output. To achieve this, an additional minimap and WOT run were conducted for the pre-chamber setups with the same input parameters as the baseline spark plug when operating at its most optimum efficiency, with the exception of the ignition timing with the target instead being to achieve the same combustion phasing. The accumulated heat release were then analyzed and the in-cylinder heat losses were calculated. The heat lost to the exhaust was also computed and compared as this is also a parameter influenced by the different combustion duration. The energy balance will thereafter work as a summery of the full system losses and the final fuel conversion efficiency.

5.2.1 Rapid Angle and Heat Transfer Losses

This study focuses primarily on the burning angles and in-cylinder heat transfer during the combustion process for different setups. As previously discussed, to effectively analyze the necessary parameters, it is important to isolate as many variables as possible to minimize their impact on the final results. The burning angles were calculated and the accumulated heat release curve was generated using the expression determined in Section 4.3.4, and a correlation between these was analyzed for each setup. For this section, only PC2 and PC3 will be presented, with PC2 analysed more in depth. Note, however, that all pre-chambers exhibit very similar behavior. The heat transfer during combustion will be expressed as a percentage of the total chemical energy released after combustion, measured 90 CAD ATDC.

The burning speeds for the setups are presented in figures 5.6 and 5.8. With all else being equal, the rapid burning angles are considerably faster for the pre-chambers setups than the baseline spark plug across all loads and engine speeds. Though the maximum in-cylinder pressure remains the same for all setups during this test (see Figure 5.5), meaning that the maximum heat flux generated are similar between the setups, the rate of in-cylinder pressure rise rate (RMax) as a consequence of the faster burning angle is clear, as seen in Figure 5.7 and 5.9. Table 5.3 summaries the differences in the rapid burning angle and Rmax with percentage reference being the baseline spark plug.

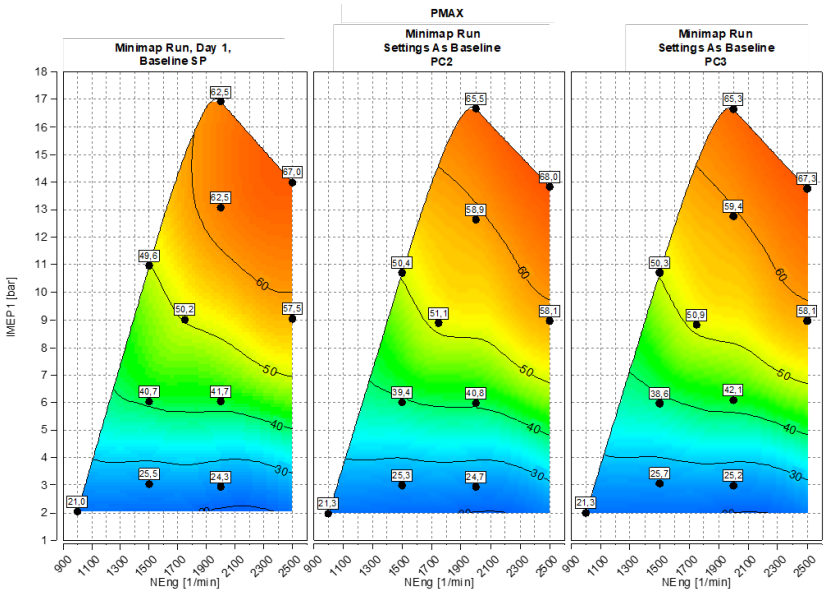

Figure 5.5: Minimap Run, Maximum In-Cylinder Pressure [Bar].

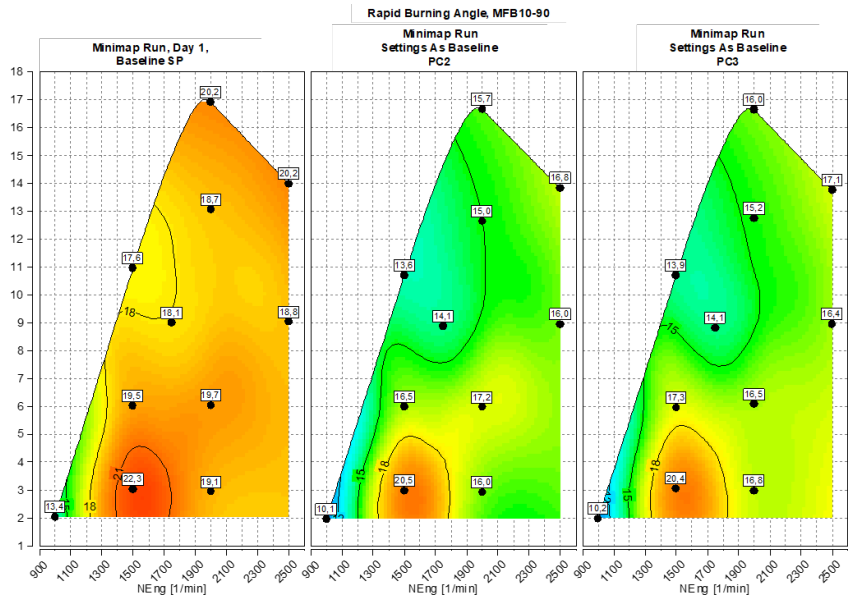

Figure 5.6: Minimap Run, Rapid Burning Angle [CAD].

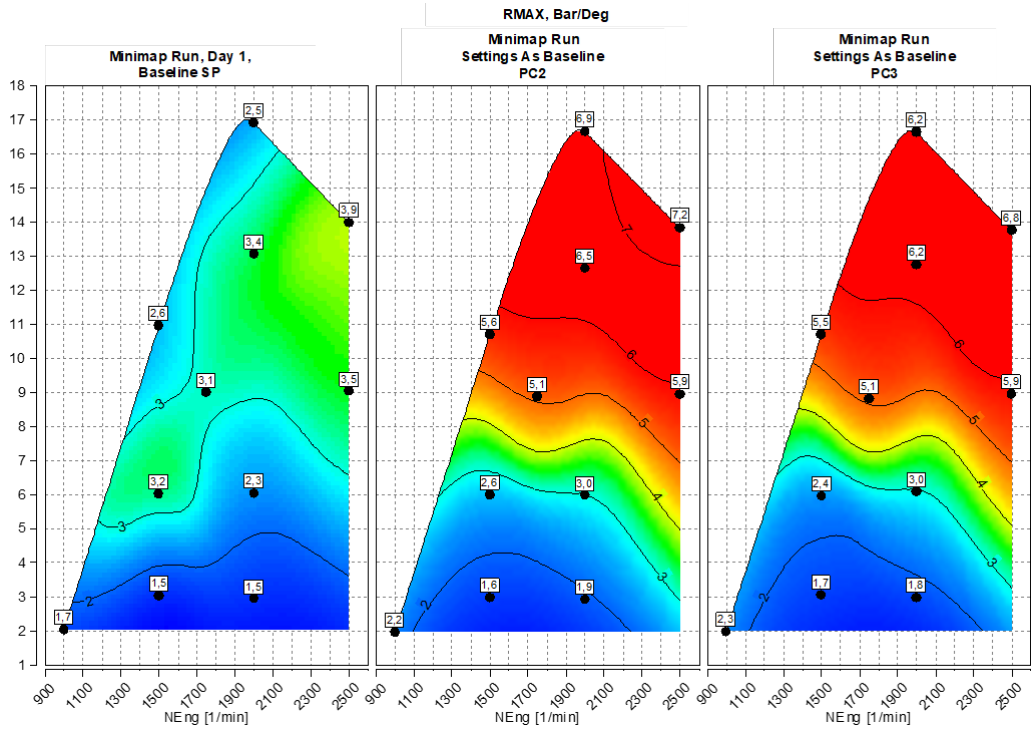

Figure 5.7: Minimap Run, RMAX, $[Bar/CAD]$.

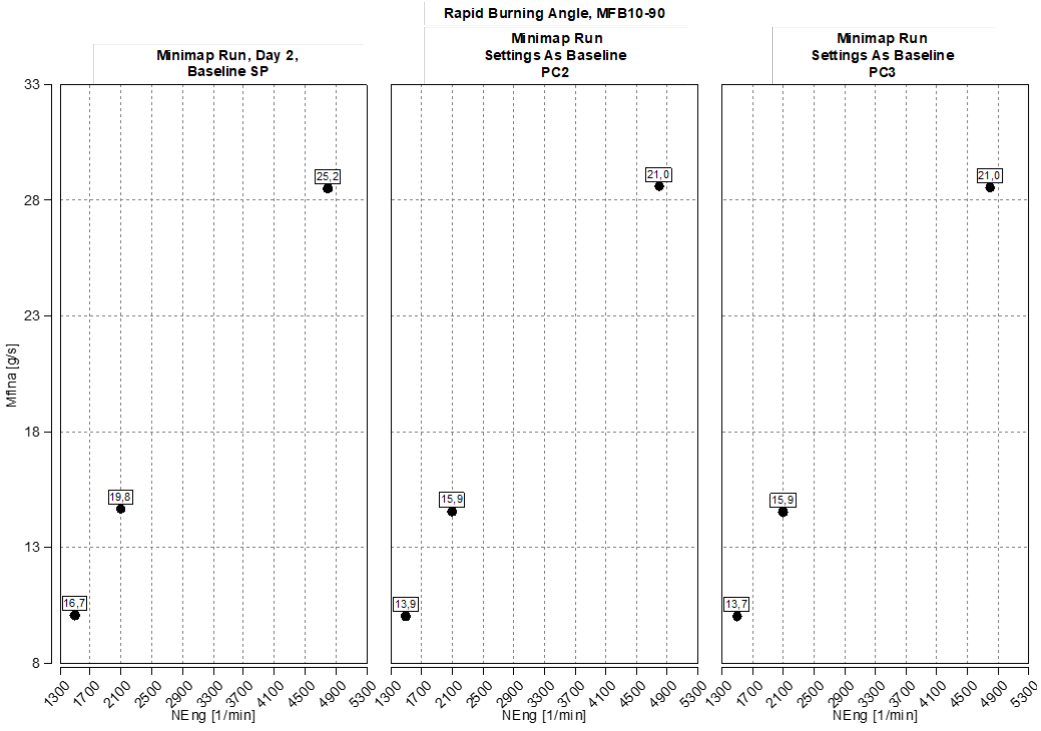

Figure 5.8: WOT, Rapid Burning Angle.

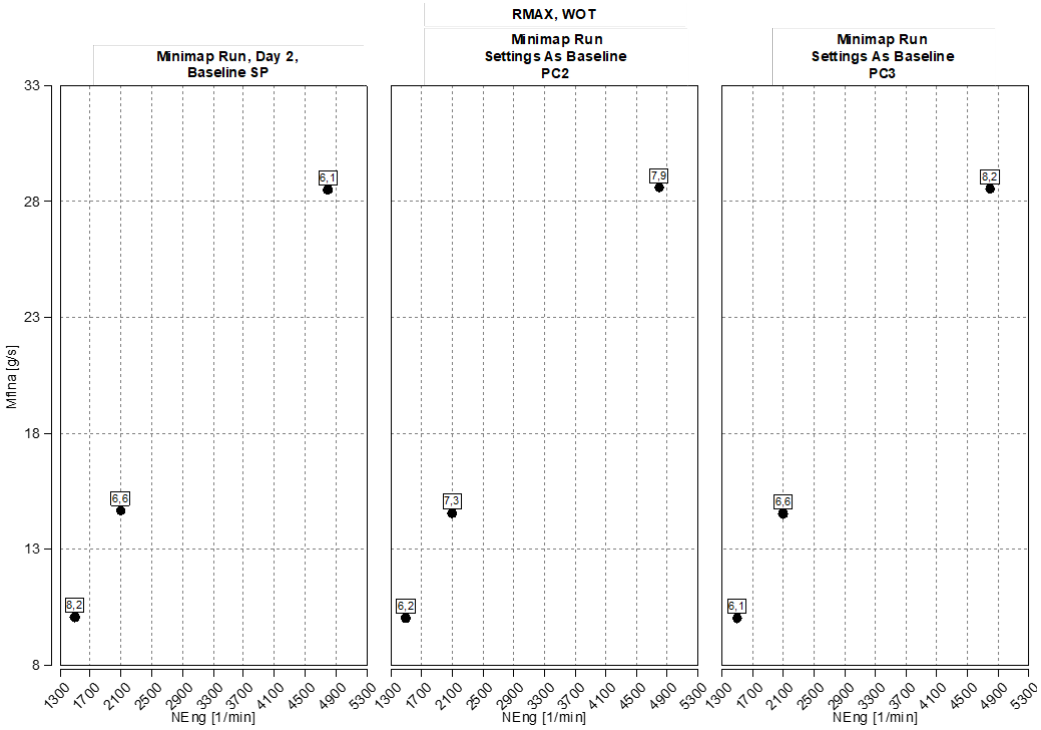

Figure 5.9: WOT, RMAX, *Bar/CAD*.

[RPM]/[IMEP]	Rapid Burning Angle Difference PC2 [%]	Rapid Burning Angle Difference PC3 [%]	RMax Difference PC2 [%]	RMax Difference PC3 [%]
1000/2	24.6	23.9	29.4	35.3
1500/3	8.1	8.5	6.7	13.3
1500/6	15.4	11.3	-18.8	-25.0
1500/11	22.7	21.0	115.4	111.5
1500/17.7	16.8	18.0	86.0	83.0
1750/9	22.1	22.1	64.5	64.5
2000/3	16.2	12.0	26.7	20.0
2000/6	12.7	16.2	30.4	30.4
2000/13	19.8	18.7	91.2	82.6
2000/17	22.3	20.8	176.0	148.0
2100/19	19.7	19.7	171.7	145.7
2500/9	14.9	12.8	68.6	68.6
2500/14	16.8	15.3	84.6	74.4
4800/17.1	16.7	18.0	126.0	134.6

Table 5.3: Summery of Rapid Burning Angle Difference and RMax Difference.

The short burn duration from the pre-chamber is due to its ability to generate multiple highly energized jets that is able ignite the main mixture at multiple spots in the combustion chamber. This results in a flame front with a much larger area

compared to that of a spark-ignited flame front, which expands from the center. As a result, the mixture is consumed at a higher rate, and the pressure rise rate (RMax) follows. The load dependency of the pressure rise rate, thereby, yields a good insight to the behavior of the jets which results in the observed shortened combustion duration. A higher rate of heat release would indicate that jet penetration depth is high, resulting in higher turbulence inducement and longer ignition delay before ignition of the bulk mixture commences. Lower RMax would therefore indicate lower jet penetration depth resulting in lower turbulence inducement and shorter ignition delay. As was derived in Chapter 3, the longer the ignition delay is present, the longer the jets will travel and the closer the flame will develop to the cylinder liner. The further from the center of the main combustion chamber the flame develops, the more directions the flame will propagate before coalescing. These effects, coupled with the increase in in-cylinder turbulence, result in the observed shortened combustion duration. However, due to the different combustion process and the increase in in-cylinder turbulence level, the heat transfer losses are, therefore, different for the different ignition source setups. This difference is confirmed when analysing the heat transfer losses. Figures 5.10 and 5.11 depict the AHR (right) and the heat transfer losses as percentage of the chemical energy released during combustion (left) from two examples from the minimap.

The AHR curve and heat transfer losses for the remaining operating points tested for PC2 are presented in the Appendix, see figures A.10, A.11, A.12, A.13, A.14, A.15, A.16, A.17, A.18, A.19, A.20 and A.21. The summary of the heat transfer losses for PC2 and the baseline spark plug, expressed as a percentage of the chemical energy released during combustion, as well as the percentile point difference between the two setups, are presented in Table 5.4.

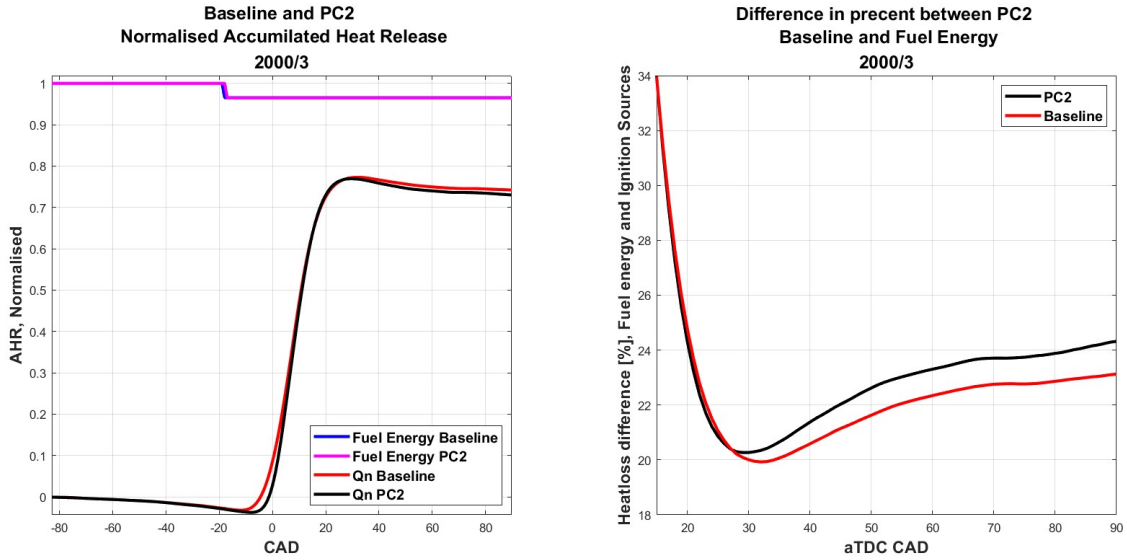

Figure 5.10: AHR PC2 and Baseline SP [Right], Heat Transfer Losses as Percentage of the Energy Released during Combustion [%] [Left], 3 Bar IMEP @ 2000RPM.

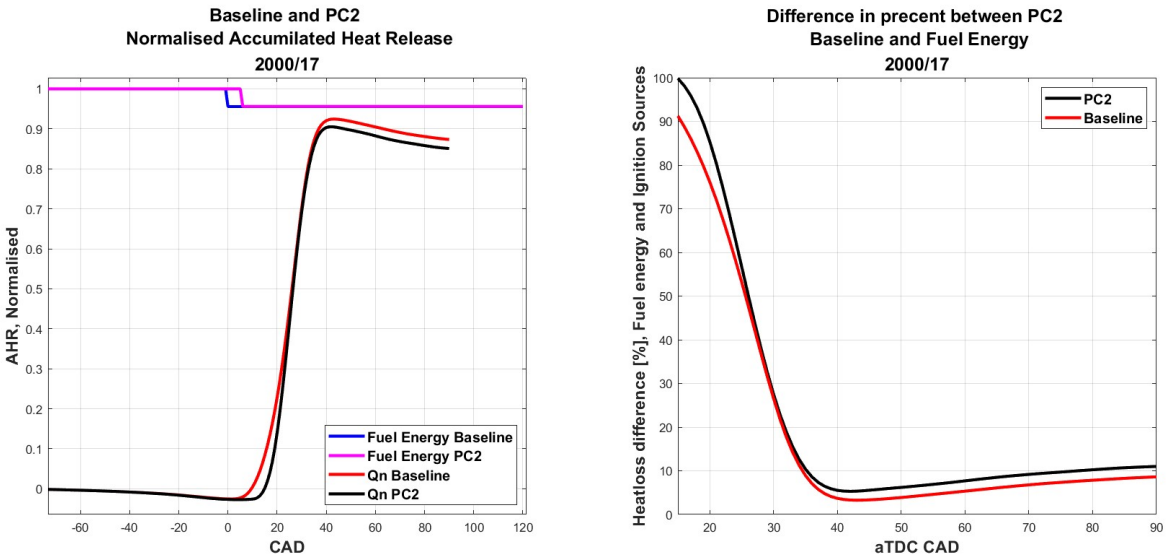

Figure 5.11: AHR PC2 and Baseline SP [Right], Heat Transfer Losses as Percentage of the Energy Released during Combustion [%] [Left], 17 Bar IMEP @ 2000RPM.

[RPM]/[IMEP]	Heat Transfer Loss Percentage, Baseline	Heat Transfer loss Percentage, PC2	Percentile Point Difference
1000/2	36.3%	38.0%	1.7
1500/3	24.6%	24.5%	-0.1
1500/6	20.1%	21.6%	1.5
1500/11	14.5%	17.40%	2.9
1500/17.7	8.3%	10.9%	2.6
1750/9	16.7%	18.8%	2.1
2000/3	23.1%	24.3%	1.2
2000/6	18.9%	20.0%	1.1
2000/13	12.0%	13.4%	1.4
2000/17	8.6%	11.00%	2.4
2100/19	6.4%	8.2%	1.8
2500/9	15.7%	17.5%	1.8
2500/14	10.4%	12.00%	1.6
4800/17.1	3.8%	6.1%	2.3

Table 5.4: Heat Transfer Loss as Percentage of Chemical Energy Released During Combustion and Difference between Ignition Sources.

As the engine load increases while keeping the engine speed constant, the in-cylinder relative heat transfer loss from the pre-chamber decreases. However, generally, the rate of decrease is slower than that of the baseline spark plug. This phenomenon can be contributed to a number of factors including the phasing of combustion, the increase in the conduction area due to the pre-chamber volume increasing the total surface area, the aforementioned increase in in-cylinder turbulence and the increase in the cross-sectional area of burned gas making contact with various surfaces of the

combustion chamber. These factors are closely related to the emergence of stronger jets as the engine load increases. As more mass is compressed and burned inside the pre-chamber, the pressure difference between the pre-chamber and the main combustion chamber becomes greater, leading to a steeper jet ejection gradient (compare the gradients in Figure 5.12a and 5.12b). This results in faster jets that induce more turbulence and penetrate deeper into the main combustion chamber before ignition. As the jet penetrates deeper, the likelihood of the flame to develop closer to the outskirts of the combustion chamber, where the surface to volume ratio is high, increases, which may lead to contact being established with the different in-cylinder surfaces earlier. This, combined with the dispersed nature of the pre-chamber jets which results in six ignition points, may causes an increase in the burned gas conduction area. However, to quantify the contribution of the various aspects of the in-cylinder losses stated, more advance calculation must be utilised.

Generally, keeping the engine load constant and increasing the engine speed increases the rapid burning angle and reduces the residence time of the gas, thereby reducing the heat transfer losses. For these cases, this was not true for engine loads below 4 bar IMEP. However, above this load, the pre-chamber's rapid burning angle increased faster or on par with the baseline spark plug, causing the percentile difference to reduce.

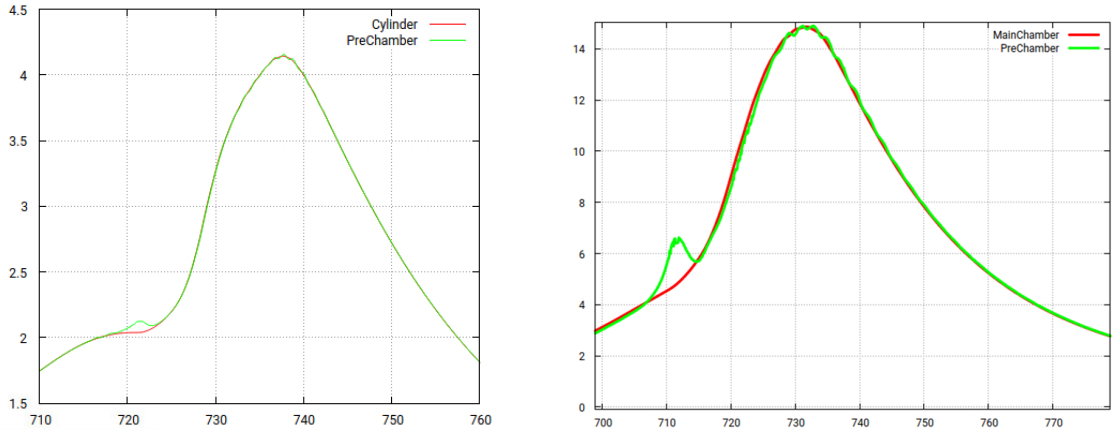

(a) 6 bar IMEP @ 1500RPM. **(b)** 17.1 bar IMEP @ 4800RPM.

Figure 5.12: CFD derived Pre-chamber and Main chamber Pressure Trace From the Repeated Minimap Runs.

5.2.2 Exhaust Heat Losses

The enthalpy lost to the exhaust is an important parameter to analyze when evaluating the system heat losses, as it has a significant impact on the overall efficiency of the system depending on engine load and speed. This is particularly important in certain applications where the exhaust system is only permitted to operate within a specific temperature range. As the ignition system setups used in this study give rise to differences in combustion duration and in-cylinder heat losses, which ultimately affect the final exhaust temperature and enthalpy.

The heat energy lost to the exhaust as a fraction of the chemical energy released during combustion is depicted in Figure 5.13. The percentile values are expressed in Table 5.5 with there corresponding percentile point difference.

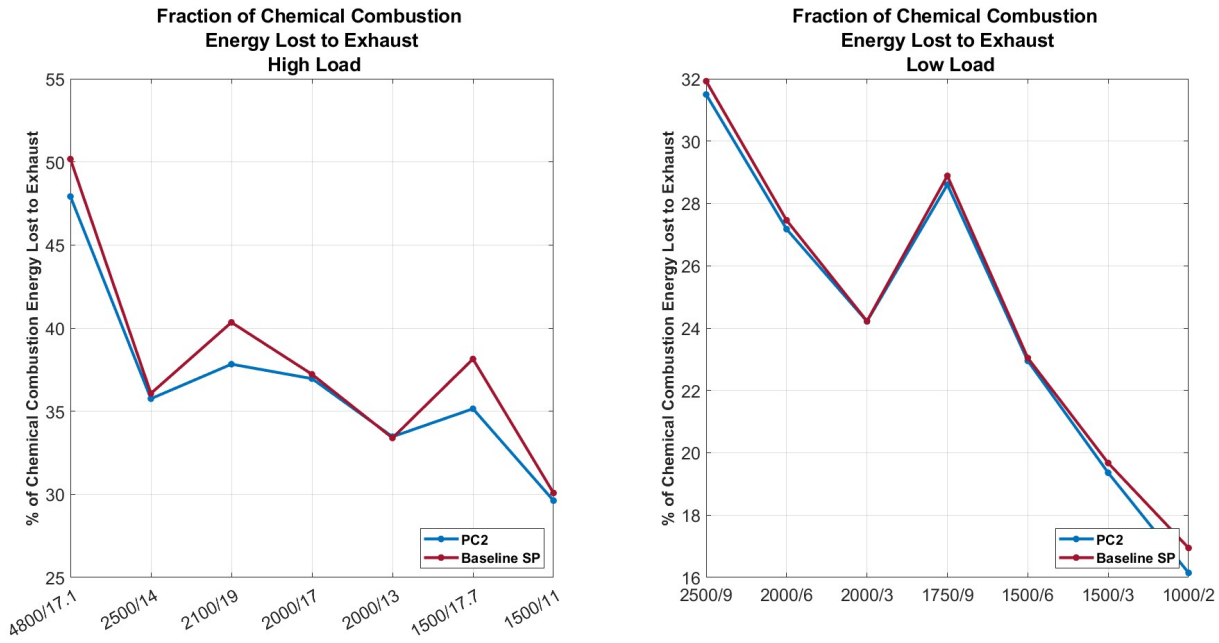

Figure 5.13: Exhaust Energy as the Fraction of Chemical Energy Released During Combustion.

[RPM]/[IMEP]	Exhaust Heat Losses Baseline SP [%]	Exhaust Heat Losses PC2 [%]	Percentile Point Difference [%]
1000/2	17.0	16.2	-0.8
1500/3	19.7	19.4	-0.3
1500/6	23.0	23.9	-0.1
1500/11	30.1	29.6	-0.5
1500/17.7	36.6	35.2	-1.4
1750/9	28.9	28.6	-0.3
2000/3	24.2	24.2	0
2000/6	27.5	27.2	-0.3
2000/13	33.4	33.5	0.1
2000/17	37.2	37.0	-0.2
2100/19	39.2	37.8	-1.4
2500/9	32.0	31.5	-0.5
2500/14	36.1	35.8	-0.3
4800/17.1	48.3	48.0	-0.3

Table 5.5: Exhaust Heatloss as Percentage of Combustion Fuel Energy and Difference between Ignition Sources.

When analyzing the exhaust heat loss in Figure 5.13 for high, part, and low load operation, it is generally observed that the baseline spark plug has a higher magnitude of exhaust heat losses when directly compared to the pre-chamber setups. One of the primary reason for this difference is the longer combustion duration resulting from the slower burn speed of the spark plug, which is shown in Figures 5.14a and 5.14b. This longer combustion duration leads to more of the available chemical energy and enthalpy being released further into the expansion stroke, which results in higher gas temperatures at the end of this stroke. This, combined with the lower in-cylinder heat loss possessed by the spark plug, leads to the higher observed exhaust energy.

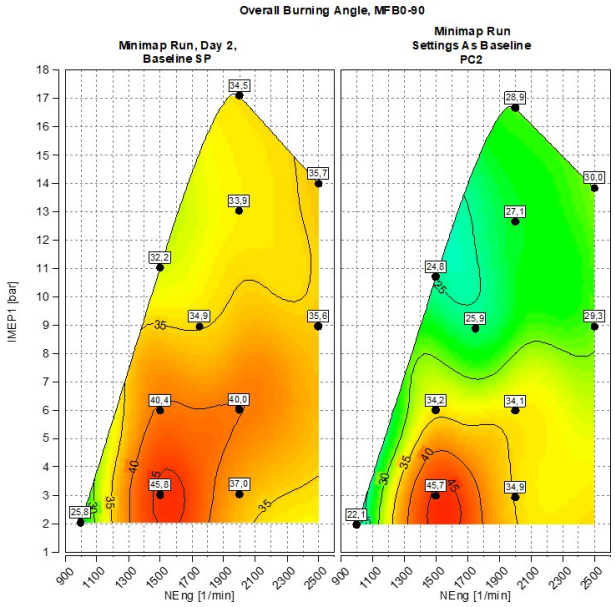

(a) Minimap Operation Points.

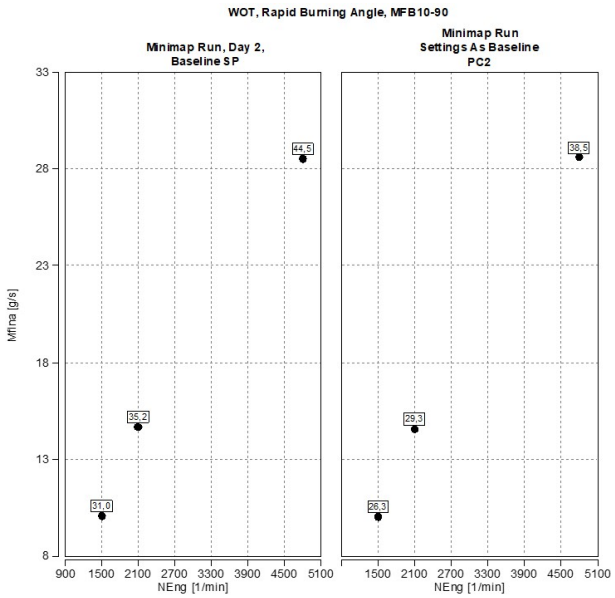

(b) WOT operation Points.

Figure 5.14: Overall Burning Angle, Baseline Spark Plug and PC2.

5.2.3 Energy Balance and Total System Losses

The energy balance calculation is a useful tool for gaining insight into the disposition of input energy in an engine. Understanding the individual heat losses and their contributions resulting from different ignition sources is of great interest. However, it is also important to comprehend the combined effect of all losses on the system and their ultimate impact on the indicated fuel conversion efficiency. The energy balance method allows for the visualization of the overall dissipation of the major contributors to the losses, as well as their final impact on fuel conversion efficiency. Figures 5.15 and 5.16 illustrate the losses with respect to the input fuel energy, highlighting that all kinds of losses make up the majority of the input energy into the system. Since the input settings are the same for both setups, the pumping losses should mirror each other with only slight differences. The overall heat losses and the final fuel conversion efficiency for each operating point are summarized in Table 5.6. Note that the overall heat losses in Table 5.6 are obtained by adding the exhaust heat losses and the in-cylinder losses. It also important to remind the reader that in-cylinder losses and the heat transfer losses are derived differently and are not the same (although they convey comparable information), with the former utilizing the energy balance equation and the latter utilizing the AHR curve. See Section 4.3.5 and 4.3.4 for the full overview.

RPM/IMEP	Overall Heatloss Baseline [%]	Overall Heatloss PC2 [%]	Fuel Conversion Efficiency Baseline [%]	Fuel Conversion Efficiency PC2 [%]
1000/2	59.81	59.80	26.20	25.64
1500/3	56.60	56.48	33.65	33.51
1500/6	55.25	55.40	33.65	40.03
1500/11	56.42	57.27	39.21	38.42
1500/17.7	58.25	59.16	37.1	35.79
1750/9	54.93	55.31	40.9	40.48
2000/3	55.83	56.11	33.76	33.29
2000/6	54.31	54.43	40.57	40.33
2000/13	54.44	55.34	40.57	39.32
2000/17	56.93	57.78	38.32	38.04
2100/19	57.33	57.72	41.72	41.43
2500/9	53.35	53.82	41.72	41.43
2500/14	54.11	54.65	41.47	40.98
4800/17.1	53.77	53.74	40.53	40.00

Table 5.6: Overall Heat Losses for Each Setup and Fuel Conversion Efficiency.

As explored in Sections 5.2.1 and 5.2.2, the heat transfer and exhaust losses are different between the ignition setups and this again becomes clear when observing figures 5.15 and 5.16. The distribution of the heat losses is different between the pre-chamber and the baseline spark plug. The pre-chamber has higher in-cylinder losses and lower exhaust losses, while the baseline spark plug has the opposite distribution. However, this effect does not improve the overall heat losses for the pre-chamber, as they are either higher or on par with those of the baseline spark plug. Furthermore,

the pre-chamber setup has slightly higher pumping losses and lower combustion efficiency, resulting in the setup with the baseline spark plug achieving higher fuel conversion efficiency.

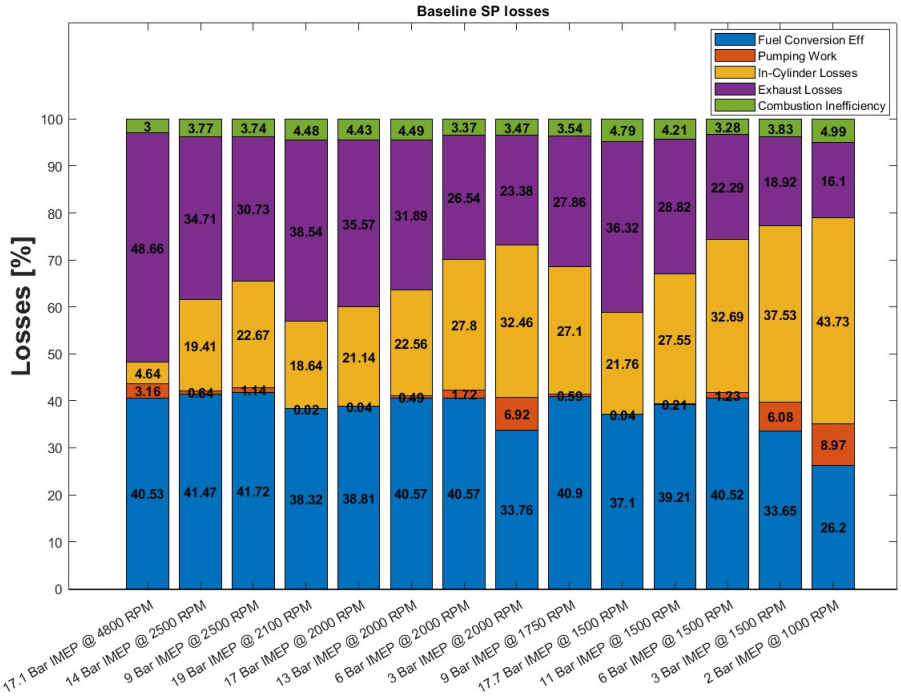

Figure 5.15: Baseline Spark Plug Losses, Bar Chart.

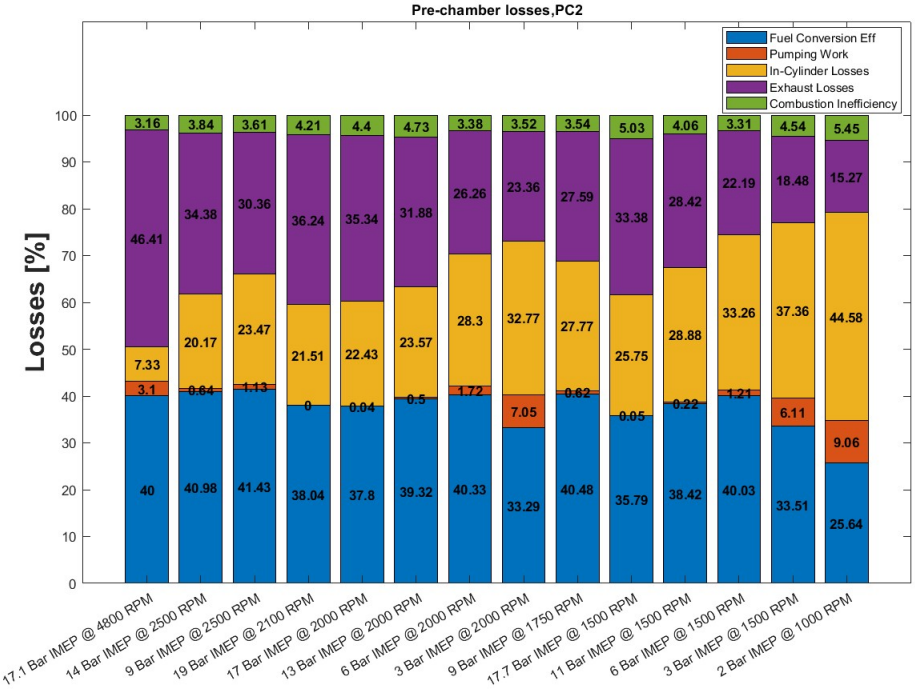

Figure 5.16: Pre-Chamber Losses (PC2), Bar Chart.

These results, combined with the findings regarding the in-cylinder and exhaust heat losses, confirm the hypothesis that the pre-chamber setup is more susceptible to high in-cylinder heat loss compared to the spark plug. However, the pre-chamber has a higher potential for efficiency improvement, and these efficiency numbers may change as the input parameters are optimized for more efficient operation of the pre-chamber setup. This potential is explored and presented in the following section.

5.3 Minimap Runs

The aim of this section is to compare the performance of the pre-chamber when it is optimally operated to that of the baseline spark plug. The previous section focused on a direct comparison between different ignition sources, which meant that all ignition sources where operated with identical combustion phasing and input parameter(such as camshaft phasing and mass airflow). The baseline spark plug was operated at maximum efficiency, and the pre-chamber setups were configured with the same input settings as the spark plug. This revealed that the pre-chamber's performance is highly sensitive to in-cylinder losses and heat transfer when it is not operated optimally.

This section will thus compare the performance of the pre-chamber when it is optimally operated with that of the baseline spark plug. The evaluation of performance will include a comparison of fuel consumption, thermal losses, and fuel conversion efficiency. In addition, repeatability and robustness will also be considered as crucial performance indicators in this evaluation.

5.3.1 Repeatability and Robustness

The definition of repeatability implies that the output can be reproduced with the same input. Three repeated minimap runs were conducted through three days and this test is to confirm that the results gathered are trustworthy, repeatable and that the system as a whole is robust. Robustness implies how sensitive the system is to small variations in the input parameters. Due to the input parameters being set as target values, some discrepancy in the output ISFC is to be expected. However, the ISFC from these days should still concentrate around one value since the target input values are all the same for each setup for all days ran. Thereby, the repeatability aspect of this test is to understand how well the setup handles these fluctuating conditions. However, even though small variation in the input parameter might be present not effecting the system, high cycle-to-cycle variation can cause the output parameter to diverge since the fluctuations in the pressure trace can cause the output power to vary between the measurements. This test will thereby also analyse the repeatability of the operating point from this point of view. The boundary conditions for repeatability and robustness was defined in Section 4.3.1 and this section will present the data gathered to determine if the individual setups are robust and operation point is repeatable.

5.3.1.1 Run 1, Baseline Spark Plug

The first run was conducted using the baseline spark plug with the minimap runs depicted in Figure 5.17 with respect to the ISFC. The variance from the median for each run can be seen in Figure 5.18 with tabular depiction in Table 5.7 with respect to the numerical difference from the reference median. Seven operating points were deemed repeatable, with five of these points being robust.

An analysis of the input parameters, such as intake pressure and temperature, ambient pressure, intake and exhaust variable valve timing (iVVT and eVVT), intake mass flow, fuel pressure and temperature, and oil temperature, in figures A.22, A.23, A.24, A.25, A.26, A.27, A.29, A.28, A.30, A.32 respectively, revealed fluctuations present in all parameters, with a small degree variance of absolute value between the days. The output ISFC from the three days of testing resulted in 10 operation points showing some type of numerical discrepancy between the days. This is particularly true at low load (below 4 bar IMEP), where none of the runs were able to be repeated. For loads above 4 bar IMEP, the variations were smaller, and the majority of the operating points were repeatable and robust. However, even though the variations in the input parameters do contribute to some fluctuations in the output ISFC, the CoV_{IMEP} is a significant factor. Analyzing Figure 5.19, it is clear that the cyclic variation are high ($CoV_{IMEP} > 1.2$) for all operating points except three. The correlation between operating points producing high CoV_{IMEP} and lack of robustness is present. Therefore, the resulting CoV_{IMEP} from these operation points is likely the cause of the high variation in the ISFC between the days.

The high CoV_{IMEP} at low loads is mainly due to the lower gas-exchange efficiency, seen in Figure A.34. A lower gas exchange efficiency leads to a higher amount of internal-EGR being trapped in the combustion chamber, which subsequently results in higher σ_{IMEP} as the conditions and EGR level near the spark plug change cycle-to-cycle, causing differences in the flame-development and overall burning angle. This leads to higher variance in the indicated power output, which subsequently translates to the ISFC varying from measurement to measurement. The lack of robustness for some operation points above 4 bar IMEP can also be attributed to the high CoV_{IMEP}. However, in these cases, it is more likely due to the setup's sensitivity to cyclic variation in the flow field and lambda distribution around the spark plug area. This phenomenon is known to cause cycle-to-cycle variation, which is further amplified as combustion is phased further from MBT.

The results obtained at high, part, and low loads indicate that, although the ignition source reliably generates energy to ignite the mixture, the high cycle-to-cycle variation causes the measurements to diverge. The results demonstrate that this setup lacks robustness, but some measurements can be reproduced. The run that will be used as the representative run for the remainder of analysis in this chapter will be Day 1, as it shows the least discrepancy from the median for all operating points.

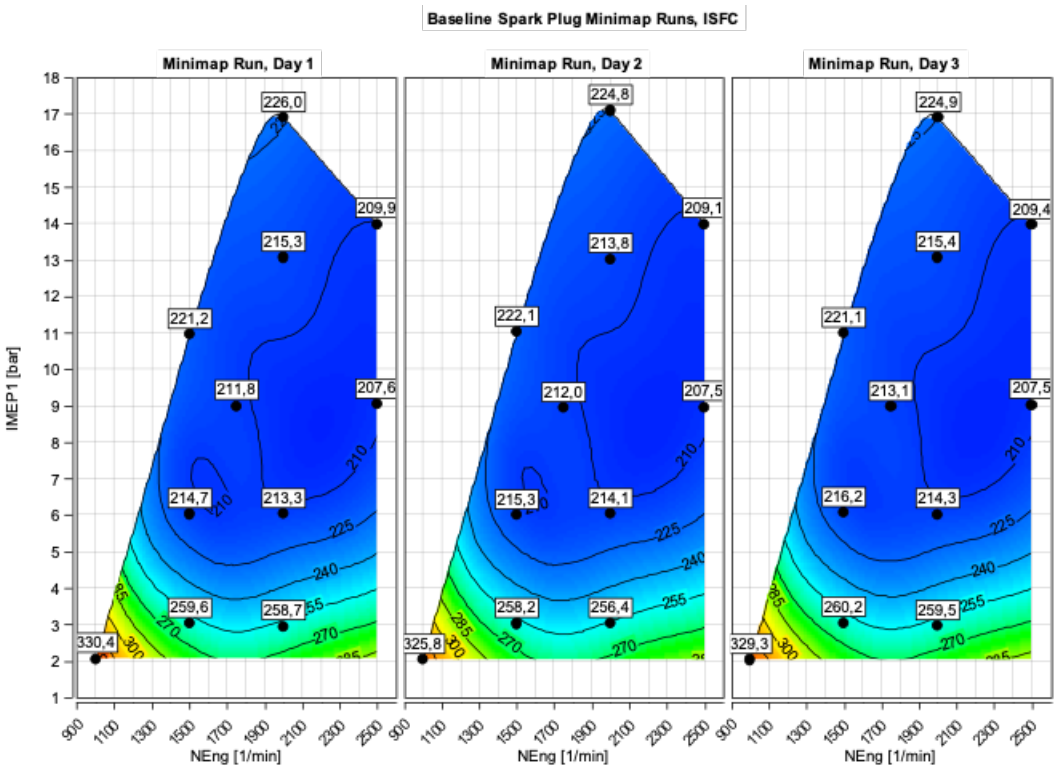

Figure 5.17: Minimap runs for Baseline Spark Plug, ISFC $[g/kWh]$.

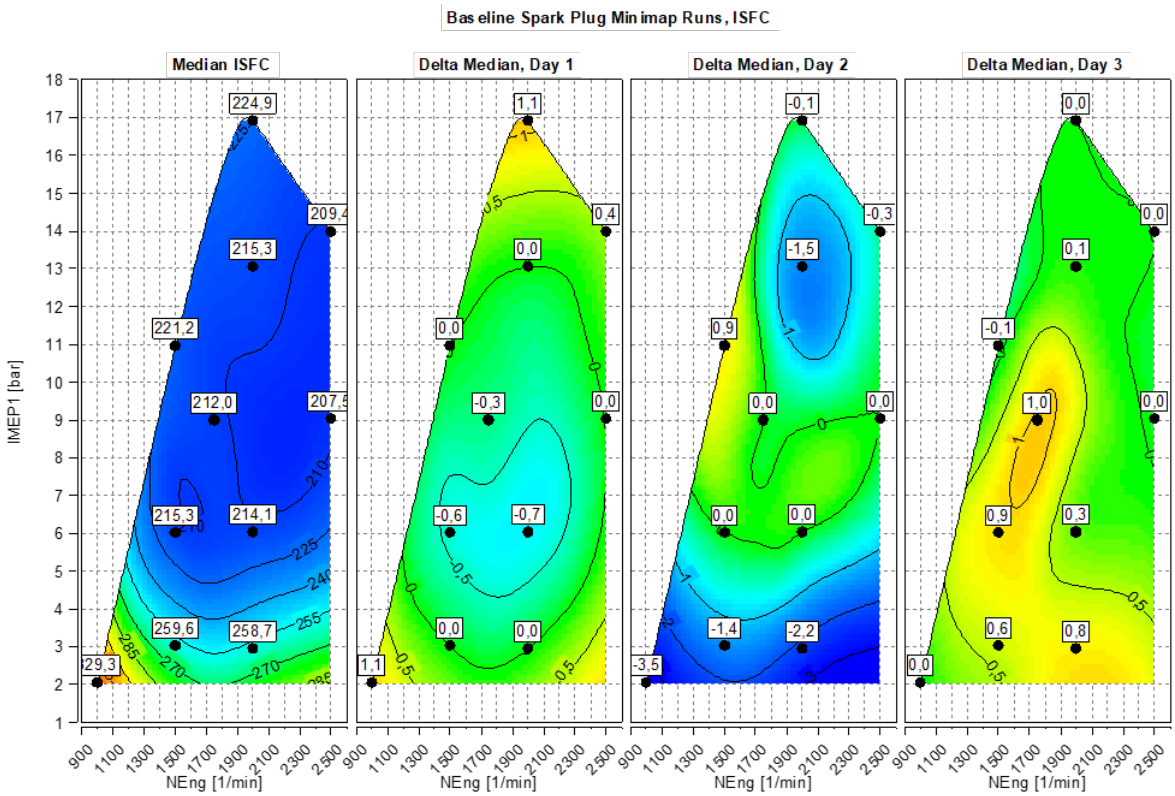

Figure 5.18: Minimap runs for Baseline Spark Plug, Median ISFC $[g/kWh]$ and Delta.

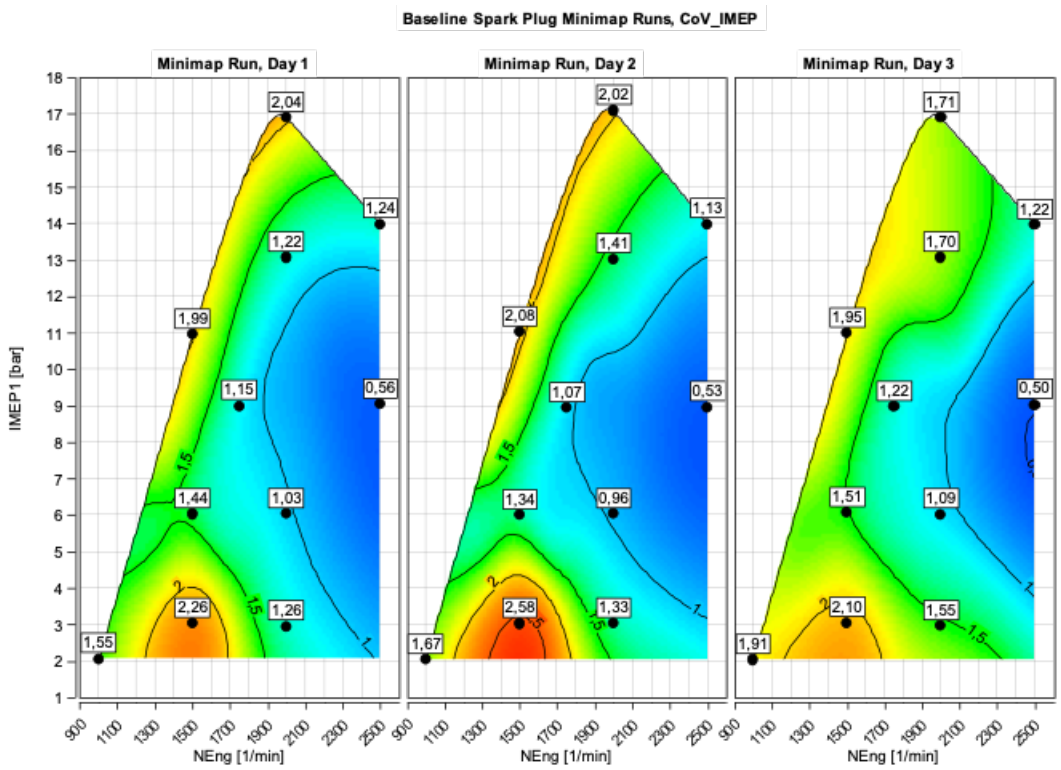

Figure 5.19: Minimap runs for Baseline Spark Plug, CoV_{IMEP} [%].

IMEP @ RPM	ISFC Median	Delta Day 1	Delta Day 2	Delta Day 3	Repeatable	Robust
14 Bar @ 2500	209.4	0.4	-0.3	0	Yes	Yes
9 Bar @ 2500	207.5	0	0	0	Yes	Yes
17 Bar @ 2000	224.9	1.1	-0.1	0	Yes	No
13 Bar @ 2000	215.3	0	-1.5	0.1	Yes	No
6 Bar @ 2000	214.1	-0.7	0	0.3	Yes	Yes
3 Bar @ 2000	258.7	0	-2.2	0.8	No	No
9 Bar @ 1750	212	-0.3	0	1	Yes	Yes
11 Bar @ 1500	221.2	0	0.9	-0.1	Yes	Yes
6 Bar @ 1500	215.3	-0.6	0	0.9	No	No
3 Bar @ 1500	259.6	0	-1.4	0.6	No	No
2 Bar @ 1000	329.3	1.1	-3.5	0	No	No

Table 5.7: Baseline SP Variance of the Runs With Respect to the Median.

5.3.1.2 Run 2, Pre-Chamber 1

The second run was made using PC1 and the minimap runs with respect to the ISFC is depicted in Figure 5.20. The variance from the reference median can be seen in Figure 5.21 and Table 5.8. For this ignition source, all points expect for the lowest operation point were deemed repeatable and all operation points expect for

three were deemed robust. Analysing the input parameters such as intake pressure and temperature, ambient pressure, iVVT, eVVT, intake massflow, fuel pressure and temperature and oil temperature, in figures A.35,A.36, A.37,A.38, A.39, A.40, A.42,A.41, A.43, A.45 respectively, minor fluctuations are present in all parameters. However, the resulting variance in the ISFC between the days indicate that the effect from these fluctuation are small.

Analysis of the CoV_{IMEP}, shown in Figure 5.22, reveals the reason for the improved robustness and repeatability of the pre-chamber. The majority of the operating points resulted in an CoV_{IMEP} below one, indicating that the pre-chamber jets are less sensitive to cyclic variations in the flow field and λ-distribution around their respective main chamber ignition points. This effect is best visualized when analyzing the pressure traces for two examples in the minimap in figures 5.23 and 5.24 (more examples are available in the Appendix as Figures A.87, A.88, and A.89). As seen, the cyclic variance in the pressure traces for the pre-chamber is lower than that of the baseline spark plug. One of the reasons, as derived from Chapter 3, is the pre-chambers ability to induce high ignition energy.

Comparing the ignition energy from the ignition setups, the nominal ignition energy of the baseline spark plug is around $100mJ$. The ignition energy of the pre-chamber setups can be derived from the fuel energy that, in theory, should enter into the pre-chamber volume during stoichiometric conditions and if the mixture is evenly distributed across the combustion chamber and the pre-chamber volume. Depending on the load, and not accounting for potential losses during pre-chamber combustion and jet formation process, this energy ranges from $4.4J$ during the lowest operating point to $24.5J$ during the highest load. During genuine operating circumstances, variations in air-fuel and EGR flow into the pre-chamber volume is to be expected, which may be the cause of some of the observed cycle-to-cycle variations as the energy content of the pre-chamber varies cycle-to-cycle. Nevertheless, this pre-chamber setup provides a substantial improvement in cycle-to-cycle variation compared to the baseline spark plug, with its jets being able to reliably and repeatedly ignite the bulk mixture in the main combustion chamber without misfire events and without being detrimentally affected by energy variation or the potential energy losses in its chamber.

Additionally, when combustion phasing is retarded, CoV_{IMEP} remains low as the highly energized and distributed ignition sites are able to ignite the main bulk mixture reliably and repeatably. As the load decreases, the CoV_{IMEP} increases, which is most likely due to the high RMF in the pre-chamber volume starting to effect its combustion process and thereby the ignition energy, which causes disparities in jet appearance between cycles. However, the cyclic variations are still lower than the baseline spark plug. Nevertheless, PC1 outperforms the spark plug in terms of repeatability and robustness, as shown by these results. The run used as the representative run for the rest of the analysis in this chapter will be Day 2.

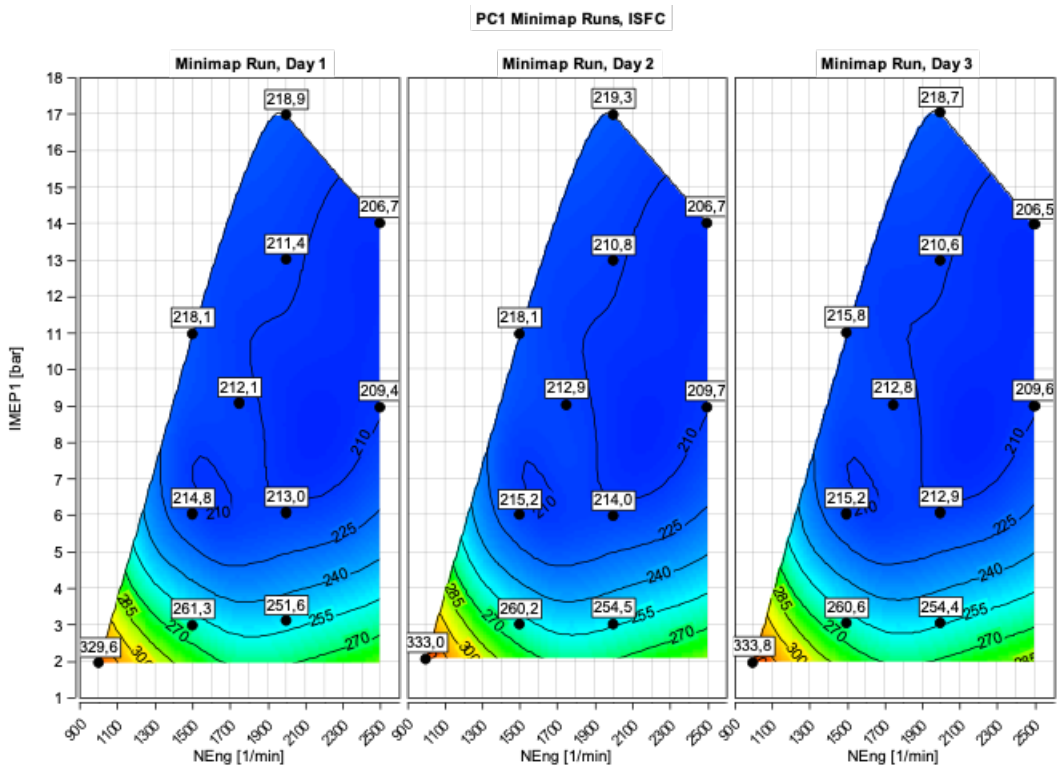

Figure 5.20: Minimap runs for PC1, ISFC $[g/kWh]$

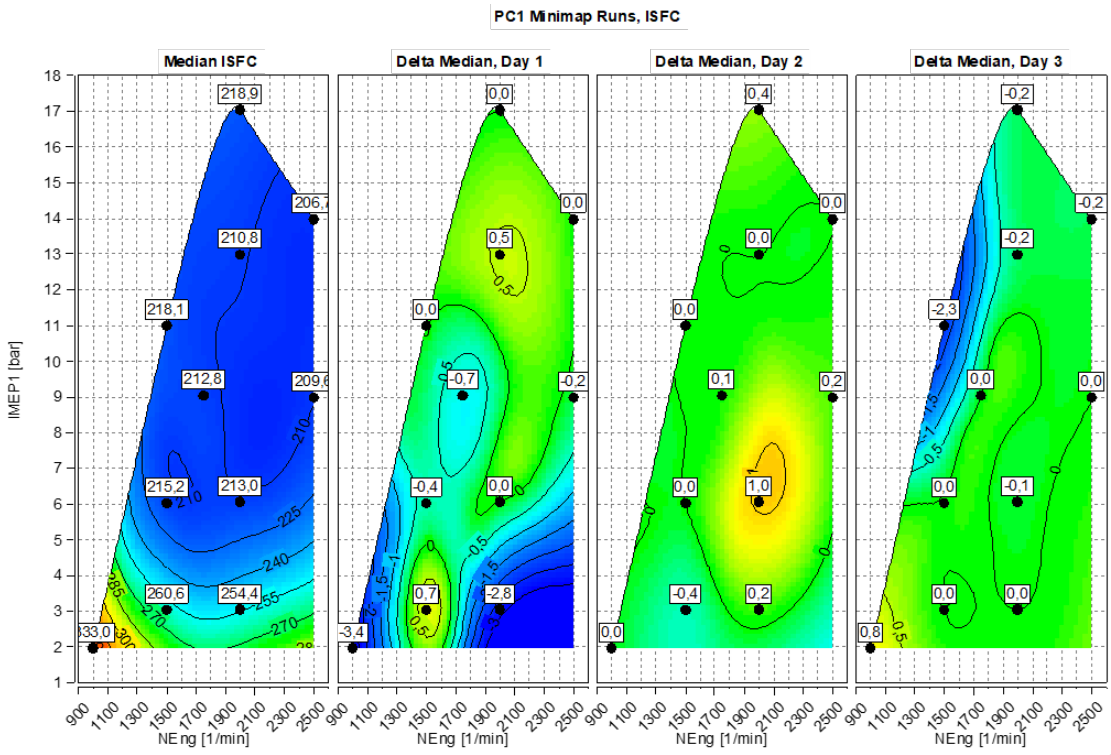

Figure 5.21: Minimap runs for PC1, Median ISFC $[g/kWh]$ and Delta

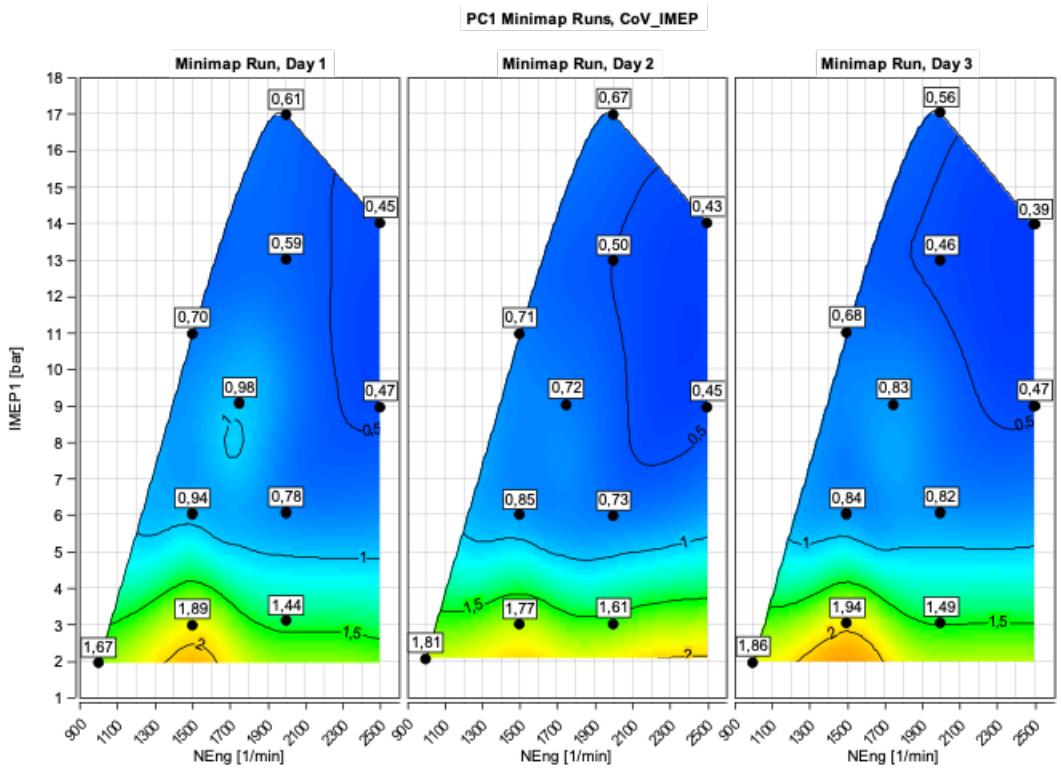

Figure 5.22: Minimap runs for PC1, CoV_{IMEP} [%]

IMEP @ RPM	ISFC Median	Delta Run 1	Delta Run 2	Delta Run 3	Repeatable	Robust
14 Bar @ 2500	206.7	0	0	-0.2	Yes	Yes
9 Bar @ 2500	209.6	-0.2	0.2	0	Yes	Yes
17 Bar @ 2000	218.9	0	0.4	-0.2	Yes	Yes
13 Bar @ 2000	210.8	0.5	0	-0.2	Yes	Yes
6 Bar @ 2000	213.0	0	1	-0.1	Yes	Yes
3 Bar @ 2000	254.4	-2.8	0.2	0	Yes	No
9 Bar @ 1750	212.8	-0.7	0.1	0	Yes	Yes
11 Bar @ 1500	218.1	0	0	-2.3	Yes	No
6 Bar @ 1500	215.2	-0.4	0	0	Yes	Yes
3 Bar @ 1500	260.6	0.7	-0.4	0	Yes	Yes
2 Bar @ 1000	333.0	-3.4	0	0.8	No	No

Table 5.8: PC1 Variance of the Runs With Respect to the Median

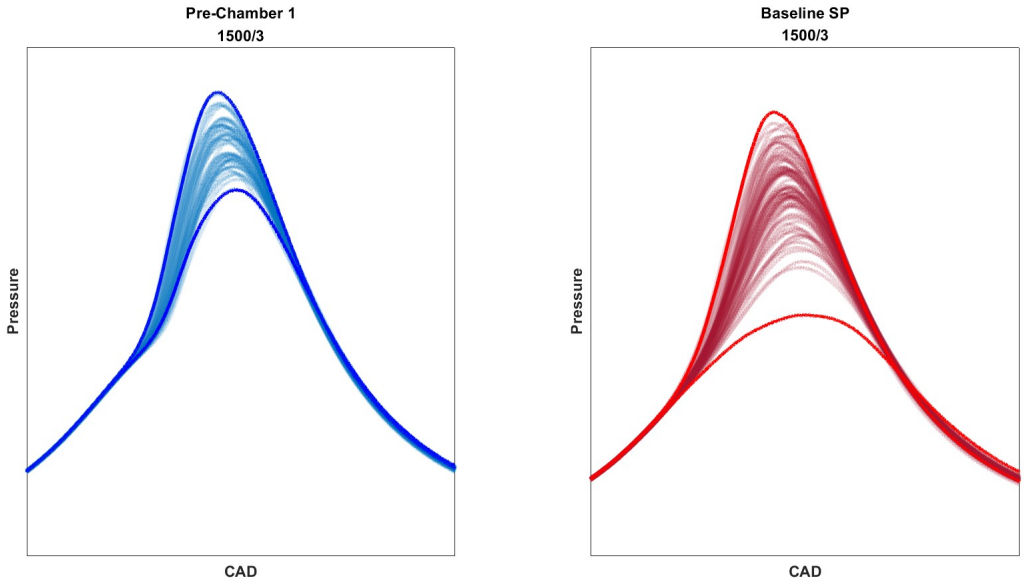

Figure 5.23: Pressure Traces, 3 bar IMEP @ 1500RPM, PC1 and Baseline SP, 100 Cycles.

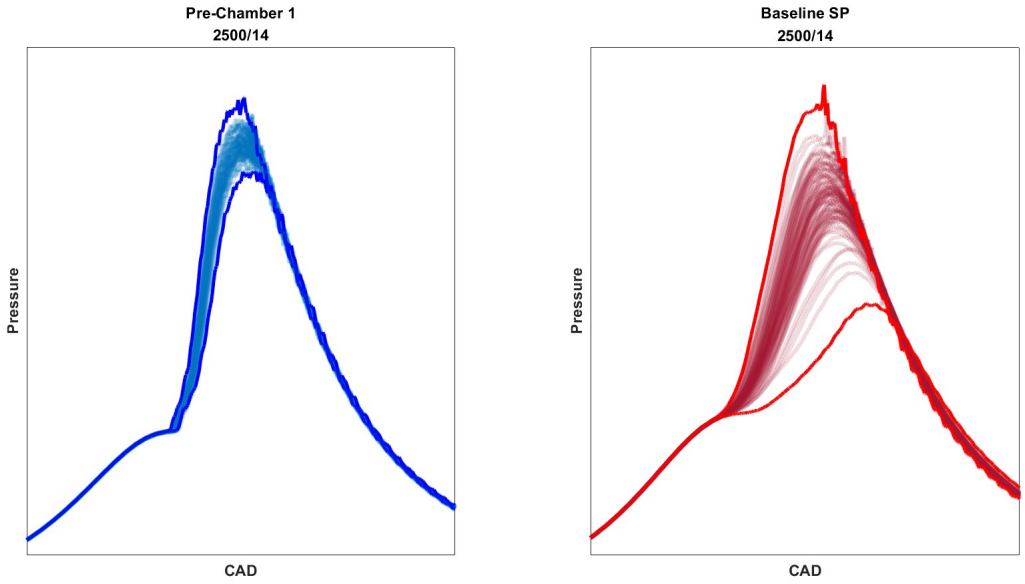

Figure 5.24: Pressure Traces, 14 bar IMEP @ 2500RPM, PC1 and Baseline SP, 100 Cycles.

5.3.1.3 Run 3, Pre-Chamber 2

The third run was conducted using PC2 as the ignition source and the results of the minimap runs with respect to the ISFC are presented in Figure 5.25. The variance

from the reference median can be seen in Figure 5.26 and Table 5.9 provides a numerical representation of the discrepancy from the median.

Upon analyzing the input parameters, such as intake pressure and temperature, ambient pressure, iVVT, eVVT, intake massflow, fuel pressure, fuel temperature, and oil temperature (as seen in figures A.48,A.49, A.50,A.51, A.52, A.53, A.55,A.54, A.56, and A.58 respectively), minor fluctuations are present in all parameters. However, similar to PC1, these fluctuations seem to have a much smaller effect on this setup compared to the baseline spark plug.

Almost all operating points are repeatable, with the exceptions being 2 bar IMEP @ 1000RPM and 3 bar IMEP @ 2000RPM. Additionally, the setup is very robust, with only three points showing inconsistency. The CoV_{IMEP} follows a similar trend as PC1, with the only major difference being that PC1 is slightly more stable at the highest load operation point (17 bar IMEP @ 2000 RPM). For the lowest load operation point (2 bar IMEP @ 1000 RPM), minimap day 1 shows an unusual high CoV_{IMEP}, but this is primarily attributed to external factors related to the test facility's equipment, rather than to the test engine or the pre-chamber. Therefore, this should not be a cause for concern.

The conclusion is the same as with PC1, as the results are very repeatable and the setup is very robust. The run that will be used as the representative run for the remainder of the analysis in this chapter will be Day 3.

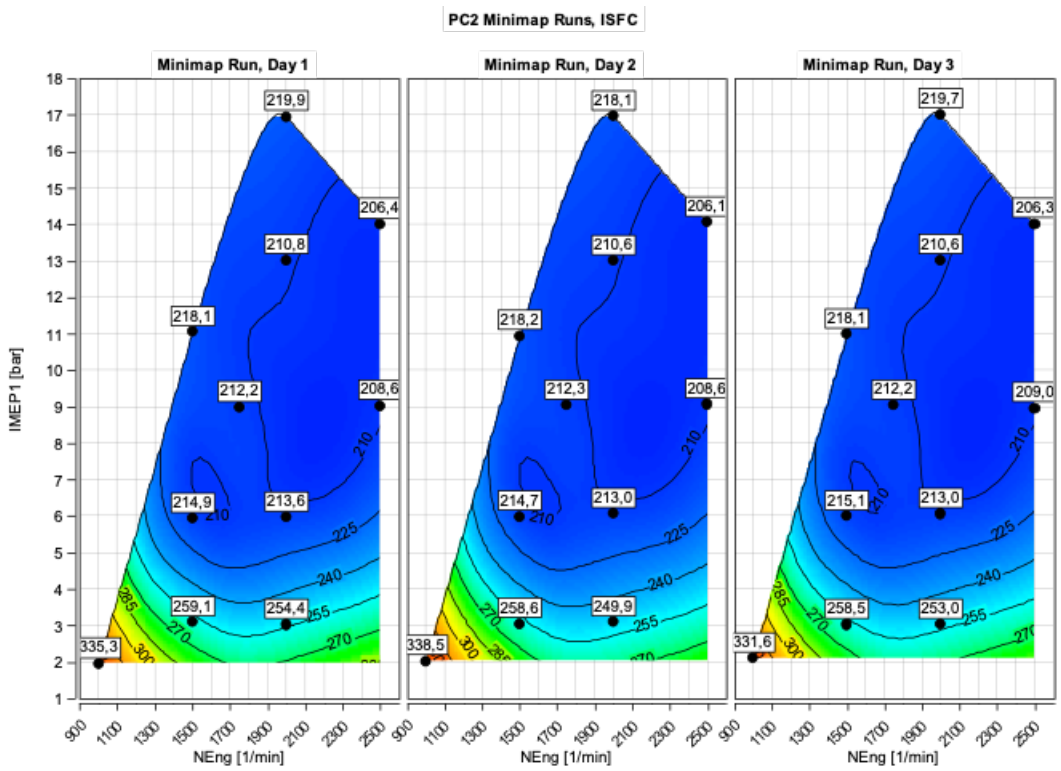

Figure 5.25: Minimap runs for PC2, ISFC $[g/kWh]$

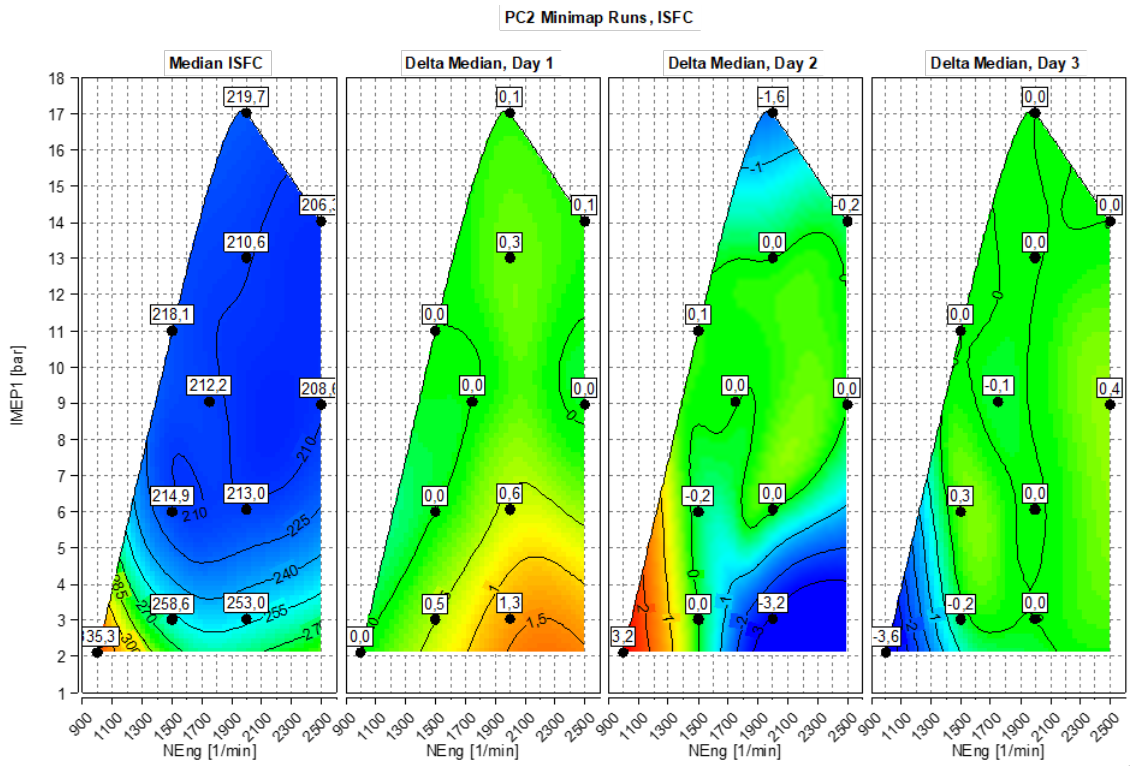

Figure 5.26: Minimap runs for PC2, Median ISFC $[g/kWh]$ and Delta

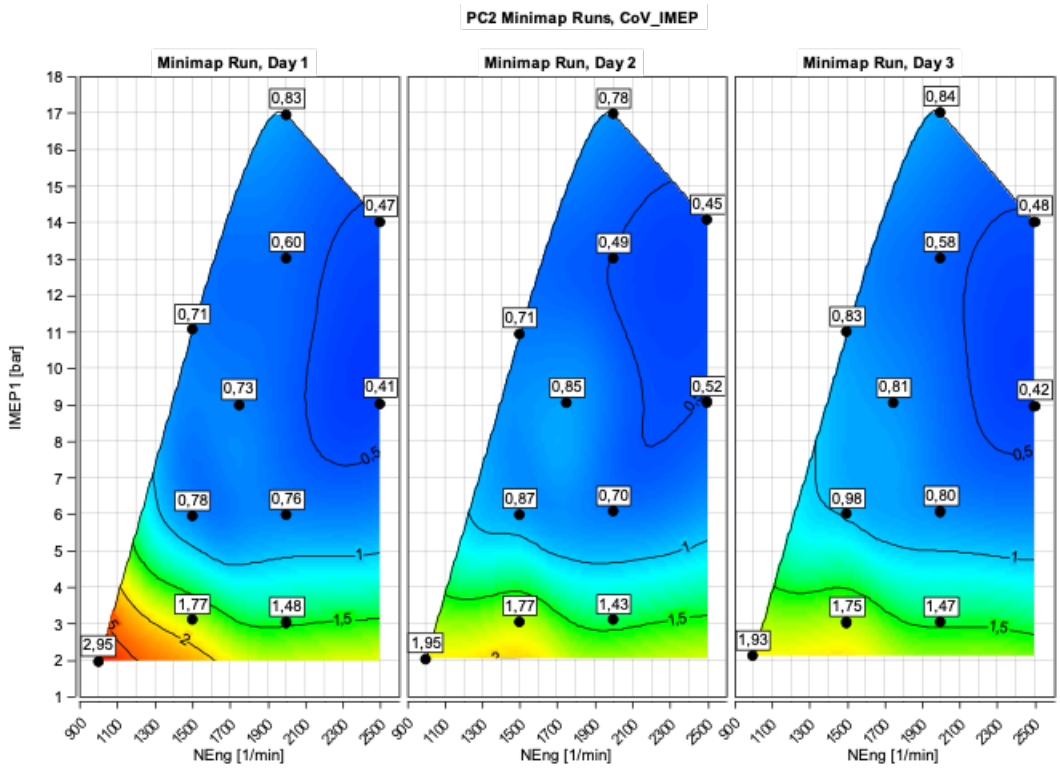

Figure 5.27: Minimap runs for PC2, CoV_{IMEP} [%]

IMEP @ RPM	ISFC Median	Delta Run 1	Delta Run 2	Delta Run 3	Repeatable	Robust
14 Bar @ 2500	206.3	0.1	-0.2	0	Yes	Yes
9 Bar @ 2500	208.6	0	0	0.4	Yes	Yes
17 Bar @ 2000	219.7	0.1	-1.6	0	Yes	No
13 Bar @ 2000	210.6	0.3	0	0	Yes	Yes
6 Bar @ 2000	213.0	0.6	0	0	Yes	Yes
3 Bar @ 2000	253.0	1.3	-3.2	0	No	No
9 Bar @ 1750	212.2	0	0	-0.1	Yes	Yes
11 Bar @ 1500	218.1	0	0.1	0	Yes	Yes
6 Bar @ 1500	214.9	0	-0.2	0.3	Yes	Yes
3 Bar @ 1500	258.6	0.5	0	-0.2	Yes	Yes
2 Bar @ 1000	335.3	0	3.2	-3.6	No	No

Table 5.9: PC2 Variance of the Runs With Respect to the Median

5.3.1.4 Run 4, Pre-Chamber 3

The fourth run was conducted using PC3, and the minimap runs with respect to the ISFC are depicted in Figure 5.28. The variance from the reference median is shown in Figure 5.29, and Table 5.9 depicts the numerical discrepancy from said median. As with all other runs, minor fluctuations are present when analyzing the input parameters (such as intake pressure and temperature, ambient pressure, iVVT, eVVT, intake massflow, fuel pressure and temperature, and oil temperature, in figures A.61, A.62, A.63, A.64, A.65, A.66, A.68, A.67, A.69, and A.71 respectively). Similarly to the conclusions drawn for PC1 and PC2, this setup is also found to be insensitive to variations in input parameters.

All operating points for this setup were found to be repeatable, and the setup was determined to be robust with only three inconsistent points. The CoV_{IMEP} exhibited a similar trend to that observed for PC1 and PC2, with a slight disparity during low load operation. The run that will be used as the representative run for the remainder of the analysis in this chapter is Day 1.

5.3.1.5 Evaluation of Repeatability and Robustness for the Setups

The results of this evaluation demonstrate that utilizing a pre-chamber as the primary ignition source significantly enhances the system's repeatability and robustness across the tested minimap operation points. The pre-chamber's unique features, such as distributed ignition sites and high energy jets, make it insensitive to flow field and lambda distribution around the main chamber ignition area. As a result, the pre-chamber setup exhibits a low CoV_{IMEP} and a highly repeatable and robust configuration. When comparing the different pre-chamber orientations, it is difficult to determine which one is superior, as all of them exhibit similar levels of repeatability and robustness. The observed discrepancy during the lowest operation point is contributed factors outside of the authers control and is not due to inconsistencies with the pre-chamber setup. Therefore, it can be concluded that all pre-chambers are equally robust and repeatable.

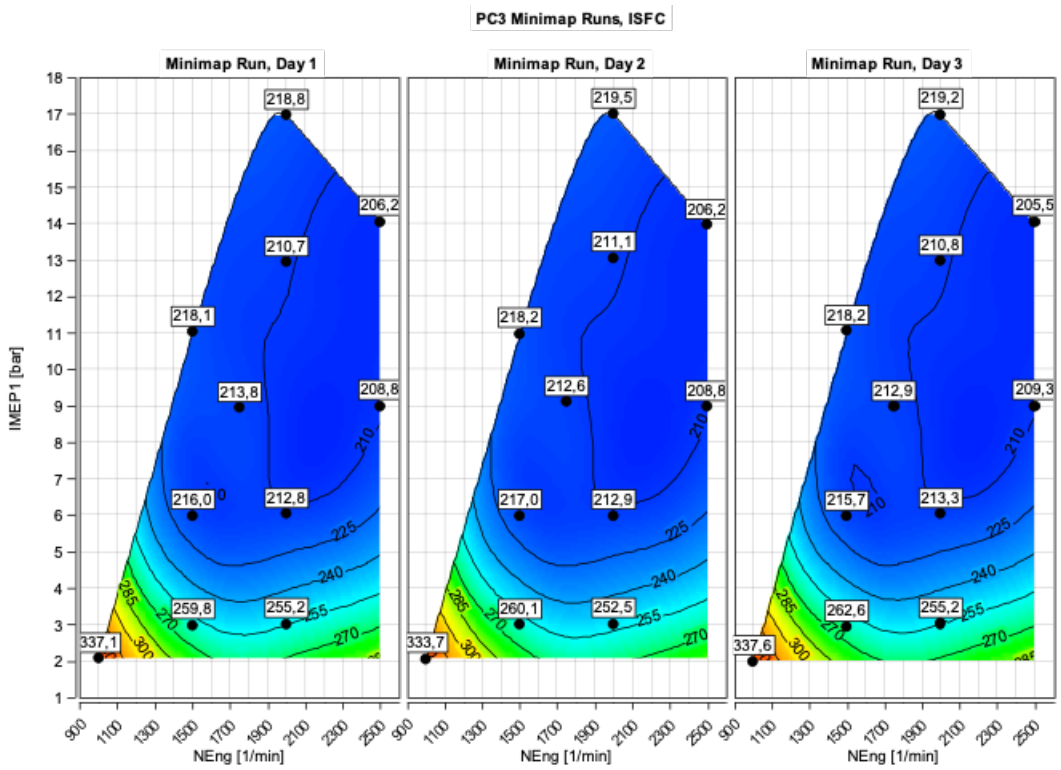

Figure 5.28: Minimap runs for PC3, ISFC $[g/kWh]$

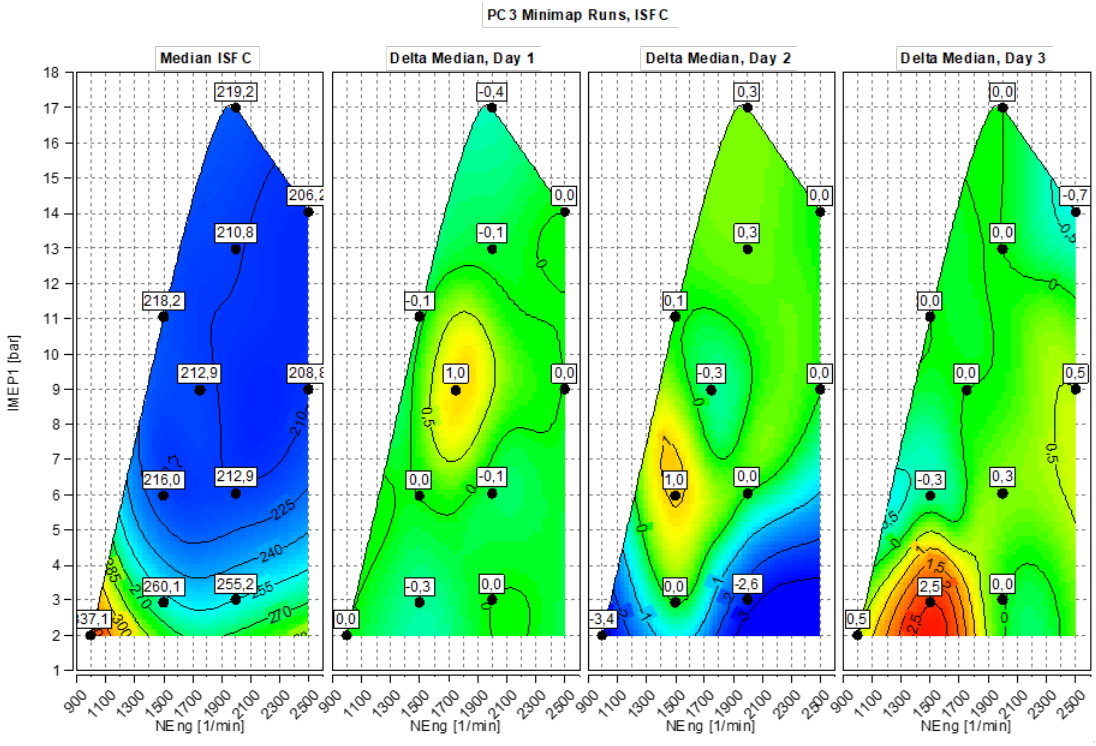

Figure 5.29: Minimap runs for PC3, Median ISFC $[g/kWh]$ and Delta

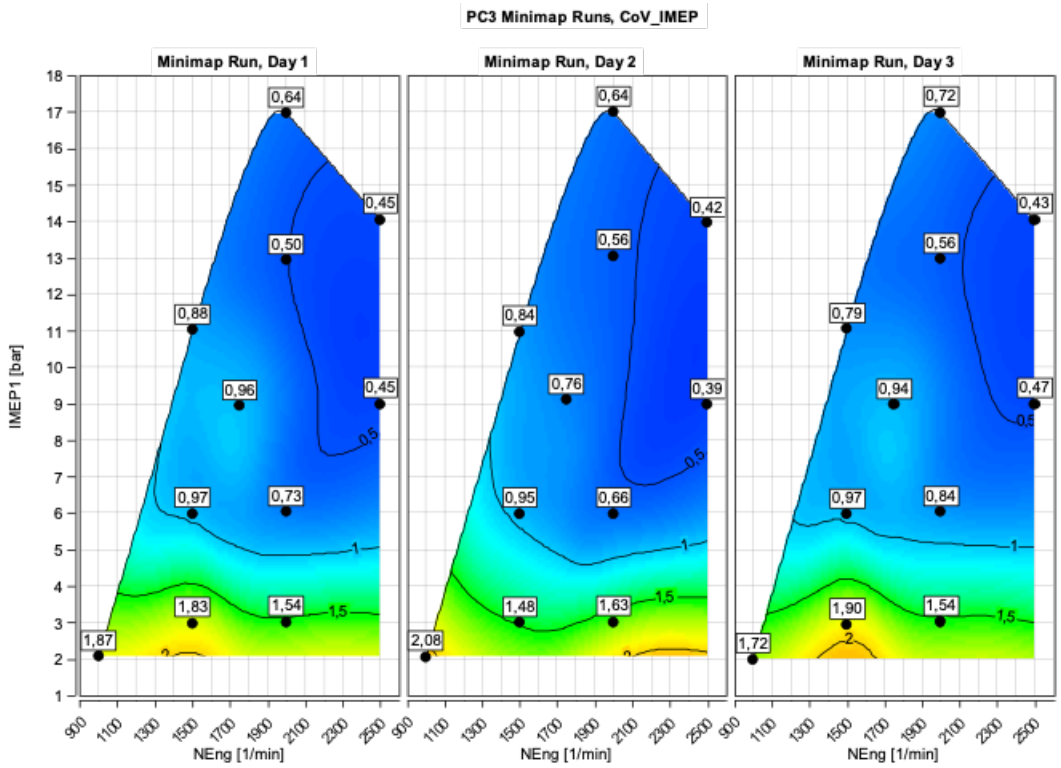

Figure 5.30: Minimap runs for PC3, CoV_{IMEP} [%]

IMEP @ RPM	ISFC Median	Delta Run 1	Delta Run 2	Delta Run 3	Repeatable	Robust
14 Bar @ 2500	206.2	0	0	-0.7	Yes	Yes
9 Bar @ 2500	208.8	0	0	0.5	Yes	Yes
17 Bar @ 2000	219.2	-0.4	0.3	0	Yes	Yes
13 Bar @ 2000	210.8	-0.1	0.3	0	Yes	Yes
6 Bar @ 2000	212.9	-0.1	0	0.3	Yes	Yes
3 Bar @ 2000	255.2	0	-2.6	0	Yes	No
9 Bar @ 1750	212.9	1	-0.3	0	Yes	Yes
11 Bar @ 1500	218.2	-0.1	0.1	0	Yes	Yes
6 Bar @ 1500	216.0	0	1	-0.3	Yes	Yes
3 Bar @ 1500	260.1	-0.3	0	2.5	Yes	No
2 Bar @ 1000	337.1	0	-3.4	0.5	Yes	No

Table 5.10: PC3 Variance of the Runs With Respect to the Median

5.3.2 Indicated Specific Fuel Consumption and Energy Balance

The ISFC $[g/kWh]$ represents the fuel flow $[g/h]$ required to produce per unit indicated power $[kW]$, or the ratio between the fuel flow and the indicated power. Therefore, it is a sensible parameter to use when comparing the performance of

each ignition source. The representative runs were determined in Section 5.3.1 and these runs will be used when comparing the performance of the different ignition sources.

The representative minimap runs with respect to ISFC are depicted in Figure 5.31. The differences in performance compared to the baseline spark plug are shown in both absolute values and percentage in figures 5.32 and 5.33, respectively.

The analysis of the presented figures concludes that the performance of the different pre-chamber setups is remarkably similar. However, when compared to the baseline spark plug, apparent differences in performance were discovered. The performance differences vary with engine speed and load and are therefore heavily dependent on these factors. These variations in performance led to the identification of different regions, or tipping points, where one ignition source outperforms the other or where their relative performance is similar. A total of three regions have been identified, and their tipping points are detailed in Figure 5.34. Each region's name emphasizes the engine and ignition source performance trends in that specific area. These regions have been classified as the "High-Load Gain Region," the "Excess Heat Loss Region," and the "Low-Load Balanced Region."

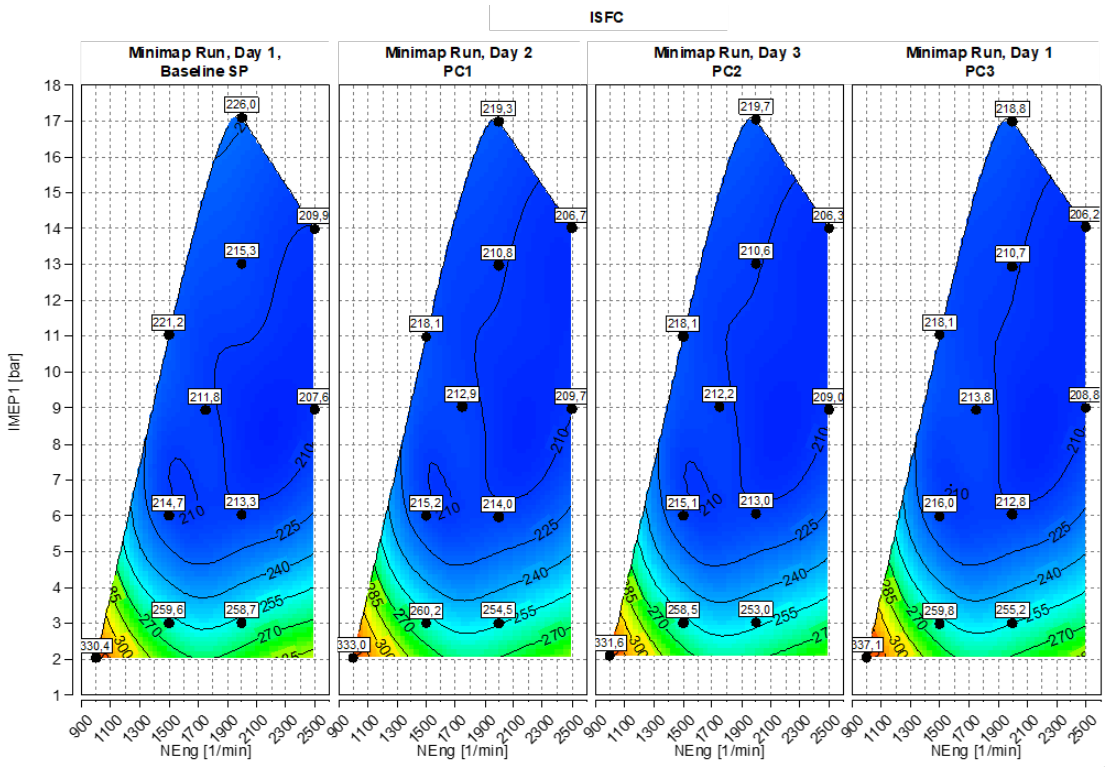

Figure 5.31: ISFC $[g/kWh]$, Representative Minimap Runs for Each Setup

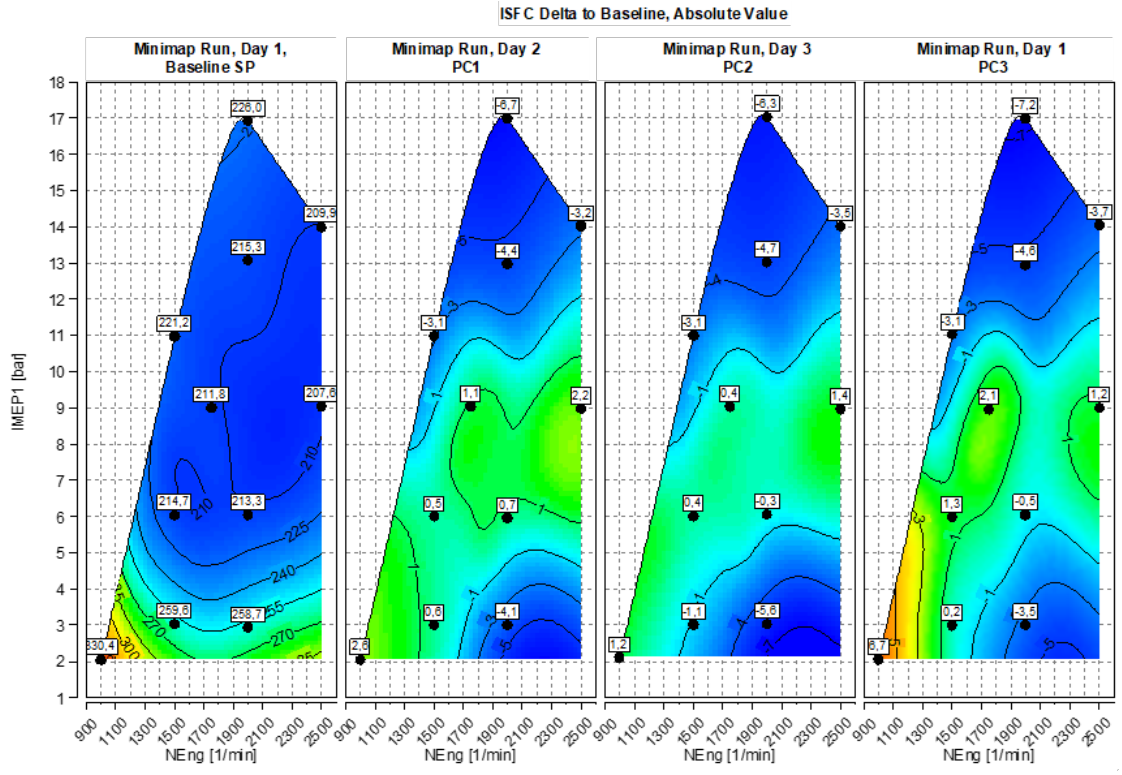

Figure 5.32: ISFC Delta To Baseline, Absolute Values $[g/kWh]$

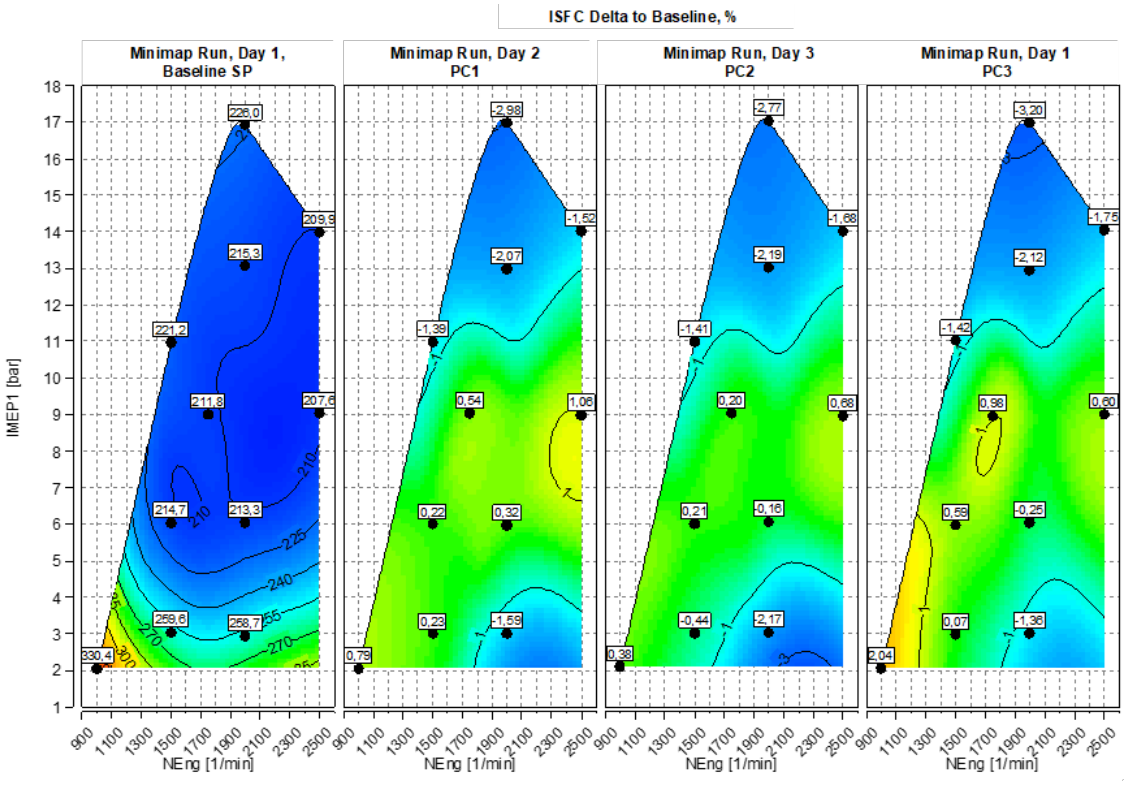

Figure 5.33: ISFC Delta To Baseline, Percent [%]

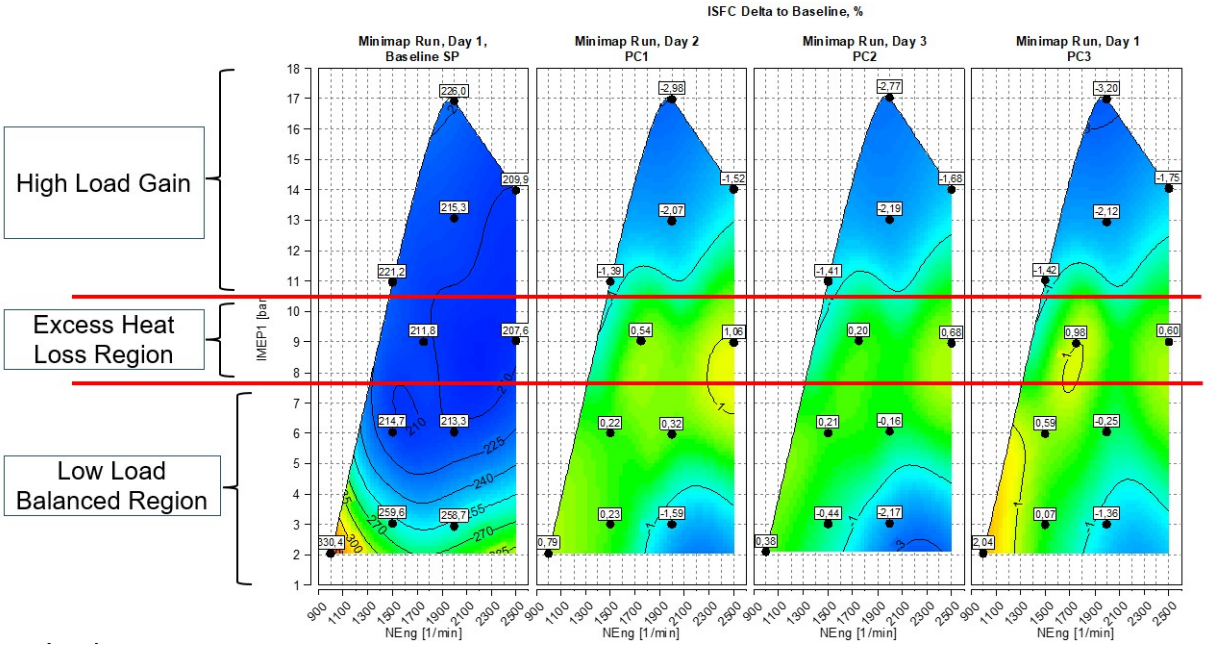

Figure 5.34: Pre-Chamber Regions.

5.3.2.1 High Load Gain Region

In this region, the setups containing the pre-chamber was been found to consistently result in improved fuel consumption. On average, the improvements range from 1.4% to 3.2% when compared to the baseline spark plug.

The reason for this gain in fuel consumption can be attributed to the ability to advance combustion phasing, evident by the data presented in Figure 5.36, which depicts the combustion phasing for each setup. Advancing the combustion phasing results in higher percentage of the total available enthalpy released during the combustion process to be excreted on the piston as work, leading to a higher fuel conversion efficiency and reduced fuel consumption.

Figures 5.37 and 5.38 depict the energy balance for the different setups in this region and it is clear that the fuel conversion efficiency for the pre-chamber setups are consistently and considerable higher. Interesting to note that the same distribution of losses are present here as in Section 5.2. However, due to the pre-chamber setup inheriting more advanced combustion phasing, which, apart from the already mentioned benefit, also results in reduced exhaust heat losses. This, thereby, leads to the total heat loss in this region being on par or lower for the pre-chamber setups compared to the baseline spark plug.

The ability to mitigate knocking combustion is the primary factor enabling the advanced combustion phasing achieved with the pre-chamber setups. By inducing highly turbulent and energized jets that are evenly distributed across the main combustion chamber, the pre-chamber setups reduce the combustion duration significantly, as illustrated in Figure 5.35. This reduction in the combustion duration, thereby, allows the end gases to consumed before reaching auto-ignition tempera-

ture, effectively preventing knocking combustion.

The differences between the pre-chambers are not as significant as the difference between the pre-chambers and the baseline spark plug. However, on average, PC1 performs better then PC2 and PC3, indicating that the orientation has little influence at this high load.

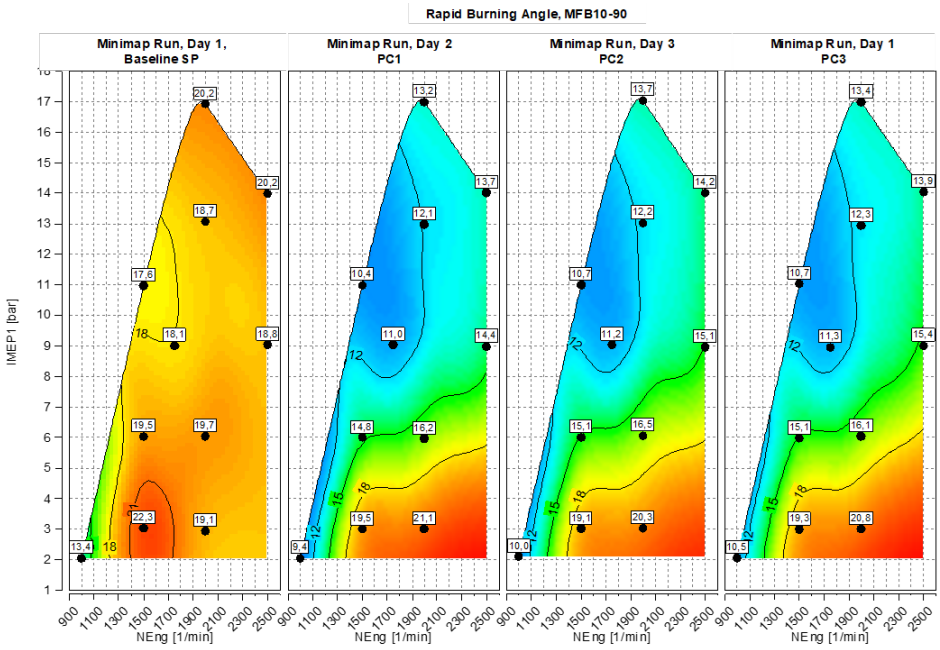

Figure 5.35: Rapid Burning Angle, Representative Minimap Runs for Each Setup

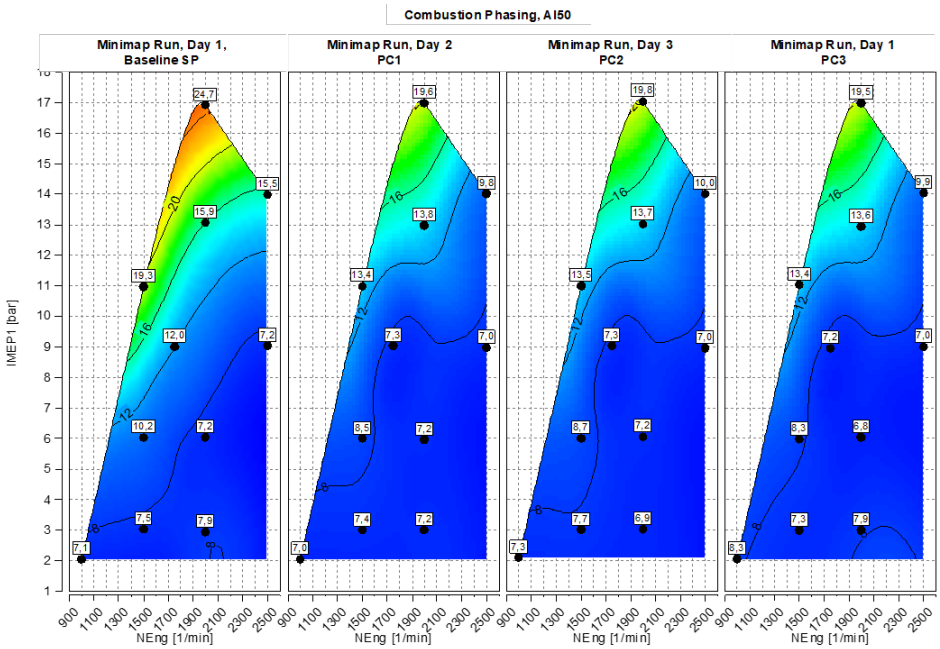

Figure 5.36: Combustion Phasing [°CA ATDC], Representative Minimap Runs for Each Setup

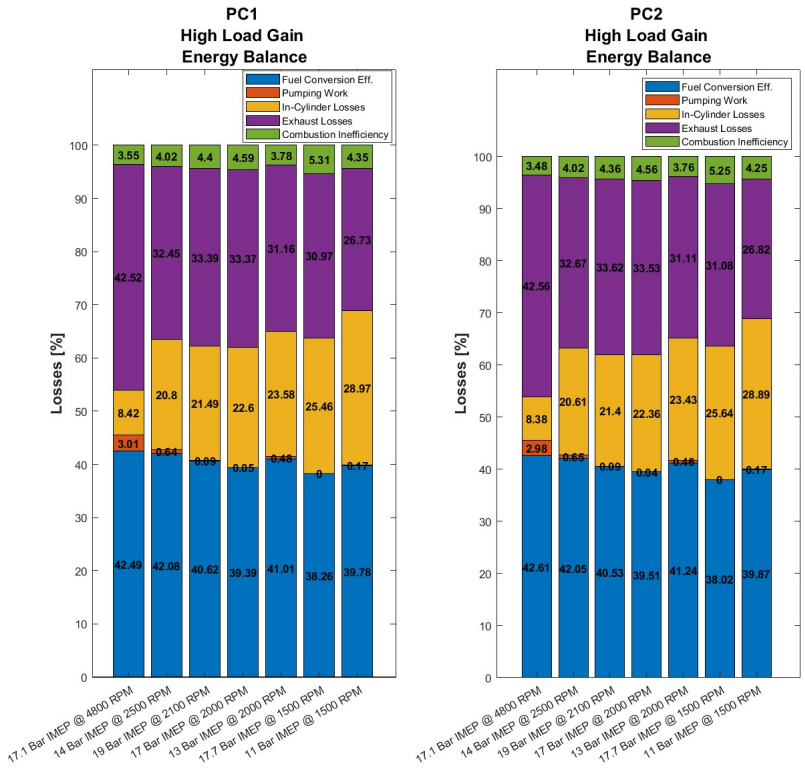

Figure 5.37: Energy Balance PC1 and PC2, High Load Gain Region

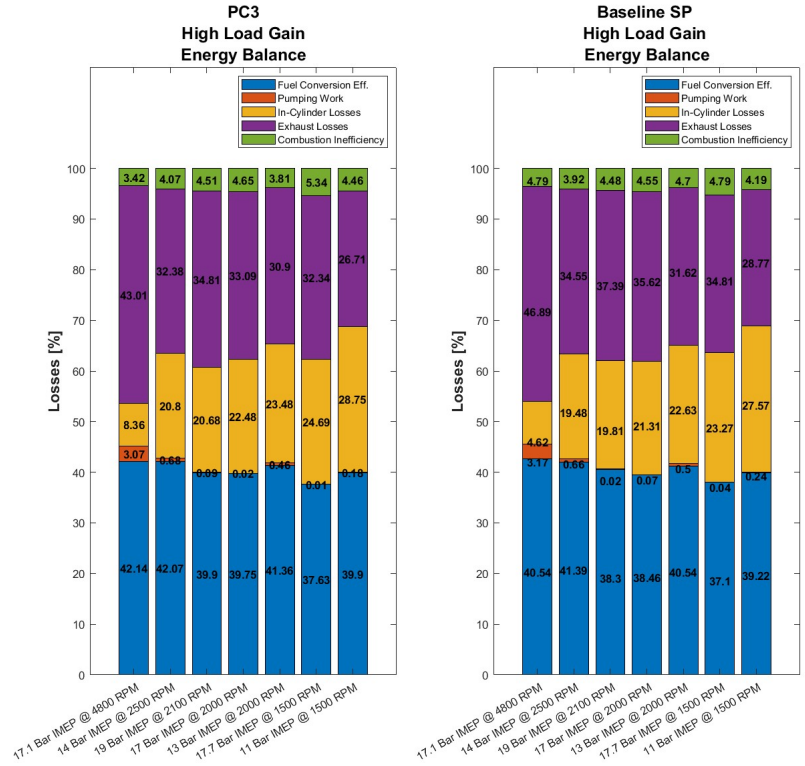

Figure 5.38: Energy PC3 and Balance Baseline SP, High Load Gain Region

5.3.2.2 Excess Heat Loss Region

The "excess heat loss region" refers to a range of operation points which contain 9 bar IMEP. This region is where the in-cylinder heat losses become dominant leading to a reduction in fuel conversion efficiency. Given that many of the input parameters, including the combustion phasing, and the resulting combustion and gas exchange efficiency, are similar for both pre-chamber and baseline spark plug setups, the decrease in fuel efficiency can be attributed to excess in-cylinder heat transfer loss.

Analysing the accumulated heat release curve for both of these load points in the left figures of 5.39 and 5.40 for the setups containing PC1 and the baseline spark plug, the evidence for excess heat transfer becomes clear. These losses in heat transfer are more clearly demonstrated in right figures 5.39 and 5.40 as a percentage of the chemical combustion energy. The heat transfer loss during combustion is 18.6% for PC1 for 9 bar @ 2500 RPM, 3 percentile points higher than the baseline spark plug and 22.3% for PC1 @ 1750 RPM, 5.6 percentile points higher than the baseline spark plug.

With PC2 and PC3 showing a similar trend, the conclusion is that the advantages of the pre-chamber cannot be fully exploited in this region. As was derived in Section 5.2.1, when the input settings and the combustion phasing between the baseline spark plug and pre-chamber are similar, the in-cylinder losses endured by the pre-chamber become decisive. Furthermore, the higher intake mass flow required for the pre-chamber setups to achieve the desired IMEP results in higher in-cylinder pressures, which further aggravate the in-cylinder heat transfer losses by contributing to higher heat flux generation. Thereby, the inability take advantage of the multiple ignition points and higher in-cylinder turbulence to advance the combustion phasing lead to these properties exerting excess in-cylinder heat transfer, ultimately leading to a decrease in fuel conversion efficiency.

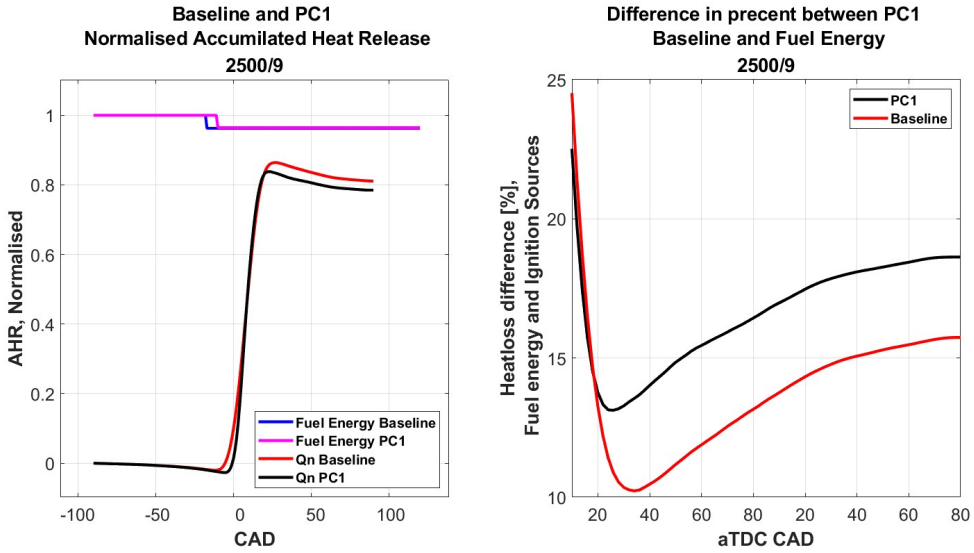

Figure 5.39: AHR (Left) and Heat Transfer Loss (Right) for PC1 and Baseline, 9 bar IMEP @ 2500RPM

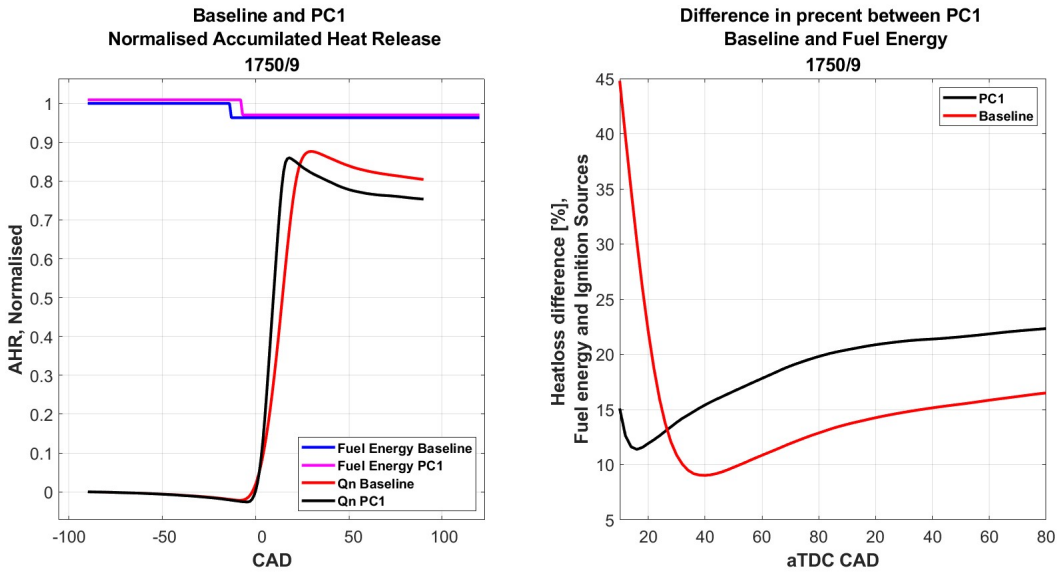

Figure 5.40: AHR (Left) and Heat Transfer Loss (Right) for PC1 and Baseline, 9 bar IMEP @ 1750RPM

5.3.2.3 Low Load Balanced Region

The region dubbed the "low load balance" is appropriately named to emphasize the delicate balance between exhaust and in-cylinder heat losses. As explored in Section 5.2, the pre-chamber setup increases the in-cylinder losses, but lowers the losses to the exhaust. Therefore, if the in-cylinder losses can be reduced with variance means, similar total heat losses between the baseline spark plug and pre-chamber can be achieved.

With the camshaft phasing set to high overlap, the resulting internal-EGR dilutes both the main chamber and the pre-chamber. When ignition of this diluted mixture in the pre-chamber occurs, the resulting jet formation is weak, characterized by lower jet speeds which ultimately results in early ignition of the bulk mixture in the main chamber. Figure 5.41 demonstrates the effect of internal-EGR on the pre-chamber pressure trace. During spark and subsequent pre-chamber combustion, the pressure difference between the main combustion chamber and pre-chamber becomes low (if compared to the high load operation at 17.7 bar IMEP @ 4800 RPM in Figure 5.44). The resulting pressure gradient thereby also becomes low, resulting in a jet that has low speed and penetration depth which results in early ignition. As ignition commences earlier, its location is more centralized in the combustion chamber and the lower jet speeds result in less induced turbulence. This resulted in a reduction of in-cylinder heat losses, but they still remain higher than those of the baseline spark plug. However, the exhaust losses were somewhat lower for the pre-chambers which results in the overall heat losses being the same for both ignition systems. Note, however, not all operation points in this region were able to exhibit this desired attribute of heat loss "offsetting".

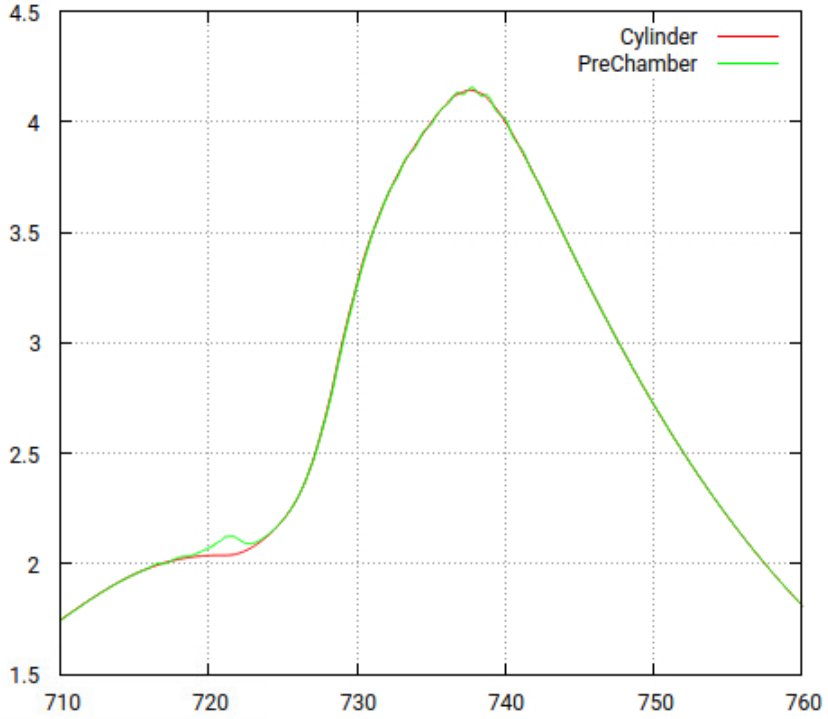

Figure 5.41: Pre-chamber and main chamber pressure trace for 6 bar IMEP at 1500RPM. Derived from CFD.

Successful heat loss offsetting was achieved for the operation points of 6 bar IMEP @ 2000 RPM, 6 bar IMEP @ 1500 RPM and 3 bar IMEP @ 2000 RPM. Therefore, the observed gains or losses in fuel consumption in this region were primarily due to the difference in combustion efficiency or pumping losses.

However, successful execution of heat loss offsetting was not achieved for the remainder of the operation points in this region. At 3 bar IMEP @ 1500RPM, the internal-EGR trapped for the pre-chamber setups was too insufficient to reduce the in-cylinder heat losses enough to enable offsetting by the exhaust heat losses. This, combined with the lower combustion efficiency, results in the lower fuel conversion efficiency for the pre-chamber setups.

During close to idle operation, 2 bar IMEP @ 1000RPM, the setting of the camshaft phasing is set at its default position with minimum overlap for all setups. Consequently, this operation point produced result similar the "excess heat loss" region due to the input settings being the similar for both the baseline spark plug and pre-chamber setups. As a result, the in-cylinder heat losses again became decisive, resulting in a loss in fuel conversion efficiency.

Evaluating the each pre-chamber at this region, the best performing is PC2, as it produces the best fuel consumption and fuel conversion efficiency. It is then closely followed by PC1 and finally PC3.

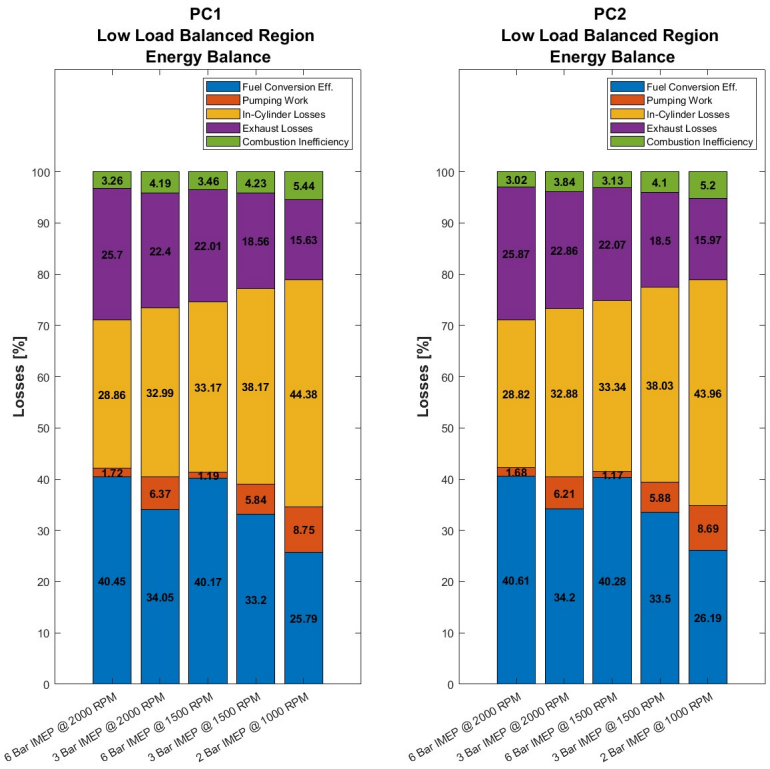

Figure 5.42: Energy Balance, Low Load Balanced Region, PC1 and PC2

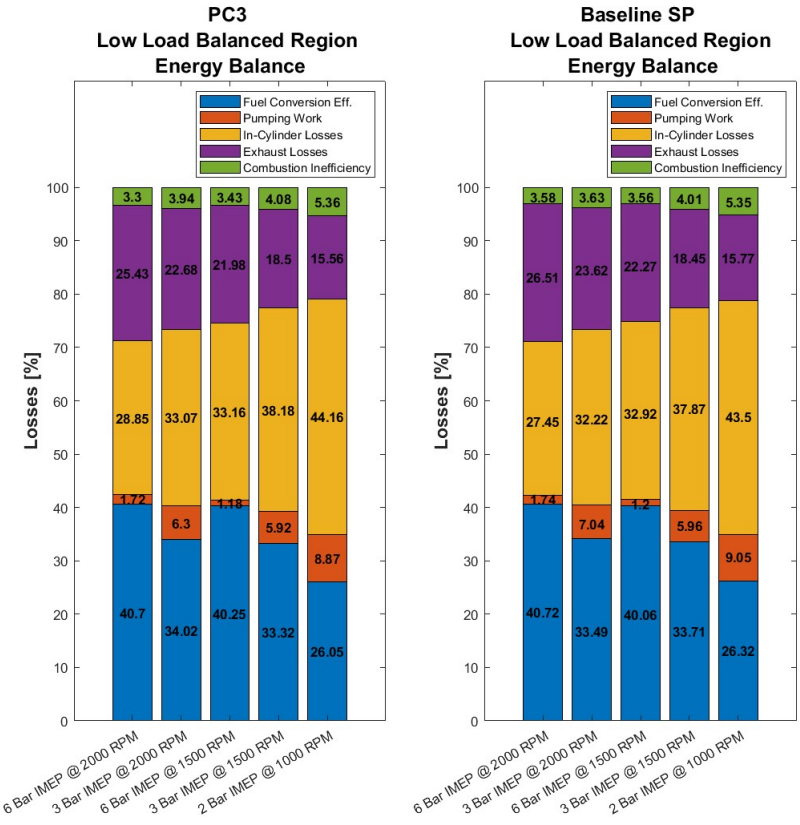

Figure 5.43: Energy Balance, Low Load Balanced Region, PC3 and Spark Plug

5.4 WOT Test

The wide-open throttle test is a test procedure to evaluate the performance of the engine and the ignition setups at their maximum load. The performance parameters of interest are the same as for the minimap runs, being fuel consumption and fuel conservation efficiency. For the purposes of this test, the pre-chambers were ran twice, one to match the performance of the baseline spark plug and one for maximum power extraction.

The first ran was conducted with the baseline spark with the achieved IMEP and fuel consumption shown in Table 5.11 with the limiting factor being the combustion phasing or met airflow requirement.

Engine Speed [RPM]	**Achieved Load [IMEP]**	**ISFC [g/kWh]**
1500	17.7	217.4
2100	19	227.0
4800	17.1	234.8

Table 5.11: Baseline Spark Plug Maximum Load Achieved and Fuel Consumption.

The pre-chambers were then installed and this IMEP was targeted. The ISFC values are presented in Table 5.12 with the percentage difference presented in Table 5.13. As the ISFC and the delta proves, the gains in fuel consumption for these operation points are substantial. Analysis of the pre-chamber pressure trace yields a valid insight into the reason for this gain.

$\frac{Speed[RPM]}{Load[IMEP]}$	Baseline SP ISFC [g/kWh]	PC1 ISFC [g/kWh]	PC2 ISFC [g/kWh]	PC3 ISFC [g/kWh]
4800/17.1	217.4	203.9	203.8	205.6
2100/19	227.0	213.5	213.5	217.2
1500/17.7	234.8	226.6	226.6	229.9

Table 5.12: ISFC $[g/kWh]$, For all Setups, Baseline IMEP Target

$\frac{Speed[RPM]}{Load[IMEP]}$	Baseline SP ISFC [g/kWh]	PC1 Percentage Delta	PC2 Percentage Delta	PC3 Percentage Delta
4800/17.1	217.4	-6.21%	-6.26%	-5.43%
2100/19	227.0	-5.95%	-5.95%	-4.32%
1500/17.7	234.8	-3.50%	-2.85%	-2.10%

Table 5.13: ISFC $[g/kWh]$ Delta To Baseline, For all Setups, Baseline IMEP Target

The pressure trace for 17.7 bar IMEP @ 4800RPM, derived from CFD calculations, is depicted in Figure 5.44. As can be seen, the pressure gradient and difference between the pre-chamber and main combustion chamber are much greater for this instance compared to Figure 5.41. Therefore, the resulting jet speed and turbulence inducement are higher, and the jet penetrates deeper into the main combustion chamber before main chamber ignition. The end result is a shorter combustion duration, which consumes the end-gases much faster than the baseline spark plug and mitigates knocking combustion. Due to these properties, the ability to advance the combustion phasing is enabled, leading to the observed gain in fuel conversion efficiency and fuel consumption. The energy balance calculation in figures 5.45 and 5.46 showcases the improvements in fuel conversion efficiency, as all pre-chambers show higher efficiency during all of these operation points. Comparing the pre-chamber, on average, PC1 produces the highest fuel conversion efficiency and thereby the greatest decrease in fuel consumption.

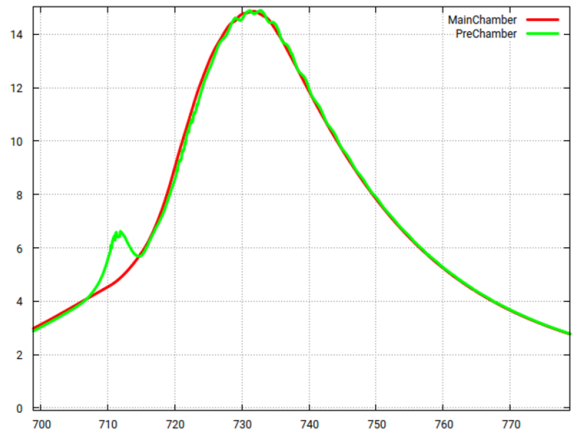

Figure 5.44: Pre-chamber and main chamber pressure trace for 17.7 bar IMEP at 4800RPM. Derived from CFD.

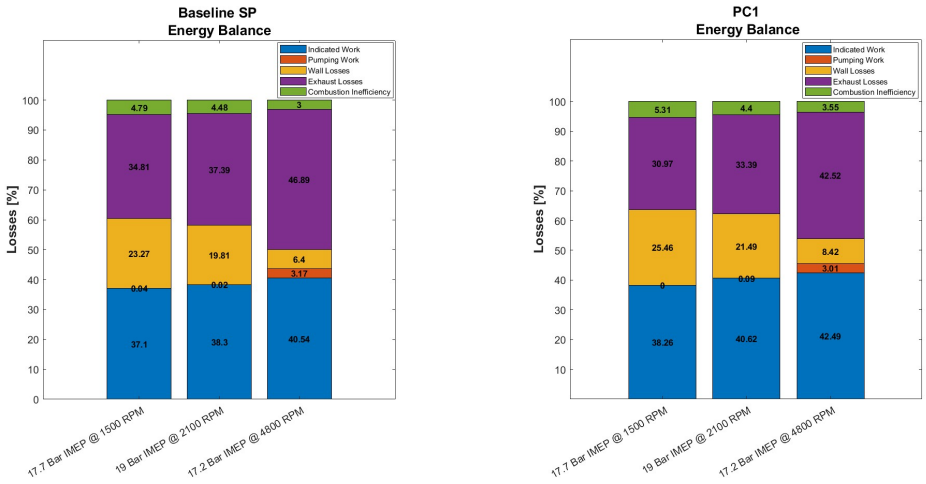

(a) Energy Balance, SP. **(b)** Energy Balance, PC1.

Figure 5.45: Energy Balance, First WOT test, Spark Plug and PC1.

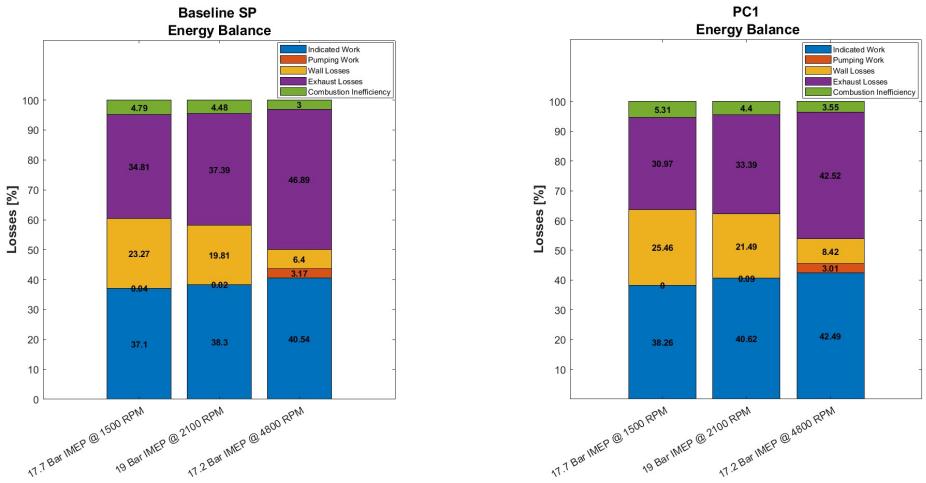

(a) Energy Balance, PC2. **(b)** Energy Balance, PC3.

Figure 5.46: Energy Balance, First WOT test, PC2 and PC3.

The final WOT test focused solely on pre-chamber setup with the aim of achieving maximum power extraction. During the previous test, the baseline spark plug was operating at its limit within the established boundary conditions. However, with the pre-chamber setups, the ability to advance the combustion phasing provided additional headroom, allowing for more load to be applied while still remaining within the boundary conditions. The results of this WOT test are presented in Table 5.14. As illustrated, the setup containing the pre-chambers enables higher power extraction with PC1 proving to be the most capable followed by PC2. It was also possible to extract more power from PC3, however limited by its tendency to run-away knock.

Engine Speed [RPM]	PC1 Max Load [IMEP]	PC2 Max Load [IMEP]	PC3 Max Load [IMEP]
4800	21.25 bar	20.22 bar	18.80 bar
2100	20.09 bar	20.01 bar	19.88 bar
1500	20.06 bar	20.03 bar	19.92 bar

Table 5.14: Maximum extraditable Indicated Power.

The energy balance calculations for the maximum power extraction from the pre-chambers are present in figures 5.47, 5.48 and 5.49 with Table 5.15 depicting the specific fuel consumption for each case. On average, PC1 produces both the best fuel consumption and the highest fuel conversion efficiency for all cases with PC3 being the worst.

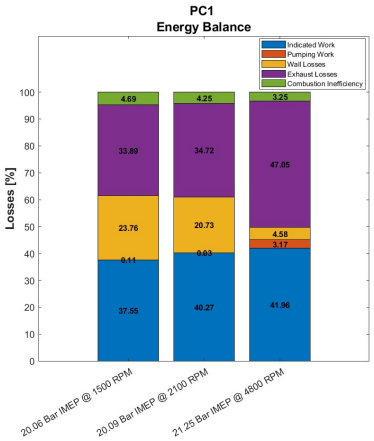

Figure 5.47: Energy Balance PC1.

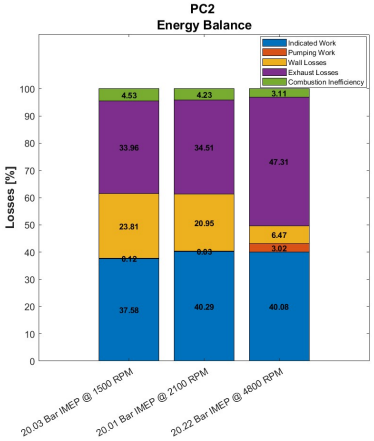

Figure 5.48: Energy Balance PC2.

Engine Speed [RPM]	PC1 ISFC	PC2 ISFC	PC3 ISFC
1500	230.8	231.1	230.4
2100	215.9	215.9	220.1
4800	212.4	213.5	213.7

Table 5.15: ISFC [g/kWH], WOT Maximum Power Extraction.

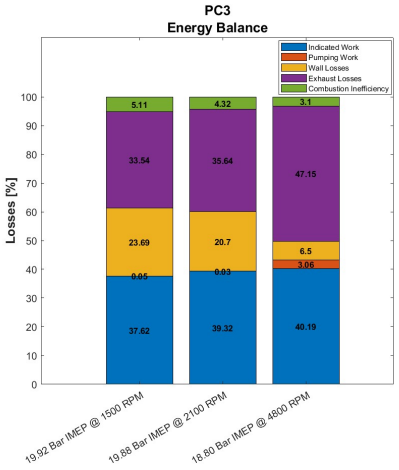

Figure 5.49: Energy Balance PC3.

5.5 Emissions Analysis

This section will focus on the emissions relating to the different setups, specifically targeting the runs runs completed in Section 5.3.2 and the WOT test where the baseline spark plug at full load with the pre-chambers matching that load. Emissions is an aspect that is heavily regulated by the governing bodies around the world, making them a vital part in the development process in any new IC engine. As the pre-chamber combustion process differs from the spark plug, emissions are therefore a important aspect to analyse.

The first emission to analyse will be the indicated specific NO_x which is depicted in figures 5.50 and 5.51 for the high ($>$ 10 bar IMEP) and low ($<$ 10 bar IMEP) load operation points respectively. During high load operation, the pre-chambers produce higher NO_x emissions which is explained by the short combustion duration

leading to higher maximum in-cylinder pressures and temperatures which are conditions favorable for NO_x formation. The maximum in-cylinder pressure is depicted in Figure A.75 for all of minimap operation points. During low load operation, this emission is generally higher for the pre-chamber, especially during the operation point at 9 bar IMEP. For the rest of the operation points, the reduction in in-cylinder O_2 concentration, facilitated by high VVT overlap and the subsequent increase internal-EGR, helps to decrease the formation of NO_x, while also suppressing the maximum in-cylinder pressures and temperatures, which further aids in the reduction of NO_x formation for the pre-chamber setups. The pre-chamber configurations show similar effects regardless of their orientation, with no setup emerging as the preferred choice.

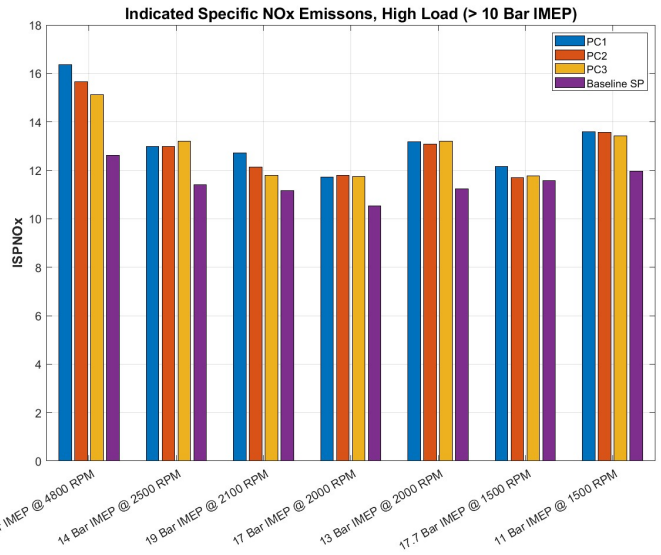

Figure 5.50: $ISNO_x$ $[g/kWh]$, High Load

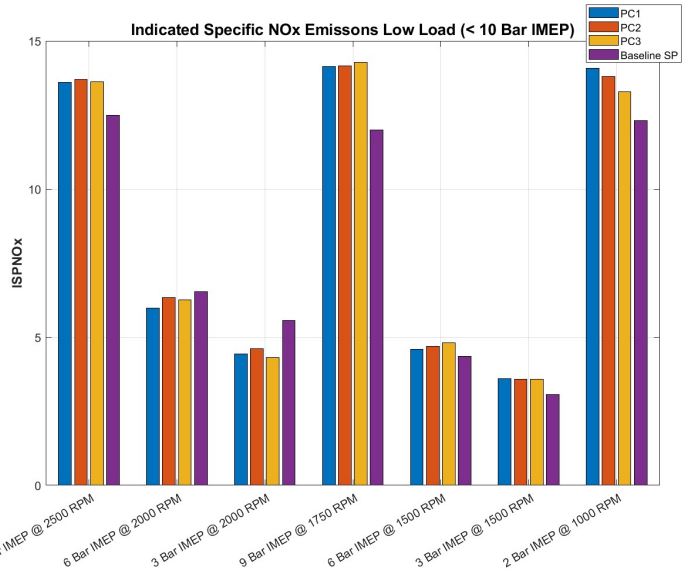

Figure 5.51: $ISNO_x$ $[g/kWh]$, Low Load

The CO emissions are depicted in figures 5.53 and 5.54, which serve as an indicator of complete combustion. Analysis of this emission produces mixed results, with the emission varying between the ignition source depending on the operation point. The low load operation points (Figure 5.54) are an example of the case where the CO values alternate between the pre-chamber setups and the spark plug.

For loads below 4 bar IMEP, the spark plug performs better on-average than the pre-chamber, possibly due to the overlap and subsequent internal-EGR causing high RMF and lambda disparity in the pre-chamber volume leading to its combustion quality degrading (as seen in Figure 5.52). However, for loads between 6 to 9 bar, the pre-chamber generates on-average less CO due to its higher combustion stability and efficiency. The cases during the high load operation points (Figure 5.53), also yield similar mixed results, with the spark plug producing on-average less CO at the WOT points and pre-chamber producing on-average less CO at the minimap points. The higher CO emissions for the baseline spark plug during the WOT operation points can possibly be explained by the fact that during high in-cylinder temperatures, the equilibrium between CO and CO_2 is shifted towards CO. However, if the in-cylinder temperatures drop too quickly, the equilibrium may not shift quickly enough towards CO_2, resulting in the CO becoming "frozen".

However, despite the mixed results, the CO emissions does follow the combustion efficiency to an extent. Besides the theories explored in this paragraph regarding this emission, other theories are also explored in next paragraph to when examining the THC emissions. When comparing the pre-chambers, it is clear that they perform about equally with no definitive preference.

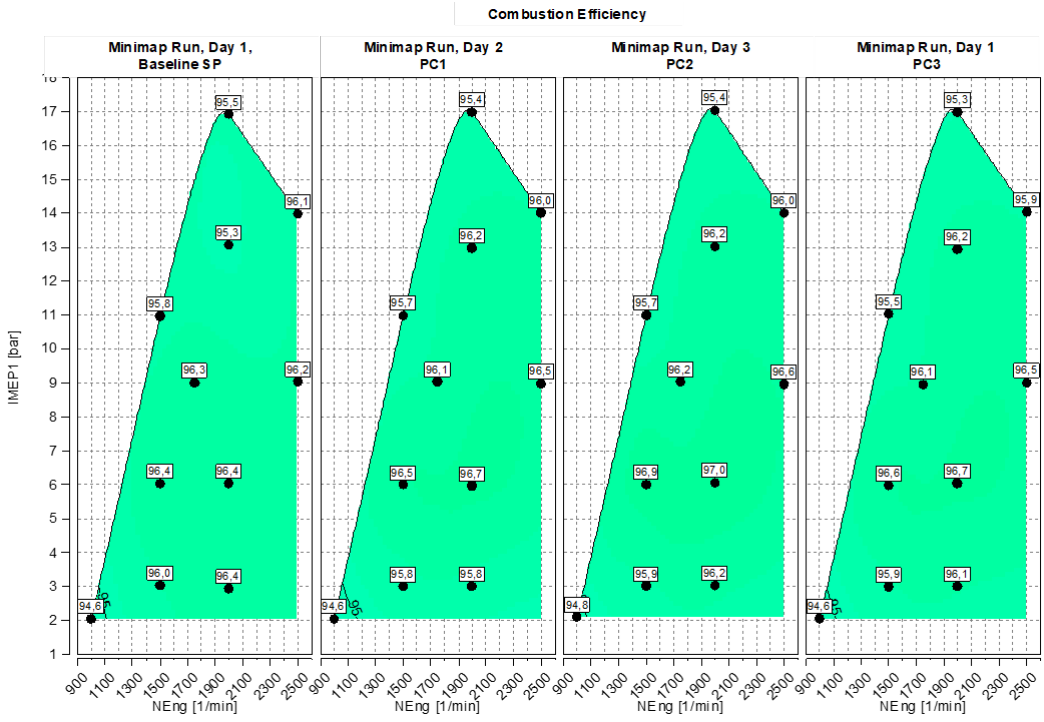

Figure 5.52: Combustion Efficiency, Reference Runs

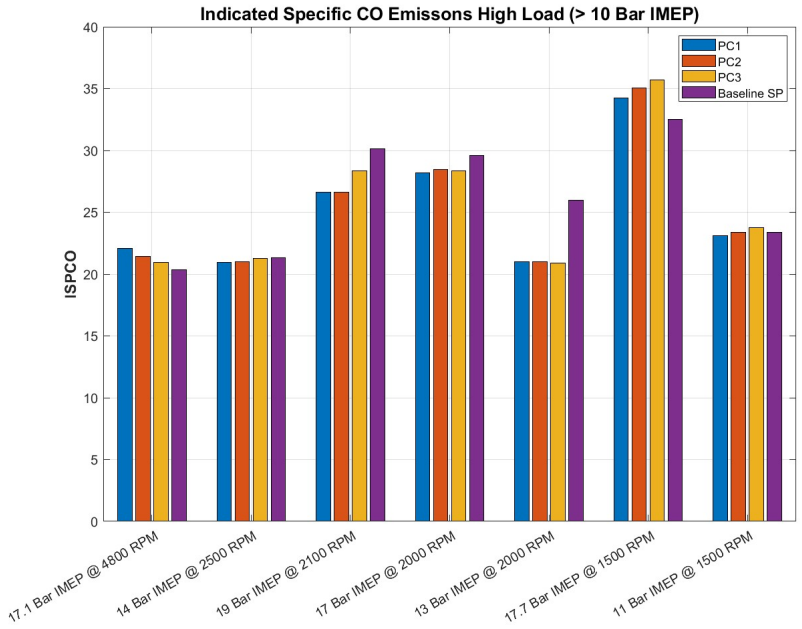

Figure 5.53: $ISCO$ $[g/kWh]$, High Load

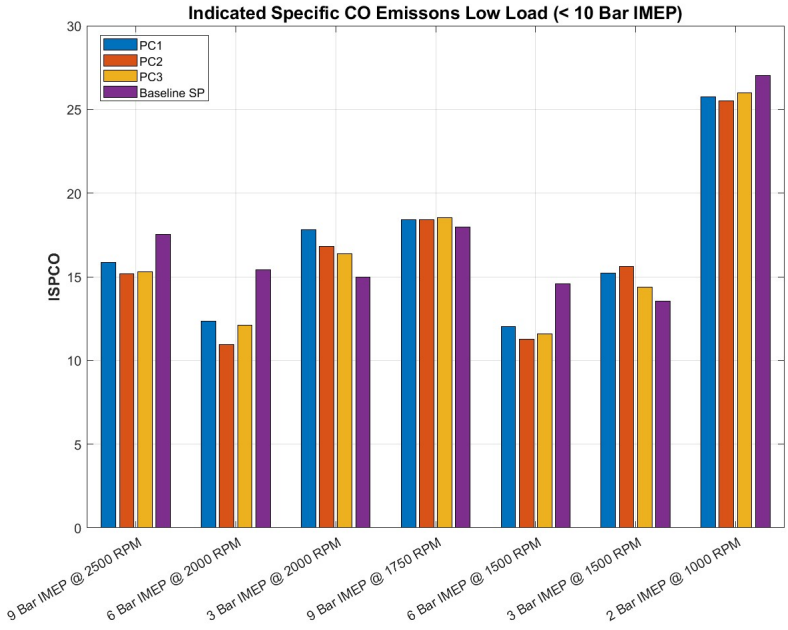

Figure 5.54: $ISCO$ $[g/kWh]$, Low Load

The THC emissions are depicted in figures 5.55 and 5.56 as high and low load, respectively. Similar to CO emissions, THC also serves as an indicator of incomplete combustion. However, this emission is also used to assess the impact of the crevice volume, as during the compression stroke, some of the air-fuel mixture will be forced into these small volumes and escape the combustion process. During combustion and expansion, HC emerges from these volumes and flows into the exhaust, thereby resulting in THC emissions. Higher compression ratios promote the effects of these

small volumes, as the increase in mixture density results in more mass being forced into these small volumes.

The pre-chamber setup exhibits a lower compression ratio of 13.25 in comparison to 13.45 for the baseline spark plug setup, as the pre-chamber volume contributes to an increase in combustion chamber volume. Therefore, the crevice effect from the pre-chamber should, in theory, be lower. However, it should be noted that the pre-chamber itself can contribute to higher crevice volume, which can affect the THC emissions. However, further investigation is required through the use of CAE simulations to accurately determine the extent of the pre-chambers increased crevice volume contribution.

During low load operation, the results are on average equal. Especially interesting is PC2 and the baseline spark plug, as they generate almost the same results however differ substantially when compared with CO emissions. This may indicate that during the expansion and exhaust stroke, late cycle oxidation occurs where THC emerges from the presumed increased crevices volume due to the pre-chamber which subsequently burn up and oxidise to CO. At higher engine loads and speeds, the CO emissions are comparable for the pre-chamber and the baseline spark plug, however, the THC emissions are higher for the pre-chamber. This indicates that the HC that emerge from the presumed increased crevice volume does not have time to oxides to CO at these operation points, resulting in the observed output pattern.

Comparing the different pre-chamber setups, on average PC2 performs the best and PC3 the worst, however the differences in absolute number are very small.

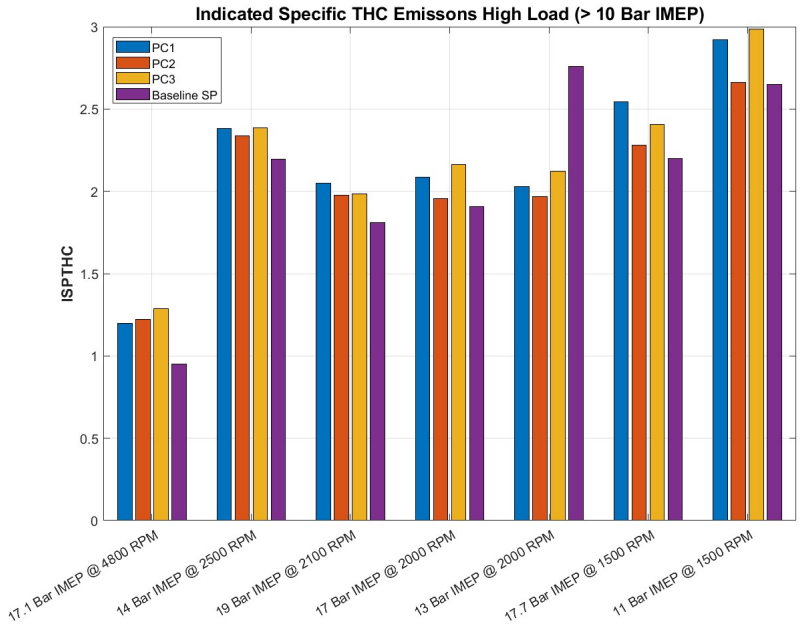

Figure 5.55: $ISTHC$ $[g/kWh]$, High Load

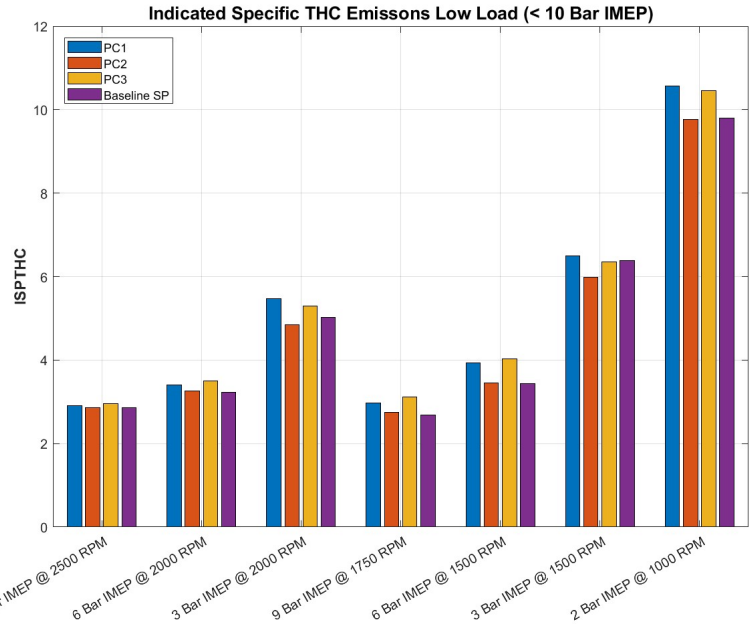

Figure 5.56: $ISTHC$ $[g/kWh]$, Low Load

5.6 EGR Test

Exhaust gas recirculation (EGR) is an interesting solution to mitigate the predominant issue regarding the pre-chamber, which is excess in-cylinder heat losses. This was evaluated through the analysis conducted in Section 5.2. Among others, EGR is primarily used to reduce the pumping loss and to mitigate knocking combustion, with the latter enabling the option for combustion phasing to be moved closer to MBT which results in increased fuel conversion efficiency. Utilizing EGR dilutes the fresh mixture inside the combustion chamber with the exhaust gases. As the mixture is diluted with EGR, the flame fron characteristics and the flame propagation process is altered. The diluted mixture leads to an extended pre-heat zone, which increases the flame thickness, reduces the laminar flame speed, and lowers the adiabatic flame temperature. These factors result in an increase in combustion duration, a reduction in the in-cylinder pressure rise rate (RMax) and reduced peak cylinder pressures and temperatures. Also, EGR increases the cylinder mass and thereby reduces the average gas temperature (same fuel has to heat up more mass).

For the case of the pre-chamber, EGR dilution would also slow down the combustion process inside the pre-chamber. This would subsequently lead to a reduced pressure difference and a more gradual pressure gradient between the pre-chamber and main combustion chamber, reducing the jet speed and turbulence inducement. Thereby, the goal of this test is to determine if the in-cylinder heat transfer losses can be reduced through increased combustion duration and reduced turbulence inducement, and if this, in turn, leads to achieving higher fuel conversion efficiency. The operation point selected for this test are chosen with these goals in mind. The EGR ratio in the intake manifold was increased until combustion became unstable. In some of the

operation points, the necessary EGR level to reach the combustion instability limit was not met, either because the control valve could not be opened further or because the pressure difference between the exhaust and intake systems was insufficient. For some operation points thereby, this test should be seen as the possibility and the potential for better fuel consumption and fuel conversion efficiency.

The first operation point to analyse is 9 bar IMEP @ 2500RPM. This is an obvious point of interest due to all setups being operated with combustion phasing at MBT. The AHR curves from the measurements are depicted in Figure 5.57a, with 5.57b depicting the fraction of energy released during combustion lost as heat transfer.

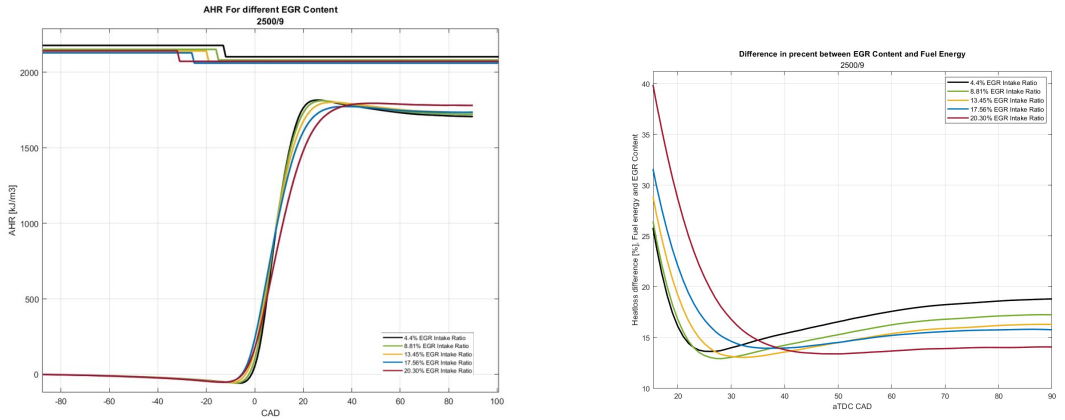

(a) AHR **(b)** In-Cylinder Heat Transfer Loss

Figure 5.57: AHR and In-Cylinder Heat Transfer Losses With EGR, 9 bar IMEP 2500RPM

The addition of EGR and the subsequent reduction in heat transfer losses were observed at every step of the EGR content increase in the intake manifold. Table 5.16 summarizes the results of this run with reference to the operating point without EGR during the minimap run. As the EGR content in the intake increases, the combustion duration increases, resulting in a reduction in pressure rise rate (RMax) and maximum in-cylinder pressure. This, in turn, leads to a decrease in heat transfer losses (as seen in Figure 5.57b), allowing for a reduction in air mass flow while maintaining the same output load due to less energy being lost as heat transfer losses.

The drop in heat transfer losses is reflected in the fuel consumption and fuel conversion efficiency, with the former peaking at a 1.8% reduction in fuel consumption and the latter reaching 1 percentile point higher. However, there is a limit to the amount of EGR that can be introduced into the intake, and that limit is 20.3% EGR ratio, as it resulted in a main chamber misfire cycles.

EGR Ratio Intake	Combustion Heat Loss Percentage	Fuel Conversion Efficiency	ISFC, % Delta To Run w/o EGR	Rapid Burning Angle Duration Difference [CAD]	RMax Difference [bar/deg]
4.4%	18.8	41.2%	-	+0.8	-0.7
8.8%	17.3	41.9%	-1.0	+2.30	-1.30
13.5%	16.3	42.2%	-1.8	+4.5	-2.1
17.6%	15.8	42.2%	-1.8	+7.2	-2.8
20.3%	14.1	42.1%	-1.3	+10.9	-3.4

Table 5.16: 9 Bar IMEP @ 2500 RPM

The second operation point to analyse is 9 bar IMEP @ 1750 RPM. This operation point also inherits high in-cylinder heat loss, thus it is also of interest to analyse if the same effects are present here as in 9 bar IMEP @ 2500 RPM. The AHR and the percentage energy delta between the energy released during combustion and the AHR curve curves are depicted in figures 5.58a and 5.58b respectively. However, unlike the the previous operation point, this operation point does not have its combustion phasing at MBT, meaning the gain in fuel conversion efficiency and reduction in fuel consumption is not only a direct result of reducing the heat transfer losses.

Nevertheless, the results for this operation point are summarised in Table 5.17. As with the previous operation point, progressively increasing the EGR content in the intake manifold results in a reduction in the in-cylinder heat losses, with the reasons being the same. The gain in efficiency is however, both due to this phenomenon and the advancement in combustion phasing. The combustion phasing for the first two runs are 9.6 and 8.9 CAD ATDC respectively, with the rest of the measurements being at MBT. Nevertheless, the gain in fuel conversion efficiency and reduction in fuel consumption is substantial, with no runs showing signs of instability. The EGR radio did not exceed 17.0% due to the EGR valve being fully open.

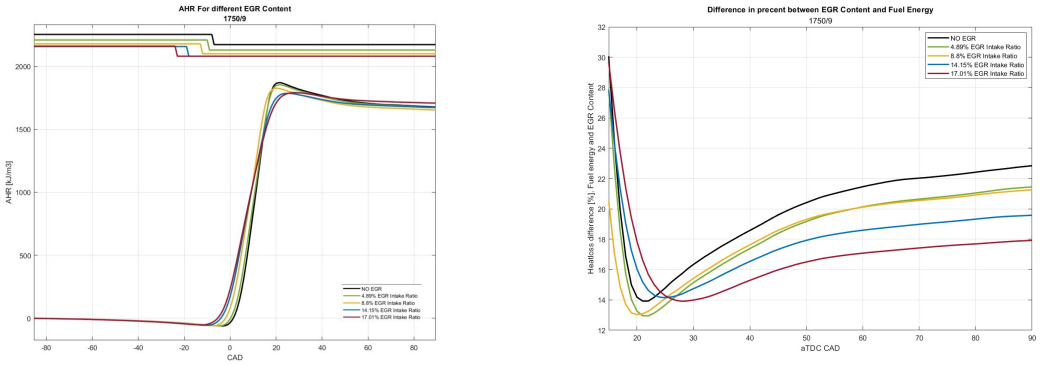

(a) AHR **(b)** In-Cylinder Heat Transfer Loss

Figure 5.58: AHR and In-Cylinder Heat Transfer Losses With EGR, 9 bar IMEP 1750RPM

EGR Ratio Intake	Combustion Heat Loss Percentage	Fuel Conversion Efficiency	ISFC, % Delta To Run w/o EGR	Rapid Burning Angle Duration Difference [CAD]	RMax Difference [bar/deg]
No EGR	22.9	39.8	Reference	Reference	Reference
4.9%	21.5	40.6	-1.6	+0.8	-1.6
8.8%	21.3	41.2	-3.0	+1.1	-0.2
14.2%	19.6	41.5	-4.1	+4.6	-4.2
17.0%	17.9	42.0	-4.5	+6.7	-4.5

Table 5.17: 9 Bar IMEP @ 1750 RPM

The last operation point is to focus on the ability for efficiency extraction predominately due to the ability to advance combustion phasing. The candidate operation point is 14 bar IMEP @ 2500RPM with the reason being the combustion phasing proximity to MBT. The AHR, percentage energy delta between the energy released during combustion and the AHR curve curves, and tabular summary are depicted in figures 5.59a, 5.59b and Table 5.18 respectively.

Progressively, the EGR ratio in the intake manifold was increased, suppressing knock and enabling the ability to advance the combustion phasing. The gain in fuel conversion efficiency is mainly due to the advancement in combustion phasing, as the in-cylinder heat losses remain roughly constant through out these runs. This run also possessed stable operation for all of the measurements recorded with the limiting factor being the fully opened EGR valve.

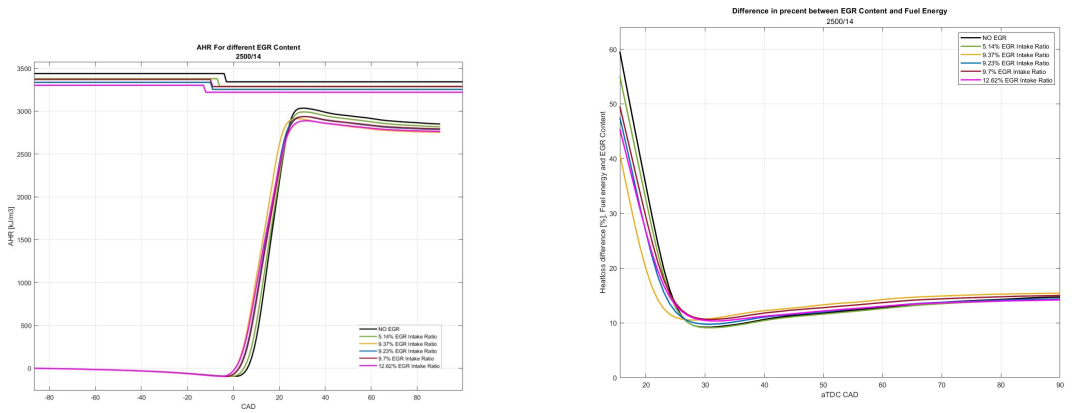

(a) AHR **(b)** In-Cylinder Transfer Heat Loss

Figure 5.59: AHR and In-Cylinder Heat Transfer Losses With EGR, 14 bar IMEP 2500RPM

EGR Ratio Intake	Combustion Heat Loss Percentage	Fuel Conversion Efficiency	ISFC, % Delta To Run w/o EGR	Rapid Burning Angle Duration Difference [CAD]	Combustion Phasing [CAD ATDC]
No EGR	14.7	40.6	Reference	Reference	15.3
5.1	14.4	41.3	-1.6	+0.9	14.5
9.4	15.4	42.0	-3.0	+2.1	13.1
9.2	14.4	42.0	-3.4	+1.8	12.8
9.7	15.0	41.7	-3.1	+1.2	11.3
12.6	14.2	42.3	-4.3	+3.1	12.1

Table 5.18: 14 Bar IMEP @ 2500 RPM

6
Conclusion

The conclusion of this research study aims to provide a comprehensive overview of the results obtained from the testing of three passive pre-chamber spark plugs with different jet orientations in a single cylinder research engine. The primary objective of this research was to gain a deeper understanding of the combustion process initiated by a passive pre-chamber and to evaluate the potential benefits and drawbacks of this ignition source compared to a standard spark plug. By utilizing various testing methods, a direct and indirect comparison between the pre-chambers and the baseline spark plug was conducted. The findings of this research will provide valuable insight into the prospects and feasibility of using a passive pre-chamber as the primary ignition source for future IC engines at Aurobay.

6.1 Pre-Chamber and Spark Plug Comparison

In this study, three pre-chambers with varying jet orientations were tested to investigate the impact on the performance, repeatability and robustness.

During the heat loss and energy balance evaluation (see Section 5.2), where all of the setups operated with the same input settings (combustion phasing, camshaft phasing and mass airflow), the results indicated that the pre-chamber combustion was remarkably similar among the different jet orientations, with a consistent level of heat loss being observed. However, a significant difference was observed between the pre-chamber setups and the baseline spark plug. The former exhibited higher in-cylinder and heat transfer losses but lower exhaust losses, while the latter exhibited lower in-cylinder and wall heat losses but higher exhaust losses. The main reason for this difference was higher turbulence inducement, increased conduction area due to the pre-chamber volume and the increase in the cross section area of the burned gas being in contact with various surfaces in the combustion chamber. This, in turn, negatively affected the fuel conversion efficiency at some operating points.

Upon adjusting the input parameters for optimal pre-chamber operation, the results of the repeated minimap cycling and WOT test showed significant improvements in performance compared to the baseline spark plug, both in terms of measurement repeatability and fuel consumption. Figures 6.1, 6.2, 6.3 and 6.4 depict the energy balance from the minimap and WOT test for all setups.

The greatest fuel consumption gains were observed at high load conditions, as

demonstrated by the "High Load Gain" region and WOT test, where all pre-chambers demonstrated substantial improvement. Part-load operation ("Excess Heat Loss" region) was found to be the only scenario where the pre-chamber combustion became a disadvantage, due to the inability to take advantage of the short combustion duration which outside this region can offset the losses due to increased heat transfer. However, the aforementioned heat loss could be effectively reduced through the use of external or internal EGR, as demonstrated by the EGR test and the "low load balanced" region. In the "low load balanced" region (during low load conditions), optimizing the phasing of the camshafts successfully increased the combustion duration and reduced the maximum in-cylinder pressures. While this did not reduce the in-cylinder losses for the pre-chamber to the same level as the baseline spark plug, it was still adequate to result in the slightly higher in-cylinder heat loss being offset by lower exhaust heat losses. This led to total heat loss becoming very similar for the pre-chamber setups and spark plug, with the improvement in fuel consumption being a byproduct of reduced pumping losses from the advanced iVVT or improved combustion efficiency. Comparing the pre-chamber setups, PC1 performed the best during the WOT test. During the minimap test, PC2 showed a very slight performs advantage.

All pre-chamber setups were found to notably improve combustion consistency and stability compared to the baseline spark plug, with the improved CoV_{IMEP} being the most significant parameter. Additionally, there were no instances of misfire during any of the low load operation points in the "low load balanced" region. A test was conducted at 800 RPM at approximately 1 bar IMEP with the VVT settings set to their default position to evaluate the pre-chamber's performance under idle conditions, which resulted in exceptional stability with no misfires or unusual combustion characteristics. Several factors contribute to the observed stability of the pre-chamber setups, most notably the favorable orifice size, count, and volume of the pre-chamber, which result in improved scavenging. Additionally, the high compression ratio of the engine used in the tests plays a key role by reducing the quenching distance and compressing the mass more densely in the pre-chamber, leading to stable and favorable ignition attributes of the emerging jet. The location of the spark plug inside the pre-chamber is also an important factor. CFD studies conducted by H. Ge et al. [26], D. E. Lee et al. [10], and M. Sens et al. [7] have indicated that the RMF is likely located near the top of the pre-chamber volume. Thereby, the centrally mounted spark plug of the Tenneco passive pre-chamber provides a distinct advantage by igniting the fresher mixture in the center of the pre-chamber.

During the remainder of the operation points in the minimap, all pre-chamber setups yielded preferable repeatability and robustness with no clear preference. In conclusion, thereby, all pre-chambers demonstrated improved consistency and robustness during all of the minimap operation points, resulting in substantial stability improvements in repeatability and robustness when compared to the baseline spark plug.

In terms of the effect of the pre-chamber jet orientation, the results conclude that

the orientation of the pre-chamber had a minimal impact on the performance with the simplest design (PC1) performing exceptionally well. Despite initial assumptions that the more uniform jet distribution of PC2 and PC3 would result in better performance, this was not the case. All pre-chambers performed exceptionally well during the majority of the testing sessions, with the only exception being the WOT test, where PC3 performed the worst due to a tendency towards run-away knock. The specific reason for this occurrence was never investigated. PC1 and PC2 did not show any of these tendencies and performed reliably during all testing. Although PC2 showed slightly better results during the minimap, its advantage was only marginal and not absolute. Given its ease of installation, simpler design, and negligible performance difference, PC1 is considered the preferred pre-chamber from the tests conducted.

In conclusion, these tests demonstrate the effectiveness of the pre-chamber in improving combustion stability and mitigating knock. The short combustion duration, combined with the robust and repeatable nature of the pre-chamber, has led to significant improvements in fuel conversion efficiency, fuel consumption, robustness and repeatability. The results of this thesis strongly suggest that pre-chamber technology has great potential for application in future Aurobay engines and is a promising avenue for future research and development.

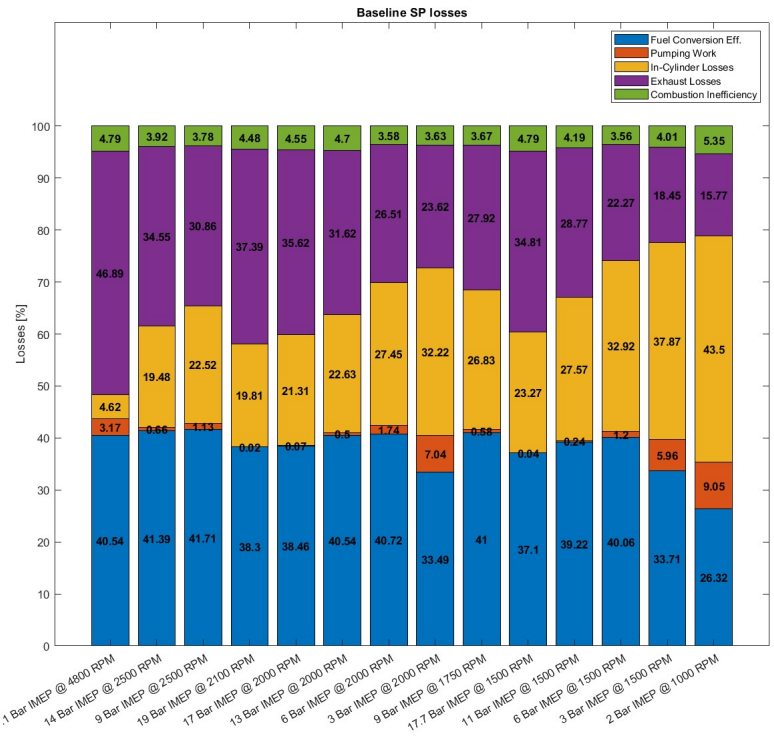

Figure 6.1: Energy Balance, Baseline Spark Plug

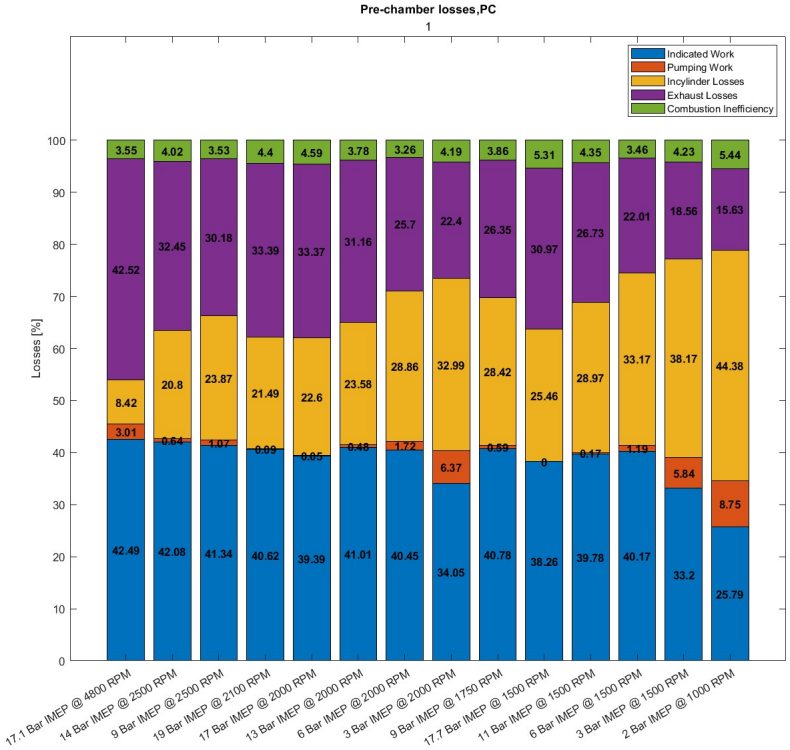

Figure 6.2: Energy Balance, PC1

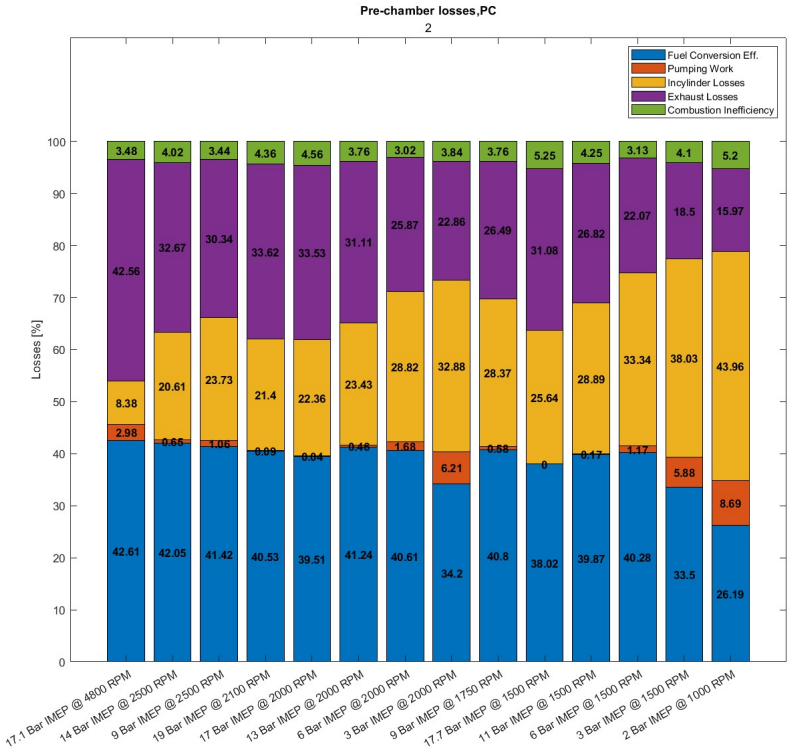

Figure 6.3: Energy Balance, PC2

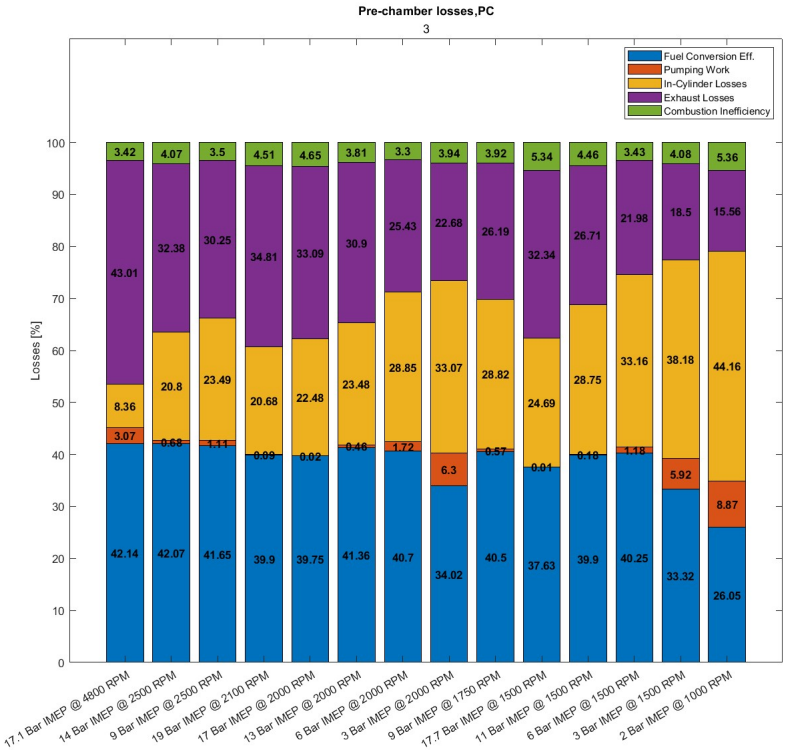

Figure 6.4: Energy Balance, PC3

6.2 CFD Analysis

The verification of the in-cylinder heat losses was conducted extensively by both the heat transfer analysis and the energy balance calculations. However, even though these calculations aid in the indication of the severity of the in-cylinder and heat transfer losses, they do not give a valid insight into the most effected in-cylinder surfaces. Furthermore, the surfaces affected by the heat conduction will in most cases give an insight to its potential reason. For example, if high in-cylinder turbulence is present, this will in most cases result in high heat conduction through the cylinder head. The CFD analysis is therefore to aid in the understanding of the most affected combustion chamber surfaces and there potential reason.

With close collaboration with the CAE department at Aurobay, a CFD model depicting the pre-chamber combustion was simulated. Figure 6.5 and 6.6 depict the in-cylinder heat loss for each surface of the combustion chamber at 6 IMEP @ 1500 RPM, were the in-cylinder pressures where approximately 2 bar higher for the pre-chamber. The figures depict the percentage delta to the reference baseline spark plug. As observed, all surfaces, apart from the from the cylinder linear, conduct more heat during pre-chamber combustion. As pre-chamber combustion commences and a pressure difference is created, a jet will form and penetrate into the main combustion chamber. Due to this penetration, the in-cylinder TKE will increase, leading to one of the main reasons for the reduction in the combustion duration. The effect of the increased turbulence due to the pre-chamber can be seen

as a increase in heat lost to the cylinder and piston head. The valves also see an increase in heat conduction however this is mainly due to the jets combusting the main mixture charge close to these components and with higher intensity. The highest heat loss ratio occurs at the pre-chamber plug, with the pre-chamber conducting 4.7J or 167% more heat than the conventional spark plug which is mainly due to the pre-chamber itself conducting heat after combustion has taken place inside the chamber. Overall, the heat losses during the end of the compression stroke are about 6% higher for the pre-chamber then the baseline spark plug. Table 6.1 depicts the in-cylinder heat losses in tabular fashion.

Surface	**Spark Plug**	**Pre-Chamber**
Intake Valve	100%	+0.58%
Exhaust Valve	100%	+4.76%
Plug	100%	+167.86%
Cylinder Head	100%	+16.61%
Piston Head	100%	+4.63%
Cylinder Liner	100%	-10.82%
Total Heat Loss	100%	+6.08%

Table 6.1: Table of the In-Cylinder Heat Loss, Percentage Delta to Reference Baseline SP

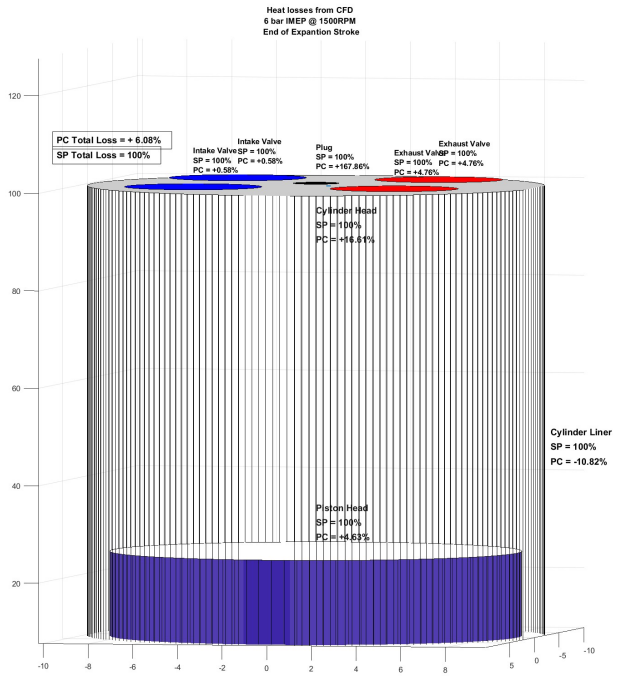

Figure 6.5: In-Cylinder Surface Heat Loss, Percentage Delta to Baseline SP, 6 bar IMEP @ 1500RPM

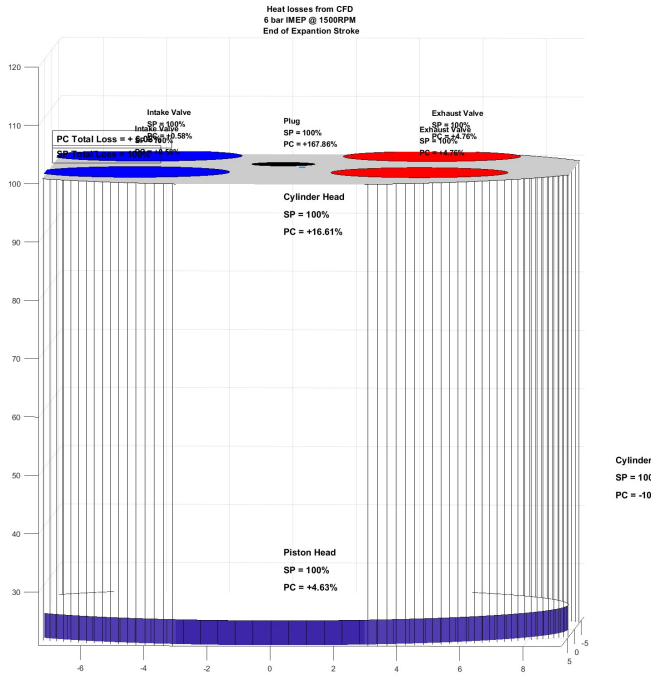

Figure 6.6: In-Cylinder Surface Heat Loss, Percentage Delta to Baseline SP, 6 bar IMEP @ 1500RPM

6.3 Further Work

The conclusion drawn from this thesis regarding the pre-chamber and its subsequent combustion process resulted to be highly beneficial in the end goal of reduced fuel consumption. Its is therefore recommended that further work and resources are allocated in this area to further take advantage of these benefits that the pre-chamber yields. This section is therefore to aid with the further development of this technology with recommendations from the author.

One of the main objectives of this thesis was to test the effect of different jet orientations. As such, the geometry of the pre-chambers remained the same throughout the testing. The test results from the minimap demonstrate that in-cylinder heat loss is one of the drawbacks of pre-chamber combustion. To alleviate this, different pre-chamber geometries should be tested that limit the pressure difference and gradient which, thereby, limits the jet speed and penetration depth. Bigger orifice diameters and/or higher orifice count or reducing the consumption rate in the pre-chamber (reducing the pre-chamber volume) should help with alleviating the pressure difference between the two chambers and limit the turbulence inducement and adjust the jets ignition characteristics closer to the center of the combustion chamber. However, take note that the pre-chamber geometry needs to be closely optimized for its intended purpose, thereby caution is advised when changing a parameter in the geometry of the pre-chamber as it might negatively impact some other parameter.

For the test engine used in for this thesis however, the short combustion duration opens up possibilities for further beneficial modifications intended to increase the fuel conversion efficiency. The short combustion duration is of drawback if in-cylinder heat losses are of concern however the high turbulence and charge motion inducement as a direct result of the pre-chamber paves the way for the possibility to use more free flowing ports to reduce the pumping loss induced by the commonly used tumble ports. Tumble ports are used to enhance the turbulence level during combustion, but if the turbulence is created by the pre-chamber ignition process instead, the tumble level can most likely be reduced. However, some level of turbulence will most likely still be required to ensure adequate mixing of the incoming air and fuel. Nevertheless, the intensity of the charge motion induced by these ports can be reduced. Other beneficial modifications that could be made to take advantage of the much shorter combustion duration and the knock mitigation properties is higher compression ratio. The single cylinder test engine used during this master thesis had a compression ratio of 13.45:1. Therefore, the next logical step should be to test compression ratios that exceed this ratio, ideally in the range close to 14:1.

As the jet exit velocity is determined by the pressure difference between the two chambers, it plays an essential role in determining the jet penetration depth, ignition delay and turbulence inducement which subsequently influences the burning angles. For the testing and analysis conducted in this thesis, the different reasoning behind the combustion duration viewed as a direct result of the pre-chamber are assumptions derived from the pre-study phase in-combination with observing the oscillations in the in-cylinder pressure trace. The true pressure difference could not be determined, as the test engine lacked a pressure sensor in the pre-chamber. A pressure sensor inside the pre-chamber volume would have yielded a better insight into how the pressure difference affects the main chamber combustion, the burning angles and the in-cylinder heat loss. A pressure sensor here would also aided in the faultfinding if a problem was to occur. For instance, if misfire at low load was observed, it's (at the moment) difficult to determine if it's due to poor scavenging leading to high RMF which causes the pre-chamber to misfire or if it's due to jet quenching against the pre-chamber orifices which can cause main chamber misfire. It should be stressed that pre-chamber combustion is an optimization problem, and thereby it's geometry and resulting pressure difference should always be optimized for it's intended purpose, or intended operation window. It is thereby recommended that a pressure sensor is installed into the pre-chamber volume for future pre-chamber tests to better optimize the pressure difference for it's usage.

As mentioned, the main driver for the jet exit velocity is the pressure difference and gradient between the pre-chamber during combustion and main combustion chamber. During some operation points, especially at high load and WOT operation, the high pressure difference and gradient between the pre-chamber and the main combustion chamber causes the jet exit velocity to be super sonic. When this occurs, a pressure pulse is generated and this pressure pulse then oscillates in the main combustion chamber. The resulting pressure pulse is picked up by the in-cylinder piezoelectric sensor and can be viewed in the in-cylinder pressure trace as oscilla-

tions (see figure A.88). This, thereby, posses a problem for the knock detector, as it presumes these oscillations to be knock. However, this is normal combustion and operation for the pre-chamber, and should not be taken with concern. This meant that the normal knock controller could not be relied upon during pre-chamber testing, leading to the author having to listen closely to the microphone installed in the test facility and pay close attention to the spark timing when the knock limit was reached. The strategy implemented by the author to reduce the inconsistency during the measurements was as follows. When the knock limit was reached for an operation point, the knock detector value was noted and when this operation point was repeated, the same knock detector value was targeted. However, for future operation it is highly recommended that a new knock detection method is implemented. A recommendation could be to follow D.J Corrigan et al [32] method for pre-chamber knock detection.

Bibliography

[1] Felipe Munoz, *Internal Combustion Engines (ICE) counted for over 90% of global car sales in H1 2019*, 2019. [Online]. Available: https://www.jato.com/internal-combustion-engines-ice-counted-for-over-90-of-global-car-sales-in-h1-2019/.

[2] "Submission to the UNFCCC Secretariat," Tech. Rep., 2021.

[3] NASA/GISS, "GLOBAL LAND-OCEAN TEMPERATURE INDEX," *Global Climate Change*, [Online]. Available: https://climate.nasa.gov/vital-signs/global-temperature/.

[4] E. Karamfilova and European Parliament. European Parliamentary Research Service. Ex-Post Evaluation Unit., *EU policy on air quality : implementation of selected EU legislation : European implementation assessment.* P. 185, ISBN: 9789284676835.

[5] California Government, *History regarding the emission legislation in California.* [Online]. Available: https://ww2.arb.ca.gov/about/history.

[6] Dr Heywood John, *Internal Combustion Engines Fundamentals 2nd Edition.* 2018.

[7] D.-I. Marc Sens *et al.*, "Pre-Chamber Ignition and Promising Complementary Technologies," Tech. Rep.

[8] Frank Markus, "Maserati's New Nettuno V-6 Engine Has Clever Tricks Up Its (Cylinder) Sleeves," *Motortrend*, 2021. [Online]. Available: https://www.motortrend.com/features/2022-maserati-mc20-nettuno-v-6-engine-tech/.

[9] Ricardo Harry, "US1271942," *INTERNAL C0MBUSI0N ENGINE PATENT US127942*,

[10] D. E. Lee *et al.*, "Misfire Behavior and Mitigations of Passive Pre-chambers at Low-Load Operation in an Optically Accessible Gasoline Engine," *SAE International Journal of Engines*, vol. 15, no. 3, Sep. 2021, ISSN: 19463944. DOI: 10.4271/03-15-03-0016.

[11] M. Bassett *et al.*, "Passive MAHLE Jet Ignition ® System Demonstrator," Tech. Rep.

[12] M. Bunce *et al.*, "The effects of turbulent jet characteristics on engine performance using a pre-chamber combustor," in *SAE Technical Papers*, vol. 1, SAE International, 2014. DOI: 10.4271/2014-01-1195.

[13] Otto Nikolaus, "Gas motor engines, US194047,"

[14] Johansson Bengt, *Förbränningsmotorer*. Lund, 2007.

[15] Mikael Wideskog, "Introducing the world's largest gas engine," Wärtsilä Power Plants, Tech. Rep.

[16] Mark Hughes, "Ferrari's Formula 1 jet ignition," *MOTORSPORT*, 2016. [Online]. Available: https://www.motorsportmagazine.com/articles/single-seaters/f1/ferraris-formula-1-jet-ignition.

[17] P. M. Allison *et al.*, "Pre-Chamber Ignition Mechanism: Experiments and Simulations on Turbulent Jet Flame Structure," Tech. Rep.

[18] P. M. Allison *et al.*, "Pre-chamber ignition mechanism: Experiments and simulations on turbulent jet flame structure," *Fuel*, vol. 230, pp. 274–281, Oct. 2018, ISSN: 00162361. DOI: 10.1016/j.fuel.2018.05.005.

[19] E. Mastorakos *et al.*, "Fundamental Aspects of Jet Ignition for Natural Gas Engines," *SAE International Journal of Engines*, vol. 10, no. 5, pp. 2429–2438, Sep. 2017, ISSN: 19463944. DOI: 10.4271/2017-24-0097.

[20] S. Biswas *et al.*, "On ignition mechanisms of premixed CH4/air and H2/air using a hot turbulent jet generated by pre-chamber combustion," *Applied Thermal Engineering*, vol. 106, pp. 925–937, Aug. 2016, ISSN: 13594311. DOI: 10.1016/j.applthermaleng.2016.06.070.

[21] S. Yamaguchi, N. Ohiwa, and T. Hasegawa, "Ignition and Burning Process in a Divided Chamber Bomb," Tech. Rep., 1985, pp. 177–187.

[22] Q. Tang *et al.*, "Simultaneous Negative PLIF and OH* Chemiluminescence Imaging of the Gas Exchange and Flame Jet from a Narrow Throat Pre-Chamber," in *SAE Technical Papers*, SAE International, Sep. 2020. DOI: 10.4271/2020-01-2080.

[23] A. Shah, P. Tunestal, and B. Johansson, "Effect of Pre-Chamber Volume and Nozzle Diameter on Pre-Chamber Ignition in Heavy Duty Natural Gas Engines," in *SAE Technical Papers*, vol. 2015-April, SAE International, Apr. 2015. DOI: 10.4271/2015-01-0867.

[24] C. Redtenbacher, "Analysis and optimization of Pre-chamber combustion process for large gas engines," Tech. Rep.

[25] X. Yu *et al.*, "The Impact of Pre-Chamber Design on Part Load Efficiency and Emissions of a Miller Cycle Light Duty Gasoline Engine," in *SAE Technical Papers*, SAE International, Apr. 2021. DOI: 10.4271/2021-01-0479.

[26] H. Ge *et al.*, "CFD Optimization of the Pre-Chamber Geometry for a Gasoline Spark Ignition Engine," *Frontiers in Mechanical Engineering*, vol. 6, Jan. 2021. DOI: 10.3389/fmech.2020.599752.

[27] A. Stadler *et al.*, "The Potential of Gasoline Fueled Pre Chamber Ignition Combined with Elevated Compression Ratio," in *SAE Technical Papers*, vol. 2020-April, SAE International, Apr. 2020. DOI: 10.4271/2020-01-0279.

[28] K. Bureshaid *et al.*, "Experimental Studies of the Effect of Ethanol Auxiliary Fuelled Turbulent Jet Ignition in an Optical Engine," *SAE International Journal of Engines*, vol. 12, no. 4, Jul. 2019, ISSN: 19463944. DOI: 10.4271/03-12-04-0026.

[29] L. A. Gussak, "The Role of Chemical Activity and Turbulence Intensity in Prechamber-Torch Organization of Combustion of a Stationary Flow of a Fuel-Air Mixture," Tech. Rep.

[30] L. A. Gussak, "High Chemical Activity of Incomplete Combustion Products and a Method of Prechamber Torch Ignition for Avalanche Activation of Combustion in Internal Combustion Engines," Tech. Rep.

[31] L. A. Gussak, V. P. Karpov, and Y. V. Tikhonov, "The Application of Ldg-Proc6SS in Prechamber Engines THE NEW PRINCIPLE OF THE INITIATION OF COMBUSTION AND THE METHOD OF PRECHAMBER-TORCH IGNITION IN INTERNAL COMBUSTION ENGINES," Tech. Rep., 1980.

[32] D. J. Corrigan *et al.*, "Engine Knock Detection Methods for Spark Ignition and Prechamber Combustion Systems in a High-Performance Gasoline Direct Injection Engine," *SAE International Journal of Engines*, vol. 15, no. 6, pp. 883–897, Feb. 2022, ISSN: 19463944. DOI: 10.4271/03-15-06-0047.

A

Appendix 1

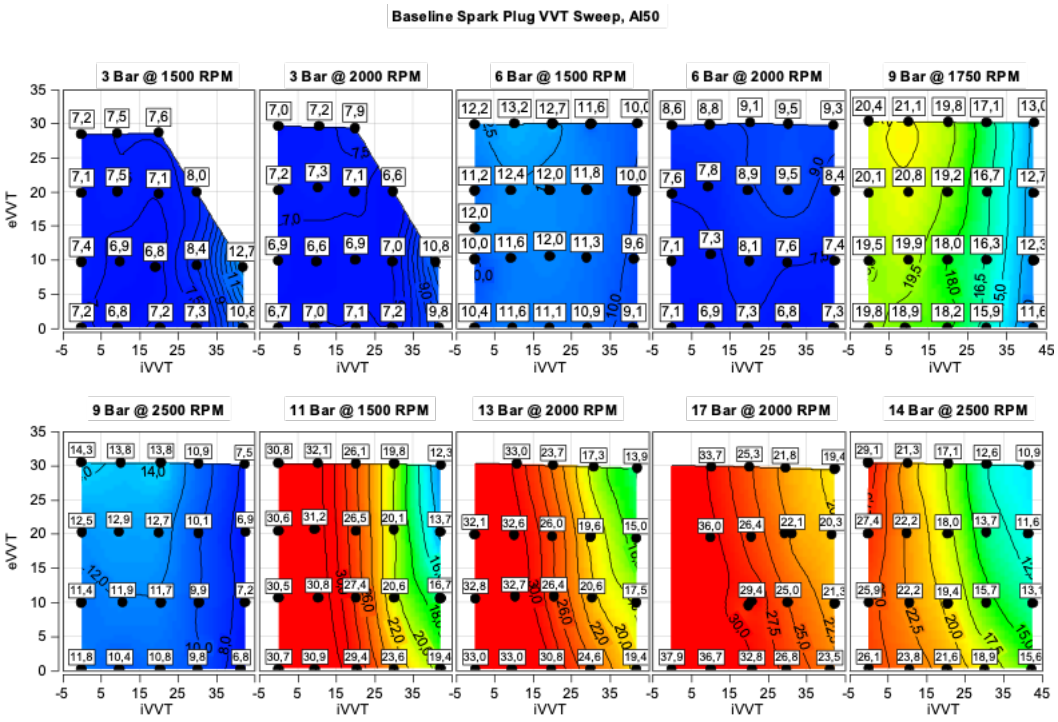

Figure A.1: VVT Sweep for Baseline Spark Plug, AI50 [CAD]

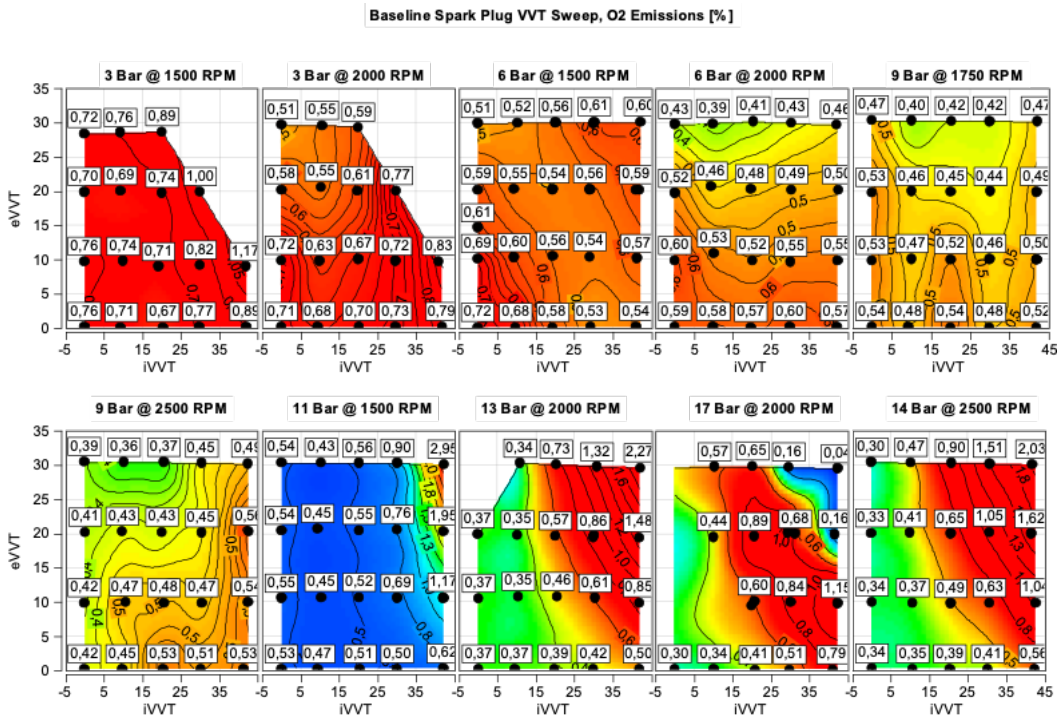

Figure A.2: VVT Sweep for Baseline Spark Plug, $O2$ Emissions [%]

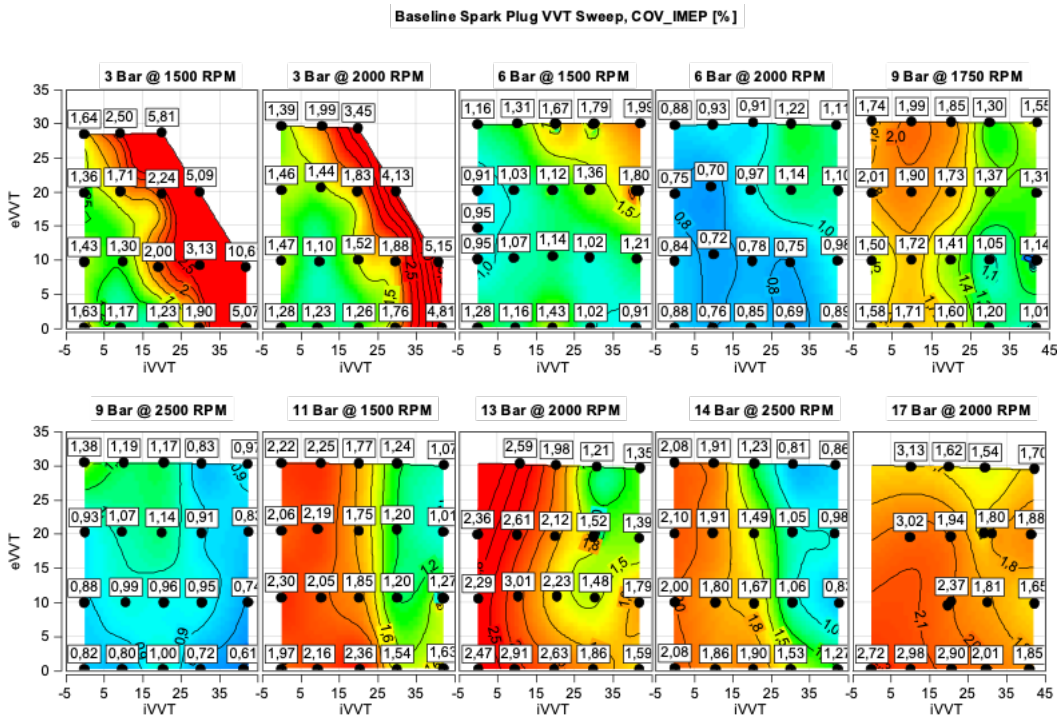

Figure A.3: VVT Sweep for Baseline Spark Plug, CoV_{IMEP} [%]

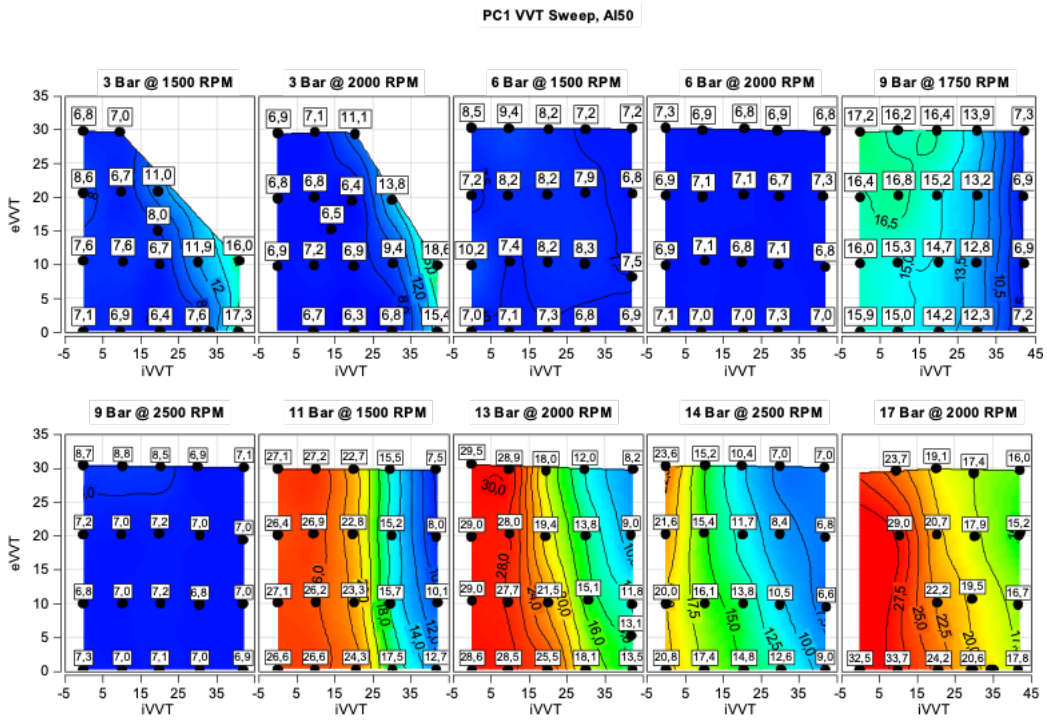

Figure A.4: VVT Sweep for PC1, AI50 [CAD]

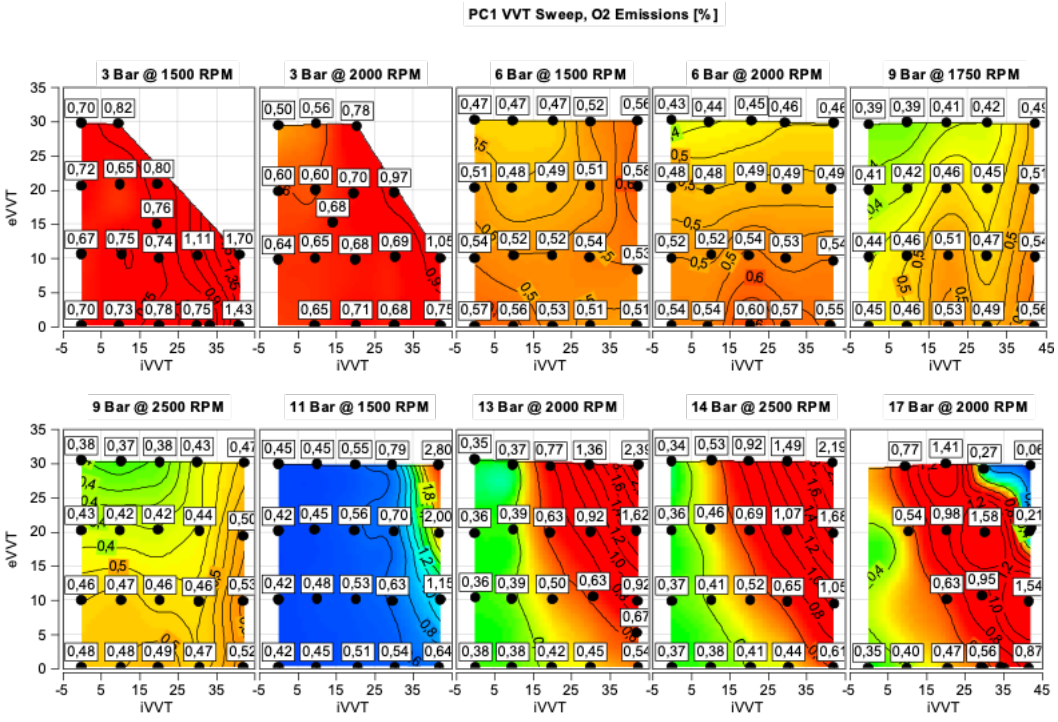

Figure A.5: VVT Sweep for PC1, O_2 Emissions [%]

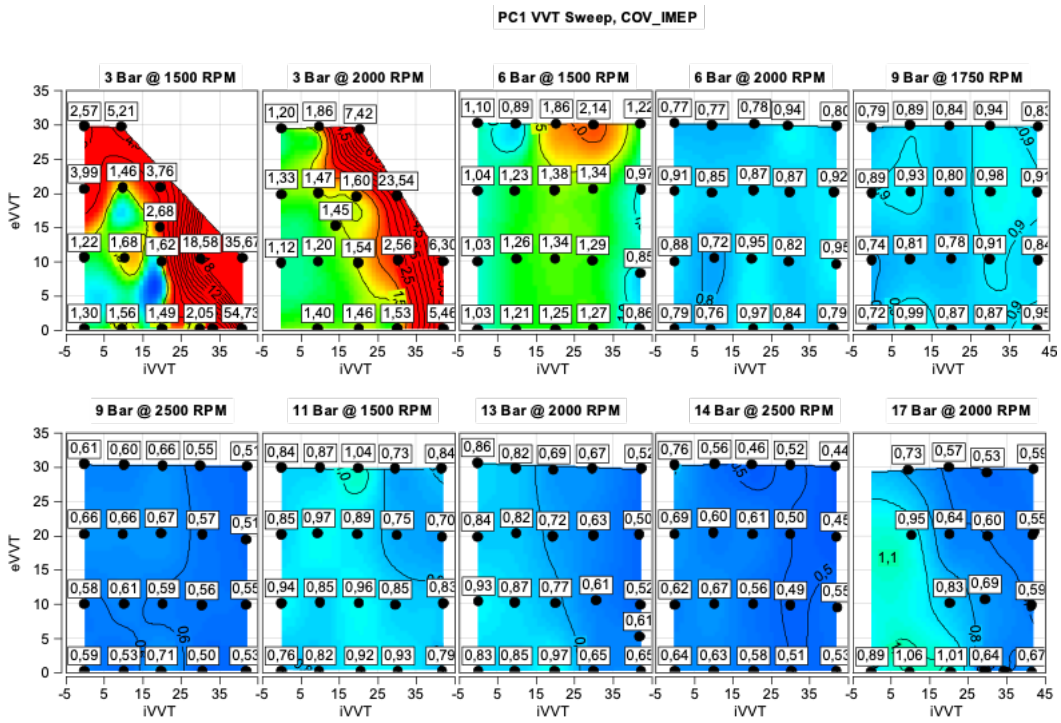

Figure A.6: VVT Sweep for PC1, CoV_{IMEP} [%]

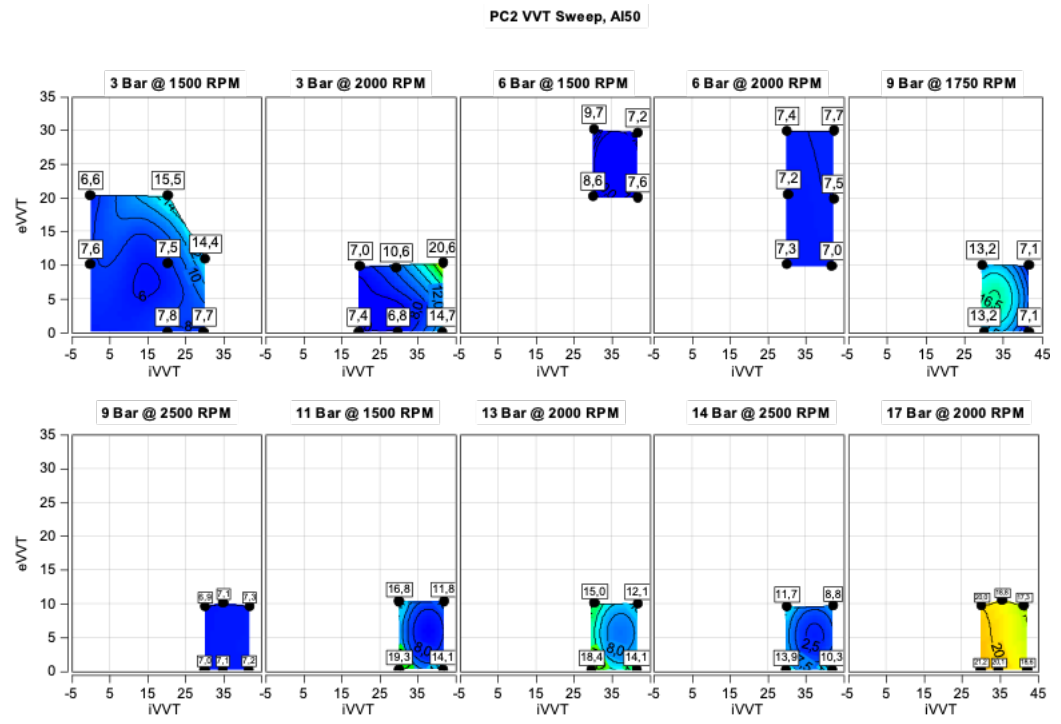

Figure A.7: VVT Sweep for PC2, AI50 [CAD]

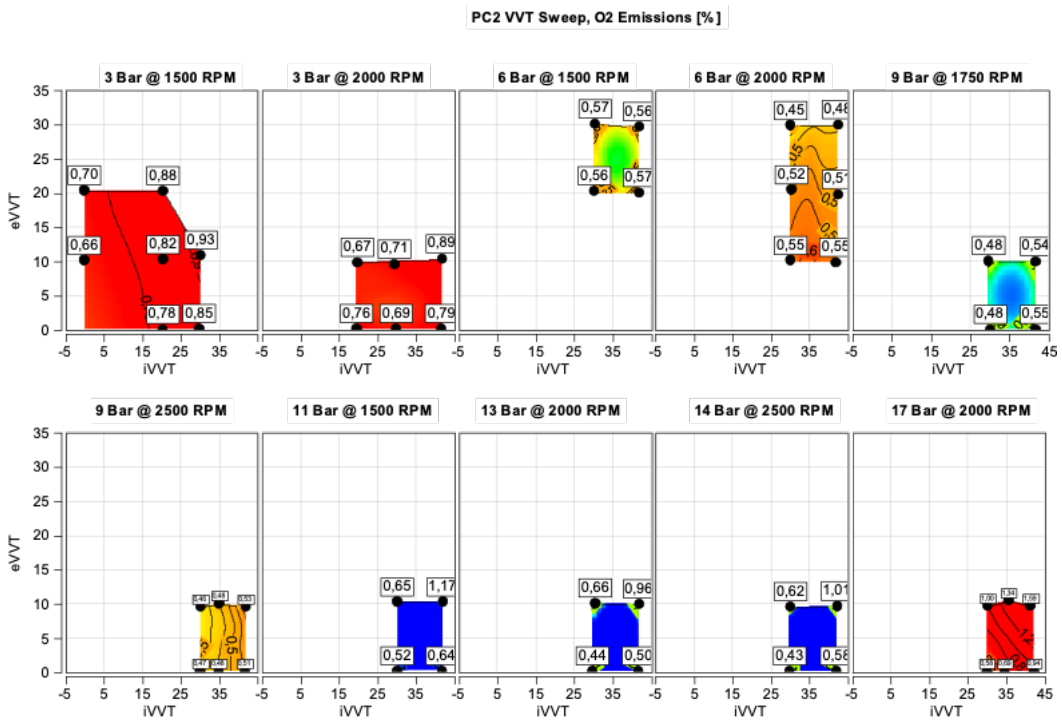

Figure A.8: VVT Sweep for PC2, O_2 Emissions [%]

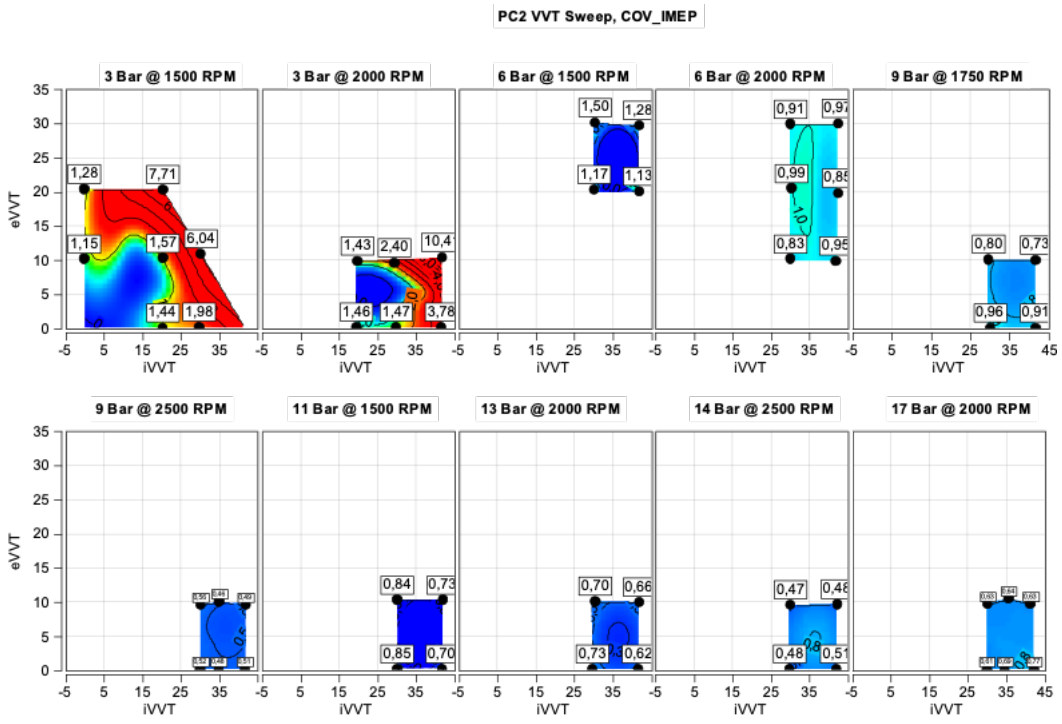

Figure A.9: VVT Sweep for PC2, CoV_{IMEP} [%]

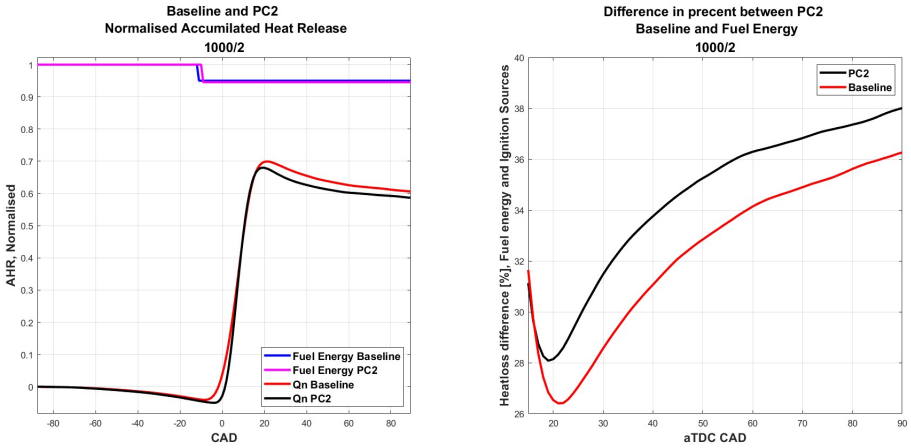

Figure A.10: AHR PC2 and Baseline SP [Right], Wall Heat Losses as Percentage of the Energy Released during Combustion [%] [Left], 2 Bar IMEP @ 1000RPM

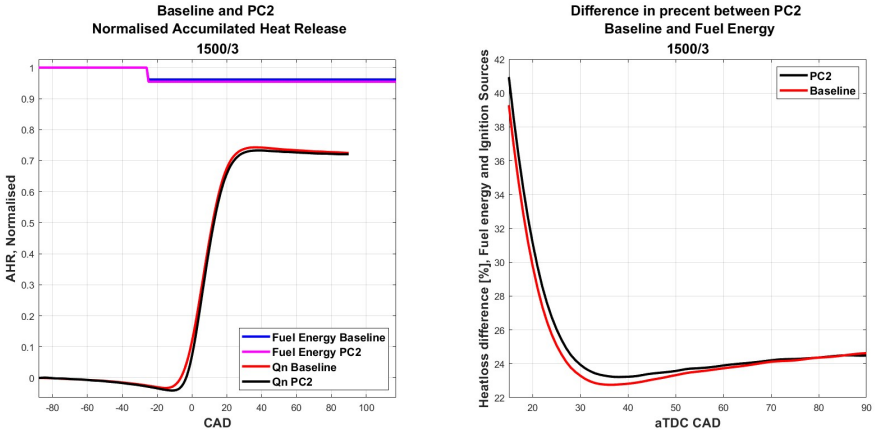

Figure A.11: AHR PC2 and Baseline SP [Right], Wall Heat Losses as Percentage of the Energy Released during Combustion [%] [Left], 3 Bar IMEP @ 1500RPM

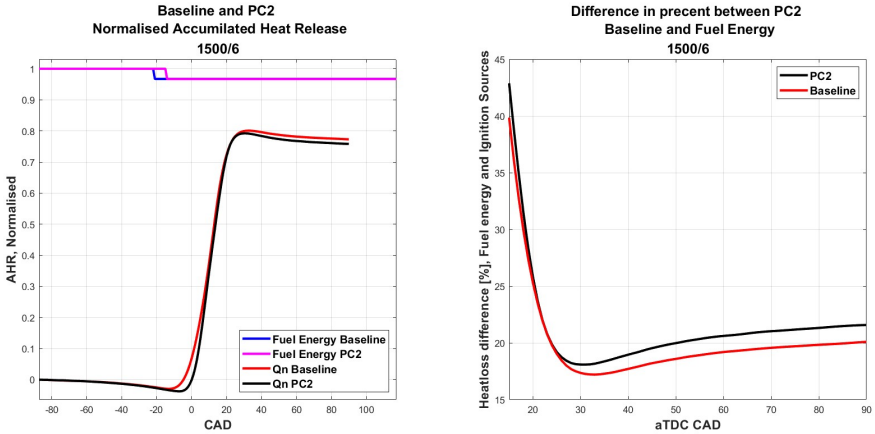

Figure A.12: AHR PC2 and Baseline SP [Right], Wall Heat Losses as Percentage of the Energy Released during Combustion [%] [Left], 6 Bar IMEP @ 1500RPM

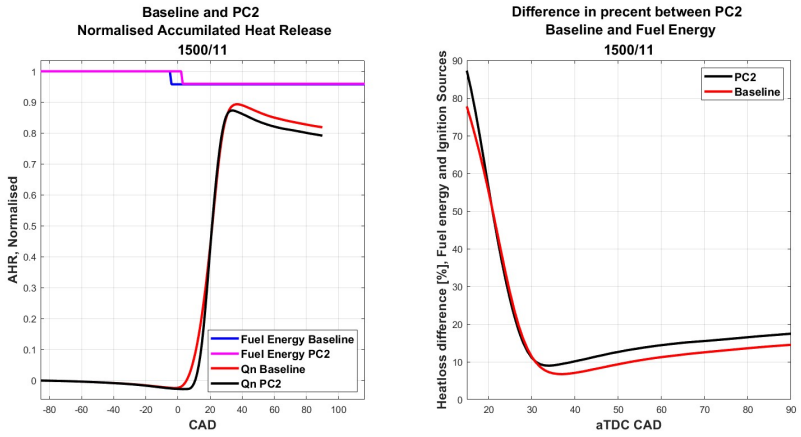

Figure A.13: AHR PC2 and Baseline SP [Right], Wall Heat Losses as Percentage of the Energy Released during Combustion [%] [Left], 11 Bar IMEP @ 1500RPM

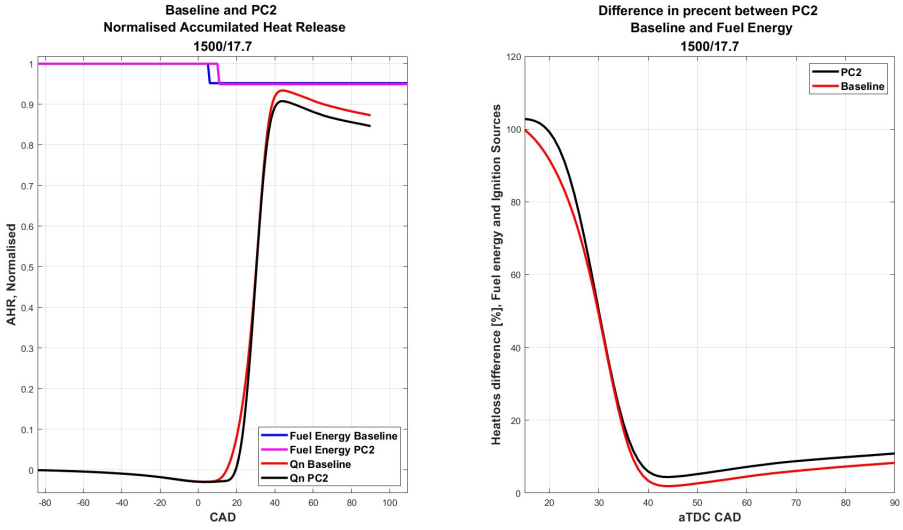

Figure A.14: AHR PC2 and Baseline SP [Right], Wall Heat Losses as Percentage of the Energy Released during Combustion [%] [Left], 17.7 Bar IMEP @ 1500RPM

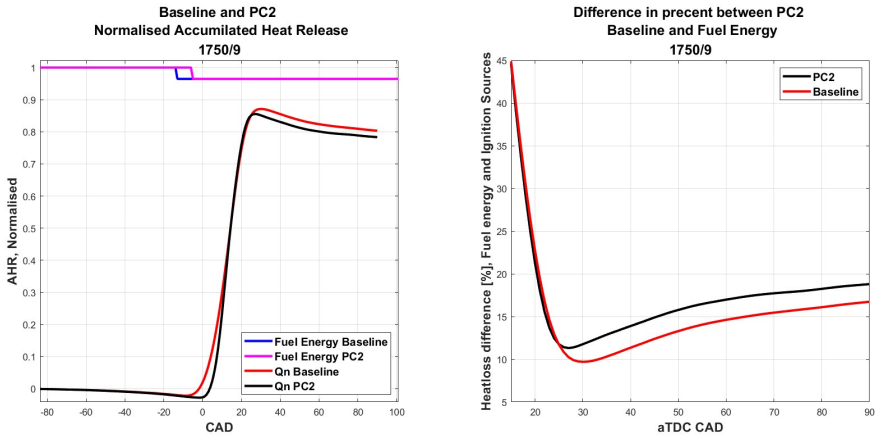

Figure A.15: AHR PC2 and Baseline SP [Right], Wall Heat Losses as Percentage of the Energy Released during Combustion [%] [Left], 9 Bar IMEP @ 1750RPM

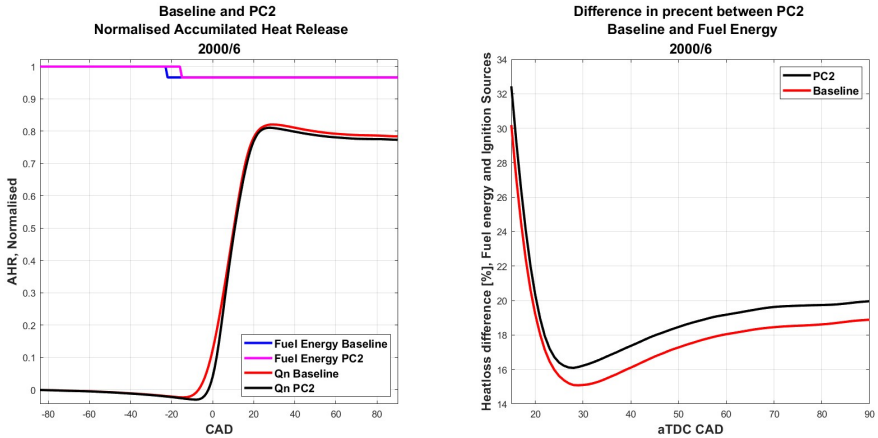

Figure A.16: AHR PC2 and Baseline SP [Right], Wall Heat Losses as Percentage of the Energy Released during Combustion [%] [Left], 6 Bar IMEP @ 2000RPM

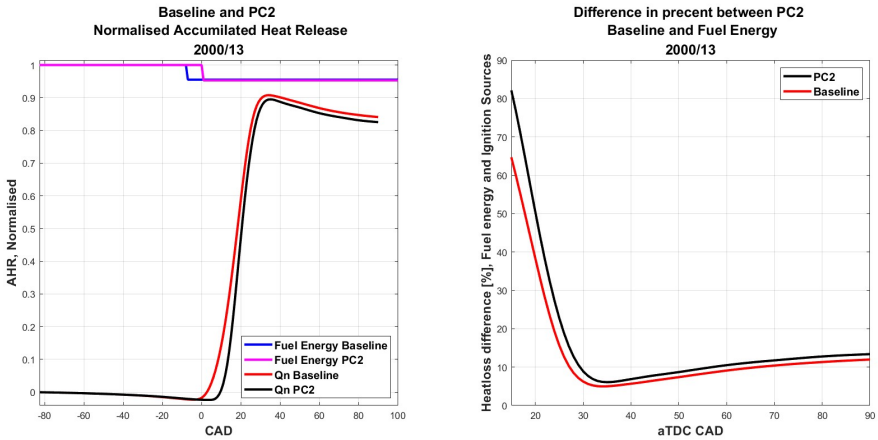

Figure A.17: AHR PC2 and Baseline SP [Right], Wall Heat Losses as Percentage of the Energy Released during Combustion [%] [Left], 13 Bar IMEP @ 2000RPM

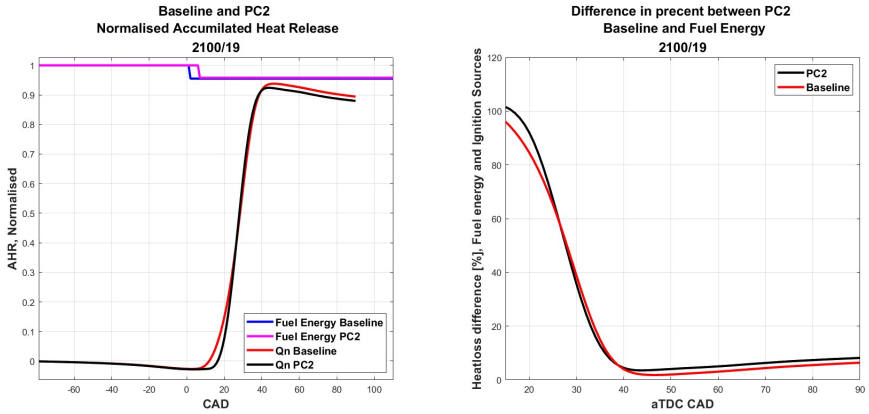

Figure A.18: AHR PC2 and Baseline SP [Right], Wall Heat Losses as Percentage of the Energy Released during Combustion [%] [Left], 19 Bar IMEP @ 2100RPM

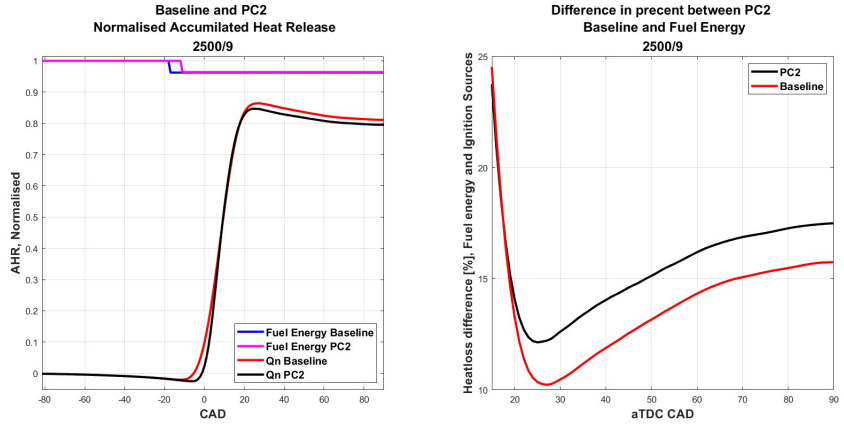

Figure A.19: AHR PC2 and Baseline SP [Right], Wall Heat Losses as Percentage of the Energy Released during Combustion [%] [Left], 9 Bar IMEP @ 2500RPM

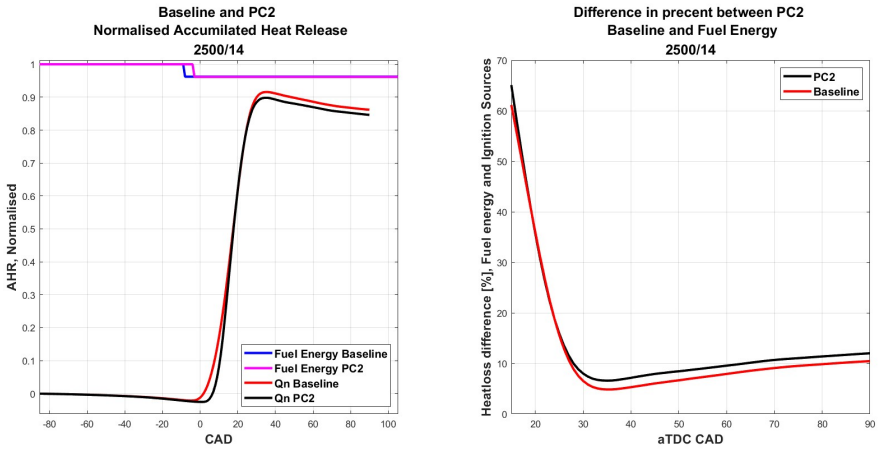

Figure A.20: AHR PC2 and Baseline SP [Right], Wall Heat Losses as Percentage of the Energy Released during Combustion [%] [Left], 14 Bar IMEP @ 2500RPM

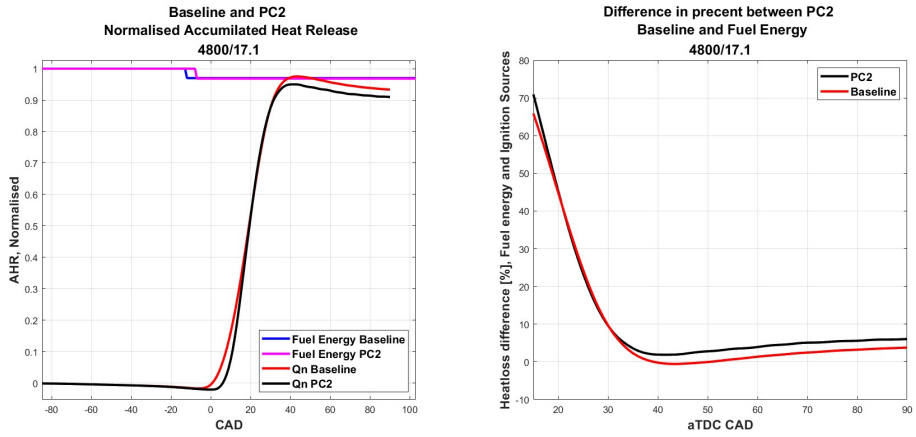

Figure A.21: AHR PC2 and Baseline SP [Right], Wall Heat Losses as Percentage of the Energy Released during Combustion [%] [Left], 17.1 Bar IMEP @ 4800RPM

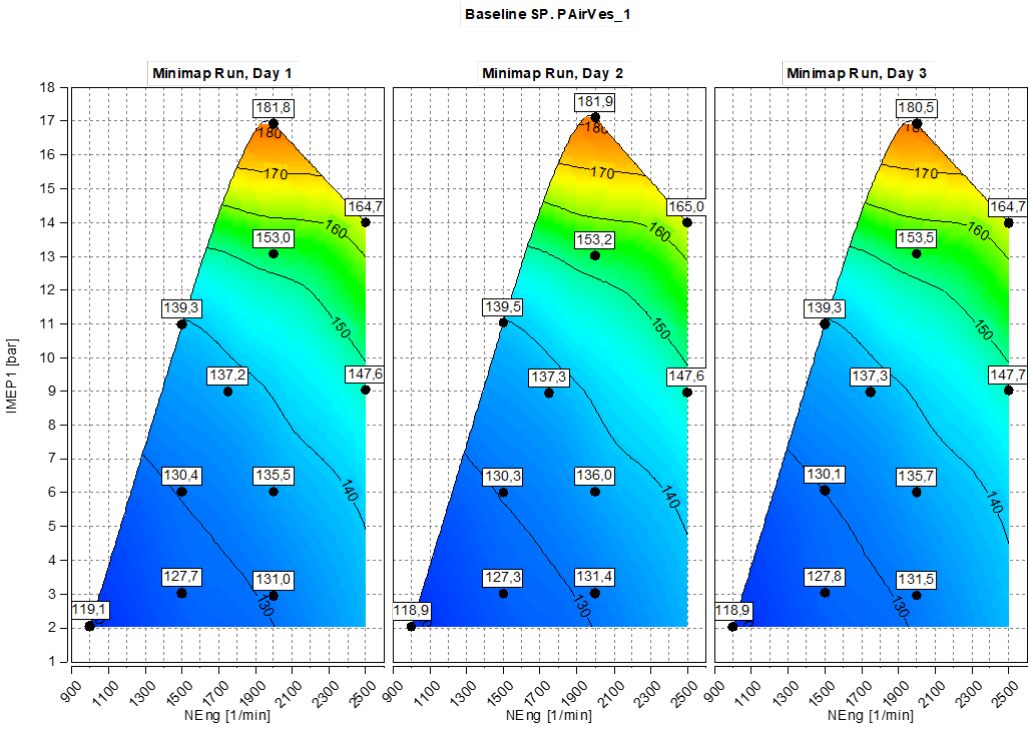

Figure A.22: Baseline Intake Pressure, Vessel Bank 1 [kPa]

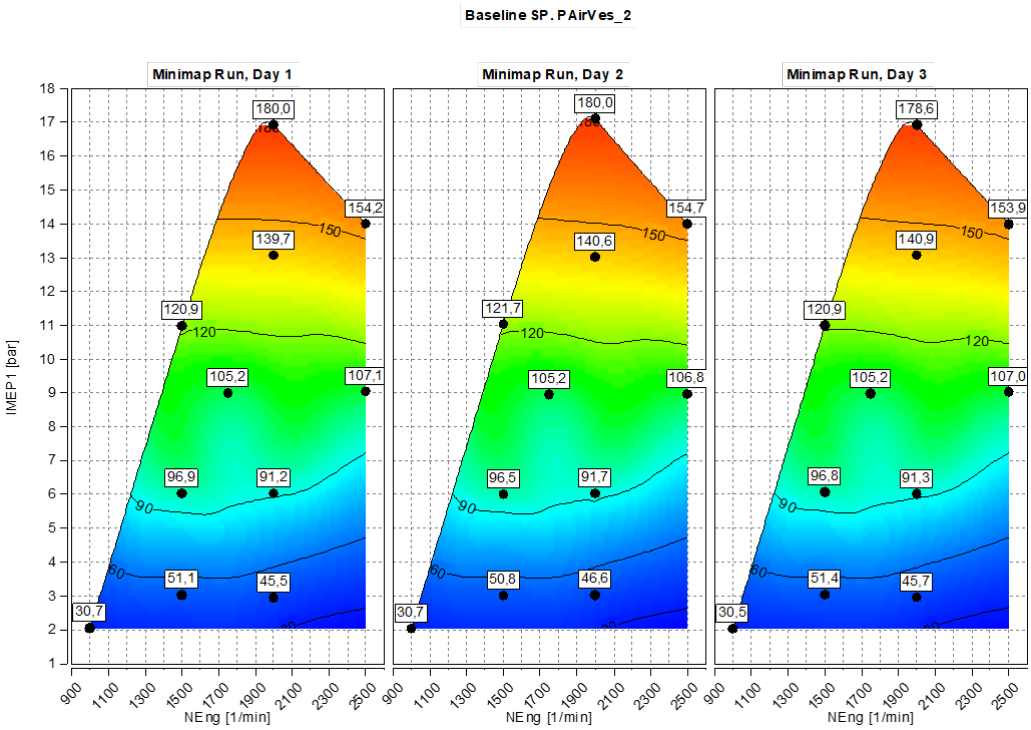

Figure A.23: Baseline Intake Pressure, [kPa]

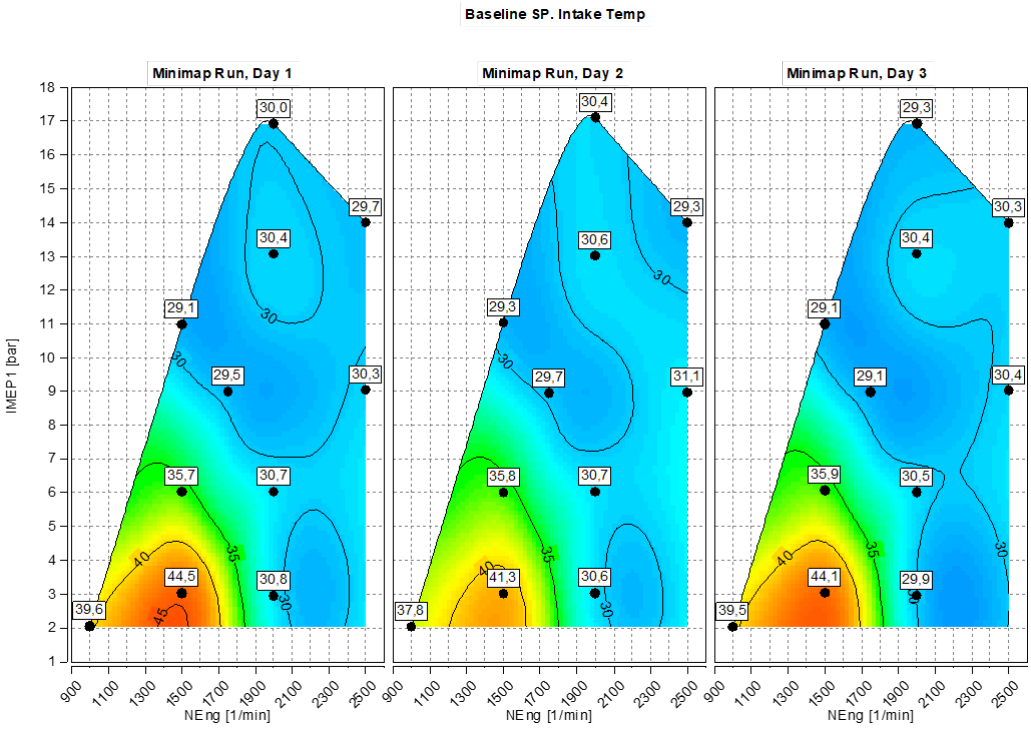

Figure A.24: Baseline Intake Temperature, [°C]

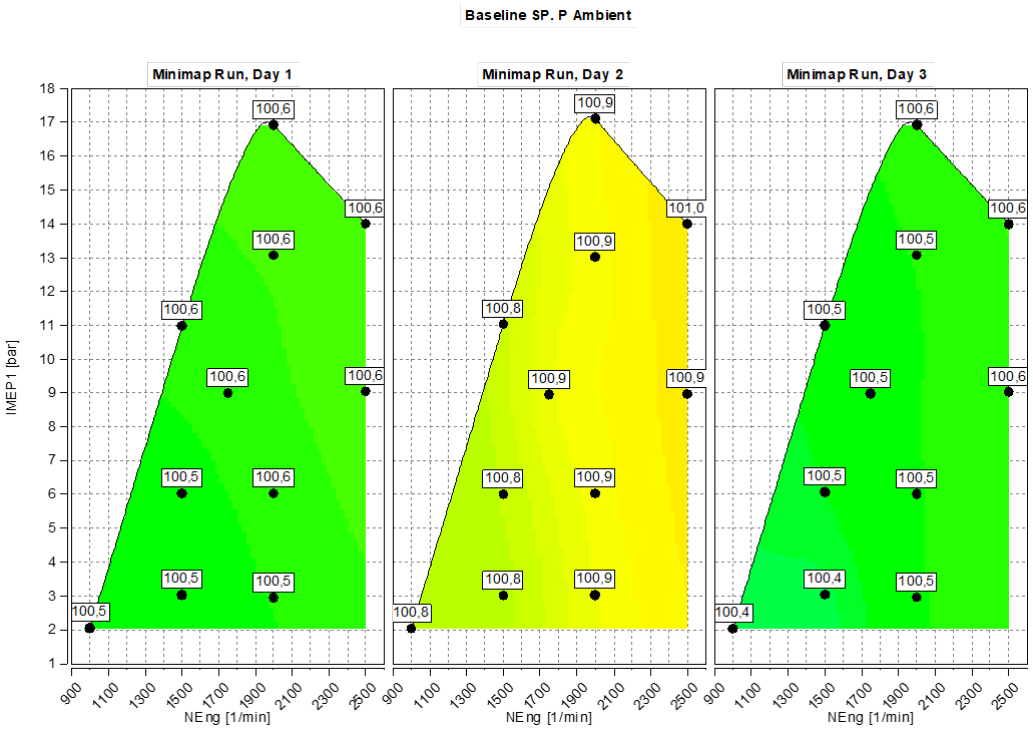

Figure A.25: Baseline Ambient Pressure, [kPa]

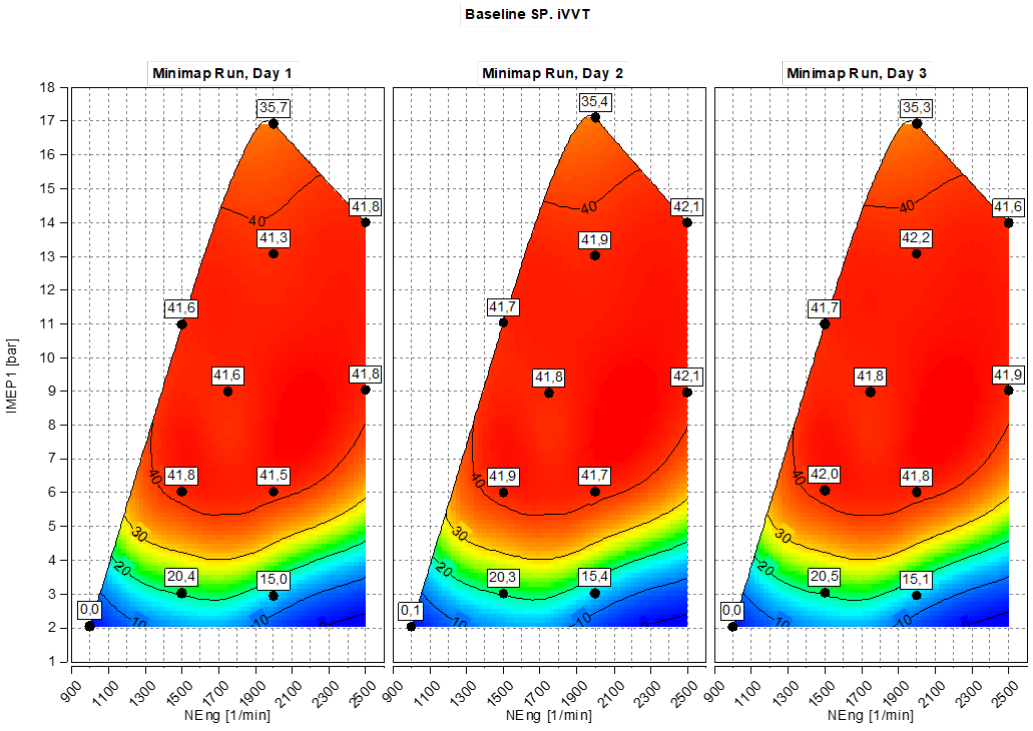

Figure A.26: Baseline iVVT

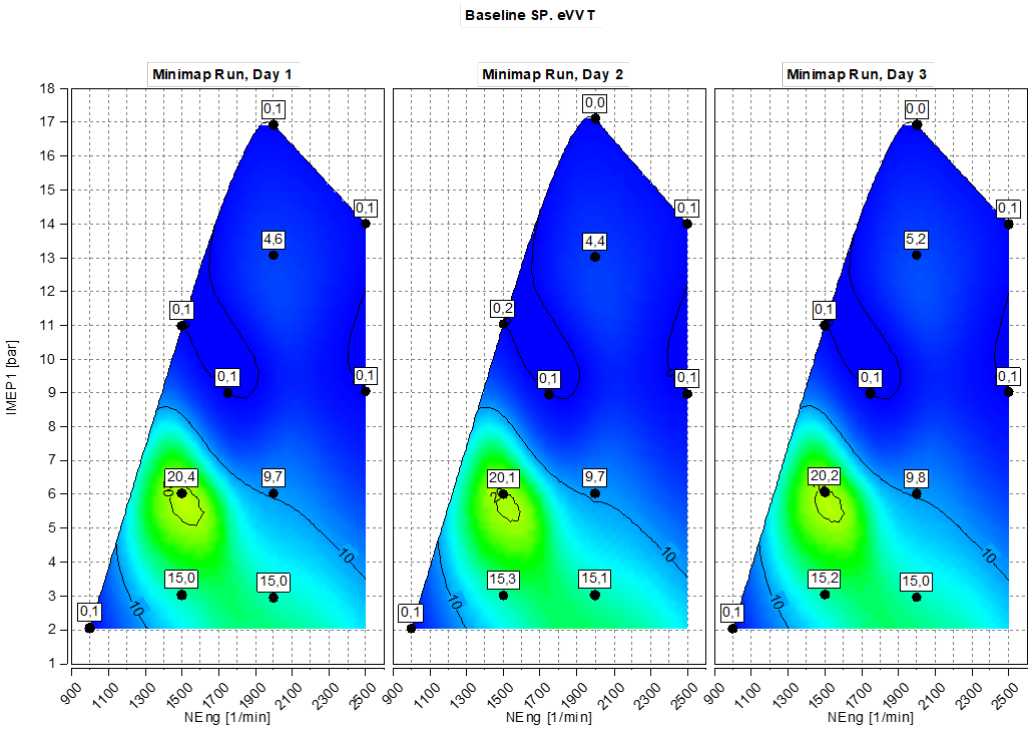

Figure A.27: Baseline eVVT

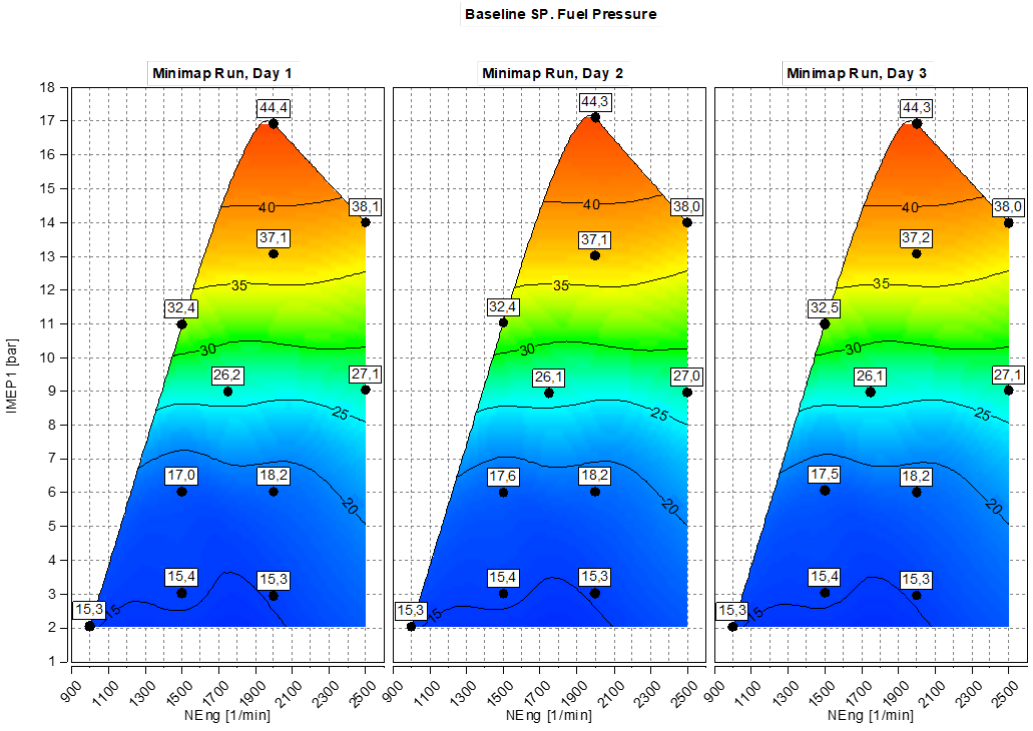

Figure A.28: Baseline Fuel Pressure,[MPa]

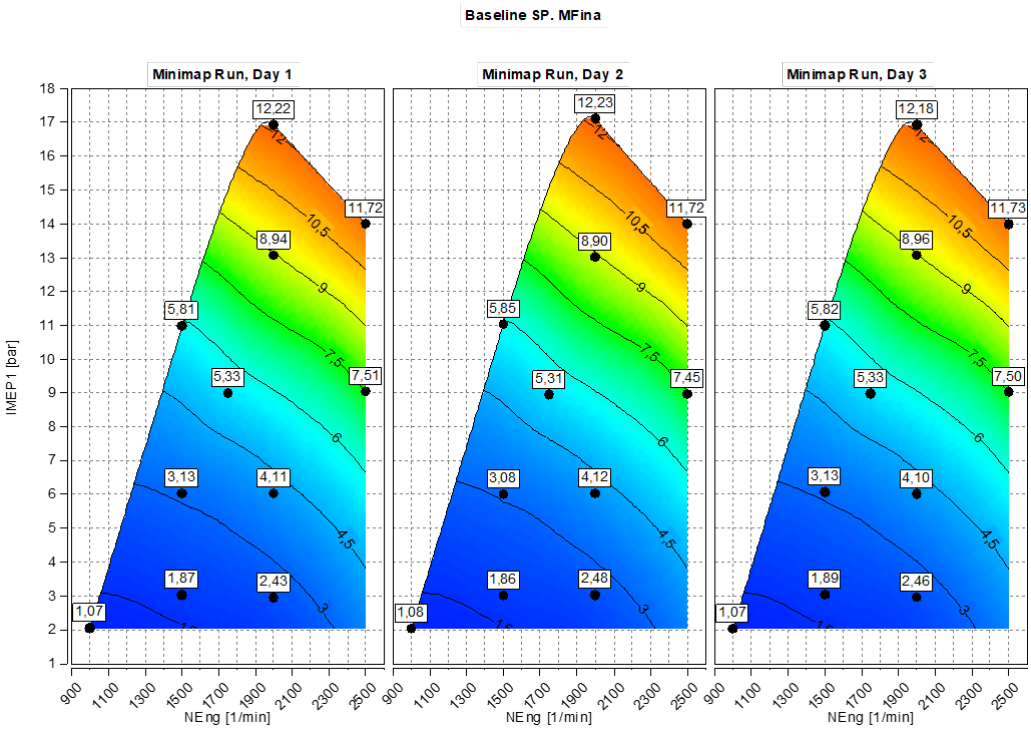

Figure A.29: Baseline Intake Massflow, [g/s]

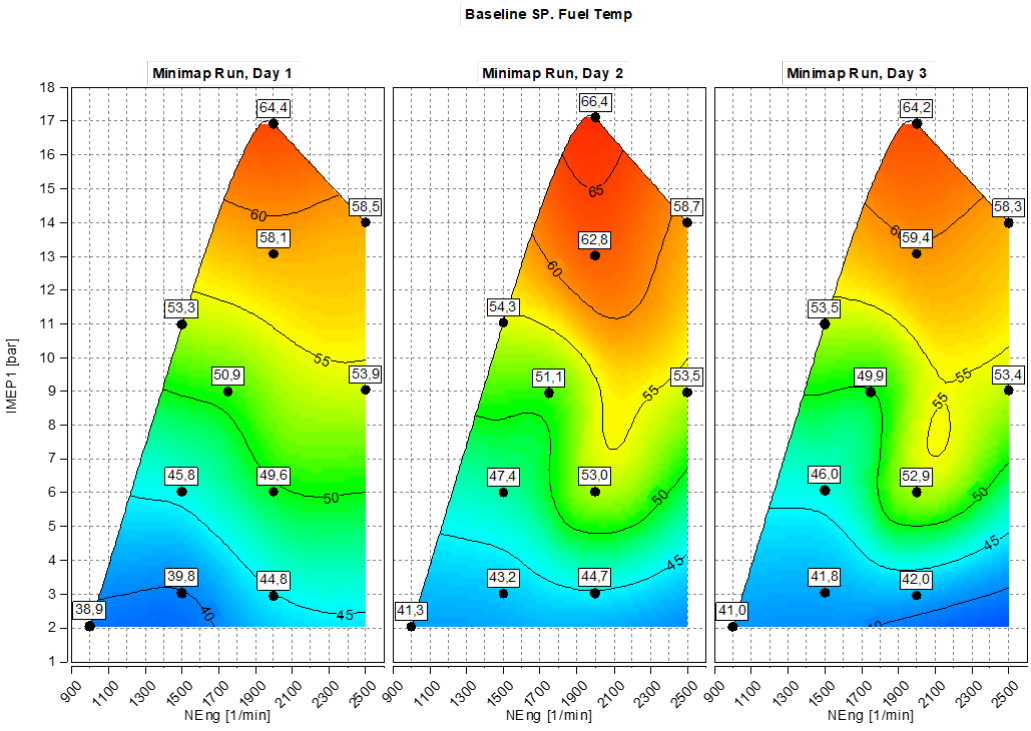

Figure A.30: Baseline Fuel Temperature, [°C]

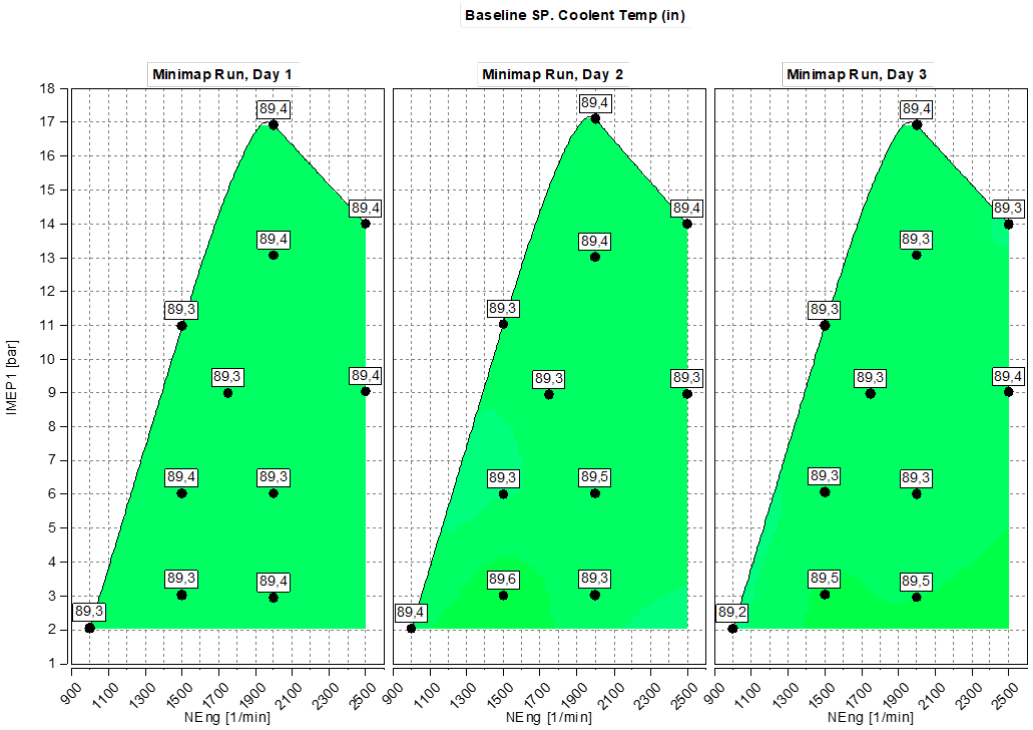

Figure A.31: Baseline Coolant Temperature, [°C]

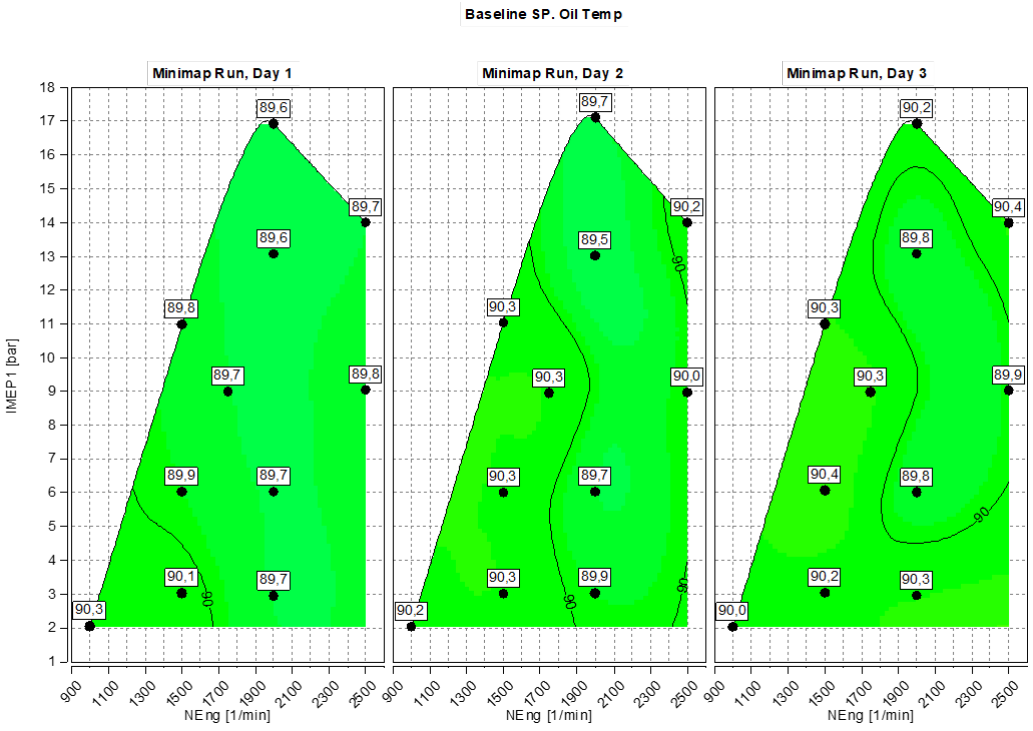

Figure A.32: Baseline Oil Temperature, [°C]

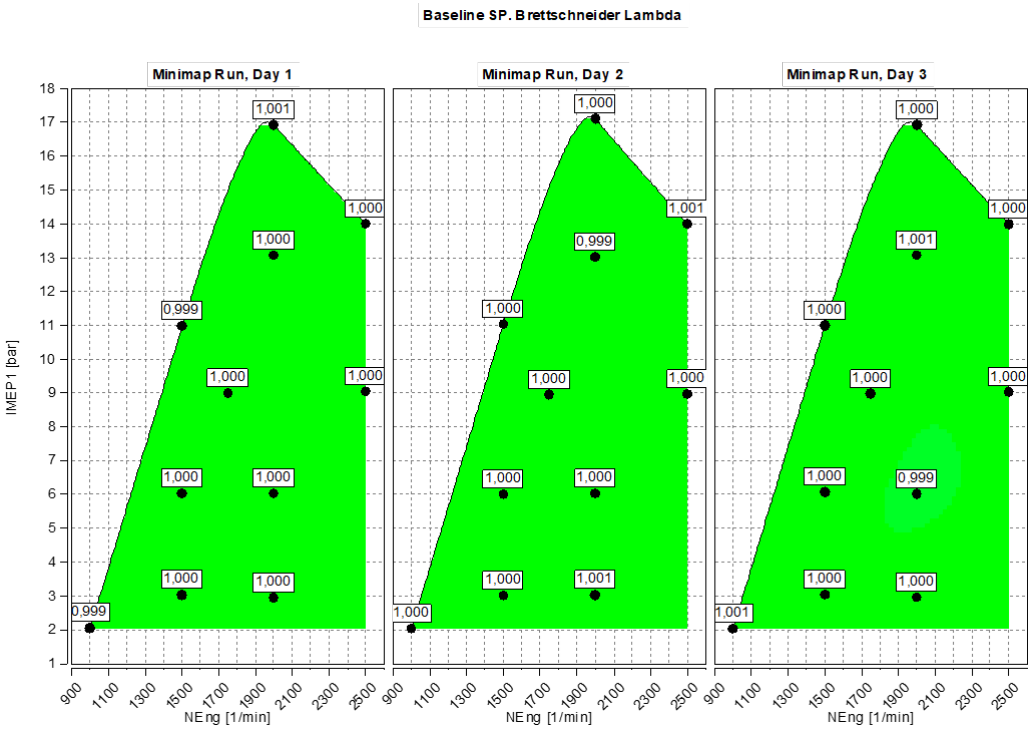

Figure A.33: Baseline Lambda Brettschneider

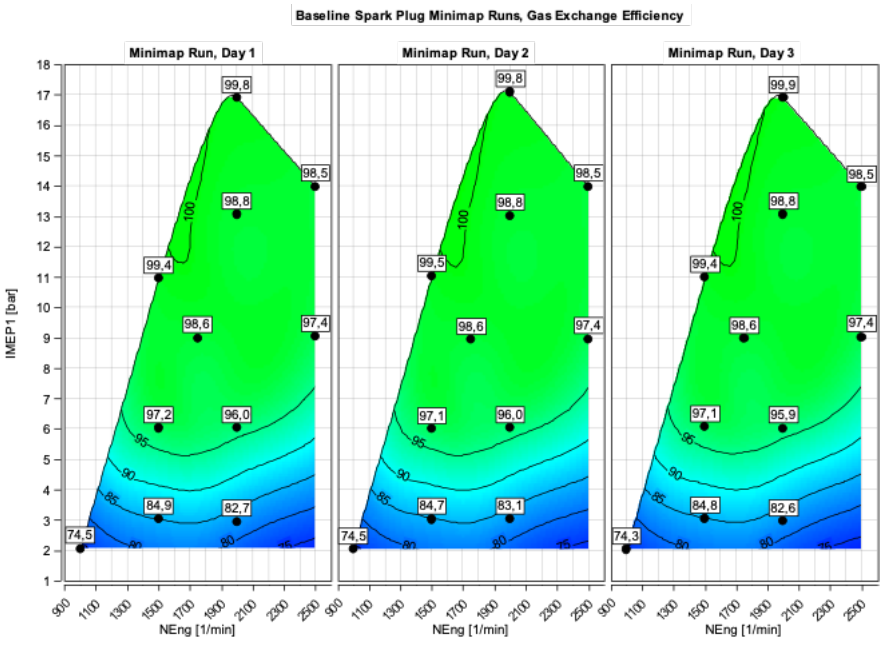

Figure A.34: Baseline Gas Exchange Efficiency [%]

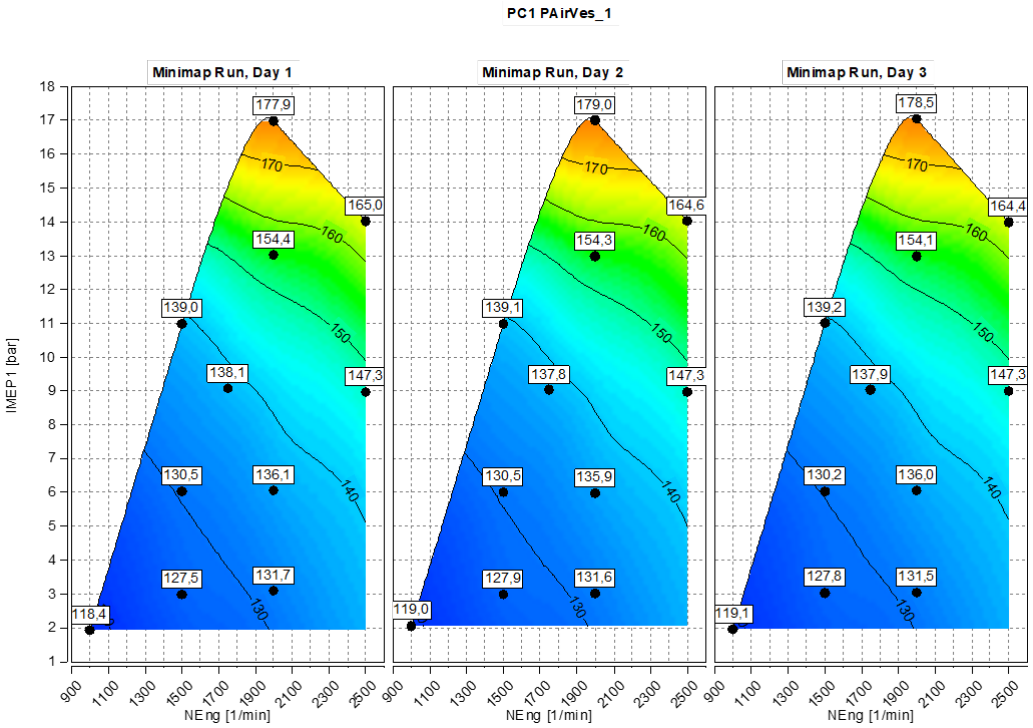

Figure A.35: PC1 Intake Pressure, Vessel Bank 1 [kPa]

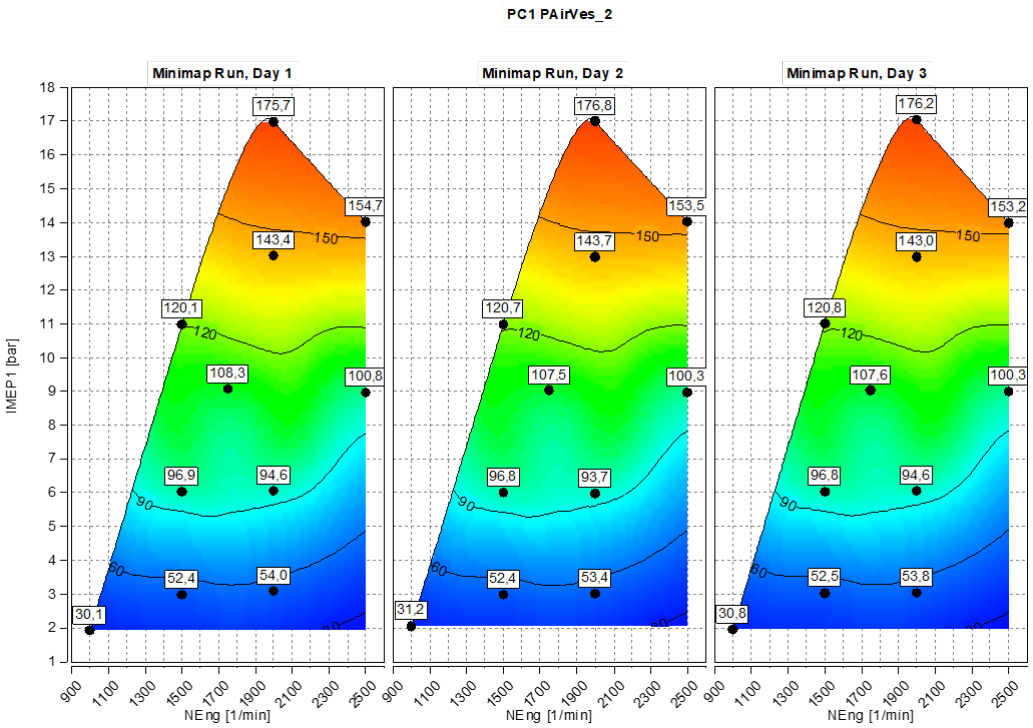

Figure A.36: PC1 Intake Pressure, [kPa]

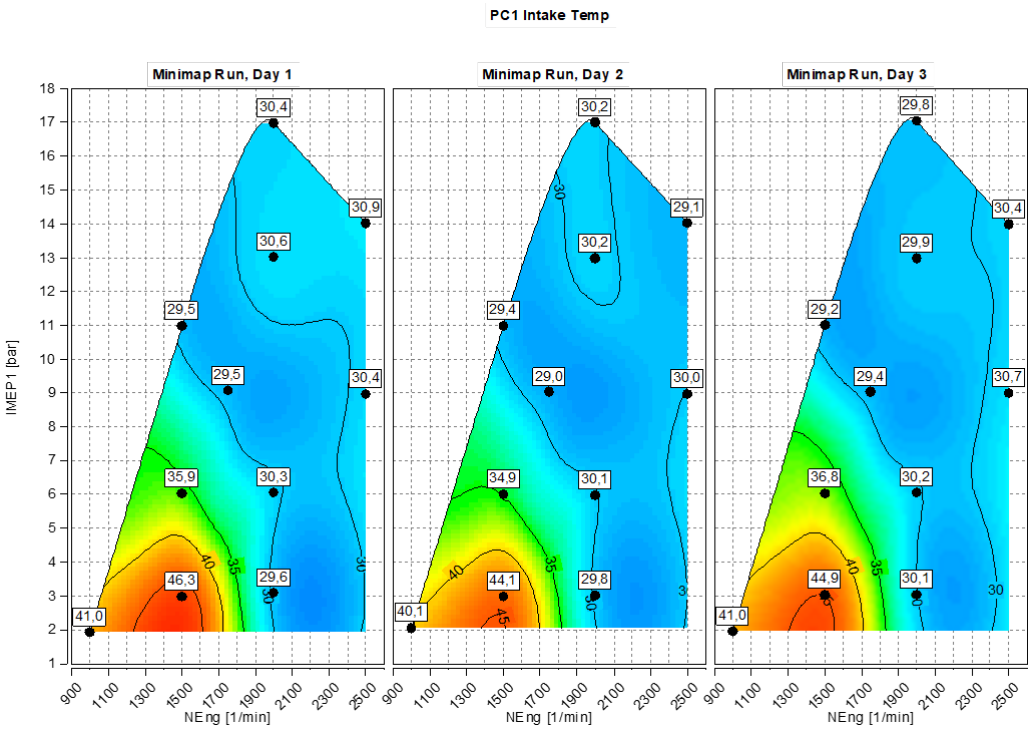

Figure A.37: PC1 Intake Temperature, [°C]

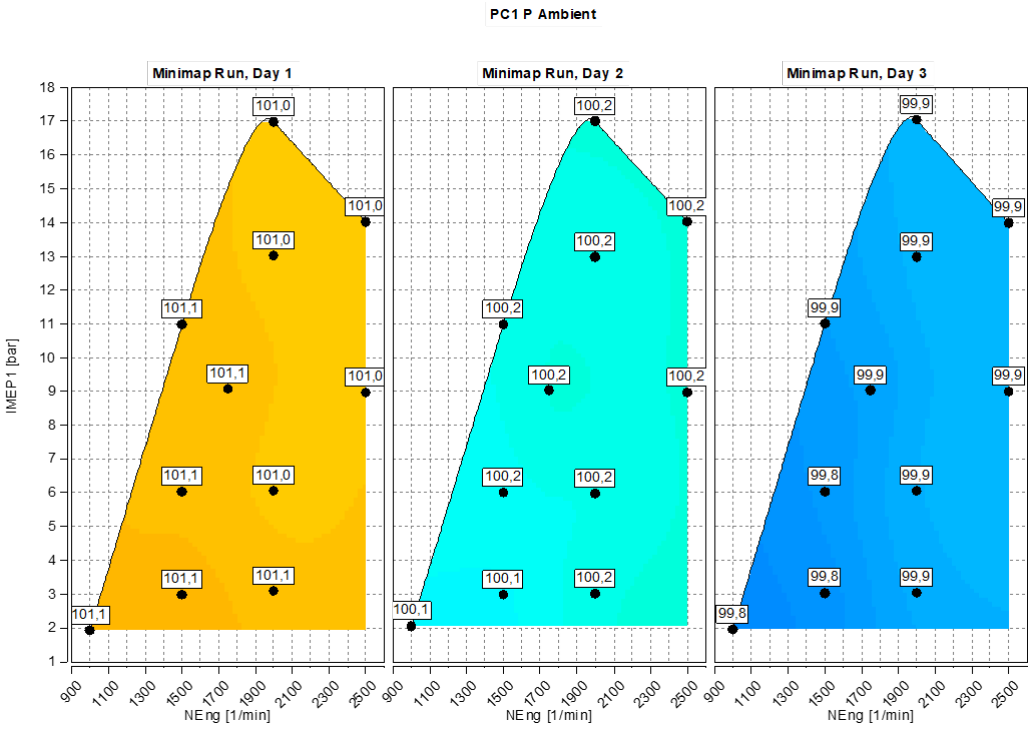

Figure A.38: PC1 Ambient Pressure, [kPa]

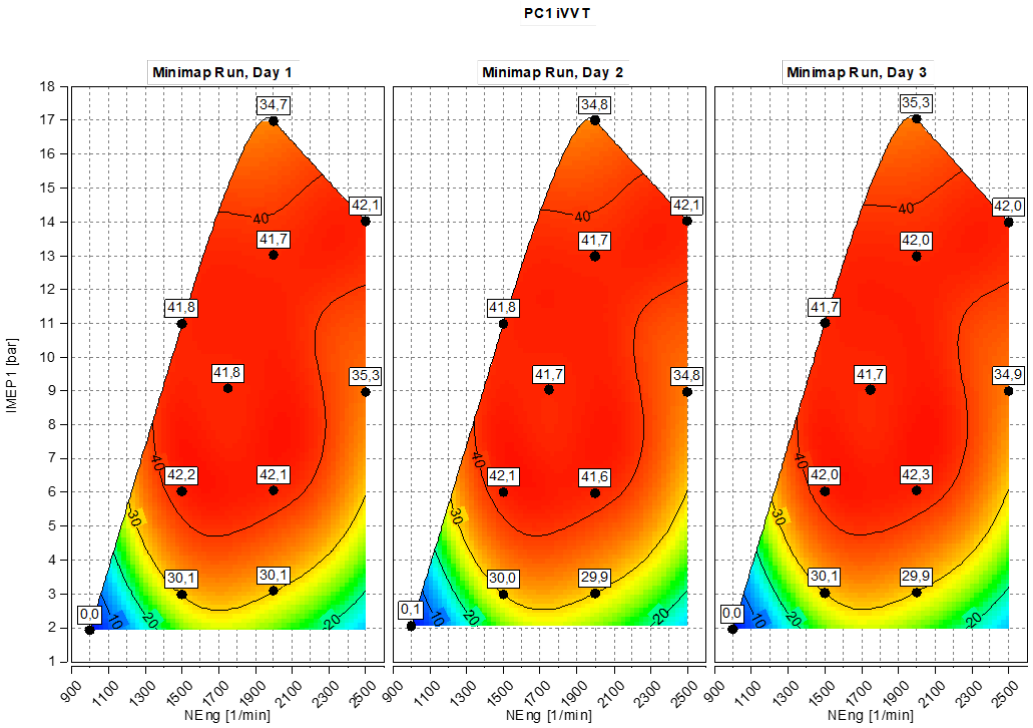

Figure A.39: PC1 iVVT

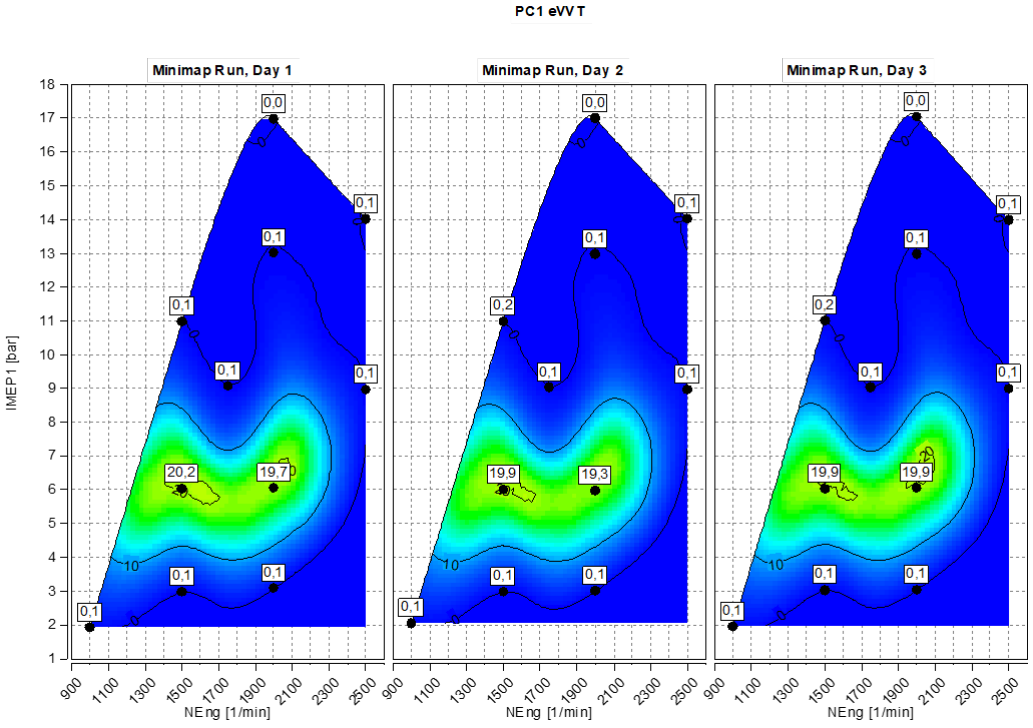

Figure A.40: PC1 eVVT

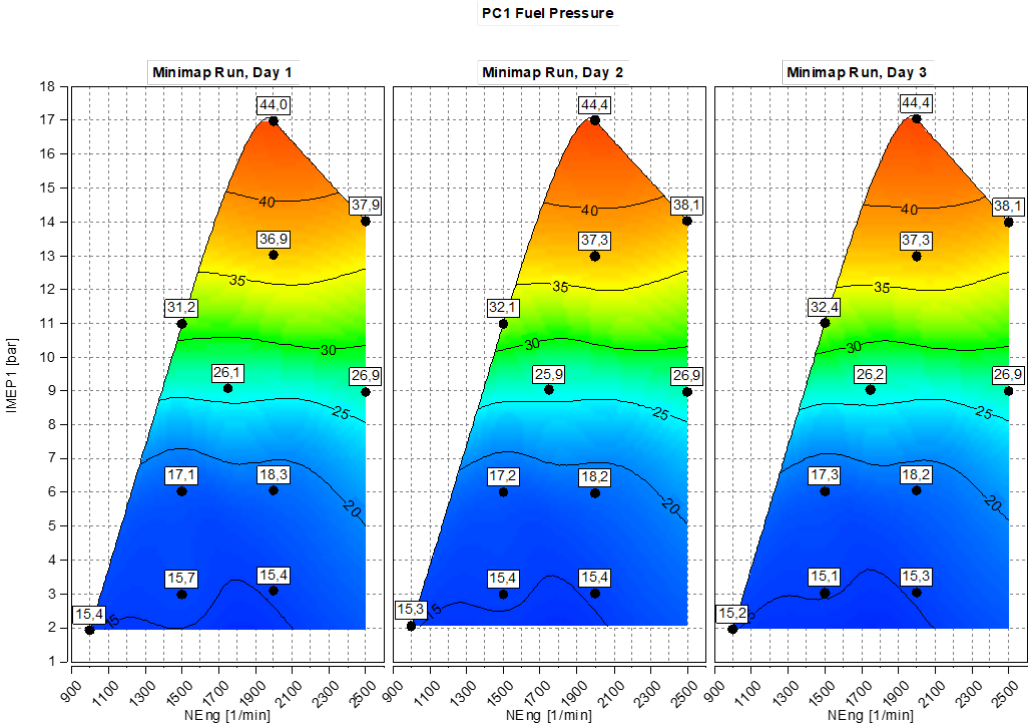

Figure A.41: PC1 Fuel Pressure,[MPa]

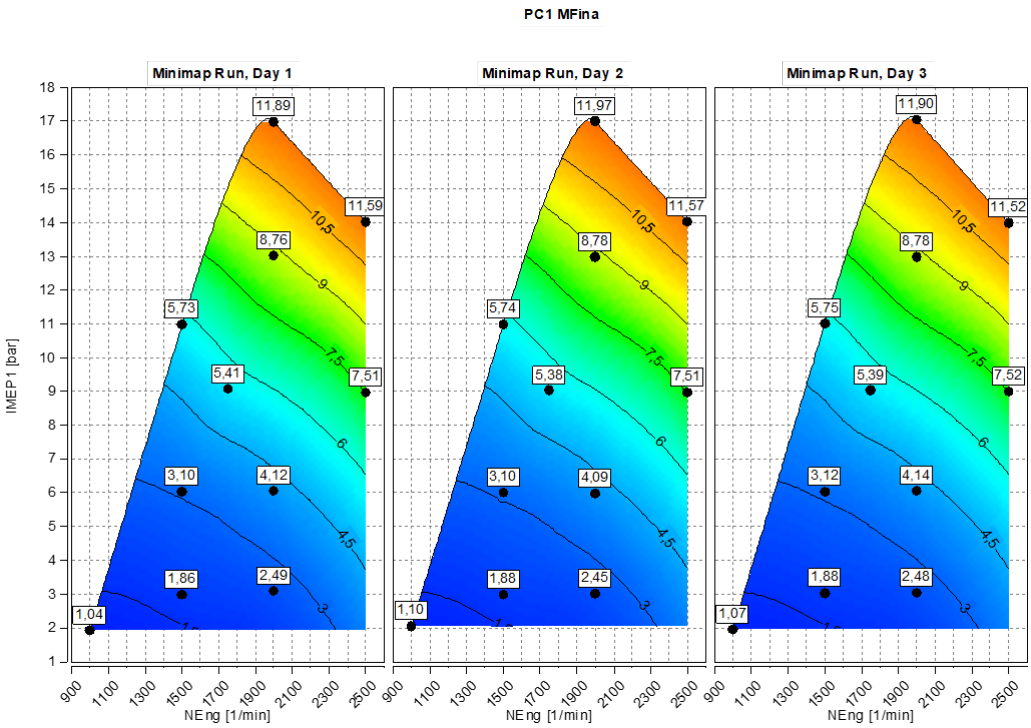

Figure A.42: PC1 Intake Massflow, [g/s]

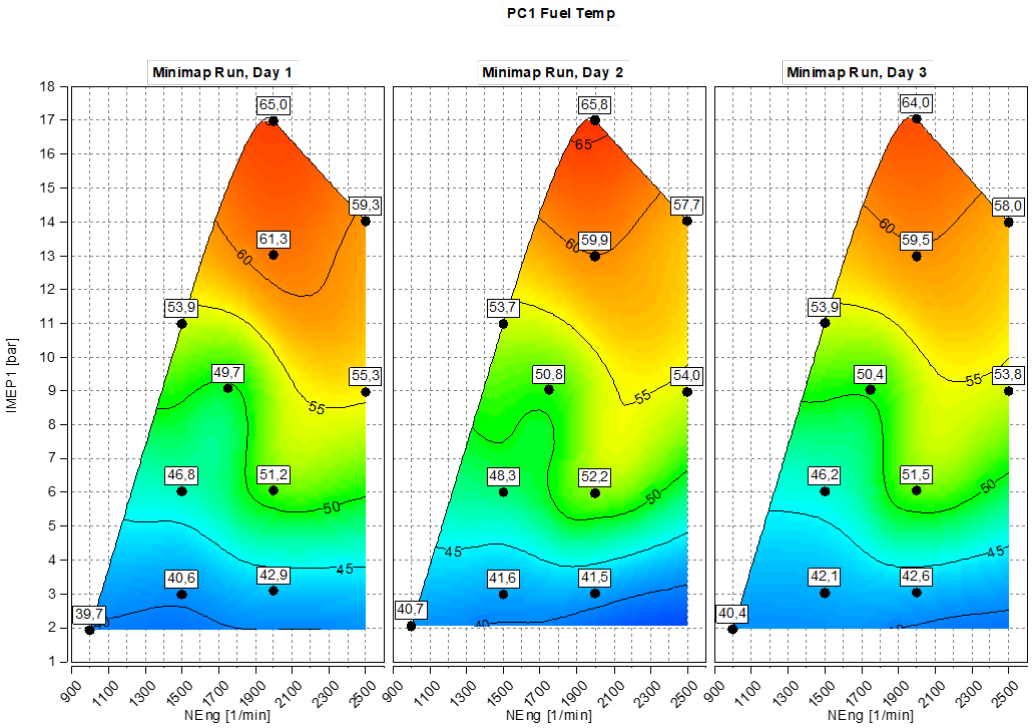

Figure A.43: PC1 Fuel Temperature, [°C]

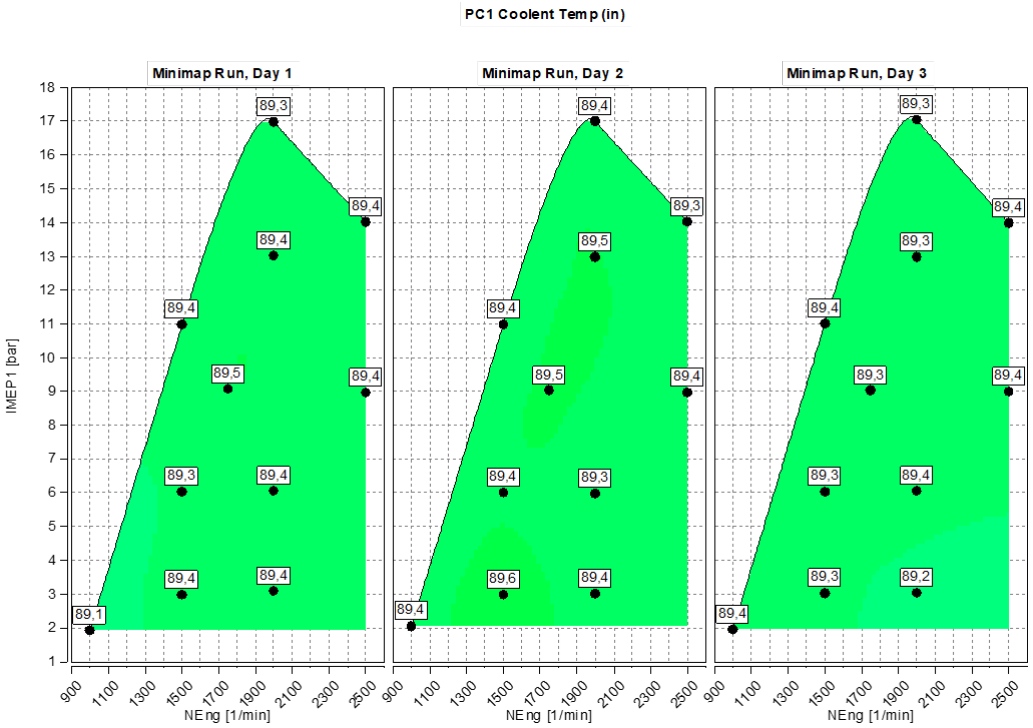

Figure A.44: PC1 Coolant Temperature, [°C]

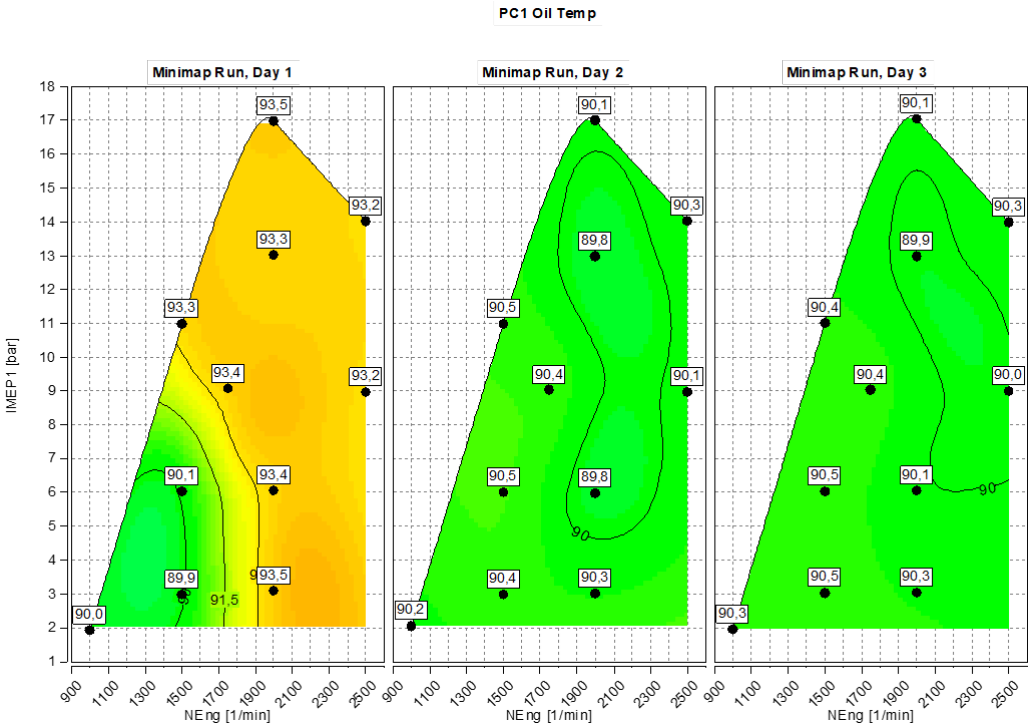

Figure A.45: PC1 Oil Temperature, [°C]

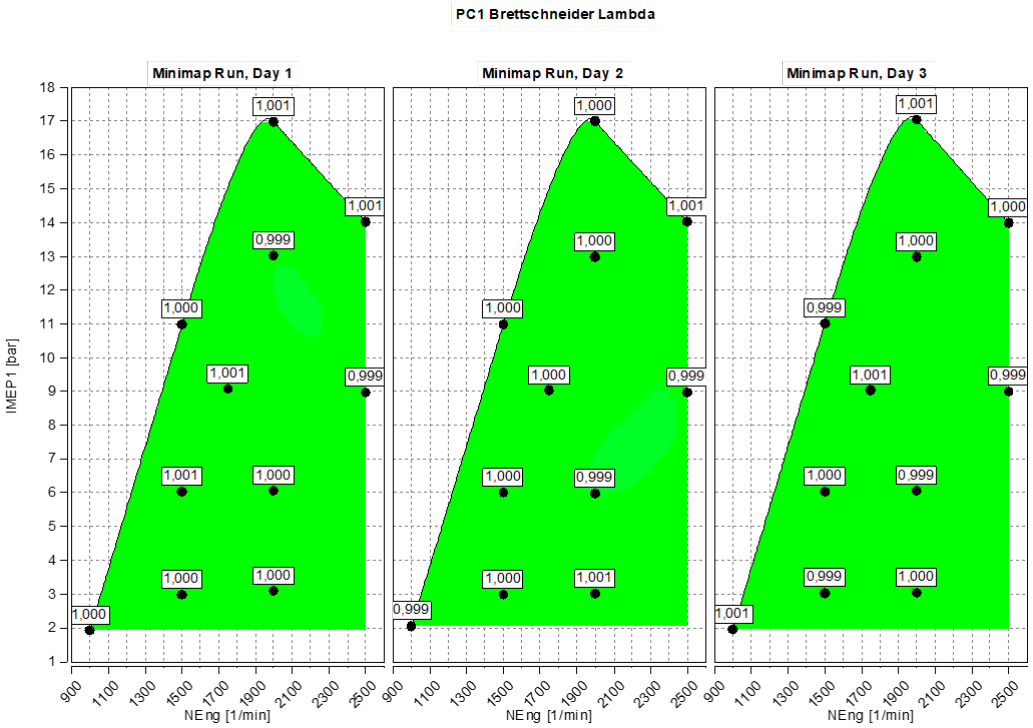

Figure A.46: PC1 Lambda Brettschneider

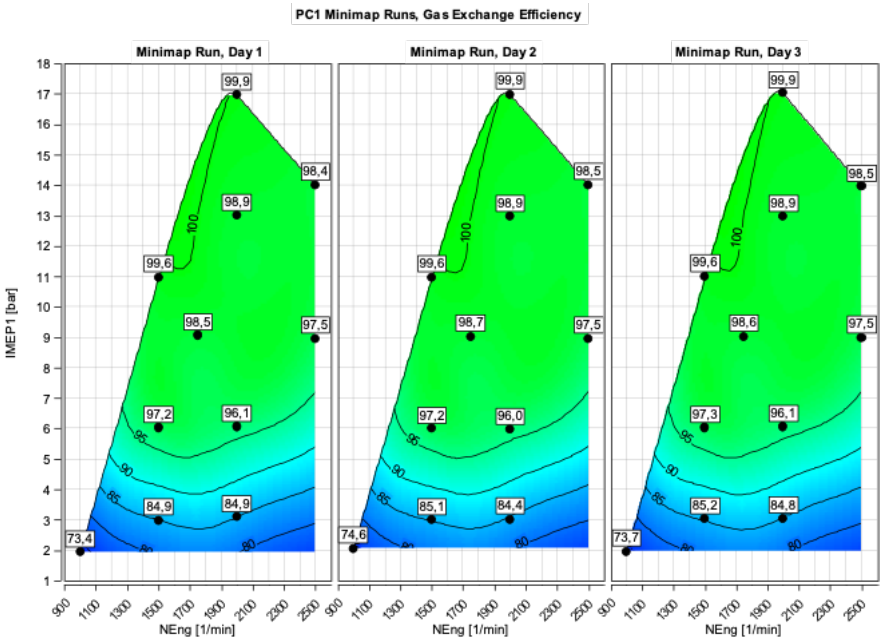

Figure A.47: PC1 Gas Exchange Efficiency [%]

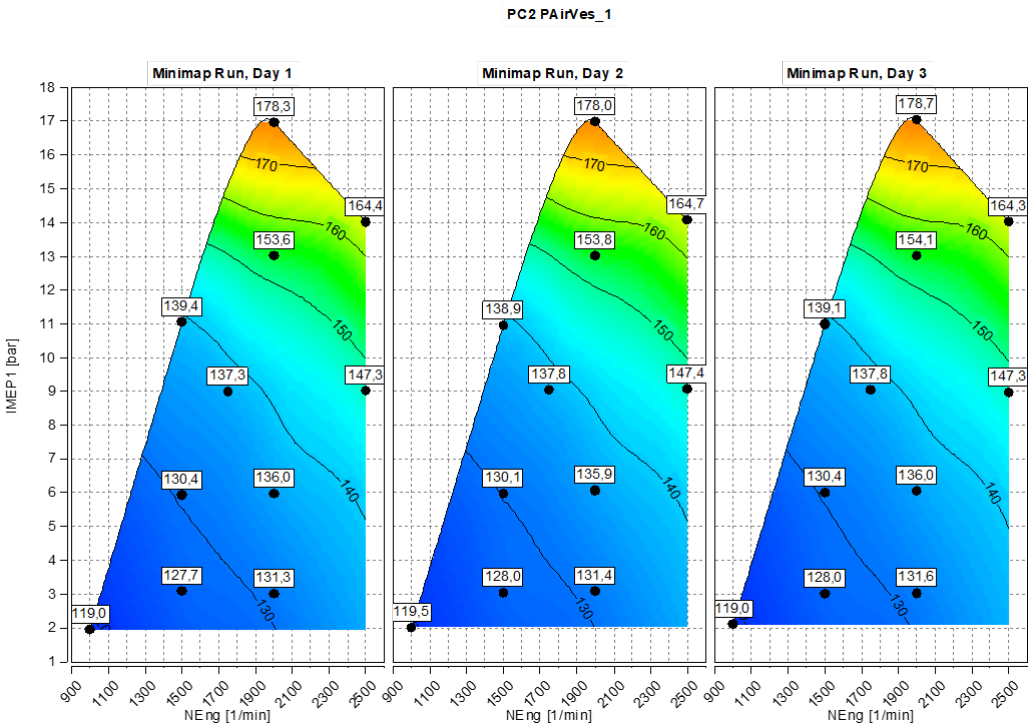

Figure A.48: PC2 Intake Pressure, Vessel Bank 1 [kPa]

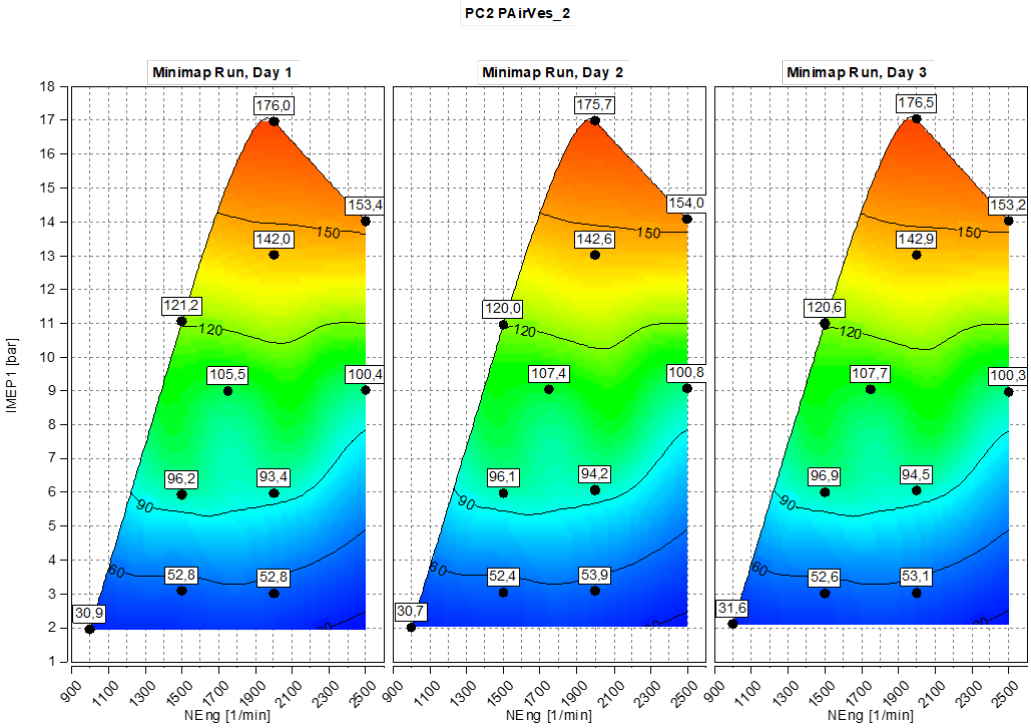

Figure A.49: PC2 Intake Pressure, [kPa]

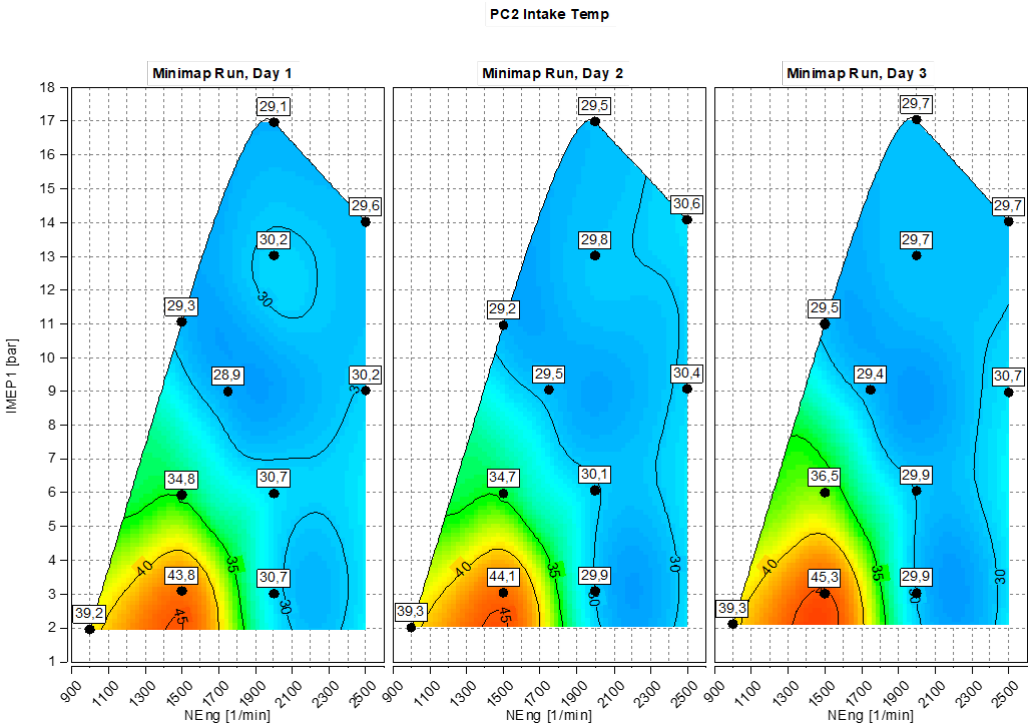

Figure A.50: PC2 Intake Temperature, [°C]

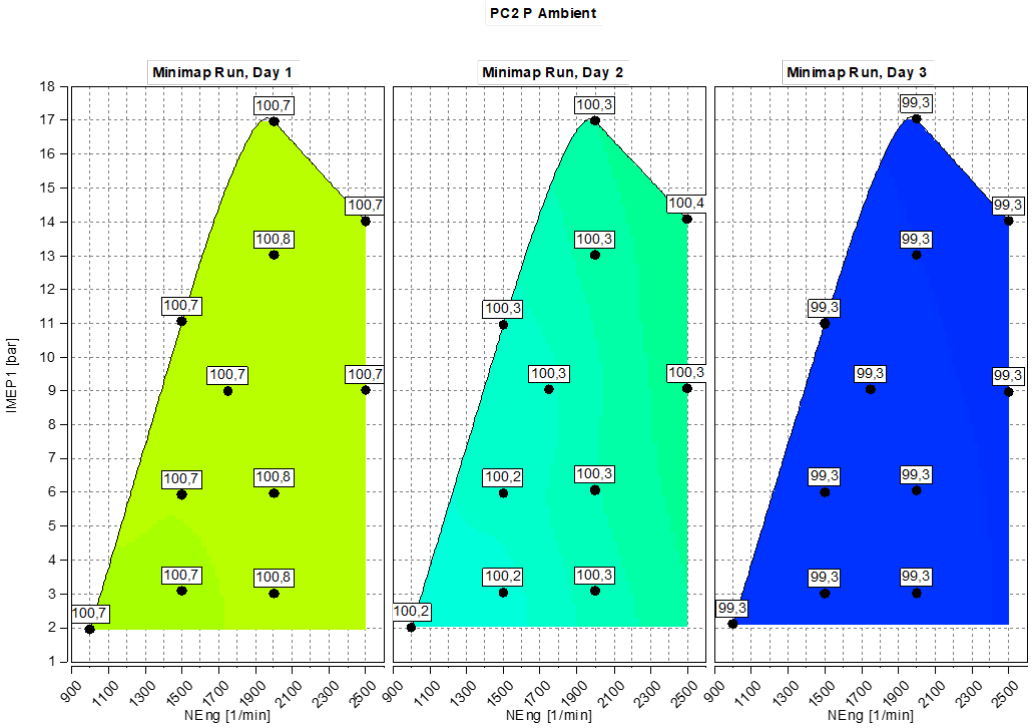

Figure A.51: PC2 Ambient Pressure, [kPa]

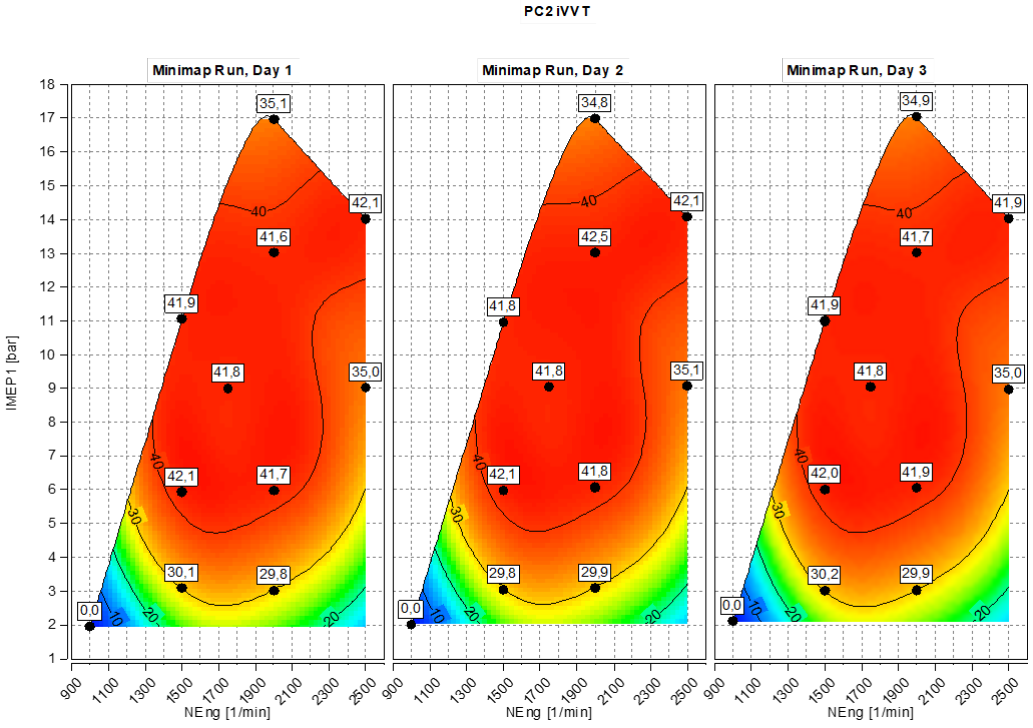

Figure A.52: PC2 iVVT

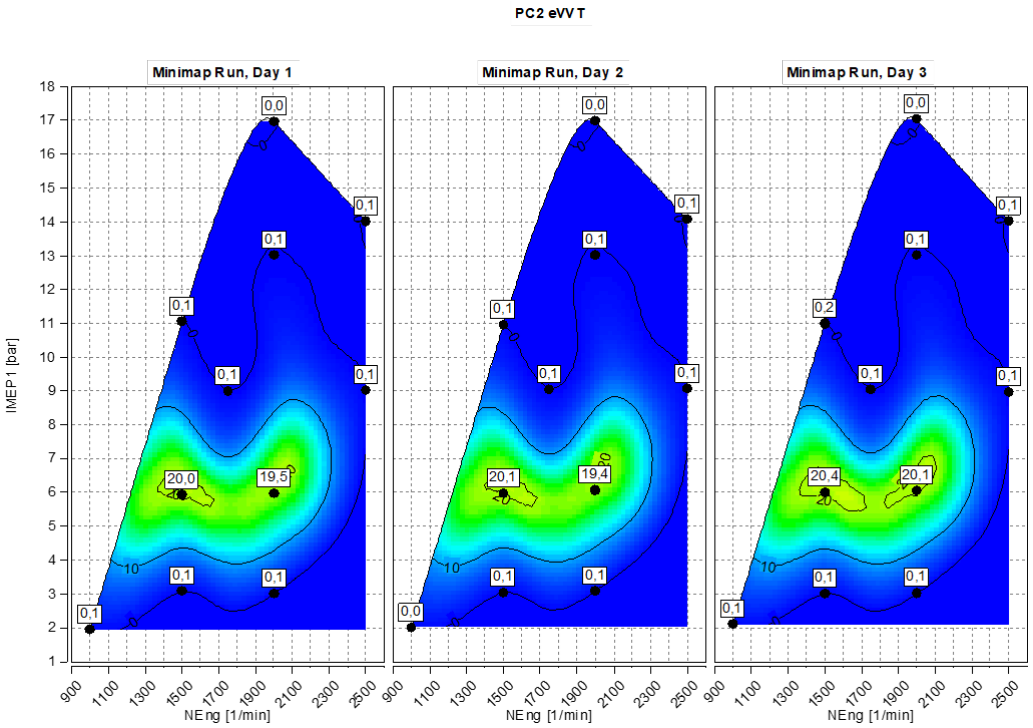

Figure A.53: PC2 eVVT

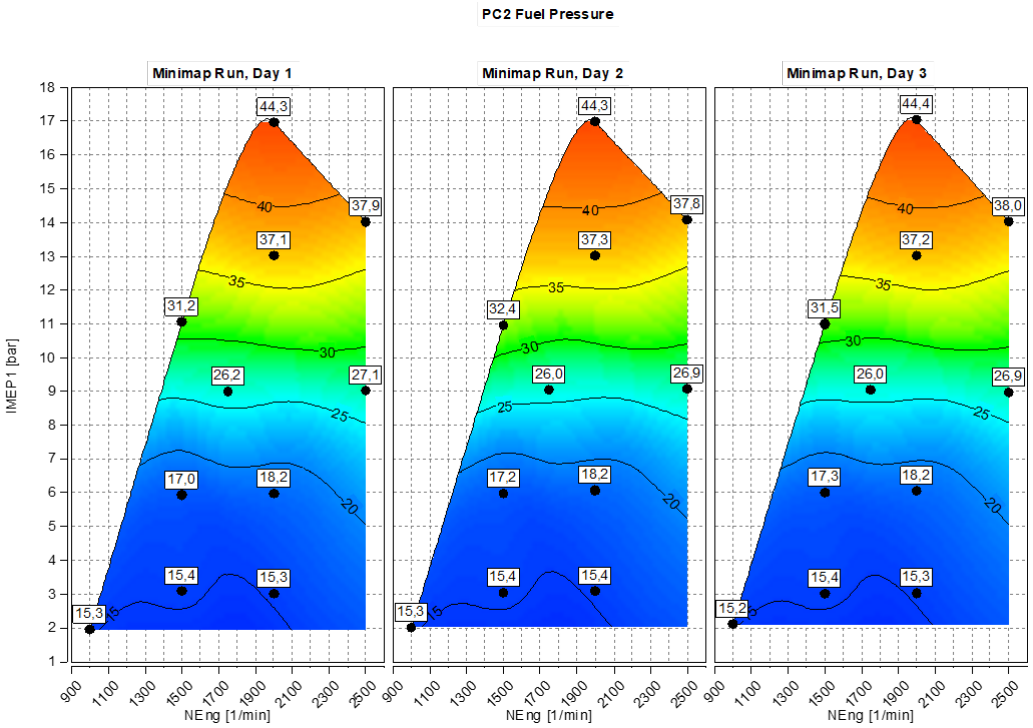

Figure A.54: PC2 Fuel Pressure,[MPa]

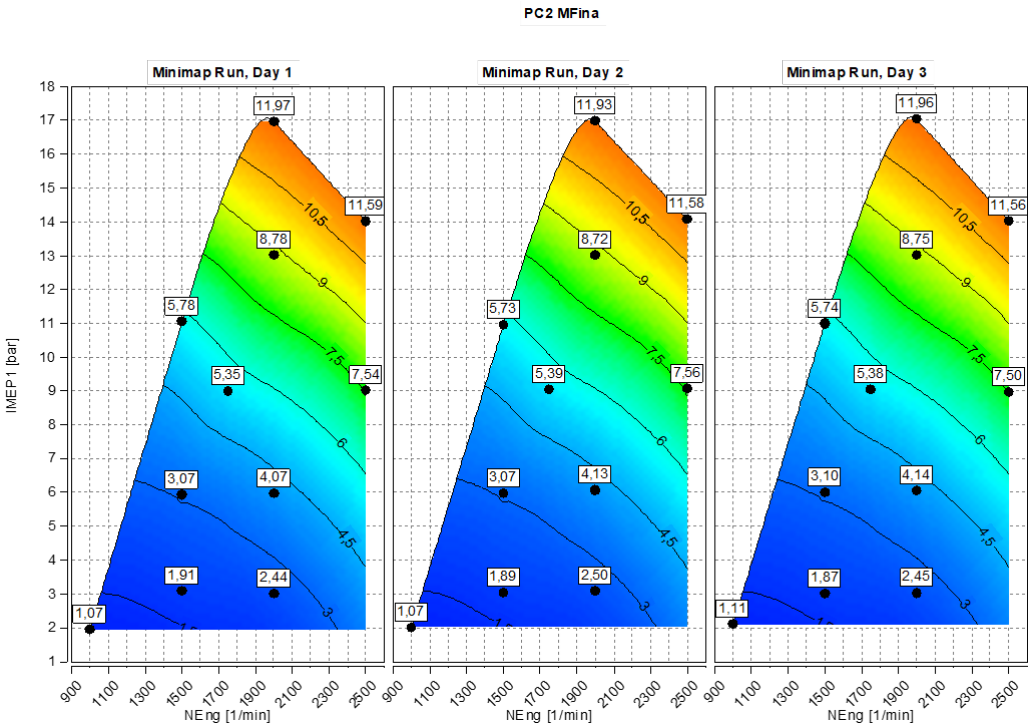

Figure A.55: PC2 Intake Massflow, [g/s]

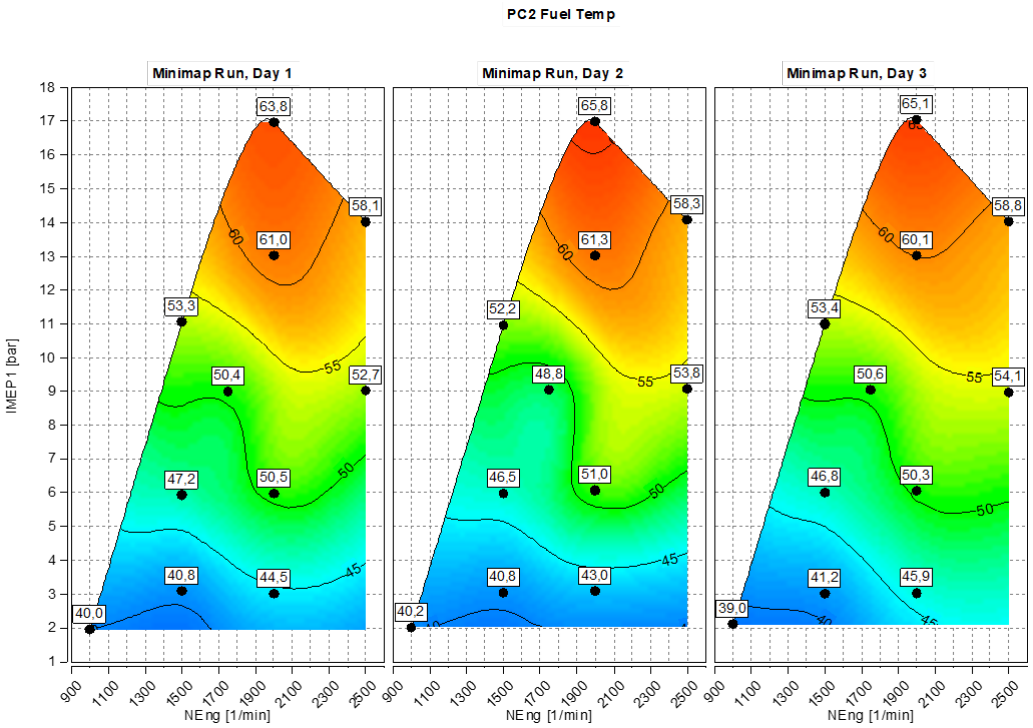

Figure A.56: PC2 Fuel Temperature, [°C]

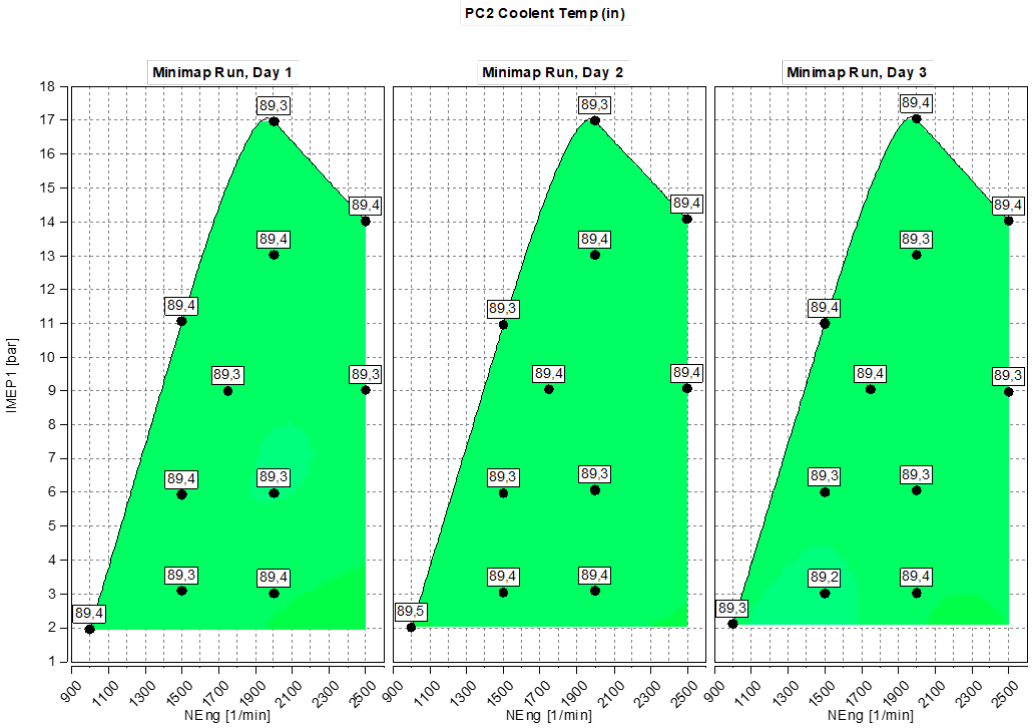

Figure A.57: PC2 Coolant Temperature, [°C]

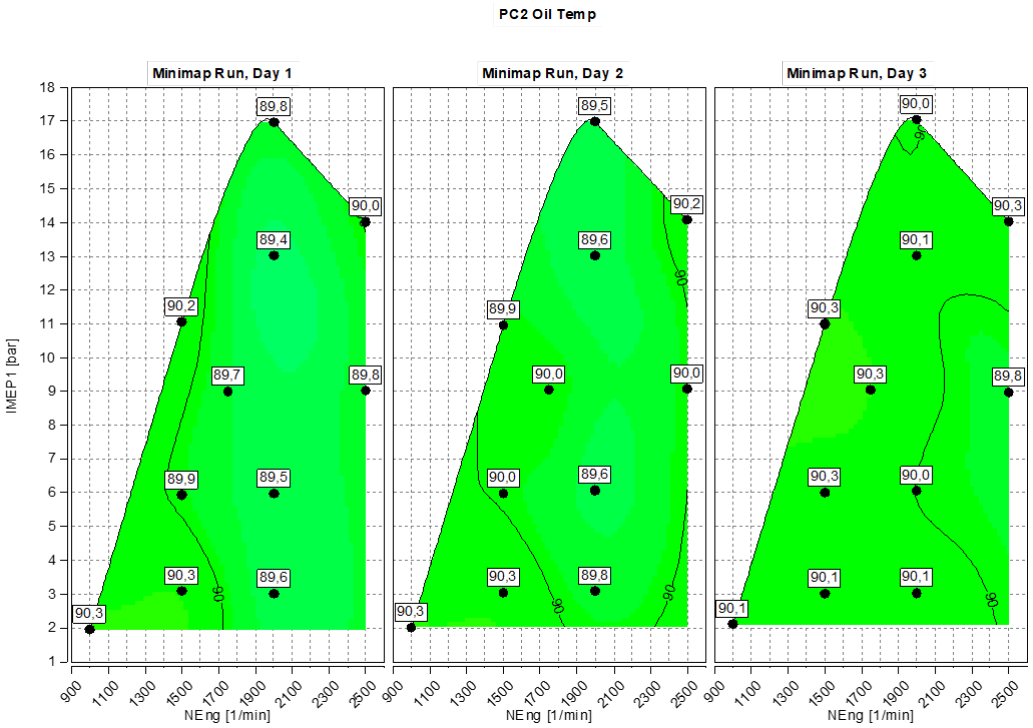

Figure A.58: PC2 Oil Temperature, [°C]

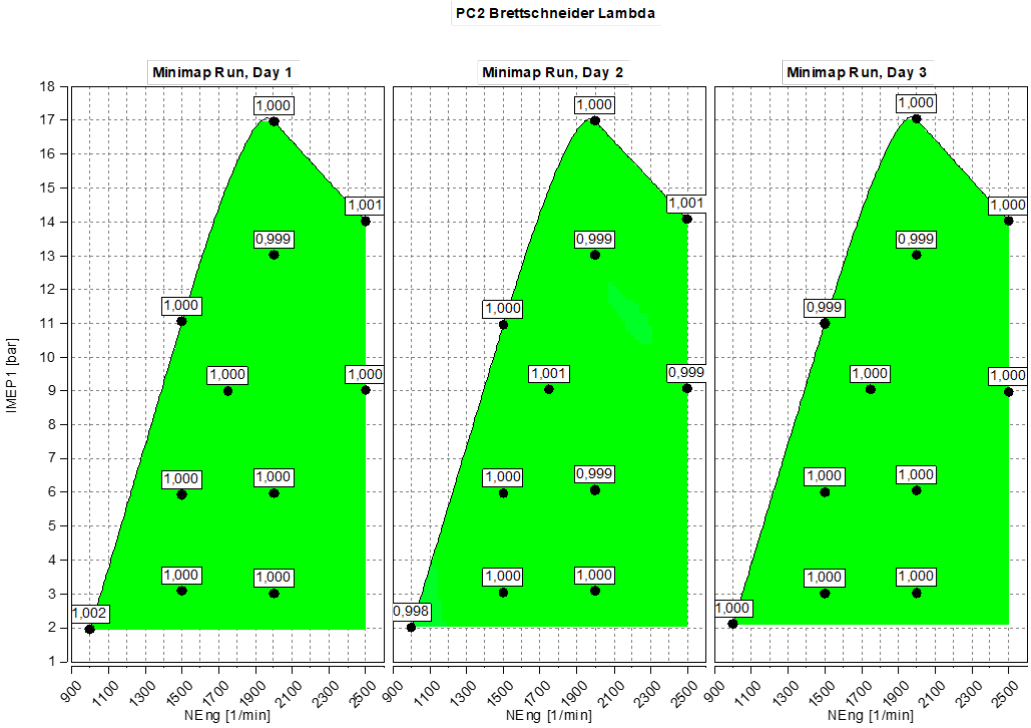

Figure A.59: PC2 Lambda Brettschneider

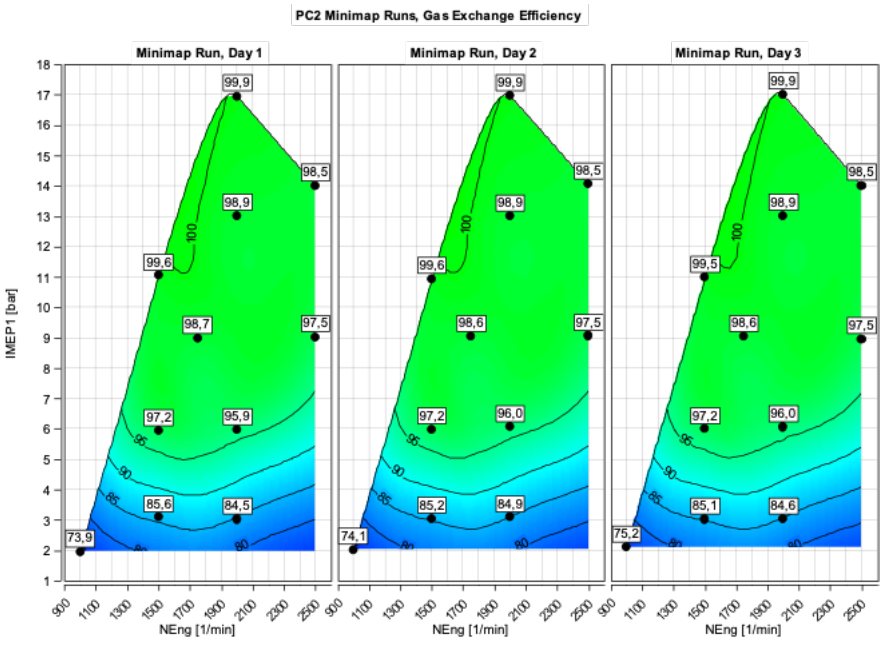

Figure A.60: PC2 Gas Exchange Efficiency [%]

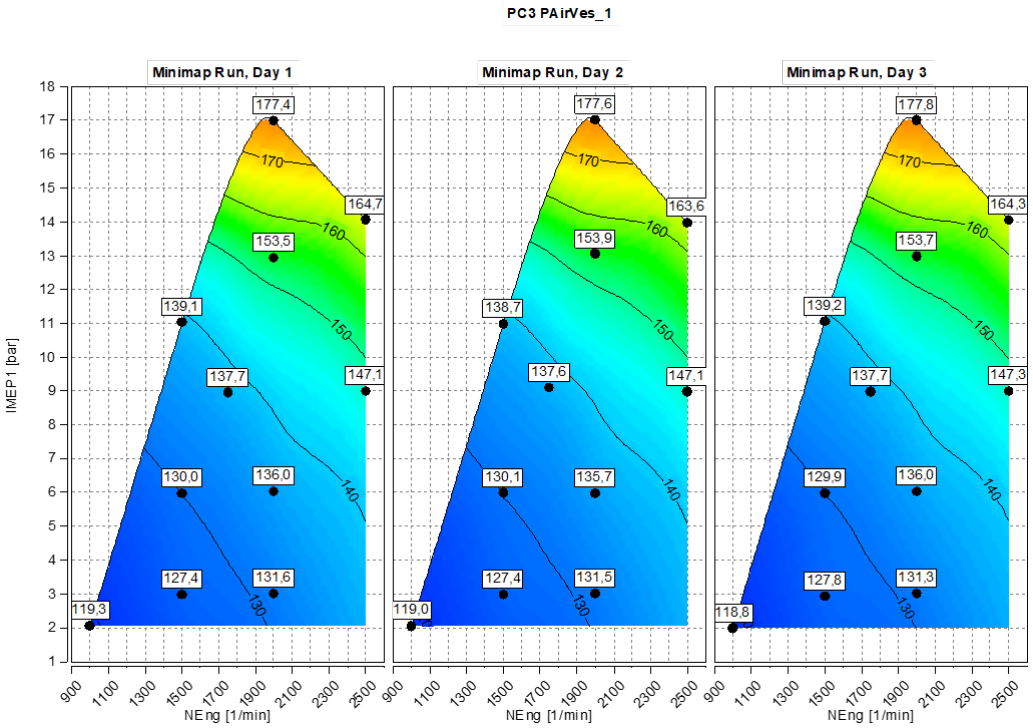

Figure A.61: PC3 Intake Pressure, Vessel Bank 1 [kPa]

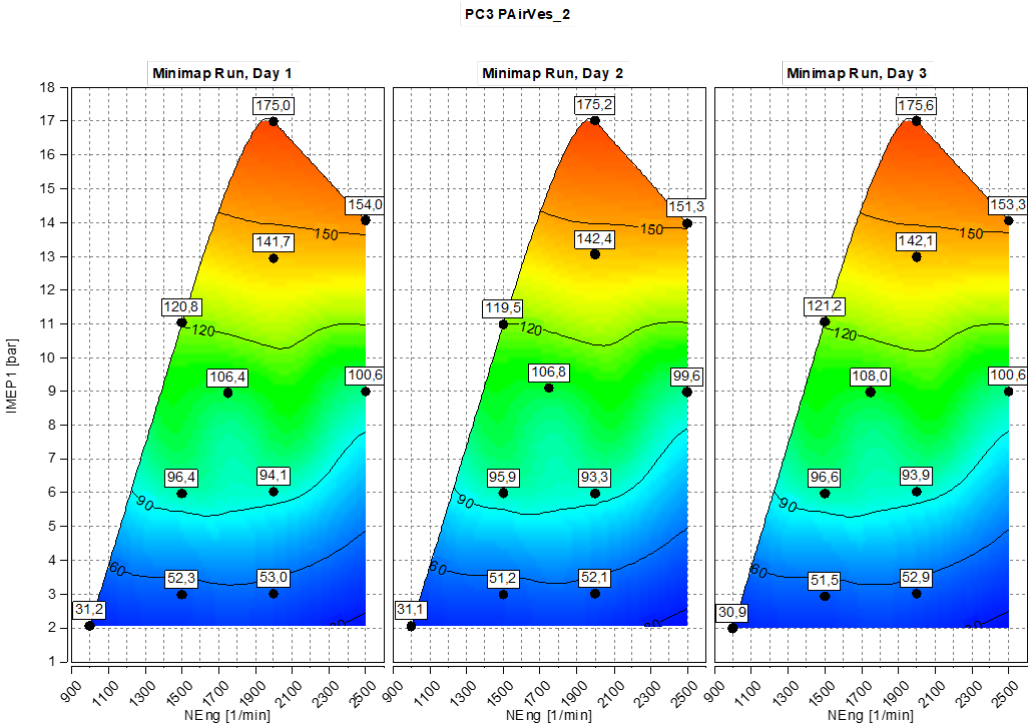

Figure A.62: PC3 Intake Pressure, Vessel Bank 2 [kPa]

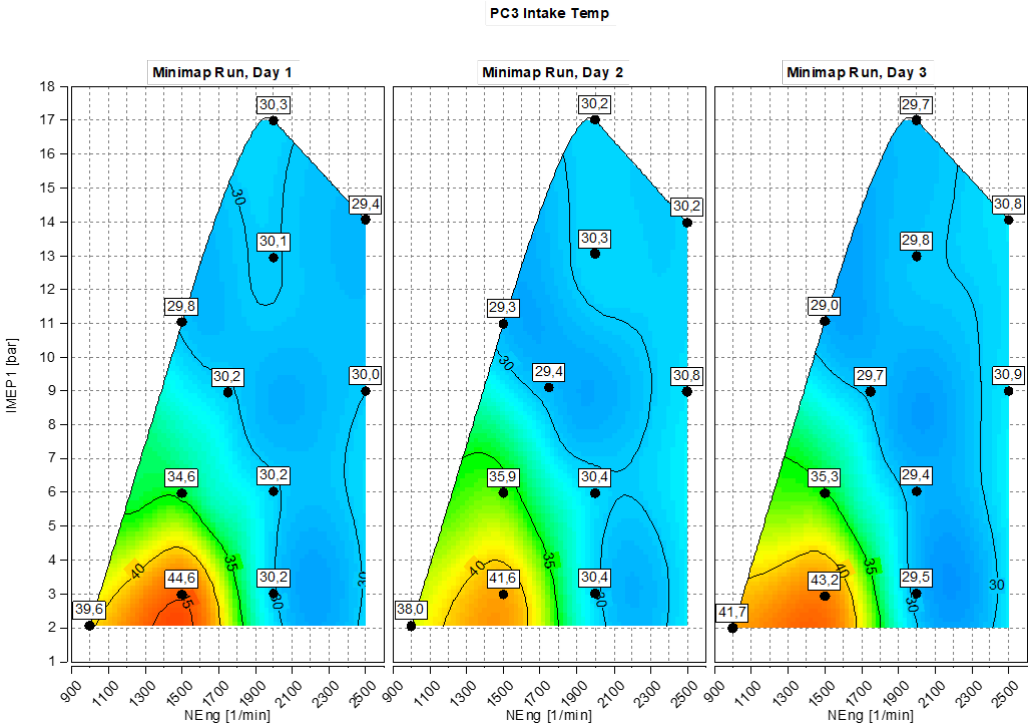

Figure A.63: PC3 Intake Temperature, [°C]

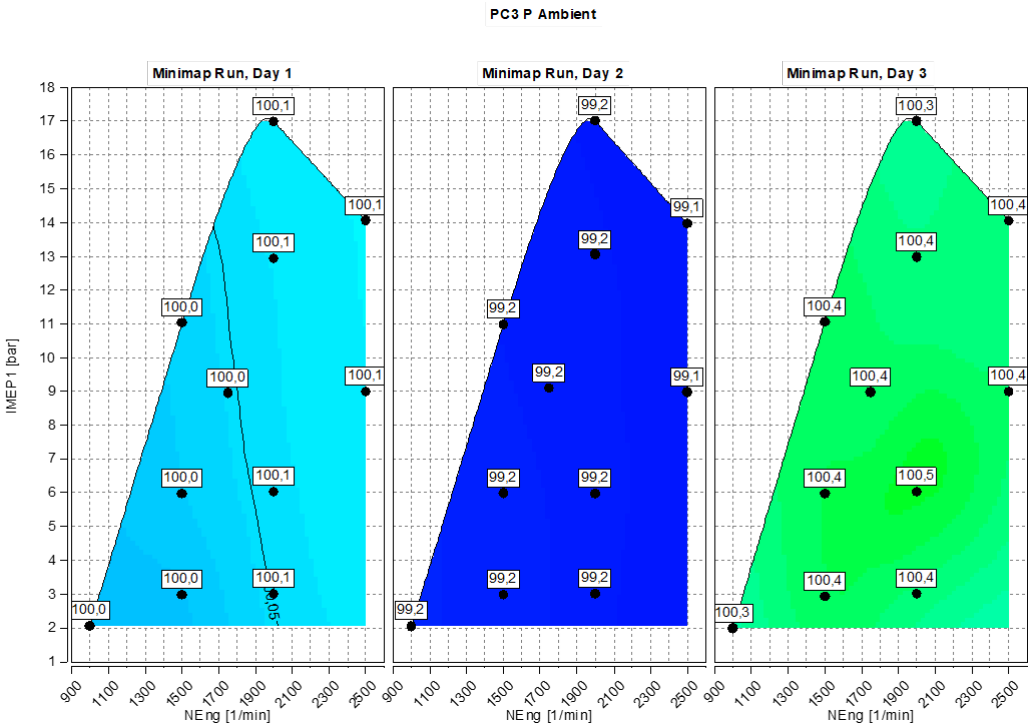

Figure A.64: PC3 Ambient Pressure, [kPa]

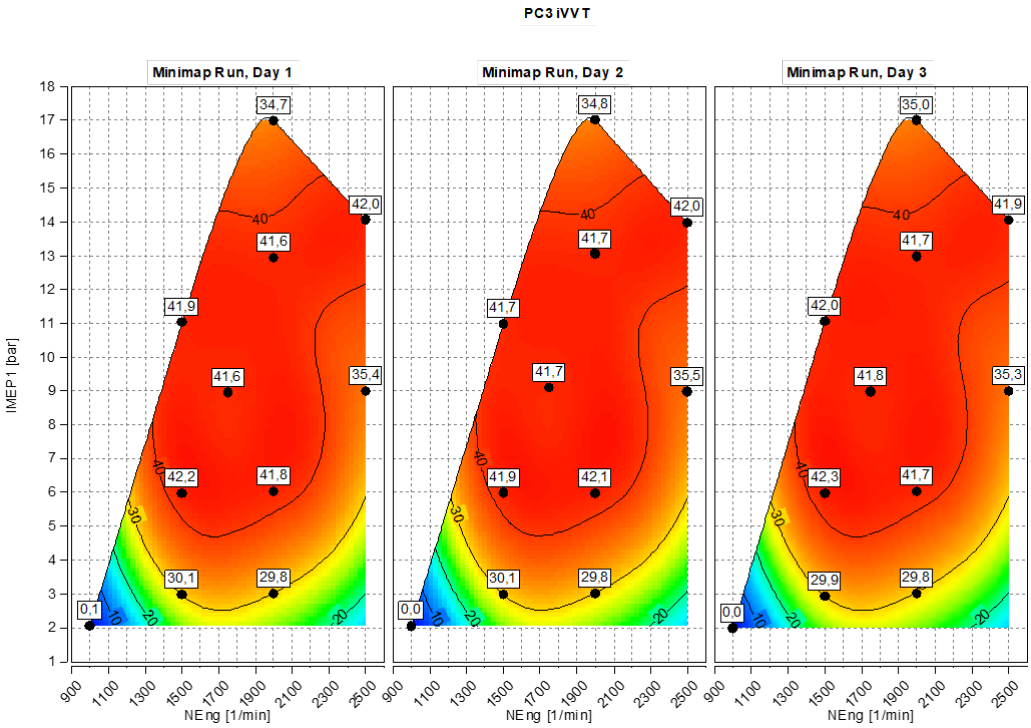

Figure A.65: PC3 iVVT

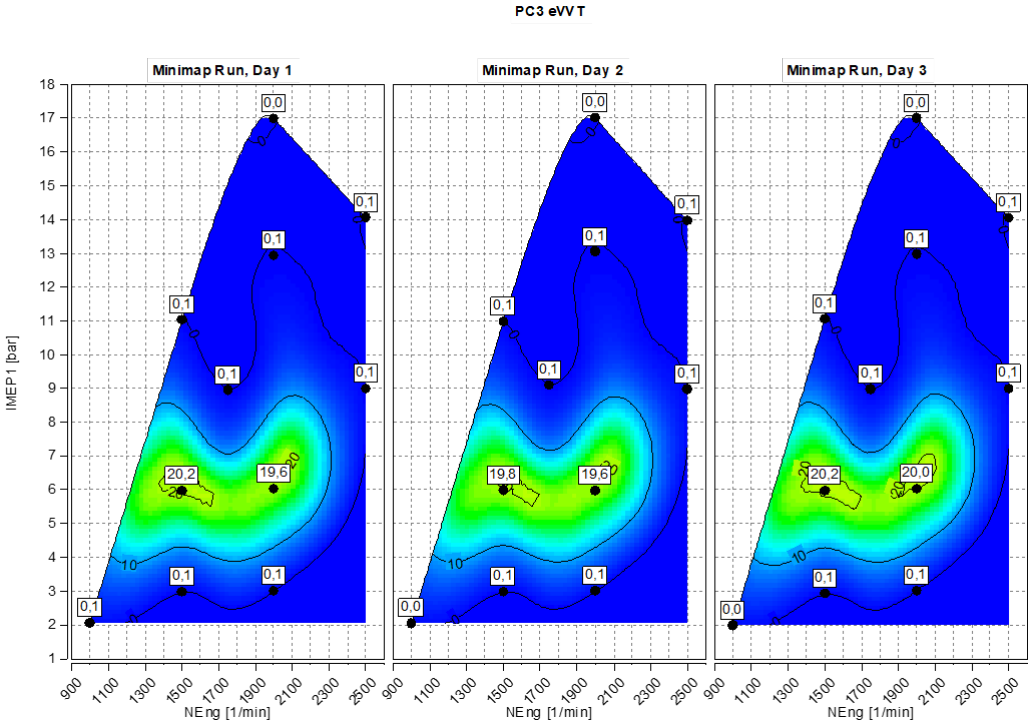

Figure A.66: PC3 eVVT

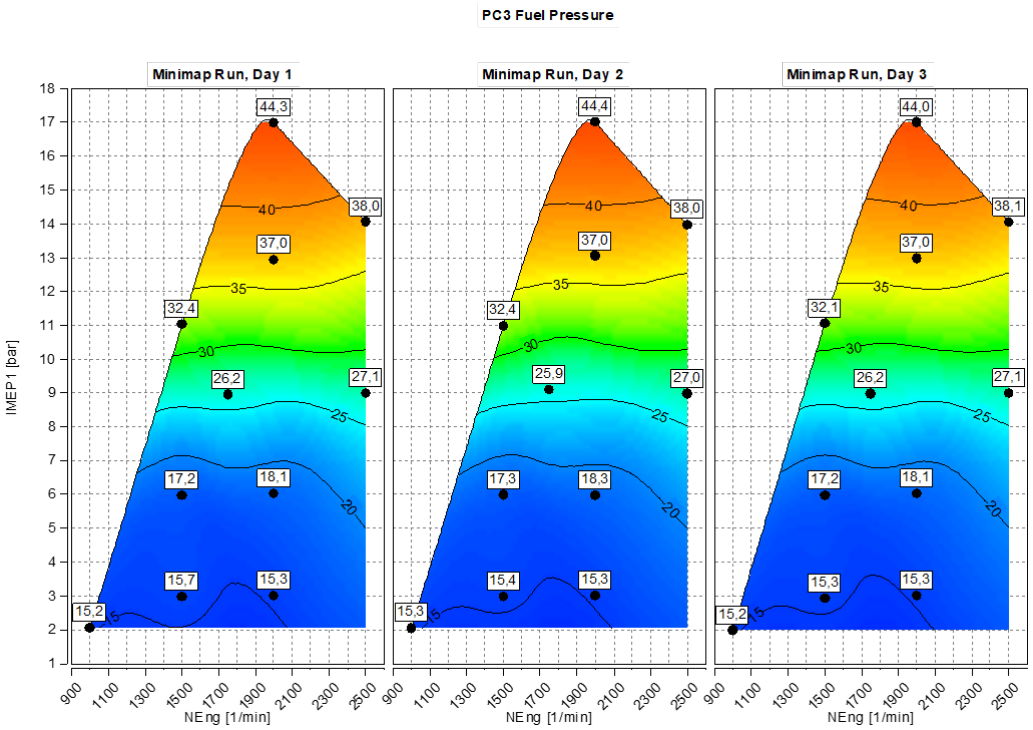

Figure A.67: PC3 Fuel Pressure,[MPa]

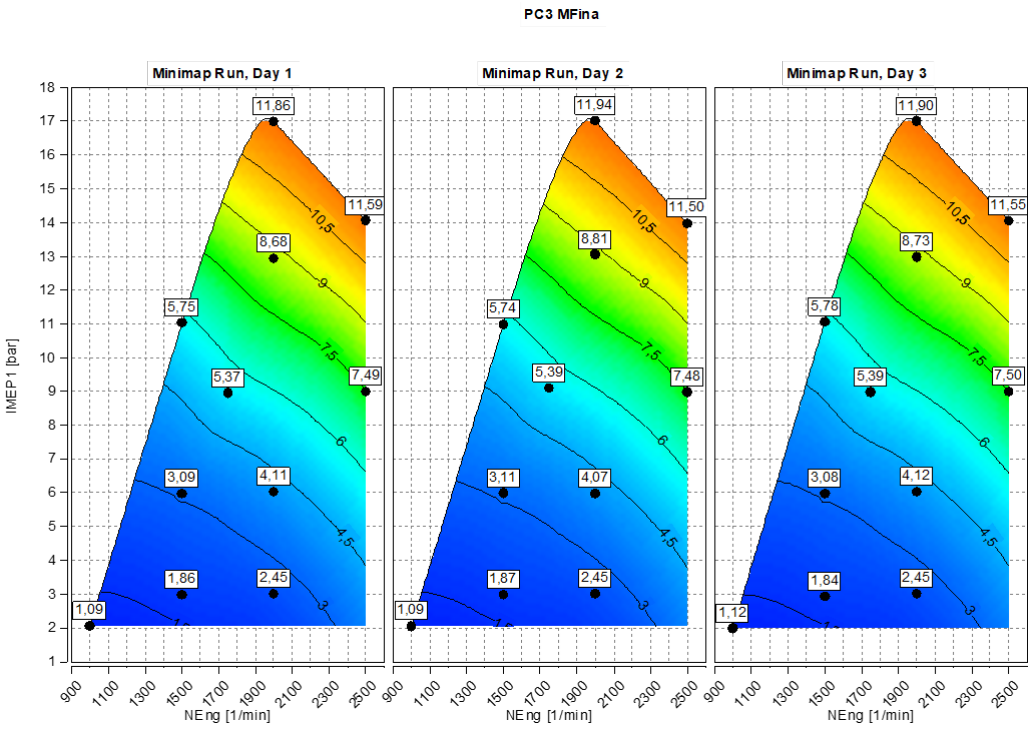

Figure A.68: PC3 Intake Massflow, [g/s]

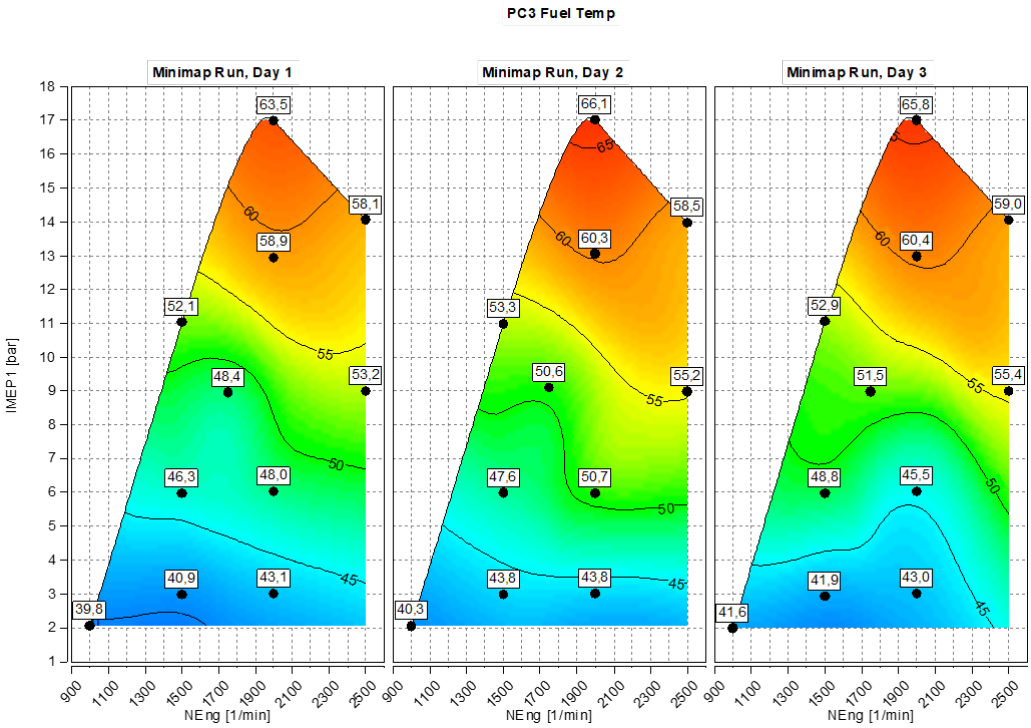

Figure A.69: PC3 Fuel Temperature, [°C]

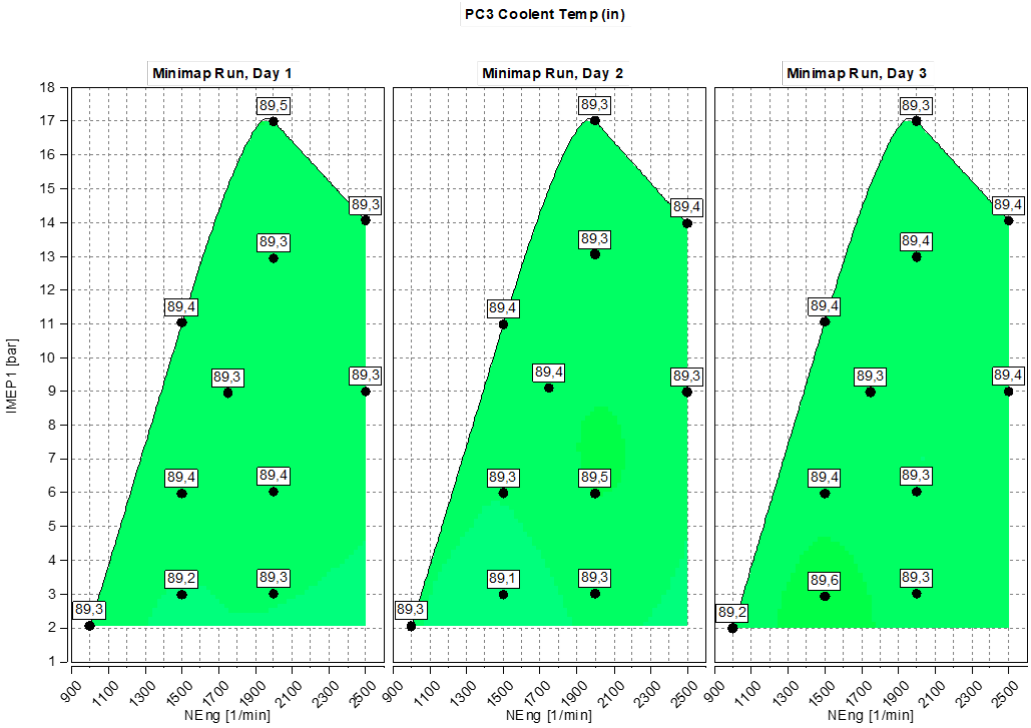

Figure A.70: PC3 Coolant Temperature, [°C]

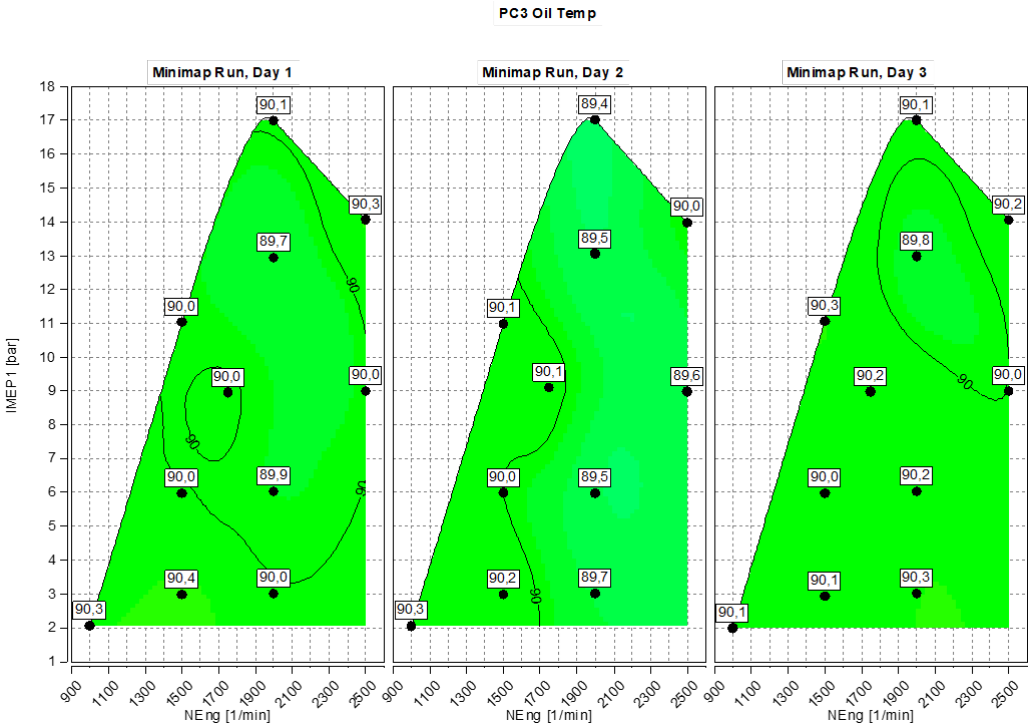

Figure A.71: PC3 Oil Temperature, [°C]

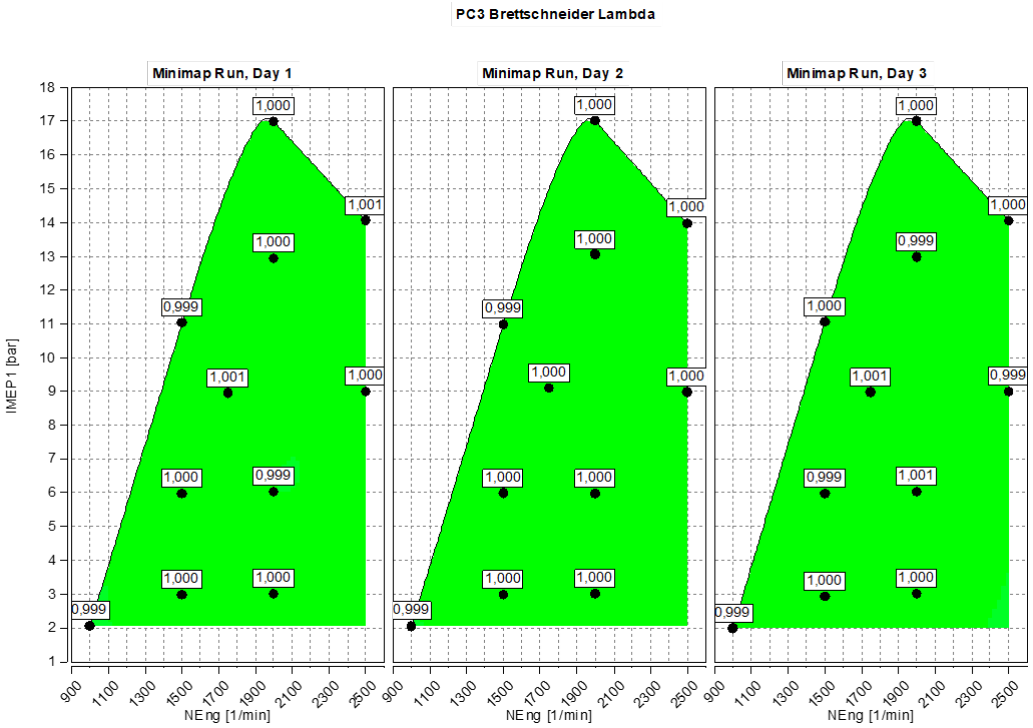

Figure A.72: PC3 Lambda Brettschneider

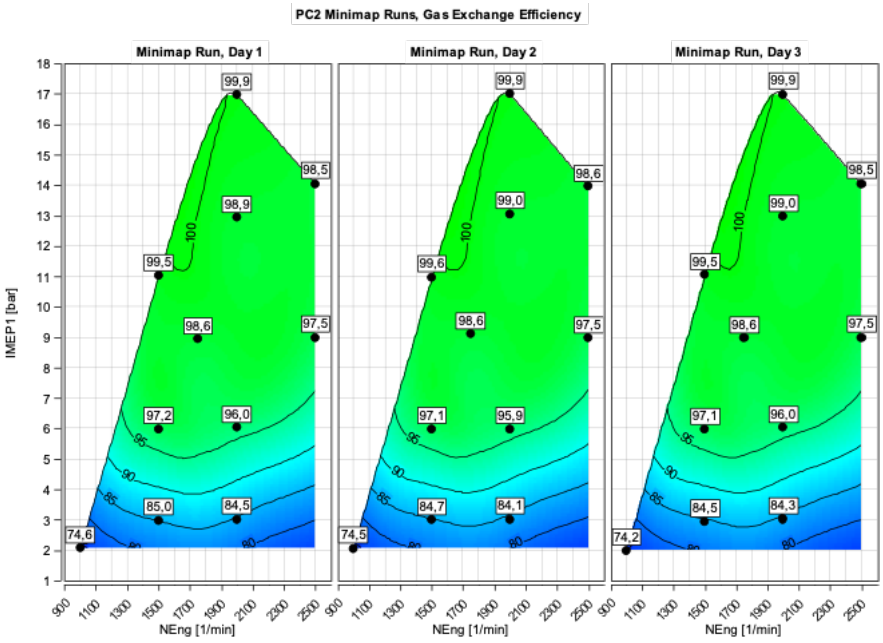

Figure A.73: PC3 Gas Exchange Efficiency [%]

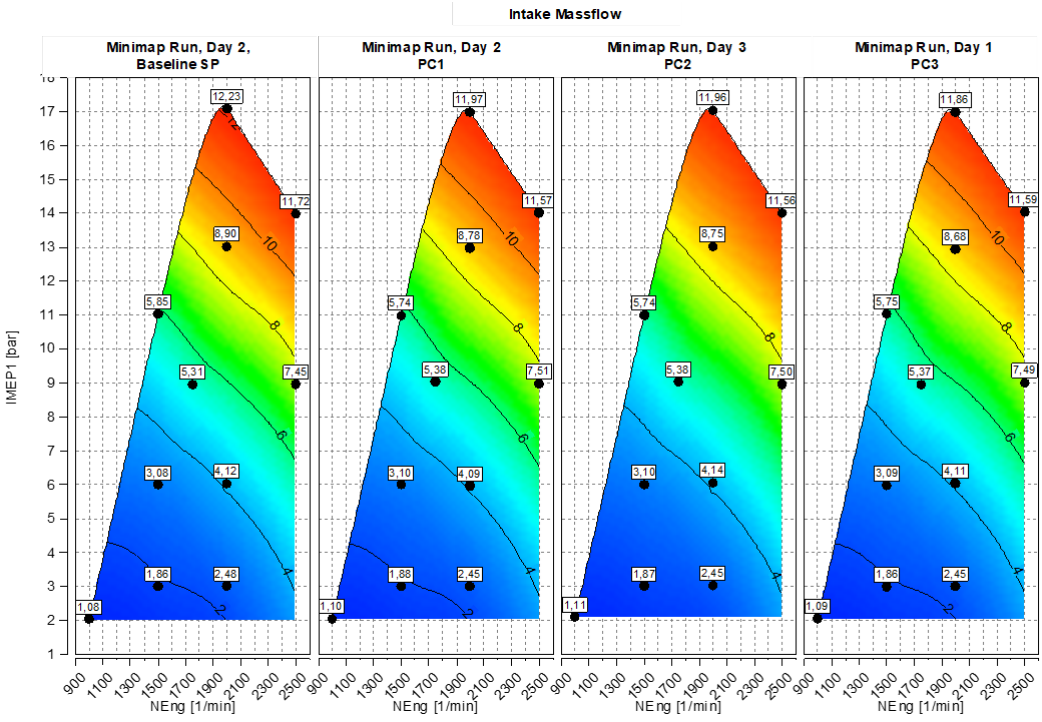

Figure A.74: Intake Mass Flow Air, Representative Runs

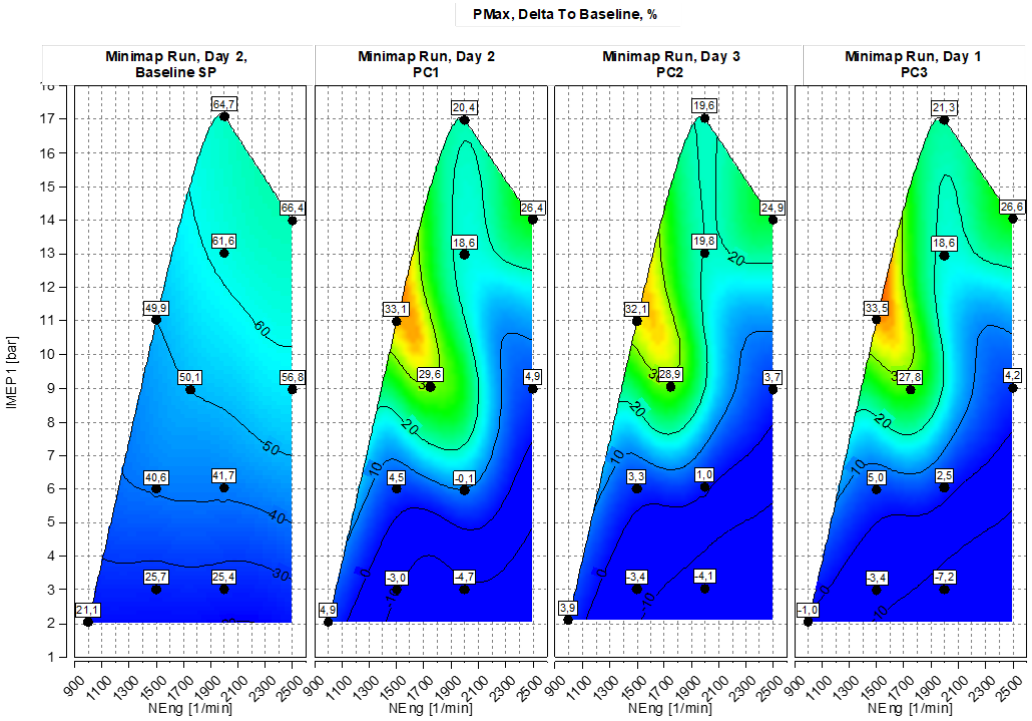

Figure A.75: PMax, Percentage Delta To Baseline

The AHR plots for the minimap runs with PC1 and baseline SP are the following

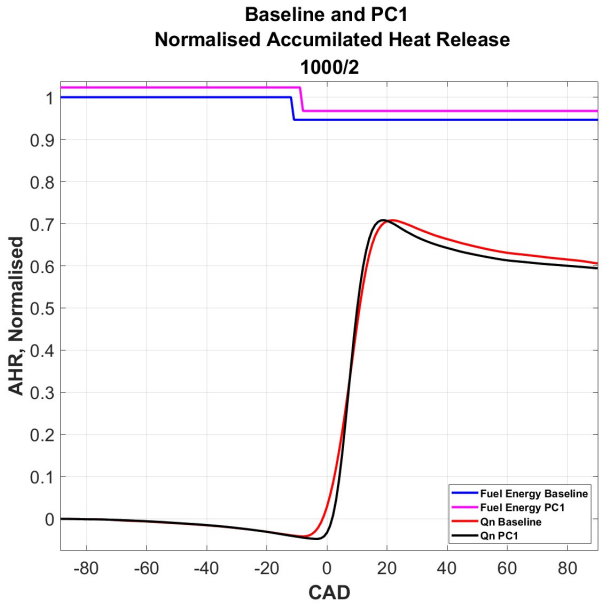

Figure A.76: AHR, Baseline SP and PC1, 2 bar IMEP @ 1000RPM

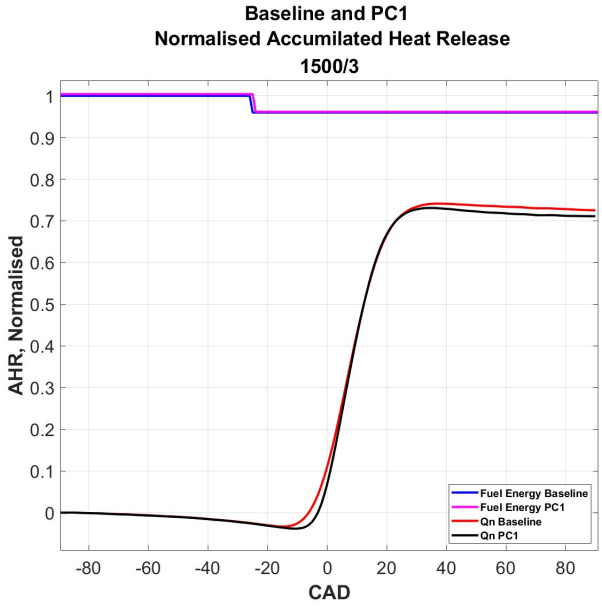

Figure A.77: AHR, Baseline SP and PC1, 3 bar IMEP @ 1500RPM

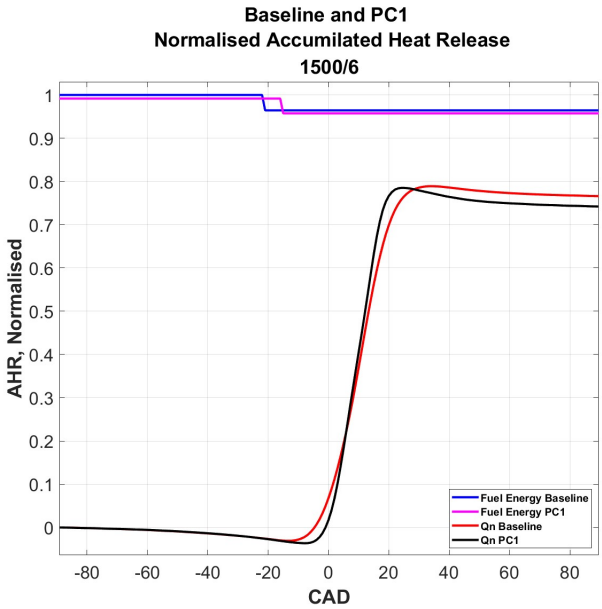

Figure A.78: AHR, Baseline SP and PC1, 6 bar IMEP @ 1500RPM

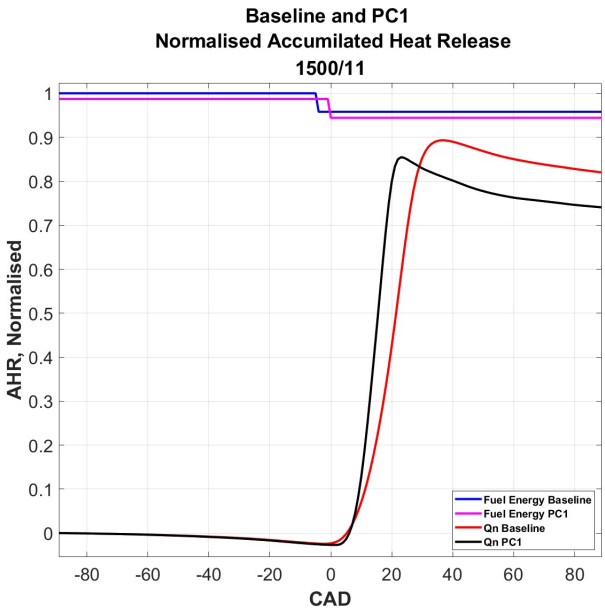

Figure A.79: AHR, Baseline SP and PC1, 11 bar IMEP @ 1500RPM

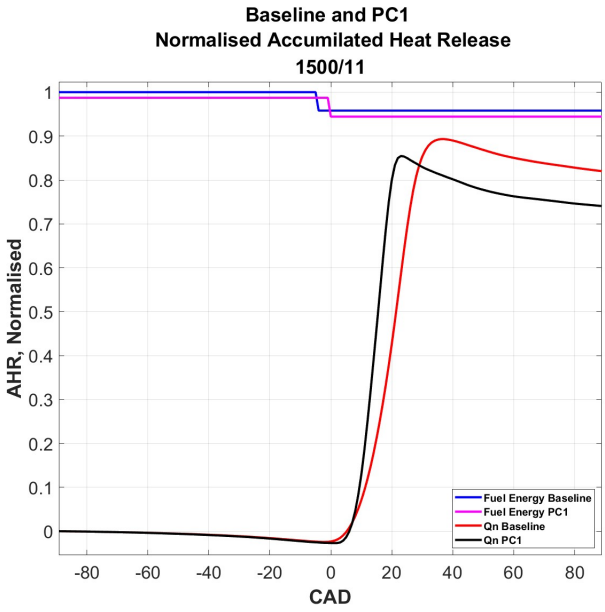

Figure A.80: AHR, Baseline SP and PC1, 9 bar IMEP @ 1750RPM

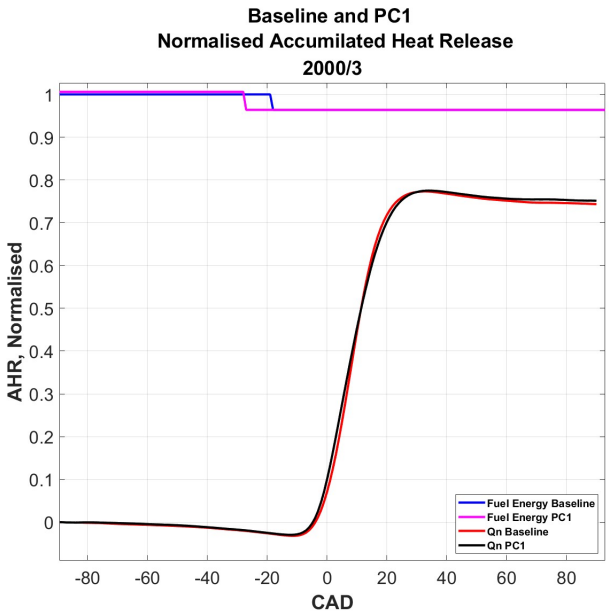

Figure A.81: AHR, Baseline SP and PC1, 3 bar IMEP @ 2000RPM

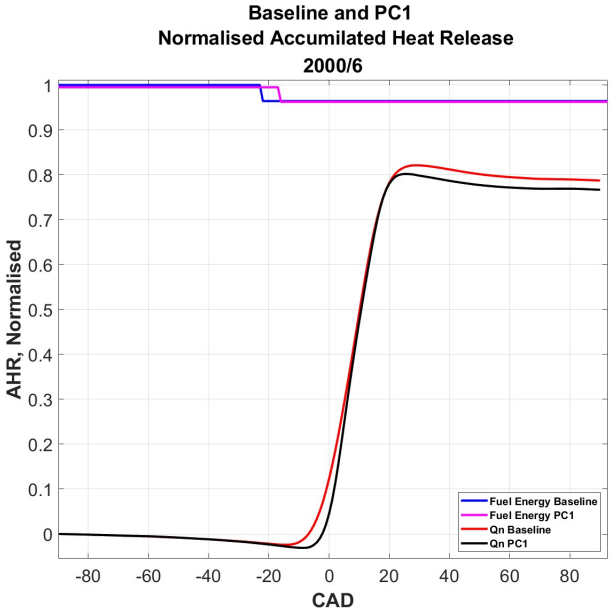

Figure A.82: AHR, Baseline SP and PC1, 6 bar IMEP @ 2000RPM

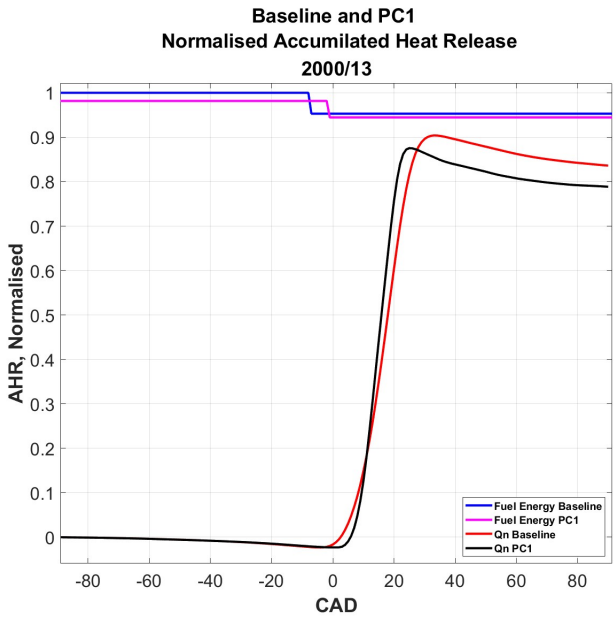

Figure A.83: AHR, Baseline SP and PC1, 13 bar IMEP @ 2000RPM

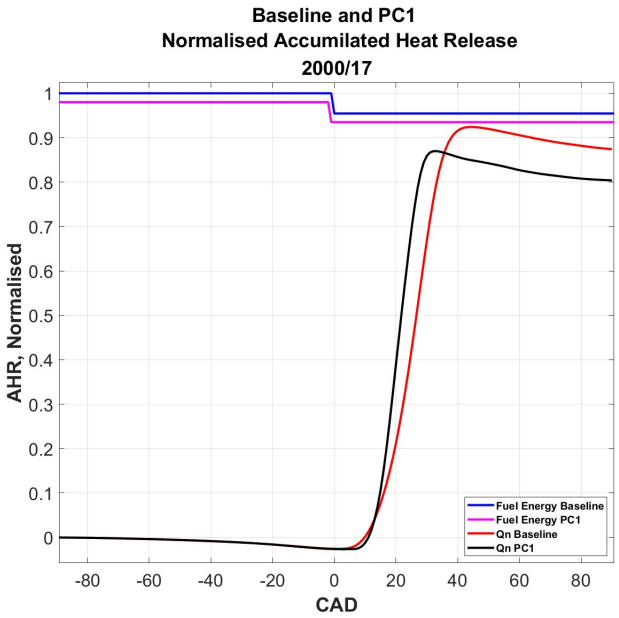

Figure A.84: AHR, Baseline SP and PC1, 17 bar IMEP @ 2000RPM

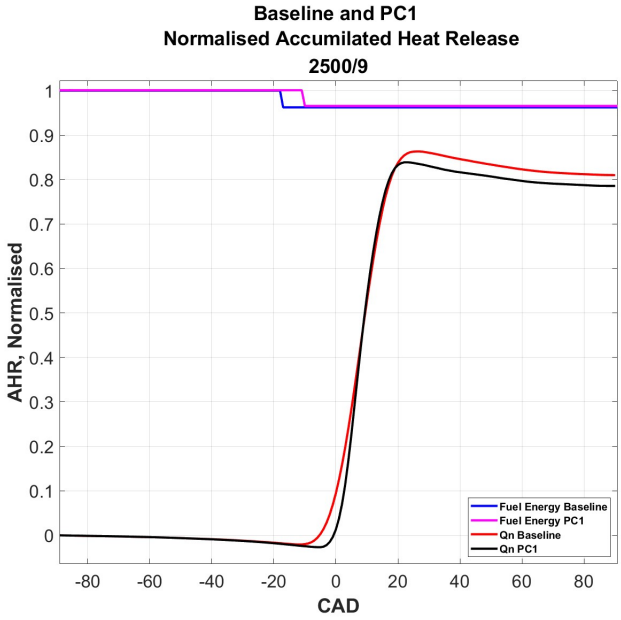

Figure A.85: AHR, Baseline SP and PC1, 9 bar IMEP @ 2500RPM

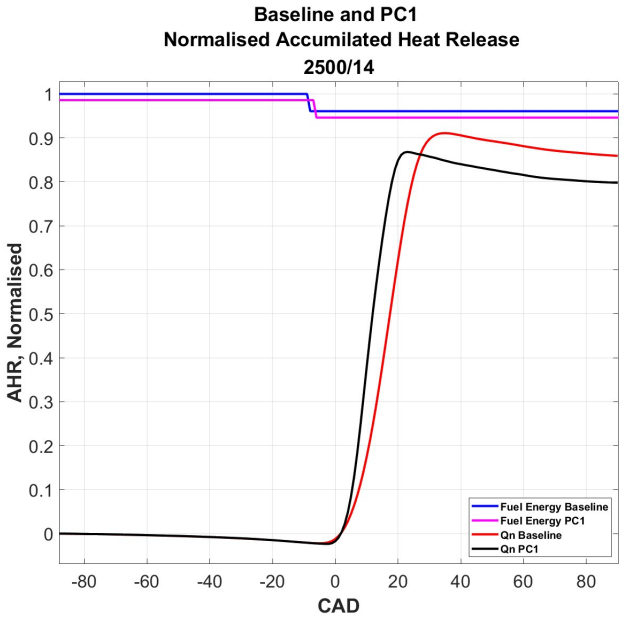

Figure A.86: AHR, Baseline SP and PC1, 14 bar IMEP @ 2500RPM

The cylinder pressure traces for some operation points in the minimap for PC1 and baseline SP.

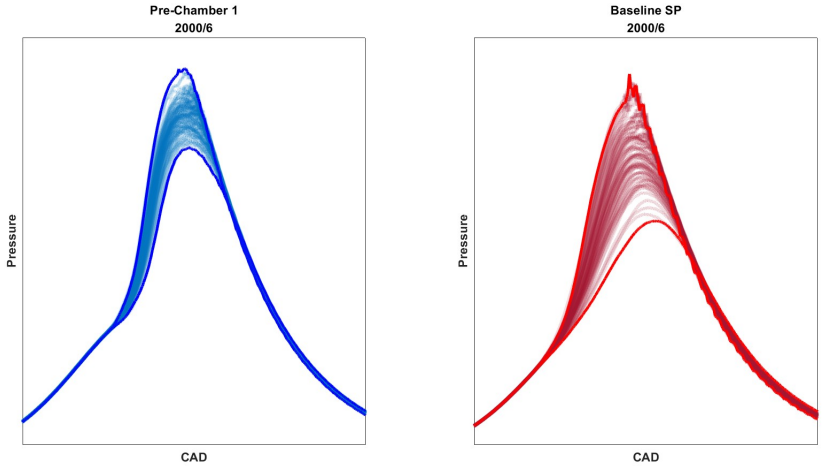

Figure A.87: Pressure Traces, 6 bar IMEP @ 2000RPM, PC1 and Baseline SP, 100 Cycles.

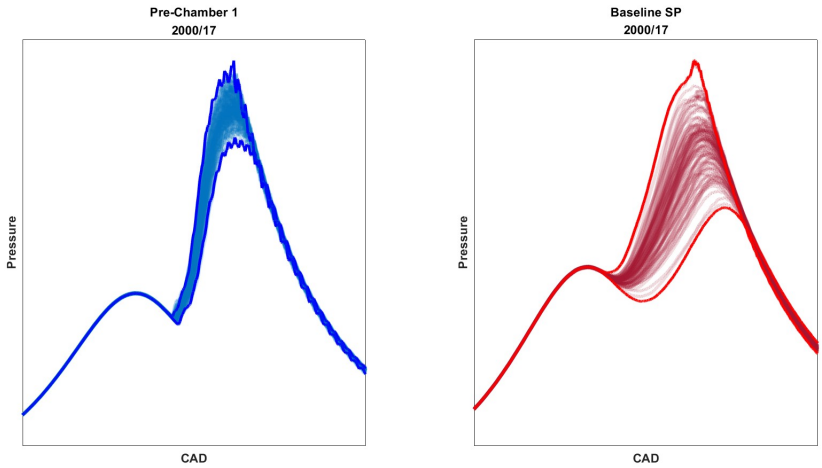

Figure A.88: Pressure Traces, 17 bar IMEP @ 2000RPM, PC1 and Baseline SP, 100 Cycles.

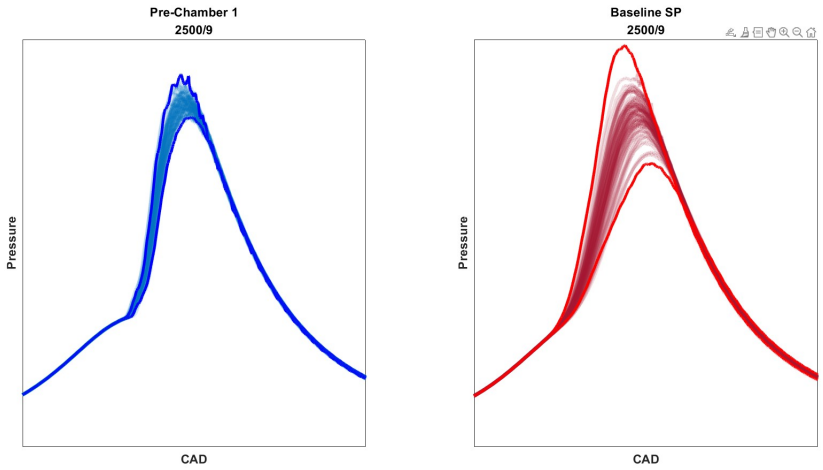

Figure A.89: Pressure Traces, 9 bar IMEP @ 2500RPM, PC1 and Baseline SP, 100 Cycles.

The emissions for the maximum power extraction for the pre-chambers during WOT test from Section 5.4 are depicted in figures A.90, A.91 and A.92 for CO, NO_x and THC respectively.

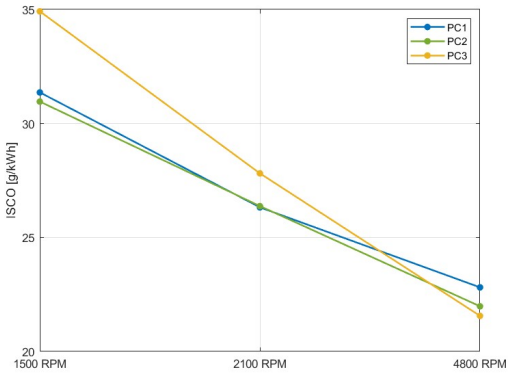

Figure A.90: CO Emissions

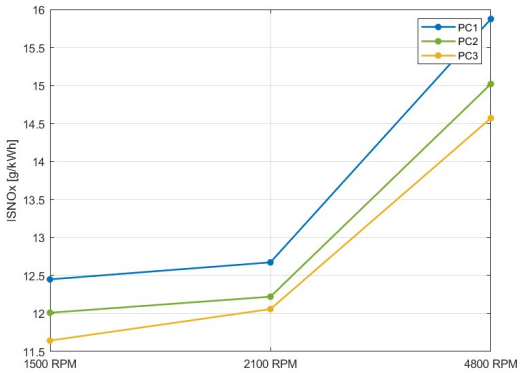

Figure A.91: NO_x Emissions

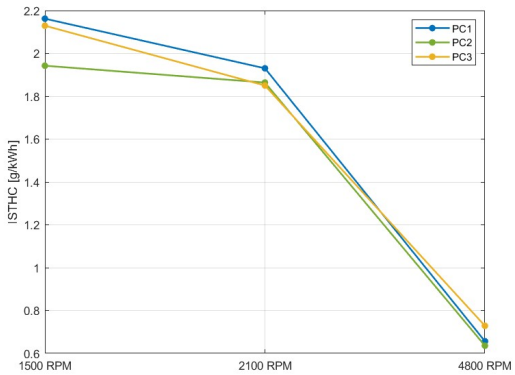

Figure A.92: THC Emissions

DEPARTMENT OF SOME SUBJECT OR TECHNOLOGY
CHALMERS UNIVERSITY OF TECHNOLOGY
Gothenburg, Sweden
www.chalmers.se

CHALMERS
UNIVERSITY OF TECHNOLOGY